論文 / 著書情報
Article / Book Information

題目(和文)	マライタ島に産する捕獲岩から読む、オントンジャワ海台下マントルの形成・発達過程
Title(English)	Evolution of sub-Ontong Java Plateau mantle : implications from petrogenesis of Malaitan xenoliths
著者(和文)	石川晃
Author(English)	Akira Ishikawa
出典(和文)	学位:博士(理学), 学位授与機関:東京工業大学, 報告番号:甲第4979号, 授与年月日:2002年3月26日, 学位の種別:課程博士, 審査員:
Citation(English)	Degree:Doctor (Science), Conferring organization: Tokyo Institute of Technology, Report number:甲第4979号, Conferred date:2002/3/26, Degree Type:Course doctor, Examiner:
学位種別(和文)	博士論文
Type(English)	Doctoral Thesis

Evolution of sub-Ontong Java Plateau mantle: implications from petrogenesis of Malaitan xenoliths

Akira Ishikawa

Tokyo Institute of Technology,

Department of Earth and Planetary Sciences

February 2002.

Contents

Abstract

The Ontong Java Plateau (OJP), which is the largest of the world's LIPs is partly exposed in Malaita, Solomon Islands. The 122 Ma basement was intruded by the 34 Ma alnöite, which contains a varied suite of mantle-derived xenoliths represented as fragments of sub-OJP mantle. Petrological, geothermobarometric and geochemical studies of more than 150 rock samples have been studied to reconstruct the mantle stratigraphy at the time of eruption and to identify the dominant processes which operated to produce the diverse lithology and chemistry observed. Major classification is grounded on lithology: peridotite suites (modal olivine > 40%), pyroxenite suites (usually no olivine) and megacryst suites (usually monomineralic). Further classification is based on equilibrium conditions: low-temperature type (LT-type: <1100˚C, < 2.7 GPa) and high-temperature type (HT-type: >1200˚C, > 3.0 GPa), showing that both peridotite and pyroxenite suites resided over a large depth interval (Moho ~ 120 km).

(1) LT-type pyroxenites are dominated by cooling metamorphic reaction. Primary mineralogy and chemistry could result from single fractionation process representing as early cumulate. The inferred crystallization sequence is clinopyroxene-orthopyroxene-spinel-garnet, showing on apparent lack of olivine precipitation. (2) The chemical signatures of LT-type peridotites require the involvement of mainly two processes: partial melting and subsequent metasomatism. LREE abundances in clinopyroxenes are varied owing to chromatographic enrichment process, whereas HREE abundances in clinopyroxenes significantly correlate with other depletion indicators (Cr# in spinel and Fo# in olivine), showing close similarity with abyssal peridotites. Possible depletion-depth correlation indicates that they consisted the part of melting column of ascending asthenospheric mantle. (3) HT-type pyroxenites comprising quartz-garnet clinopyroxenite, refractory garnet clinopyroxenite and garnet orthopyroxenite resided in the bottom of sub-OJP lithospheric mantle based on the P-T estimates. Depleted nature of quartz-garnet clinopyroxenite indicates the presence of siliceous melt produced by genuine basalt melting in high-pressure region (> 3.0 GPa). Also subsequent reaction between the siliceous melt and surrounding peridotite is represented by the presence of orthopyroxenite with signatures of former peridotite. Their overall resemblance to

megacryst suites suggests that both are genetically related. (4) Most chemical signatures of HT-type peridotites display evidences of metasomatism caused by “megacryst melt”. Estimated P-T and REE patterns reveal the significant correlation. Deformed lherzolites with highest P-T have indistinguishable chemistry with megacryst suites. Whereas, relatively low P-T depleted spinel harzburgite and garnet lherzolite preserved the evidence of previous partial melting event.

These observations have made it possible to interpret the stratigraphy and speculate on the evolution of the sub-OJP mantle. Sub-OJP mantle had a two-layered structure, which were genetically unrelated. The uppermost mantle (Moho ~ 80 km) originated at mid-oceanic ridge which were located southward of the OJP (Pacific-Phoenix Ridge). Although some deeper garnet-spinel lherzolites may have been accreted under the bottom of the lithosphere without melting, it failed to detect the signature of low-degree melting because of metasomatic effect. After that the 122 Ma OJP basement was constructed through the partial melting of a heterogeneous mantle plume, which were comprised peridotite and basalt. The plume impinged upon pre-existing lithospheric mantle and was interrupted further ascending approximately 80 km in depth. LT-type pyroxenites originated as cumulate precipitating along the magma conduits developed in pre-existing lithosphere at the OJP formation. They might have brought about the metasomatic enrichment of spatially-associated peridotites (LT-type peridotite) with a residual nature. HT-type peridotites and pyroxenites consisting the lower part of the mantle (> 80 km) are represented as residues of OJP melt formed by melting of a basalt / peridotite composite source. Possible depth-lithological variation have been found in HT-type, such as upper zone: garnet-free harzburgite, middle zone: originally depleted-garnet lherzolite and deep zone: abundant pyroxenite and may be explained that the degree of depletion was systematically different at each depth of the adiabatically ascending mantle column. Some megacryst suites might have evolved from deep OJP melt which was prevented from eruption through the low-degree melting of matrix peridotite. Depth-related metasomatism followed depletion of HT-type peridotite and is attributed to the upward migration of the megacryst melt. These speculations are partly supported by the tomographic images below OJP, which have been interpreted as the presence of a low-velocity root traveling with the Pacific Plate since the OJP was formed.

1. Introduction

1-1 Significance of Malaitan xenoliths

The studies of rocks derived from the mantle have promoted our understanding of the lithological structures and the geochemical processes in the deep interior of the Earth because it is the most or only direct way in which these processes are observed. Samples derived from the mantle may be divided into (1) orogenic peridotite and part of ophiolite emplaced to the surface by tectonic movement and (2) mantle xenoliths carried to the surface by volcanic eruptions originating in the deep mantle. Both samples have different advantage and disadvantage for the investigations of the mantle. Advantage of the mantle xenoliths may be placed in their deeper and “frozen” nature relative to orogenic peridotite. On the other hand, their small sizes work as an apparent disadvantage for the understanding of spatial relationships. Most xenoliths in the Earth can be obtained as fragments of subcontinental mantle from kimberlite and alkali basalt in continental region, which have ancient origin. Some cratonic mantle xenoliths have the ages of 2-3 Ga and the same xenoliths also record the evidence of subsequent metamorphism and metasomatism prior to eruption ages (e.g. Richardson et al., 1985; Walker et al., 1989; Pearson et al., 1995). In that case it is very difficult to identify the link between surface events and signatures recorded in the xenoliths. In contrast, xenoliths from oceanic regions have restricted origin because most of the oceanic lithosphere is characterized by young ages and relatively regulated formation (e.g. Klein and Langmuir, 1987; McKenzie and Bickle, 1988; Johnson et al., 1990). However, shallow-seated xenoliths are usually dominant relative to continental region because depth of magma formation is significantly different (e.g. Nixon, 1987).

The island of Malaita, Solomon Islands, represents rare and famous locations of deep-seated garnet peridotite in spite that they derived in essentially oceanic environment (Nixon and Boyd, 1979; Neal, 1985). Most striking feature is the presence of megacryst suites, which have been used as “kimberlite indicator”. Also a similarity with kimberlite is expressed as the host magma, namely alnöite, which is of ultramafic composition. These features suggest that similar process operates in continental and oceanic regions and may be related to the unusual tectonic setting of Malaita Island.

1-2 Tectonic setting

Malaita is famous as “on-land exposure” of the Ontong Java Plateau (OJP), which is recognized as the world’s largest oceanic plateau or large igneous provinces (LIPs) occupying a 1600 x 800 km area (Fig. 1-1). The OJP, now locating in the south-west Pacific, was produced by an enormous volcanic activity during the Cretaceous, called as “Pacific Superplume” together with Manihiki Plateau, Mid-Pacific Mountains, Hess Rise and Shatsky Rise (e.g. Larson, 1991). The estimated total crustal volume of OJP is about 50 x 10^6 km^3 (Schubelt and Sandwell, 1989) and over twice as much as one-million year total volumetric output of the Earth’s sea-floor spreading today (~18 x 10^6 km^3/m.y.). According to seismic reflection and refraction measurements (Furumoto et al., 1970; Furumoto et al., 1976; Hussong et al., 1979), the crustal structure of OJP is similar to normal Pacific oceanic crust, however each layer has unusual thickness (Fig. 1-2). The average crustal thickness above the Moho is 33 km and the maximum value reaches to 38 km in the south central part of the plateau (Fig. 1-3, Richardson et al., 2000). Thickened crust and underlying mantle drifted with the Pacific Plate movement and prohibited the OJP from subducting beneath the Solomon Islands arc (e.g. Coleman and Kroenke, 1981; Petterson et al., 1999). According to the tectonic reconstruction by Petterson et al. (1999), the collision was commenced during Oligocene (25~20 Ma) expressed by ceasing arc volcanism and caused subduction flips from SW to NE direction about 12 Ma. Emergences of Malaita, Ulawa and part of Santa Isabel above sea level were achieved by the formation of an extensive fold belt with vertical stacking and major faulting in recent ~5 Ma.

1-3 Objectives of this study

Since discovery of boulders of ultrabasic rocks in streams (Rickwood, 1957), mantle-derived xenoliths of Malaitan alnöite have been investigated by many authors for considering evolution and compositions of mantle beneath OJP (e.g. Nixon and Boyd, 1979; Bielski-Zyskind et al., 1984; Neal and Nixon, 1985; Neal 1985,1988; Nixon and Neal, 1987; Neal and Davidson, 1989; Neal and Taylor, 1989; Collerson et al., 2000). Although Neal (1985) and subsequent detailed works revealed general situations of the xenoliths, there is apparent lack of a collective view for the

relationship between diverse nature of the xenoliths and origin of OJP owing to limited data and knowledge of both xenoliths and OJP itself. Therefore, study of Malaita xenoliths have still good opportunity for understanding not only origin of OJP and also general evolution of the lithospheric mantle because they were constructed by processes caused in oceanic region and not necessary for consideration of chemical modification by subducting slab.

The goals for the present study are (1) to understand the lithological diversity of the xenoliths from Malaita based on petrographic observations of newly collected samples and comparison of the xenoliths reported by previous studies. (2) to determine the major element compositions of constituent minerals and estimate the P-T conditions of individual xenoliths in order to reconstruct possible mantle stratigraphy. (3) to determine REE compositions of consisting garnets and clinopyroxenes in order to identify the kinds of process which were effective in xenolith chemistry. (4) to speculate on the evolution of sub-OJP mantle involving with consideration of observed crustal events, in particular contributions for OJP formation.

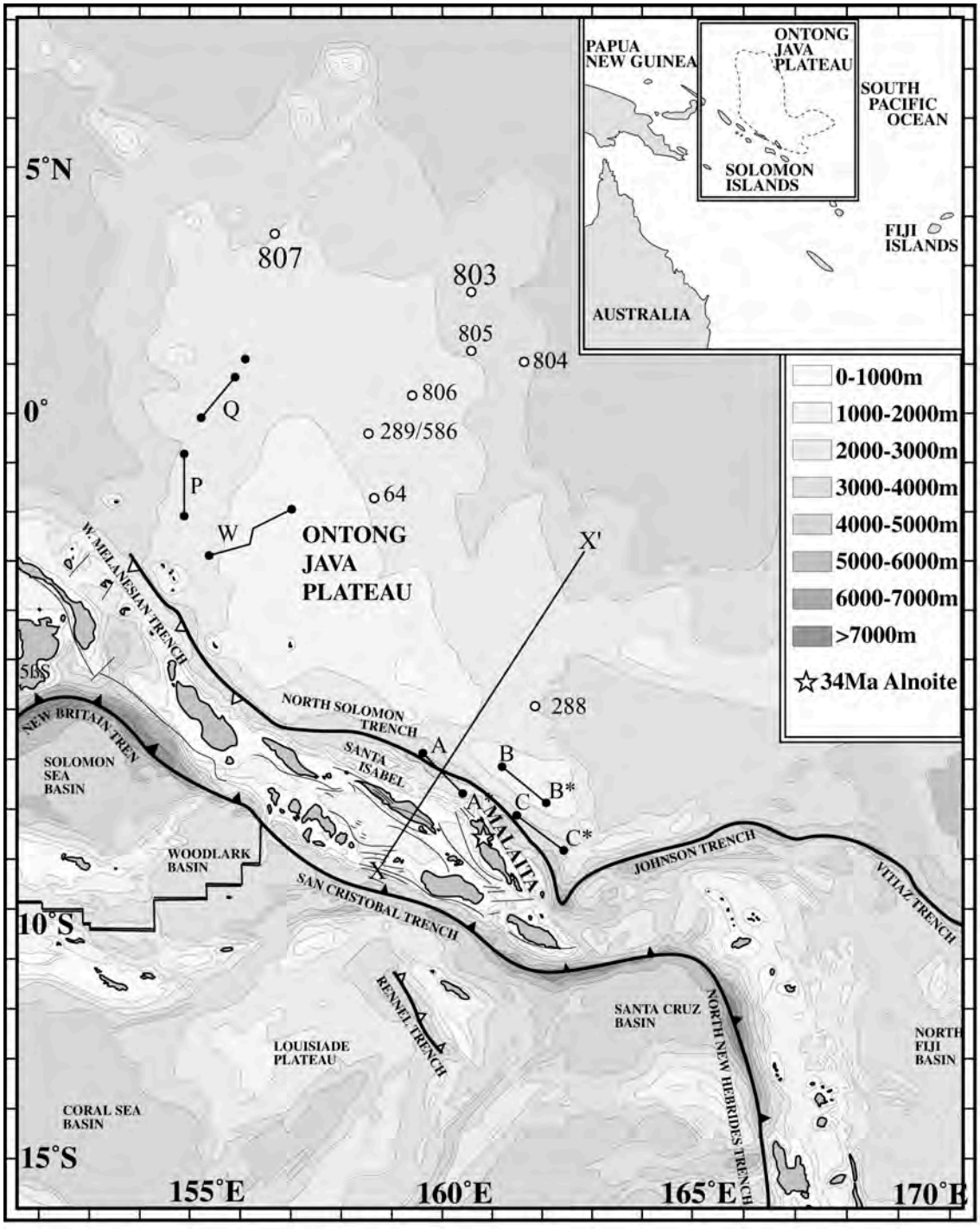

Fig. 1-1. Map of the main part of the Ontong Java Plateau and the Solomon Islands chain modified after Kroenke et al. (1993). The location of alnöite intrusions in the island of Malaita is shown as star. The locations of DSDP and ODP drill sites are shown as circles. Deep crustal seismic refraction lines are labeled A-A*, B-B* and C-C* (Furumoto et al., 1970) and W, P, Q and R (Furumoto et al., 1976) compiled by Neal et al. (1997). Inset is composite crustal-section X-X', showing in Fig. 1-2.

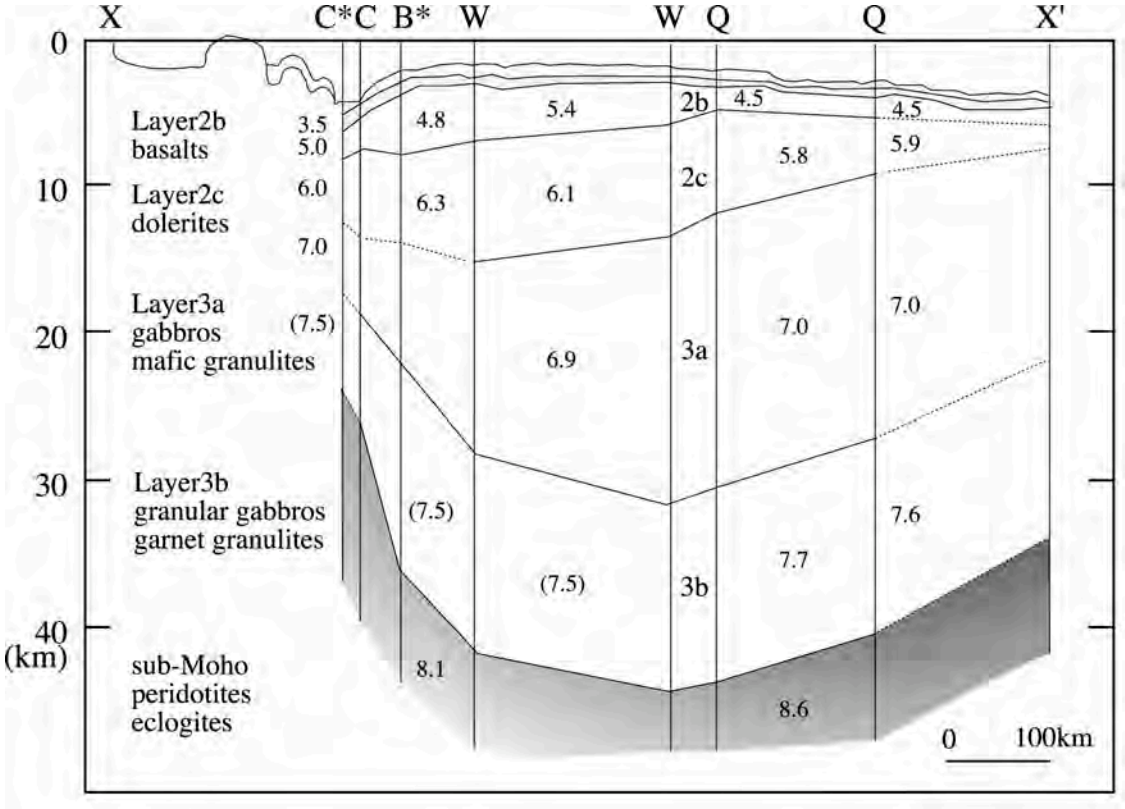

Fig. 1-2. Composite crustal-section X-X' (Fig. 1-1) of the Ontong Java Plateau modified after (Neal 1997). P-wave velocities (in km/s) are from Furumoto et al. (1970, 1976). Possible lithologies dominated in each layers are from Neal (1997).

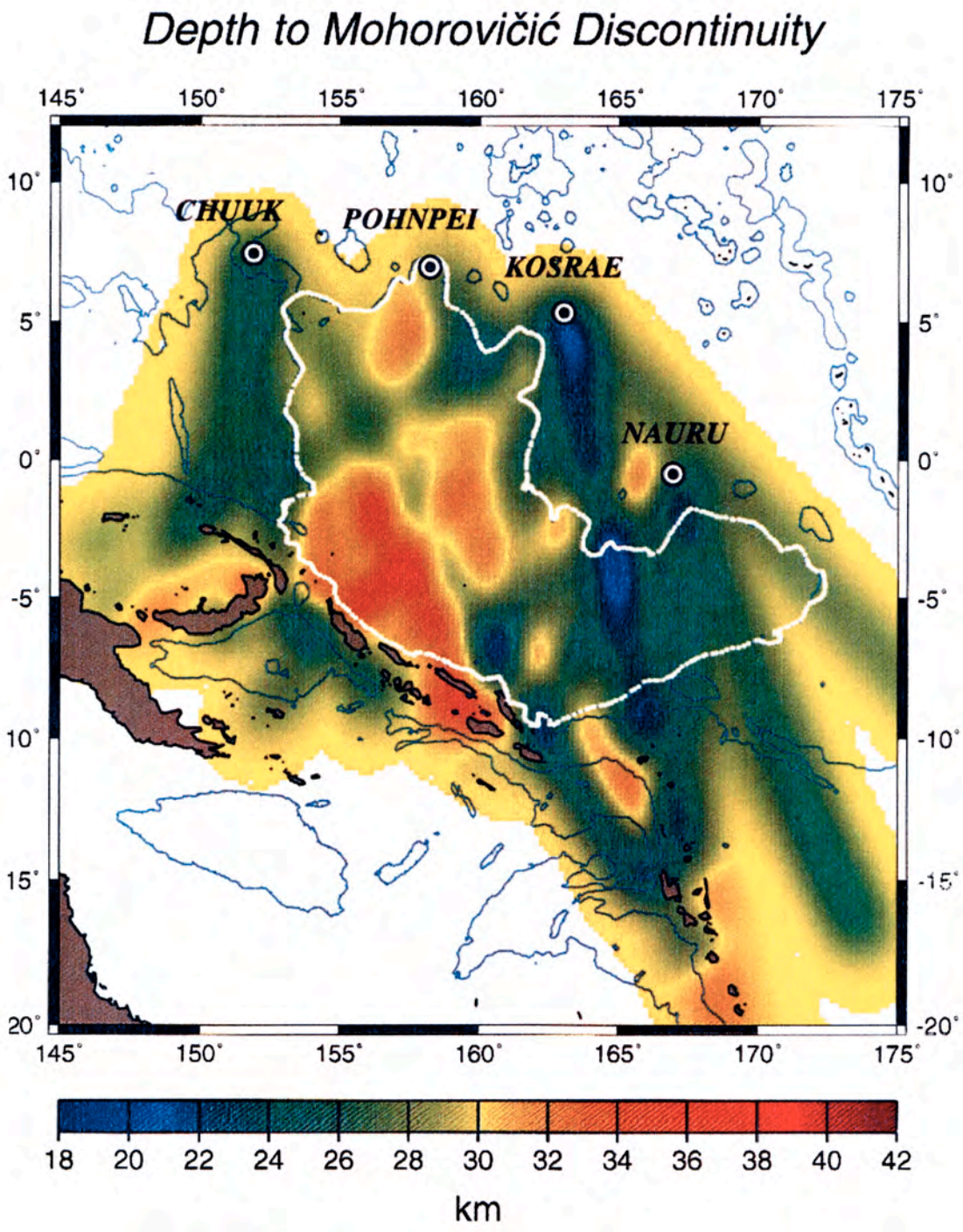

Fig. 1-3. Map of crustal thickness of the Ontong Java Plateau resulted by three-dimensional tomographic inversion (Richardson et al., 2000).

2. Sample descriptions

2-1 Sample location

Malaita comprises the plateau-forming basalt erupted in Lower Cretaceous (Malaita Older Series) and overlying sedimentary rock units (Fig. 2-1). These units were intruded by alkali basalts, which have Eocene age (Hughes and Turner, 1977; Tejada et al., 1996). Intrusions of alkaline basalt crop out in northernmost Malaita (North Malaita Alkalic Suite) and Small Malaita (Malaita Younger Series). In north-central Malaita, pipe-like bodies and sills of 34 Ma alnöite (Davis, 1977), silica undersaturated ultramafic igneous rock, were confirmed in the eroded anticline (Fig. 2-2). The alnöite contains a rich and varied suite of mantle-derived xenoliths similar occurrences of those in kimberlite. Generally, xenoliths were found in the forest area with separating from host alnöite. Our studied samples were donated from local people, who reside in villages scattering along the main road from Dala to Atori during the fieldwork in 2000 and 2001. Although no detailed information of individual sample locations are available, it can be safely said that they were derived from alnöite locating in north-central part of Malaita.

2-2 Petrography

Previous studies revealed that inclusions could be classified into two suites such as ultrabasic nodule and discrete nodule (megacryst) suites. Based on detailed observation of more than 150 samples, I confirmed the wide variety of rock-types unreported in previous studies. In particular, varied garnet-bearing pyroxenites, which contain no olivine or lesser amount than peridotite nodules occur significantly. Firstly, I prefer to describe studied samples divided into three rock suites: peridotite suites, pyroxenite suites and megacryst suites. Later, I will apply further classification for three rock suites into two types: high-temperature type (HT-type) and low-temperature type (LT-type) on the basis of their equilibrium conditions (next section). The variation of estimated equilibrium conditions should reflect a variation in depth of xenolith residence before host alnöite eruption. Actually, compositions and textures differ distinctly between both groups, for example subcalcic diopside and Ca-rich bronzite / enstatite in HT type in contrast to diopside and Ca-poor enstatite in LT-type. Other characteristics of each type are summarized in Table 2-1.

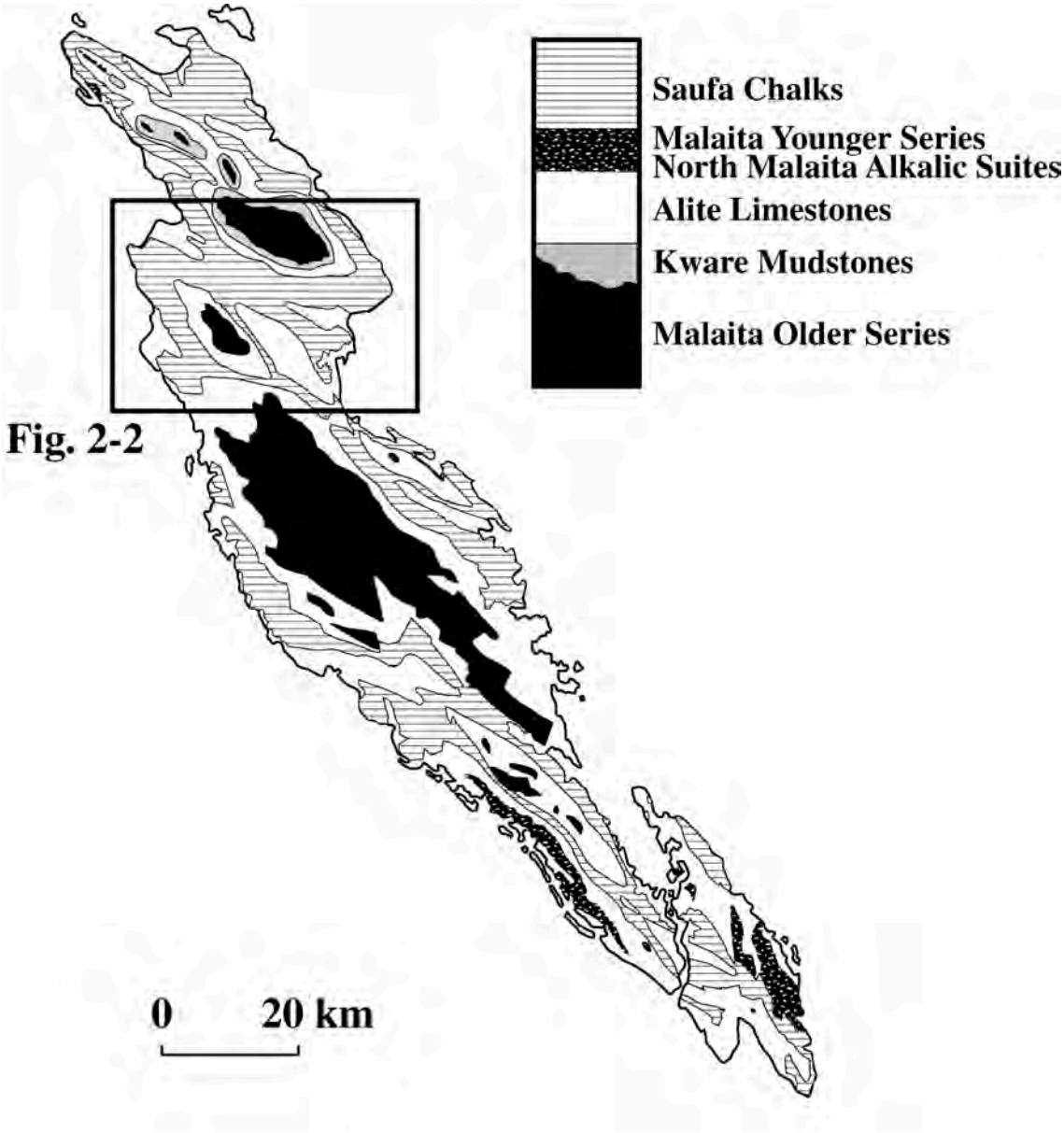

Fig. 2-1. Simplified geological map of Malaita Island modified after Petterson (1995)

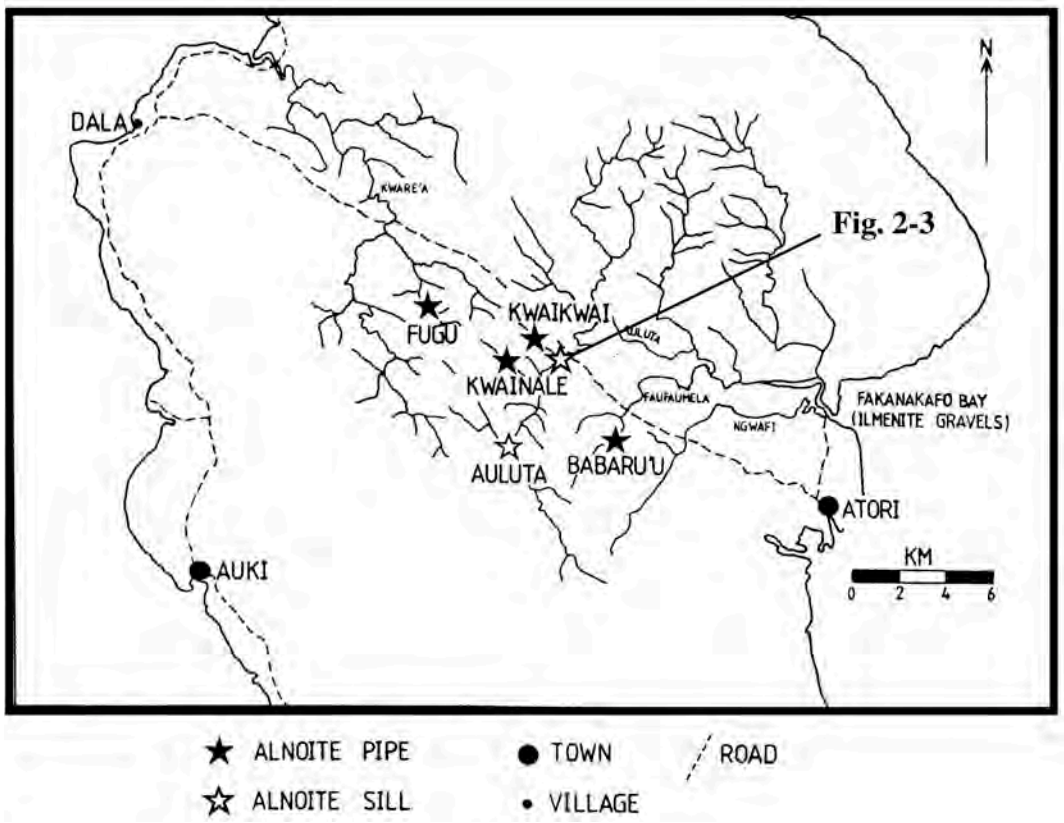

Fig. 2-2. Alnöite occurrences in Northern Malaita modified after Neal (1985).

Table 2-1. Some general characteristics of low-temperature type (LT-type) and high-temperature type (HT-type) mantle xenoliths in Malaita alnöite.

		Low-temperature type (LT-type) < 1100˚C	**High -temperature type (HT-type) > 1150˚C**
Peridotite suites	Rock types	Spinel lherzolite (SL) = most common Spinel harzburgite (SH) Garnet spinel lherzolite (GSL) Garnet lherzolite	Garnet lherzolite (GL) Spinel harzburgite (HTSH)
	Mineralogy	olivine, orthopyroxene, clinopyroxene, spinel, garnet, amphibole	olivine, orthopyroxene, clinoproxene, garnet, spinel (rare)
	Textures	Irregular shape of spinel always surrounded by garnet in GSL. The garnet tend to associate poikilitic amphibole (max. 18%). Some GSL contain carbonate after olivine . Thin exsolved lammelae of orthopyroxene and spinel in clinopyroxene of SL are observed.	Rounded garnets without spinel inclusion are in GL. Trace amounts of spinel usually armored by olivine in HTSH, but some cases touching with orthopyroxene. Exsolution texture is uncommon. Some samples show olivine grain size reduction, indicating deformation.
Pyroxenite suites	Rock types	Garnet websterite (GW) Spinel garnet clinopyroxenite (SGC) Olivine garnet clinopyroxenite (rare) Garnet clinopyroxenite (rare)	Garnet clinopyroxenite (GC) Garnet orthopyroxenite (GO) Quartz garnet clinopyroxenite(QGC)
	Mineralogy	clinoyroxene, garnet, orhtopyroxene, spinel olivine, amphibole, phlogopite, rutile (rare)	clinoyroxene, garnet, orthopyroxene, olivine, quartz (rare)
	Textures	Exsolved plates and/or blebs of garnet are common in GW clinopyroxene. Spinel is usually surrounded by garnet in GW and SGC. Some SGC show granoblastic texture and then clinoyroxene tend to touch with spinel. Rutile exsolution in garnet occur in rare case.	Poikilitic clinopyroxene and rounded garnet in GC. Anhedral garnet between discrete orthopyroxene grain in GO. Small olivine and clinopyroxene inclusions are common in GO. Small quartz aggregate concentrate along grain boundary in clinopyroxene and garnet.
Megacryst suites	Mineralogy	Garnet (MG) sometimes contain small rounded subcalcic diopside. Clinopyroxene Subcalcic diopside (MSD) Clinopyroxene-ilmenite intergrowth (MCI) Augite (MA) Clinopyroxene-rutile intergrowth(MCR) Orthopyroxene (Bronzite) Zircon Ilmenite Phlogopite Mica-Amphibole-Ilmenite-Augite rock (MAIA) coexisting with apatite	

2-2-1 Alnöite

The term alnöite has been used for suites of ultramafic lamprophyres with melilite, without feldspar in groundmass (Rock, 1986). Previous studies (Nixon et al., 1980; Neal and Davidson, 1989) reveal that the Malaita alnöite occur as several forms; intrusive consisting dyke or sill, fragmental rocks grade from tuffs to breccias. Their bulk chemistries show silica-undersaturated (intrusive: SiO_2=35.7-37.4 wt%) with enriched in Mg (intrusive: MgO: 18.0-25.1 wt%), alkali and volatile component. They consist of phlogopite, melilite, olivine, magnetite and clinopyroxene, perovskite and apatite. Fig 2-3 shows the photographs of alnöite confirmed during our field trip. This alnöite body may occur intrusive forms but the boundaries between basement rocks are inaccessible. The alnöite displays white to grayish in color attributed by the matrix of well-crystallized calcite. Black rounded ilmenites and light-brown altered olivine are prominent. The calcite matrix includes rounded discrete “glassy zone” with maximum length about 1 cm and typically < 4 mm in axis (Fig. 2-3b), containing varied minerals of phenocrysts and groundmass aforementioned and rounded small calcites. Megacrystic minerals such as subcalcic diopside, garnet, ilmenite and phlogopite tend to be surrounded by the glassy zone. Although significant evidences would be taken from alnöite petrology and chemistry, no detailed investigation was conducted in present study.

2-2-2 Peridotite suites

Most of the collected samples belong to peridotite suites and they form a high proportion of the xenolith population same as mantle xenolith derived from other kimberlite and alkaline basalt. These have rounded and weathered surface and commonly appear below 10 cm in diameter. Although most of peridotite inclusions may have been broken before sampling due to friable nature, some specimens retain about 30 cm in long axis. All of the peridotite suffered more or less alteration. Serpentine and carbonate are common as secondary mineral. There is a possibility that some carbonates were primary, but I could not distinguish between both. Because of the altered nature, small sample size and coarse-grained constituent minerals, precise modal proportions of constituent minerals are difficult to obtain (Table 2-2). But it is easily distinguish whether garnet is present or not, may be meaningful for sample classification in the first state.

Fig. 2-3. a: the photograph of alnöite outcrop located along the Auluta river. b: thin section photomicrograph of the alnöite which displays two-separated zone representing well-crystallized calcite matrix (white) including rounded glassy zone (black). Horizontal axis of the flame = 3 cm.

Table 2-2. Modal compositions of LT and HT-type peridotite. “X” shows the present phases but undetermined their modal compositions. “tr” means modal abundances below 0.5 %. Abbreviations are: Grt=garnet, Cpx=clinopyroxene, Opx=orthopyroxene, Sp=spinel, Ol=olivine, Amp=amphibole

sample no.	Ol	Opx	Cpx	Grt	Sp	Amp	sample no.	Ol	Opx	Cpx	Sp	Amp
LT-type												
Garnet-spinel lherzolite (GSL)							Spinel lherzolite and harzburgite(SL-SH)					
SAG3	43	25	8	24	tr		SAS18	57	34	6	3	
SAG10	72	18	6	4	tr		SAS17	40	46	11	3	tr
SAG12	60	8	15	14	3		SAS15	61	25	7	2	4
SAG14	61	16	14	9	tr		SAS13	61	25	10	3	
SAG17	66	15	11	7	1		SAS4	55	35	9	1	tr
SAG20	49	24	21	6			SAS34	63	25	9	3	
SAG24	72	16	7	2	3		SAS35	62	26	9	2	
SAS7	60	22	10	5	3		SAS19	61	26	11	2	
SAS9	64	20	16	tr	tr		SAS26	59	31	9	1	
							SAS28	70	24	4	2	
Amphibole rich							SAS2	70	30	tr	tr	tr
SAG4	54	20	10	12	tr	4	SAS3	74	20	4	2	tr
SAG5	41	33	12	12	tr	2	SAS14	67	30	2	tr	
SAG6	68	17	7	tr		8	SAS20	72	23	tr	2	3
SAG8	59	15	5	14	2	5	SAS30	81	18	1	tr	
SAG22	59	15	2	5	tr	18	SAS25	76	21	2	1	
SAE131	67	14	8	6	tr	5	SAS16	77	19	3	1	
							SAS23	68	22	4	1	5
Carbonatized							SAS22	85	13	2	tr	
SAG11	52	41	6	1			SAS10	X	X	X	X	
SAG18	58	17	13	12	tr		SAS5	X	X	X	X	
SAG25	77	10	10	3	tr		SAS6	X	X	X	X	
SAG26	75	10	9	6			SAS27	X	X	X	X	
SAG23	69	18	9	2	2		SAS29	X	X	X	X	
SAE123	72	10	12	6	tr		SAS31	46	36	15	3	
							SAS32	X	X	X	X	
							SAS33	X	X	X	X	
							SAS36	X	X	X	X	
							SAS24	X	X	X	X	
HT-type												
Garnet lherzolite (GL)							Spinel harzburgite (HTSH)					
SAG1	62	20	10	8			SAS1	76	22	3	tr	
SAG2	63	16	12	9			SAS8	73	27	tr	tr	
SAG7	54	30	8	8			SAS21	58	42	tr	tr	
SAG9	64	24	5	8								
SAG15	44	38	11	6								
SAG21	54	21	14	11								
SAG27	58	31	8	3								
SAG13	67	17	8	8								
SAG16	66	20	7	7								

Garnet bearing peridotite

Garnet-bearing peridotite is relatively scarce in the collection. 33 samples including small chips (< 2 cm) were found among over 100 samples of peridotite suites. Garnet-bearing peridotites are subdivided into two groups: garnet-spinel lherzolite and garnet lherzolite. Garnet-bearing harzburgite is not identified among the studied samples. Because of low abundance of spinel (< 3 %), this classification may not make sense on thin section observation. But spinel appearance and garnet morphology generally related. In garnet-spinel lherzolite, spinel usually appears in surrounding garnet. Morphology of spinel is varied from rounded small grain to irregular shape (Figs. 2-4 e and f). Garnet also shows irregular shape engaging with olivine and pyroxene. In some cases, poikilitic amphibole perfectly surrounds irregular shape of garnet including spinel (Fig. 2-4 d). These textural evidences suggest that garnets were formed by reaction involving pyroxene and spinel and/or amphibole and spinel from spinel peridotite precursor (Neal and Nixon, 1986). In the other hand, 10 of 14 spinel-free garnet lherzolite contain well-rounded shape of garnet grains (Figs. 2-4 a, b and g). Although thin surface of rounded garnet is usually replaced by small amphiboles, phlogopite, green spinel and others consisting kelyphite, no reaction relationship was observed from the texture. There is no primary amphibole in the garnet lherzolite. These textural observations led to the distinction of two main types of garnet-bearing lherzolite.

Garnet-spinel lherzolite (referred as GSL) comprises the 19 spinel-bearing garnet lherzolite and 4 of 14 spinel-free garnet lherzolites. The modal proportions of primary mineral inferred by thin section observation are highly variable, olivine (41-77%), clinopyroxene (2-21%), orthopyroxene (8-41%), garnet (< 24%), spinel (< 3%) and amphibole (< 18%). Amphibole may occur as higher abundance than spinel peridotite. Some low modal clinopyroxene samples tend to be rich in amphibole, indicating replacement of clinopyroxene is also significant. Olivine from several samples is perfectly replaced by brown turbid carbonate or well-crystallized calcite (Fig. 2-4 e). One sample (SAG26) of carbonated peridotite has garnet concentration on surface of the specimen (Fig. 2-4 c). It may be different from the composite nodule that has pyroxenite and peridotite in single nodule reported in other xenolith locations (e.g. Hawaiian xenolith; Reid and Frey, 1971). Overall textures of garnet-spinel lherzolite are characterized by coarse-grained equant and no deformation is

indicated. Another type of garnet-bearing lherzolite contains cloudy pink or milky-white stuff of possible alteration products after garnets. Of the specimens observed, there are no fresh garnets in the core of white stuff, whereas spinel is common mineral in the garnet psuedomorphs. Although I could not find out any textural differences, 16 samples belonging this type were sort out from “fresh” garnet-spinel lherzolite.

Garnet lherzolite (GL), which comprises the 10 of 14 spinel-free garnet lherzolites, shows relatively uniform modal proportions of primary mineral relative to those of GSL, including olivine (47-67 %), clinopyroxene (5-14 %), orthopyroxene (16-38 %) and garnet (3-11%). Although inferred degree of secondary alteration of olivine does not differ from those in other peridotite suites, carbonated olivine was not found in this rock type. Most of GL exhibit coarse-grained textures (Fig. 2-4 g), however two samples (SAG21 and SAG27) in GL show porphyroclastic textures with large, kinked porphyroclasts surrounded by small neoblasts (Fig. 2-4 h). SAG27 tends to show stronger deformation relative to SAG21 accompanying with the presence of thick kelyphitised garnet, which is significantly lower proportion of garnet (3 %) than others.

Spinel peridotite

Most of the collected peridotite belongs to clinopyroxene-bearing spinel peridotite that contains green clinopyroxene and no garnet on xenolith surface. Generally, spinel peridotite has petrographicaly homogeneous through the hand specimens, however only one sample (SAS32) has vein-like concentration of large clinopyroxene in center of the specimen (Fig. 2-5 b).

More than 100 spinel peridotite xenoliths were collected and 32 of them have been cut for thin sections. These and additional 28 samples were examined by crushing the pieces and observed under binocular microscope in order to check the certain mineral assemblage. Based on rough estimation using thin sections and mineral separations, these are mainly spinel lherzolite and all of studied samples contain clinopyroxene. But some can be classified as harzburgite in terms of low abundance of clinopyroxene (< 5 %). Typical modal composition of spinel lherzolite is 40-63 % olivine, 25-46 % orthopyroxene, 6-11 % clinopyroxene and 1-3 % spinel. On the other hand, harzburgite is 58-85 % olivine, 13-42 % orthopyroxene, 0.1-4 %

clinopyroxene and < 2 % spinel. Amphibole (max. 5 %) is common mineral both in lherzolite and harzburgite, occurring as replacement of clinopyroxene and poikiliticaly surrounds spinel (Figs. 2-5 e and f). Although the values of modal abundances may be not precise, the difference between lherzolite and harzburgite is reflected by their mineral compositions (see later section), indicating estimation of modal proportion is relatively successful.

Overall textures of both types in spinel peridotites are characterized by coarse-granular with slightly curved or straight grain boundaries similar to garnet-bearing peridotite (Fig. 2-5). Clinopyroxenes in some lherzolitic samples exhibit exsolution of orthopyroxene as thin lamellae. Spinel also occurs as platelets in clinopyroxene indicative of their exsolution origin. On the other hand, discrete orthopyroxene grains usually do not contain exsolution lamellae of both clinopyroxene and spinel. But interstitial grains of spinel and clinopyroxene are often present at the edge of orthopyroxene grains in lherzolite and they may be represented as granule exsolution material from host orthopyroxene. Spinel in harzburgite is distinctly lower abundance than lherzolite and their form and color tend to be different from lherzolite. Transparent brown spinel with irregular form in lherzolite sometimes occur as in a vermicular form associating with clinopyroxene and orthopyroxene (Fig. 2-5 c). Trace amounts of spinel in harzburgite tend to be dark brown to black in color and rarely occur as tiny grain with relatively euhedral form. Some harzburgite contain higher abundances of spinel, which is totally surrounded by amphibole.

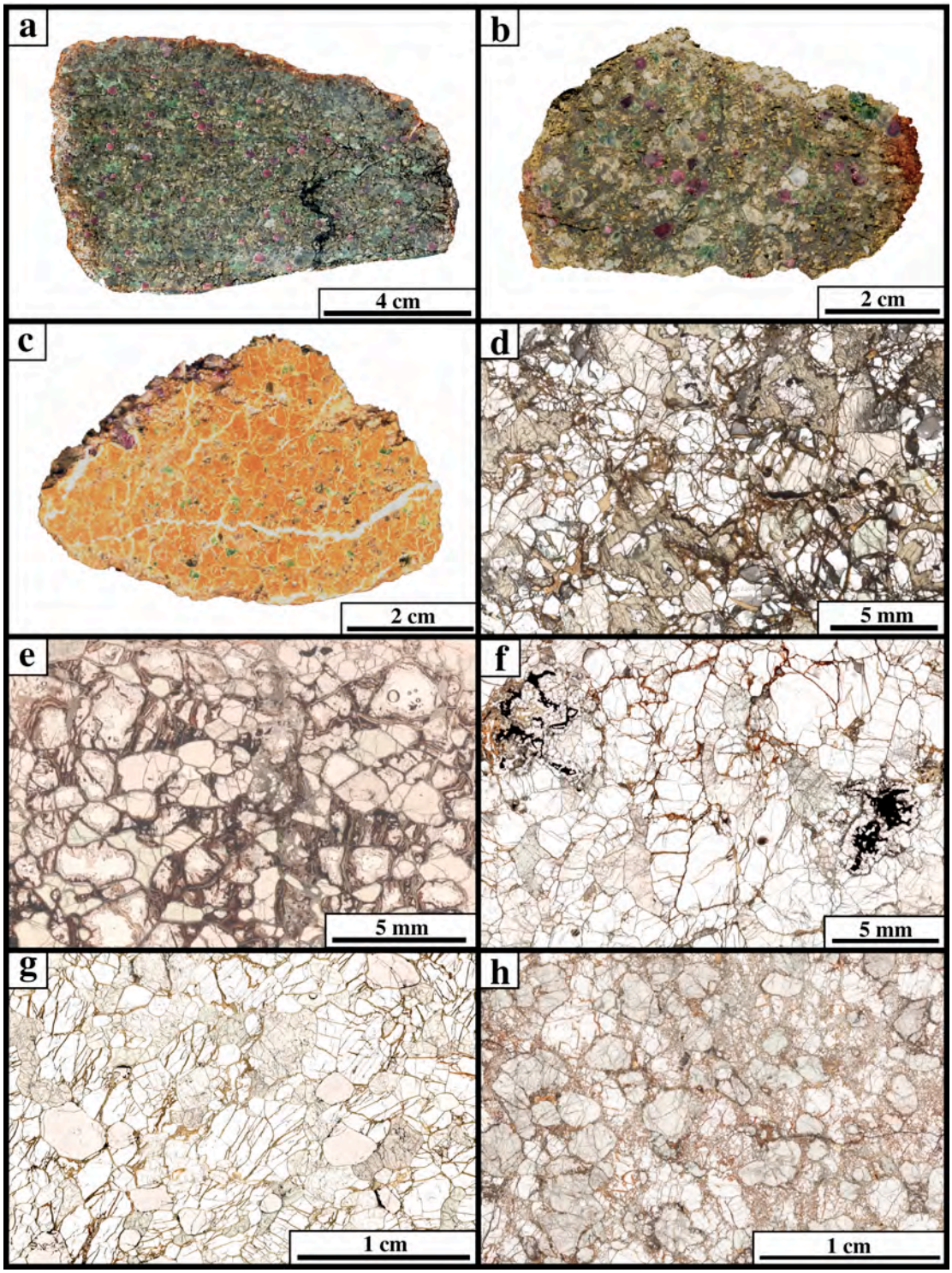
a
4 cm
b
2 cm
c
2 cm
d
5 mm
e
5 mm
f
5 mm
g
1 cm
h
1 cm

Fig. 2-4. Photographs of representative garnet-bearing peridotites (GSL and GL) from the Malaitan xenolith.

2-4 a: SAG1 – Sawed surface of garnet lherzolite (GL) containing abundant red-purple garnets and light-green clinopyroxenes.

2-4 b: SAG7 – Sawed surface of garnet lherzolite (GL) showing strong altered feature of olivine.

2-4 c: SAG26 – Sawed surface of carbonatized garnet lherzolite (SAG26-GSL), showing the concentration of purple garnet on the one side of the xenolith surface.

2-4 d: SAG22 – Photomicrograph of amphibole-rich garnet-spinel lherzolite (GSL). Garnets which include spinel (black) are totally surrounded by poikilitic amphibole (deep-green).

2-4 e: SAG18 – Photomicrograph of carbonatized garnet-spinel lherzolite (GSL) showing that well-crystallized calcite replacing olivine.

2-4 f: SAG24 – Photomicrograph of garnet-spinel lherzolite (GSL) characterized by irregular-wormy spinels (black) rimmed by thin garnets.

2-4 g: SAG9 – Photomicrograph of garnet lherzolite (GL) containing large (< 5 mm) fresh olivines with coarse-grained granular texture.

2-4 h: SAG27 – Photomicrograph of deformed garnet lherzolite (GL) showing porphyroclastic texture, with large, kinked porphyroclasts surrounded by small neoblasts.

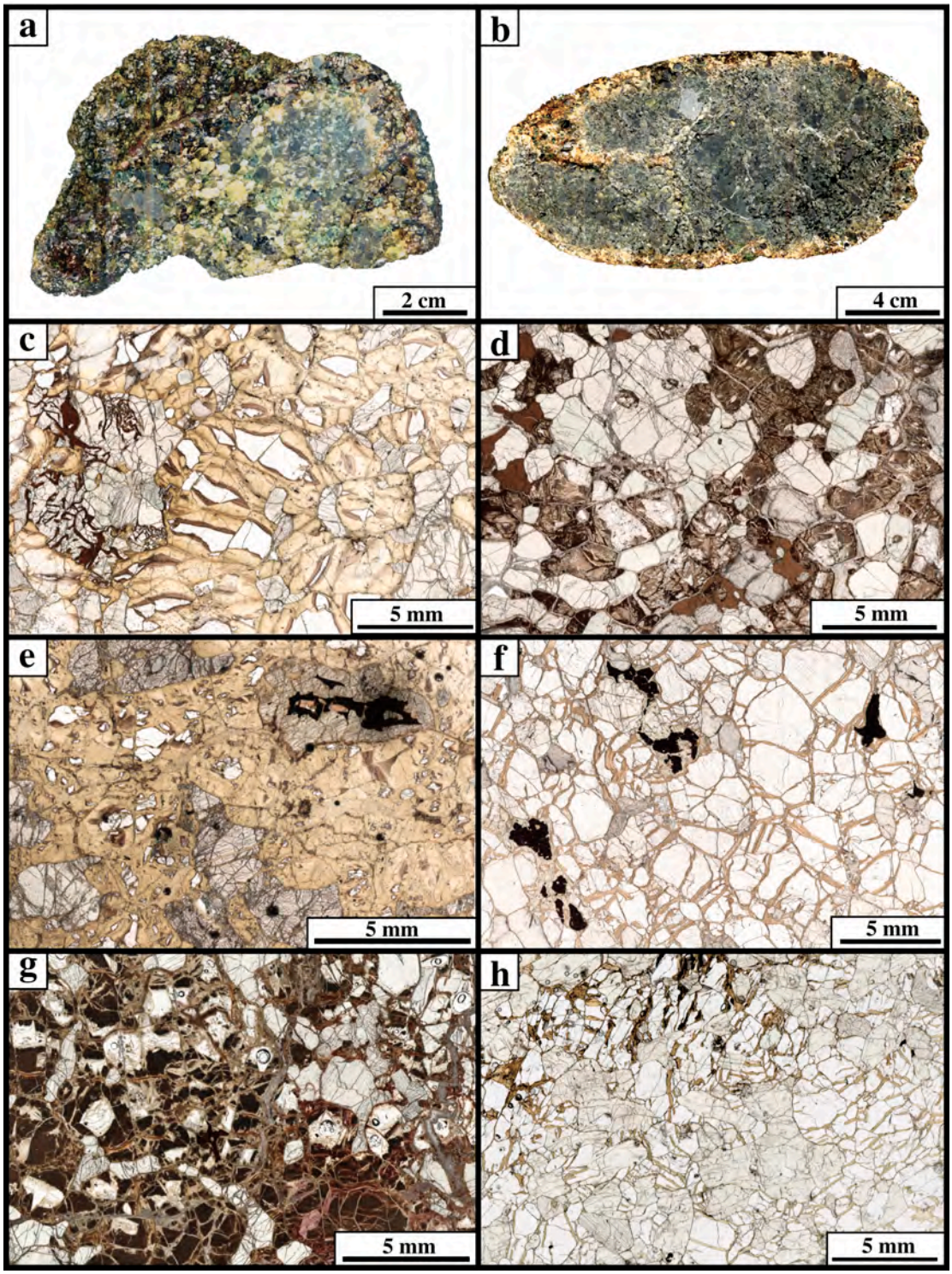
a
2 cm
b
4 cm
c
5 mm
d
5 mm
e
5 mm
f
5 mm
g
5 mm
h
5 mm

Fig. 2-5. Photographs of representative spinel peridotites from the Malaitan xenolith.

2-5 a: SAS31 – Sawed surface of spinel lherzolite (SL) showing the contrast between the fresher core including large grains (< 5 mm) of light-green olivine and altered rim of the xenolith.

2-5 b: SAS32 – Sawed surface of spinel lherzolite containing vein-like concentration of large clinopyroxene (thickness < 2 cm) in center of the specimen.

2-5 c: SAS19- Photomicrograph of spinel lherzolite (SL) characterized by vermicular form of brown-spinel intergrown with clinopyroxene and orthopyroxene. They are surrounded by partially altered olivine.

2-5 d: SAS17 – Photomicrograph of spinel lherzolite (SL) containing higher abundance of transparent brown spinel (~ 3%), which is large, and anhedral with holly-leaf shape.

2-5 e: SAS23 – Photomicrograph of spinel lherzolite (SL) showing strong alteration of olivine. Black spinel always occurs in poikilitic amphibole.

2-5 f: SAS20 – Photomicrograph of spinel harzburgite (SH) containing abundant fresher large olivine than those of SAS23. Similar to SAS23, black spinel is usually surrounded by amphibole.

2-5 g: SAS22 – Photomicrograph of spinel harzburgite showing that most olivine is replaced by brown turbid carbonates.

2-5 h: SAS21 – Photomicrograph of spinel harzburgite (HTSH) containing abundant fresh olivine and coarse grains of orthopyroxene (< 8 mm). Some olivine includes small spinel (~ 0.1 mm).

2-2-3 Pyroxenite suites

Malaitan alnöite contains the rock suites that compose mainly pyroxene (clinopyroxene and orthopyroxene) and garnet. The nomenclature of garnet-pyroxene rocks derived from mantle is confused. Some authors have used the term ‘eclogite’ for garnet-clinopyroxene rocks. Studied rocks have no omphasitic clinopyroxene and are dissimilar to those of eclogite from kimberlite and metamorphic terrains. Therefore, I referred to as garnet pyroxenite not as eclogite.

Most of garnet pyroxenite has no olivine or less amounts than peridotite suites (Tables 2-2 and 2-3) and there is the significant gap of modal olivine between peridotite and pyroxenite suites (peridotite suites; > 40 %, pyroxenite suites; < 15 %, one exception 35 %). Nixon and Boyd (1979) reported the presence of garnet-free pyroxenite, such as spinel wehlrite (PHN3542A) and spinel pyroxenite (PHN3553A). But I could not find out the above rock type and all of the studied samples belonging to pyroxenite suites contain garnet. The abundance of garnet bearing pyroxenite is higher than garnet bearing peridotite among the collection.

In garnet pyroxenite, many variants can be recognized in hand specimen due to the modal variation of the constituent primary phases and variations in the textures. In addition to garnet and clinopyroxene, other primary phases in pyroxenite suites are orthopyroxene, spinel, olivine, amphibole, phlogopite, quartz, rutile and sulfide. Based on the textural evidence, some of these phases appeared by unmixing and/or reaction. For example, both garnet and orthopyroxene have exsolved from clinopyroxene, and spinel has been surrounded by garnet similar to garnet-spinel lherzolite. For above reason, I classified the garnet pyroxenite into several types using not only modal abundance of primary phases but also textural variations.

Garnet websterite

Garnet websterites (GW) are mainly composed of clinopyroxene, orthopyroxene and garnet. Textures of this rock types are generally dominated by unmixing, most of orthopyroxene and garnet were exsolved from larger grains of clinopyroxene based on observation of thin sections (Fig. 2-6). I confirmed 12 samples belonging to this rock type among the collection.

The specimen of SAE134 is particularly large and is a 15 cm nodule in long axis. This specimen has entirely same texture (Fig. 2-6 a). 3 cm of clinopyroxene

contains thicker garnet plates (average 0.10 mm) and thinner orthopyroxene plates (~ 0.05 mm). Both phases also occur as grain boundary blebs around the clinopyroxene (Fig. 2-6 b). The specimen of SAE103 (Fig. 2-6 c) appears as small chip and is composed of single grain of clinopyroxene (~ 2 cm). The clinopyroxene contains similar size of oriented orthopyroxene and garnet blebs rather than plates. Orthopyroxene blebs tend to be surrounded by garnet blebs. Trace amounts of spinel occur in the garnet blebs. Locally amphibole is confirmed at grain boundary between orthopyroxene blebs and clinopyroxene. These rocks are originally clinopyroxenites with or without minor spinel that were reequilibrated at subsolidus conditions.

SAE122 (Fig. 2-6 d) and SAE138 (Fig. 2-6 e) are composed of clinopyroxene which have similar exsolution texture in clinopyroxene grains (up to 1 cm), but that also contain large discrete grains of orthopyroxene (up to 4 mm). Although there are no exsolution plates or blebs of either garnet or clinopyroxene in the orthopyroxene grains, garnets occur as grain boundary blebs around the orthopyroxene grains. Spinel and olivine occur as a minor phase in SAE122 and SAE138. Spinel is always mantled by garnet, and olivine associates with the garnet including spinel. This texture indicates that garnets originated not only by unmixing of aluminous clinopyroxene and orthopyroxene but also reaction of both pyroxenes and spinel to form garnet and olivine. It means that these rocks originally have been websterites with minor spinel. Garnet and olivine appeared and orthopyroxene grew up under later subsolidus condition.

On the other hand, SAE111 (Fig. 2-6 f) and SAE117 (Fig 2-6 g) have no or much less abundant exsolution plates or blebs in clinopyroxene grains than in SAE122 and SAE138. But 2 mm size of orthopyroxene and garnet occur as mainly grain boundary blebs around larger clinopyroxene grains (up to 8 mm). These textural variations suggest that retaining of exsolution blebs or plates in clinopyroxene grain depends on original clinopyroxene grain size. Although it is difficult to determine whether orthopyroxene presented above solidus conditions or not, presumably, the rocks represent an original clinopyroxenite with minor orthopyroxene. I fail to find out spinel in spite of extensive research in these two rocks.

SAE128 (Fig. 2-6 h) contains higher abundance of spinel, olivine and garnet than other garnet websterite. Large spinels (up to 2 mm) with irregular shape are

mantled by garnet. Then, olivine (up to 1 mm) associates with the garnets. Orthopyroxene occurs as three textural relations in this rock: (1) large discrete grains taking the size up to 5 mm; (2) small rounded grains mantled by garnets; (3) inclusions and/or blebs in clinopyroxene with garnet exsolution along the grain margin. Although this rock probably originates from spinel websterite, some garnets may have been crystallized from residual melt not only subsolidus reaction.

Spinel-garnet clinopyroxenite

Spinel-garnet clinopyroxenites (SGC) are mainly composed of clinopyroxene, garnet and spinel without orthopyroxene (except for thin lamellae in clinopyroxene). These rocks were referred to as “spinel griquaite” by Nixon and Boyd (1979), but in its original sense of “griquaite” in that they recognize certain bimineralic garnet-clinopyroxene rocks, comprising aggregates of megacryst suites (Dawson, 1980). I would not use the term of “griquaite” for this rock type in order to avoid the confusion with the “real griquaites” from Malaitan alnöite. I confirmed 14 samples belonging to this rock type and have been able to distinguish at least three basic textural types (group 1, 2 and 3) of spinel-garnet clinopyroxenite.

Group1 spinel-garnet clinopyroxenite (SGC1: SAE109, SAE112, SAE124 and SAE140) mainly composed of spinel, garnet and clinopyroxene without orthopyroxene. Only large clinopyroxene in SAE112 has fine orthopyroxene lamellae. Abundance of spinel is higher than garnet websterite. The brown spinel is always mantled by garnet and separated from clinopyroxene by rims of garnet. Sometimes anhedral form of olivine is associated the garnet which includes spinel (Fig. 2-7 g). Although fresh olivine was not found in SAE112, large size of specimen (8 cm) contains some olivine psuedomorphs replaced by carbonates (Fig. 2-7 c). Presumably, other two samples may not contain any olivine.

Group2 spinel-garnet clinopyroxenite (SGC2: SAE115, SAE118, SAE130 and SAE146) contains not only spinel rimmed by garnets but also inclusions in clinopyroxene. The spinel abundance is higher than group1 spinel-garnet clinopyroxenite. SAE115 and SAE118 contain also high abundance of interstitial amphibole. SAE146 (Fig. 2-7 b) comes from a large inclusion (14 cm in length) with several banding. The main part is group2 spinel-garnet clinopyroxenite in texture. The other side is made by spinel-free garnet clinopyroxenite with granoblastic

garnets. Both parts are separated by 2.5 cm of clinopyroxene rich layer with coarser grain size than in other part of this rock (< 2 cm). The clinopyroxene has exsolution lamellae of garnet. Rounded shapes of garnet in this layer are smaller than in other part (< 3 mm) and may originate as exsolution from clinopyroxene. One spinel grain occurs in this layer and is totally rimmed by garnet. The mineralogical difference between both sides may indicate that the clinopyroxene layer is not later vein.

Group3 spinel-garnet clinopyroxenite (SGC3: SAE104, SAE108, SAE110, SAE125, SAE142, SAE146 and SAE153) is characterized by its granoblastic texture and are mainly composed of polygonal, equant garnet and clinopyroxene grains. Abundance of spinel is variable but gray-green colored spinel with euhedral and straight-edged shape are common in both garnet and clinopyroxene. SAE108, which has the highest abundance of spinel among the collection, shows typical granoblastic texture; some larger spinels are accompanied by garnet and clinopyroxene with 120˚ of grain boundary (Fig. 2-7 h). PHN3551A described by Nixon and Boyd (1979) may belong to this type. Another characteristics of this type are represented by the presence of banding defined by spinel abundance in single nodule. SAE110 and SAE153 have spinel-free portion in one side of the specimens (Fig. 2-7 a: lower portion).

Garnet clinopyroxenite (LT-type)

Garnet clinopyroxenites and garnet-olivine clinopyroxenites are mainly composed of clinopyroxene and garnet. Minor orthopyroxene and spinel were confirmed in two samples of this rock type. I interpreted as transitional type between garnet websterite and spinel-garnet clinopyroxenite.

SAE105 composed coarse grain of clinopyroxene (up to 8 mm) and garnet (2 mm). Orthopyroxene never occurs as large grain but is common in garnet as small grain (< 0.5 mm). Large clinopyroxene contains orthopyroxene as thin exsolution lamellae. Garnet blebs or plates are also present in same clinopyroxene, but less abundant than garnet websterite SAE122 and SAE138. Trace amounts of spinel are rarely present in garnet. It is noted that olivine never appear in this rocks, indicating that garnet forming reaction were dominated by unmixing of pyroxenes and/or reaction between residual melt and preexisting orthopyroxene. SAE105 will be treated as garnet websterite in later section based on textural similarity.

On the other hand, SAE101 contains high abundance of olivine (about 13 %). According to nomenclature recommended by the IUGS, SAE101 belongs to olivine clinopyroxenite (with garnet). However, other characteristics are very similar to group1 spinel-garnet clinopyroxenite: (1) Trace amounts of spinel are present in garnet. (2) Orthopyroxene only occurs as small inclusion and fine exsolution lamellae in clinopyroxene. These evidences suggest that garnet and olivine mainly formed by reaction between spinel and pyroxenes. Some large clinopyroxenes exsolved thin plates of orthopyroxene in further cooling stage. SAE101 will be treated as group1 spinel-garnet clinopyroxenite in later section based on textural similarity.

SAE148 also belong to garnet-olivine clinopyroxenite, but all olivines replaced by carbonates. Clinopyroxene, garnet and former olivine are highly tangled each other. No other primary phases are observed.

SAE156 composed coarse-grained garnet (> 1 cm) with smaller clinopyroxene, however overall textures are unknown in due to small size of specimen (< 2 cm). The most conspicuous feature is the appearance of rutile. Rounded discrete rutile occurs near grain margin of large garnet. The garnet contains fine rods of rutile indicative of their exsolution origin.

Garnet clinopyroxenite (HT-type)

Garnet clinopyroxenites (GC) are principally composed of large, subhedral or rounded grains of garnet and interstitial matrix of clinopyroxene, with occasional large clinopyroxenes enclosing rounded garnets poikilitically (Figs. 2-8 a, d and e). The modal proportions of garnet and clinopyroxene vary from 17:83 to 46:54, weakly correlating with their diameter of garnets (1 to 6 mm). The rocks showing above texture (SAE107, SAE113, SAE120, SAE152 and SAE154) are easily distinguished from the LT-type garnet clinopyroxenite previously mentioned by not only their texture but also mineral chemistry. The compositional ranges of clinopyroxenes are extremely similar to those of individual subcalcic diopside megacryst (detail in later section). They may be interpreted as being aggregates of megacrysts, and as such conform to the original “griquaite”. But from the standpoint of original megacryst definition as single crystals of large size (commonly > 2 cm), I prefer to refer as to “garnet clinopyroxenite“ rather than megacryst. Actually, their

garnet compositions tend to have more magnesian than those of individual garnet megacrysts.

SAE132 (Fig. 2-7 f) is composed of large single grain of clinopyroxene with rounded garnet (up to 5 mm), showing similar texture to above rocks. However, orthopyroxene appears to associate with single garnet and the orthopyroxene has also similar composition to bronzite megacryst. The large clinopyroxene contains abundant brown-colored melt pockets or patches filled by several small minerals (not identified).

SAE141 (Figs. 2-7 c and g) is also garnet clinopyroxenite with orthopyroxene but its texture differs from other garnet clinopyroxenite because it is mainly composed of porphyroclasts of orthopyroxene and clinopyroxene with matrix of fine-grained clinopyroxenes. Anhedral garnets with thick kelyphitised rim are localized at one side of the sawed surface. Based on the observation of the whole specimen, garnet may not be abundant phase. Most conspicuous feature is the complex chemical zoning in orthopyroxene. The zonation may be ascribed to reaction with infiltrating melt in connection with its deformation texture (detail in later section).

SAE116 (Figs. 2-7 b, h and i) is quartz bearing garnet clinopyroxenite and may be an important sample for understanding the varied inclusions from Malaitan alnöite. This rock composed of clinopyroxene showing undulatory extinction, anhedral garnet and small quartz aggregates with anhedral external form. Near the aggregates, clinopyroxene appears sub-grain recrystallization, indicating that this rock suffered extensive deformation. Some quartz appears as single discrete grain of rounded inclusions in both clinopyroxene and garnet. The inclusions do not associate with radial crack, which have been confirmed in minerals including coesite psuedomorphs.

SAE147 is the small chips (< 3 cm) composed single grains of garnet and clinopyroxene (~ 2 cm). Although whole texture is inaccessible, I placed the sample to this group.

Table 2-3. Modal compositions of LT-type pyroxenite. “X” shows the present phases but undetermined their modal compositions. “tr” means modal abundances below 0.5 %. Abbreviations are: Grt=garnet, Cpx=clinopyroxene, Opx=orthopyroxene, Sp=spinel, Ol=olivine, Amp=amphibole, Rt=rutile, Phl=phlogopite.

sample no.	mineral assemblage	Grt	Cpx	Opx	Sp	Ol	Amp	Rt	Phl
LT-type									
Garnet websterite (GW)									
SAE134	Grt-Cpx-Opx	18	72	10					
SAE138	Grt-Cpx-Opx-Sp-Ol	35	43	21	tr	1			
SAE122	Grt-Cpx-Opx-Sp-Ol	25	39	36	tr	tr			
SAE117	Grt-Cpx-Opx	22	66	11			2		
SAE111	Grt-Cpx-Opx	24	65	11					
SAE103	Grt-Cpx-Opx	17	62	21	tr		tr		
SAE106	Grt-Cpx-Opx	13	66	21	tr				
SAE128	Grt-Cpx-Sp-Opx-Ol	48	28	19	1	5			
SAE144	Grt-Cpx-Opx	X	X	X					
SAE102	Grt-Cpx-Opx	X	X	X					
SAE143	Grt-Cpx-Opx	X	X	X					
SAE145	Grt-Cpx-Opx	X	X	X					
Garnet clinopyroxenite									
SAE105	Grt-Cpx-Opx-Sp	27	73	tr					
SAE156	Grt-Cpx-Rt	X	X					tr	
Garnet olivine clinopyroxenite									
SAE101	Grt-Cpx-Ol-Sp-Opx(inclusion)	56	31	tr	tr	13			
SAE148	Grt-Cpx-Ol	51	14			35			
Group1 spinel-garnet clinopyroxenite (SGC1)									
SAE109	Grt-Cpx-Ol-Sp	62	32		2	4			
SAE124	Grt-Cpx-Sp	35	64		1				
SAE112	Grt-Cpx-Sp-Opx (lamellae)	26	74	tr	tr				
SAE140	Grt-Cpx-Sp	56	43		2				
Group2 spinel-garnet clinopyroxenite (SGC2)									
SAE118	Grt-Cpx-Sp	43	50		2		5		
SAE130	Grt-Cpx-Sp	44	51		5				
SAE115	Grt-Cpx-Sp	33	58		5		4		
SAE142	Grt-Cpx-Sp	X	X		X				
SAE146	Grt-Cpx-Sp	X	X		X				
Group3 spinel-garnet clinopyroxenite (SGC3)									
SAE110	Grt-Cpx-Sp	52	48		tr				
SAE110	Grt-Cpx-Sp	57	41		2				
SAE108	Grt-Cpx-Sp	43	45		11				tr
SAE104	Grt-Cpx-Sp	39	60		1				
SAE125	Grt-Cpx-Sp	38	56		6				
SAE153	Grt-Cpx-Sp	X	X		X				

Table 2-4. Modal compositions of HT-type pyroxenite. “X” shows the present phases but undetermined their modal compositions. “tr” means modal abundances below 0.5 %. Abbreviations are: Grt=garnet, Cpx=clinopyroxene, Opx=orthopyroxene, Sp=spinel, Ol=olivine, Qz=quartz

sample no.	mineral assemblage	Grt	Cpx	Opx	Ol	Qz
HT-type						
Garnet clinopyroxenite (GC)						
SAE116	Grt-Cpx-Qz	21	75			4
SAE107	Grt-Cpx	36	64			
SAE113	Grt-Cpx	45	55			
SAE120	Grt-Cpx	46	54			
SAE152	Grt-Cpx	17	83			
SAE154	Grt-Cpx	35	65			
SAE141	Grt-Cpx-Opx	6	84	10		
SAE147	Grt-Cpx	X	X			
SAE132	Grt-Cpx-Opx	X	X	X		
Garnet orthopyroxenite (GO)						
SAE114	Grt-Opx	17		83		
SAE127	Grt-Opx	16		84		
SAE126	Grt-Cpx-Opx	52	5	44		
SAE135	Grt-Cpx-Opx	24	9	67		
SAE137	Grt-Cpx-Opx-Ol	13	tr	85	2	
SAE139	Grt-Cpx-Opx	30	tr	70		
SAG19	Grt-Opx-Ol	11		88	tr	
SAE151	Grt-Opx	15		85		
SAE136	Grt-Cpx-Opx-Ol	X	X	X	X	
SAX37	Grt-Cpx-Opx	X	X	X	X	
SAE149	Grt-Opx	X	X	X		
SAE155	Grt-Opx	X	X	X		
SAE157	Grt-Cpx-Opx	X	X	X		

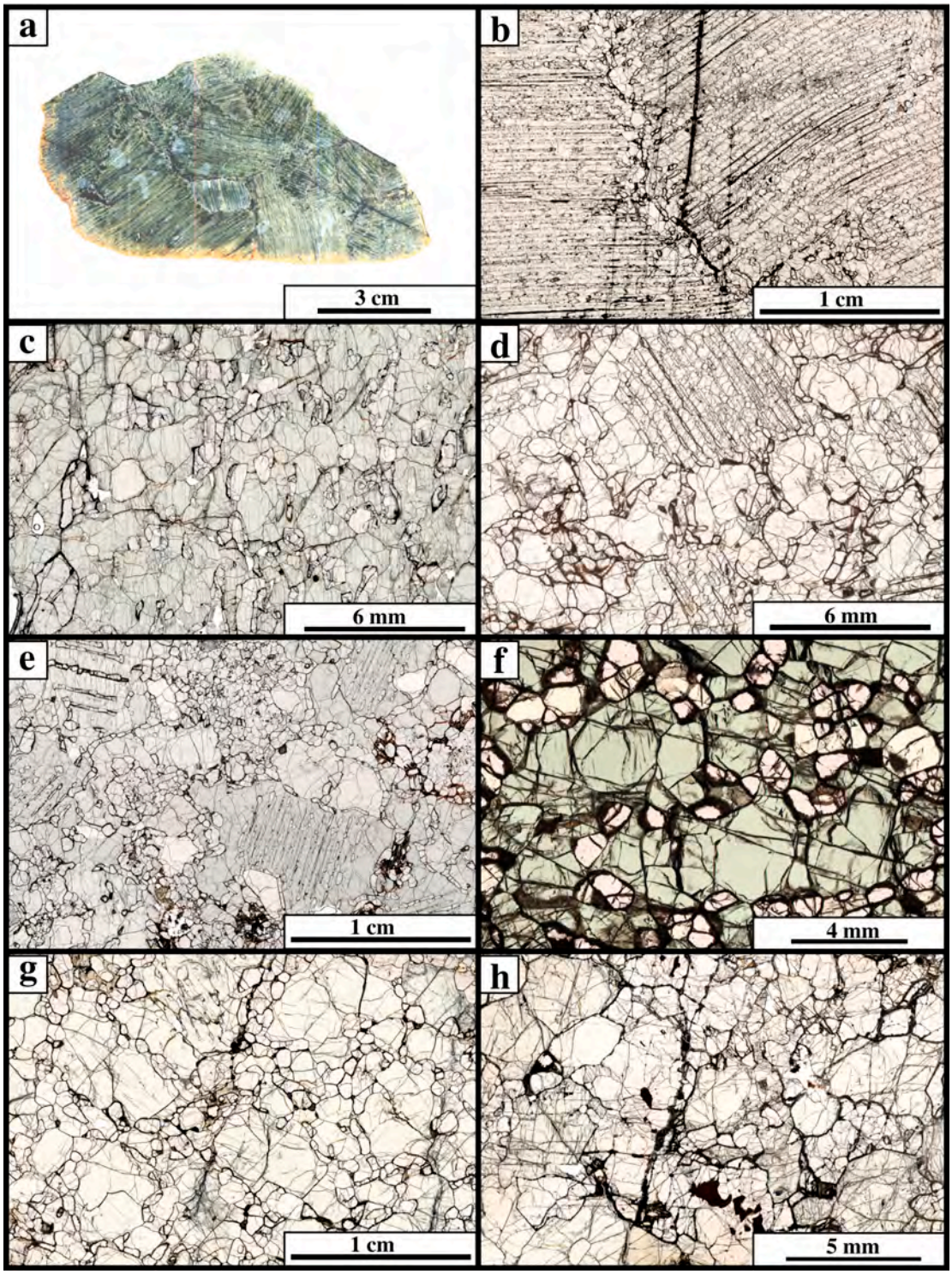

Fig. 2-6. Photographs of representative garnet websterites (GW) from the Malaitan xenolith. a: SAE134, b: SAE134, c: SAE103, d: SAE122, e: SAE138, f: SAE111, g: SAE117, h: SAE128 (a: sawed surface, b-h: ordinary lights). See text for explanation.

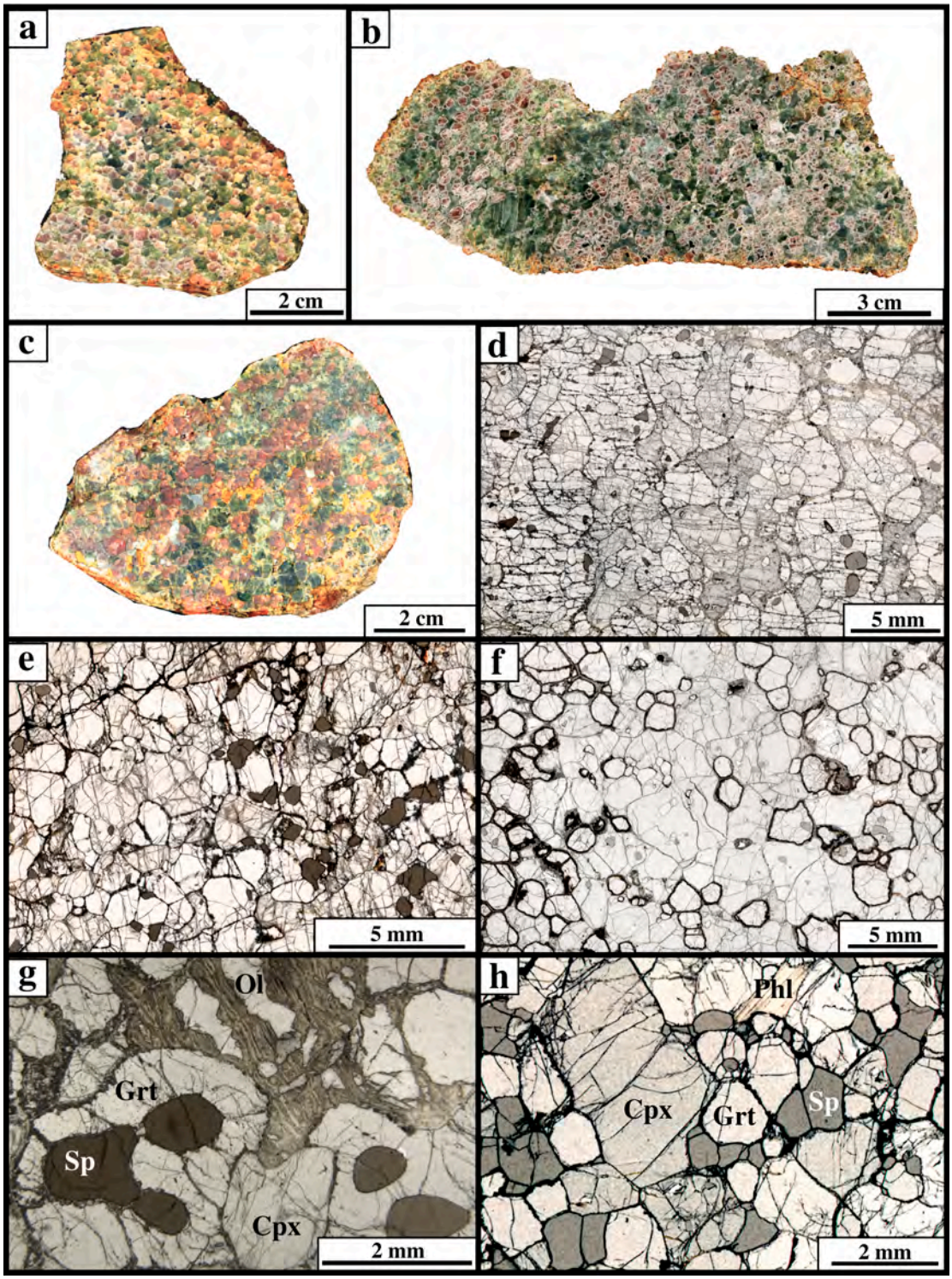

Fig. 2-7. Photographs of representative spinel-garnet clinopyroxenites from the Malaitan xenolith. a: SAE110 (SGC3), b: SAE146 (SGC2), c: SAE111 (SGC1), d: SAE140 (SGC1), e: SAE130 (SGC2), f: SAE104 (SGC3). g: SAE109 (SGC1), h: SAE108 (SGC3), (a-c: sawed surfaces, d-h: ordinary lights). See text for explanation.

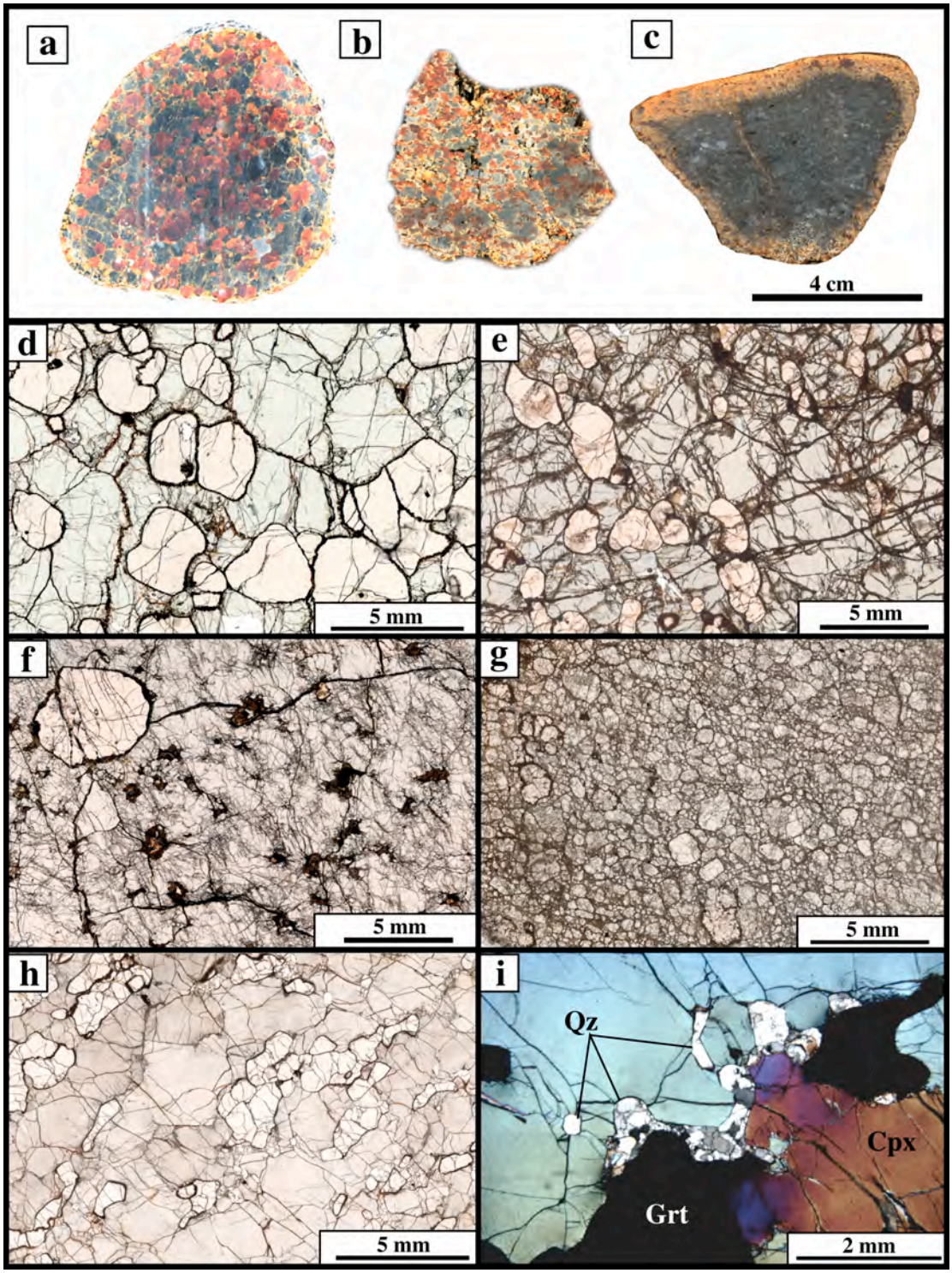

Fig. 2-8. Photographs of representative garnet clinopyroxenites (GC) from the Malaitan xenolith. a: SAE113, b: SAE116, c: SAE141, d: SAE113, e: SAE152, f: SAE133, g: SAE141, h: SAE116, i: SAE116 (a-c: sawed surfaces, d-h: ordinary lights, i: crossed nicol). See text for explanation.

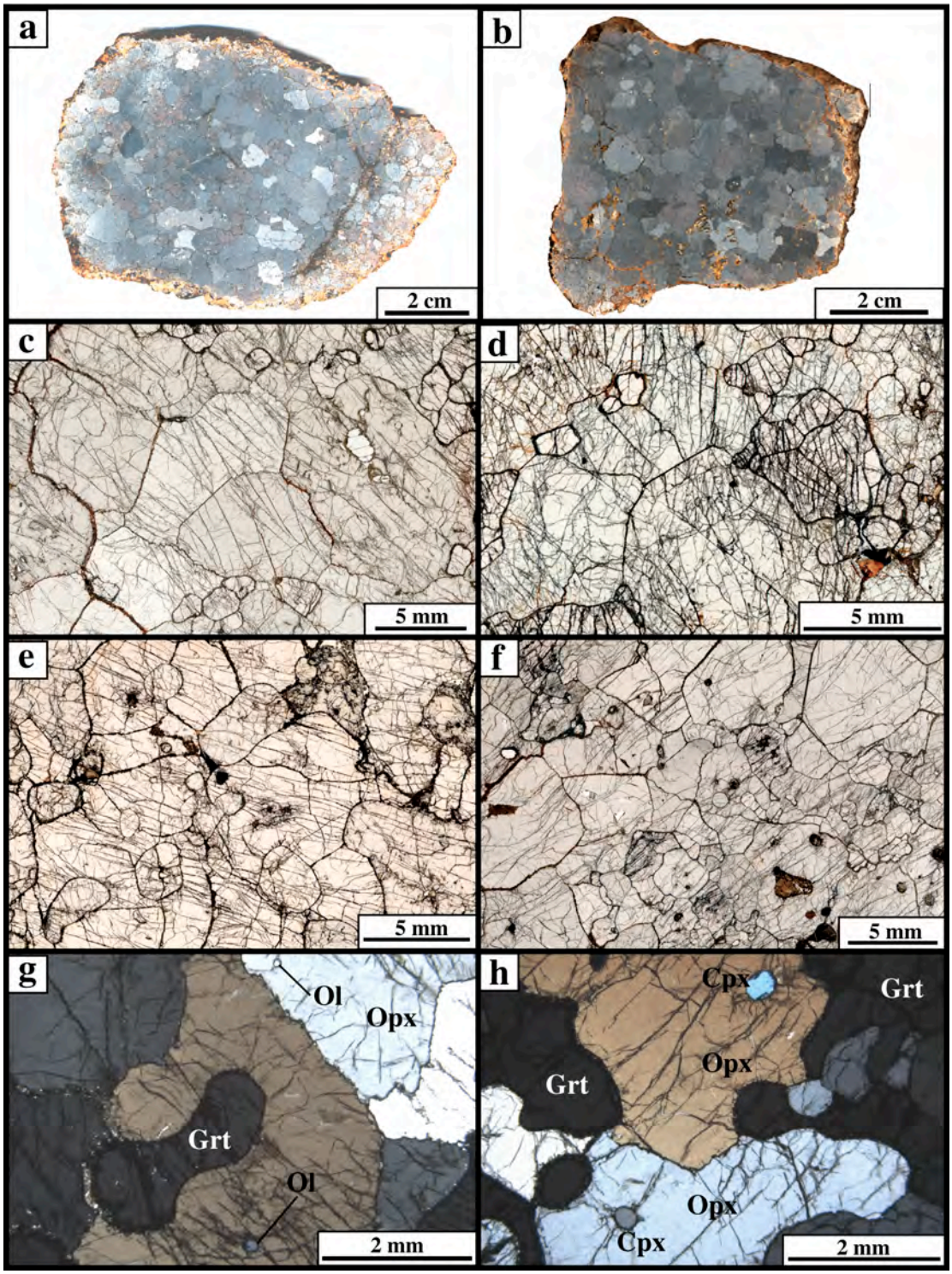

Fig. 2-9. Photographs of representative garnet orthopyroxenites (GO) from the Malaitan xenolith. a: SAE114, b: SAE136, c: SAG19, d: SAE135, e: SAE126, f: SAE137, g: SAE137, h: SAE139 (a and b: sawed surfaces, c-f: ordinary lights, g and h: crossed nicols). See text for explanation.

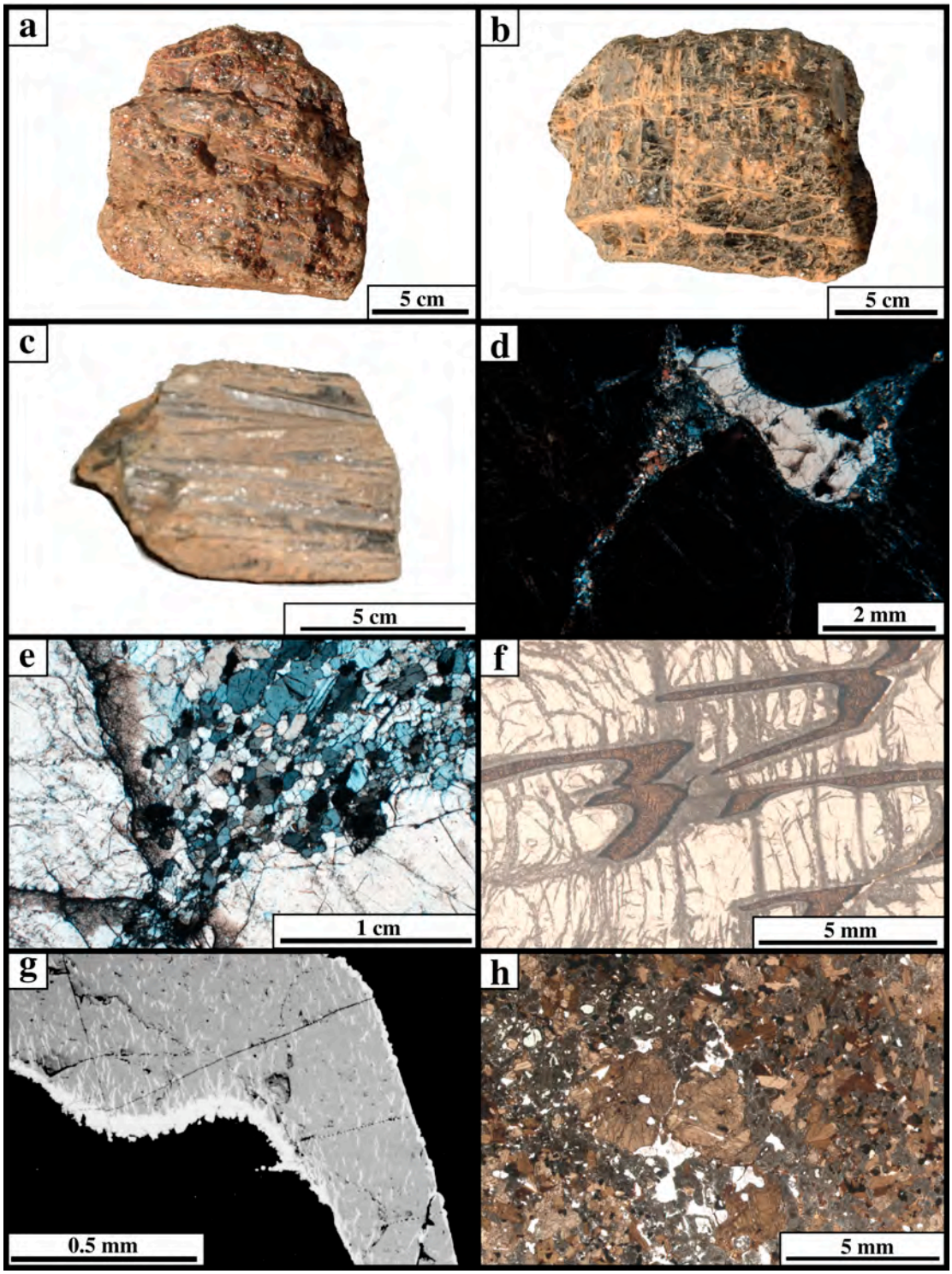

Fig. 2-10. Photographs of representative samples in megacrysts suites from the Malaitan xenolith. a: garnet megacryst (MG), b: subcalcic diopside (MSD), c: clinopyroxene-ilmenite intergrowths (MCI), d: garnet megacryst containing subcalcic diopside (SAX10, crossed nicol), e: subcalcic diopside showing subgrain recrystallization (SAX40, crossed nicol), f: clinopyroxene-rutile intergrowths (MCR, SAX34), g: back-scattered electron image of rutile (gray) in SAX34. Ilmenite (white) occurs in margins and inner cleavages of the rutile. h: mica-amphibole-ilmenite-augite rock (MAIA, SAX107).

Garnet orthopyroxenite

Garnet orthopyroxenites are mainly composed of coarse-grained (< 1.5 cm) orthopyroxene and interstitial garnets that have similar compositions to bronzite and garnet megacryst. (SAE114, SAE126, SAE127, SAE135, SAE136, SAE137, SAE139, SAE149, SAE151, SAE155, SAE157, SAG19, SAX37). Most of these samples contain small well-rounded inclusions (< usually 1 mm) of olivine and clinopyroxene in orthopyroxene, rarely garnet (olivine inclusions: Figs. 2-8 c and g, clinopyroxene inclusions: Figs. 2-8 f and h). Although SAE126 (Fig. 2-8 e) and SAE135 (Fig. 2-8 d) contain coarse clinopyroxene with anhedral surface on the orthopyroxene and garnet, their textures are dissimilar to those of garnet clinopyroxenite. SAE136 (Fig. 2-8 b), SAE137 and SAE139 contain coarser grains of garnet than others (~ 5 mm, max. 3 cm in SAE136). The garnets reveal marked chemical zonation of several elements, mainly Chromium (Other detail will be described later section).

2-2-4 Megacryst suites

Megacryst suites defined by large, rounded, single crystals mainly consist of garnet (Fig. 2-10 a), clinopyroxene (Fig. 2-10 b), orthopyroxene and ilmenite. Phlogopite and zircon are also believed as a member of megacryst suites. Moreover, presence of clinopyroxene-ilmenite graphical intergrowths (Fig. 2-10 c), which are common in kimberlitic inclusion, was already described in previous studies (e.g. Nixon and Boyd, 1979). Most common mineral is garnet and they were prepared as the thin sections of 40 fragmented samples for detail work. The occurrence of clinopyroxene megacryst is limited relative to garnet megacryst, but may reflect the weakness of resistance to surface alteration. I could collect 21 samples of clinopyroxene megacrysts including the intergrowths and all of them were investigated. 9 subcalcic diopsides, 6 augites, 5 clinopyroxene-ilmenite intergrowths and 1 rutile-clinopyroxene intergrowth were confirmed. The presence of rutile-clinopyroxene intergrowth is probably first finding in Malaitan alnöite, showing similar texture to clinopyroxene-ilmenite intergrowth (Fig. 2-10 f). Margins and inner cleavage planes of the rutile occur ilmenite (Fig. 2–10 g). The composition of clinopyroxene is homogeneous and similar to augite megacrysts rather than those of clinopyroxene-ilmenite intergrowth. SAX107 (Fig. 2-10 h), which is the largest and

heaviest sample (> 5 kg) among the collection, composed of mainly mica, amphibole, ilmenite, apatite and clinopyroxene that have the similar compositions to the augite megacryst. I will treat this rock as megacryst suites in due to its compositional similarity to augite megacryst.

3. Major element mineral chemistry and equilibrium conditions

Mineral compositions were measured by electron microprobe (JEOL-JXA8800) with a wave-dispersive analyzer system housed in the Tokyo Institute of Technology. Natural silicate minerals and synthetic oxides were used as standards. All analyzes were performed with accelerating voltage of 15 kV, and a focused electron beam with 12 nA current except for analysis of trace amounts of Ca, Al and Cr contents in olivine, which were obtained with accelerating voltage 25 kv, beam current 50 nA and counting time 100 s. Ca content in olivine was analyzed simultaneously on two spectrometers in order to improve counting statistics, and the average of the two measurements was used.

Automatic x-ray concentration maps were also collected on the JEOL-JXA8800 in Tokyo Institute of Technology. Automatic analysis used accelerating voltage of 15 kV, and a focused electron beam with 30 or 50 nA current were used. According as required quality and area, dwell time on each points and analysis points in each grids were changed.

For some representative samples, bulk rock major and trace elements were measured by X-ray fluorescence (XRF) analyzer at Tokyo Institute of Technology (major elements: SiO_2, TiO_2, Al_2O_3, FeO*, MnO, MgO, CaO, Na_2O, K_2O and P_2O_5) and Ocean Research Institute, University of Tokyo (trace elements: Ni, Sr, Rb, Ba, Nb, Zr and Y). The analytical procedure, conditions and its accuracy were described by Goto and Tatsumi (1994).

3-1 Pyroxenes

Clinopyroxene and orthopyroxene are common minerals among three rock suites and their compositional variations may be of use to classify studied samples and estimate their equilibrium conditions. Although some of pyroxenes display extensive exsolution, exsolved grains were not recalculated to their primary compositions. Their compositions are plotted in Ca-Mg-Fe* diagram (Fig. 3-1) and listed in Table 3.

Pyroxenite suites

Clinopyroxene compositions from pyroxenite suites show that they can be

divided into two main types. Clinopyroxenes of garnet websterite (GW) and spinel-garnet clinopyroxenite (SGC) are Mg-rich diopside and have restricted Mg/(Mg + Fe*) ratio (Mg#= 0.905-0.951) and varied Ca/(Ca+Mg+Fe*) ratio from 0.45 to 0.55. Because clinopyroxenes in these two rock types have unmixed textures and retain marked heterogeneous composition, all analyzed compositions are plotted in Fig. 3-1. Particularly, Al contents show significant variation and decrease from core to rim of single mineral owing to incomplete garnet forming reaction. In some samples, observed ranges of Al heterogeneity reach up to 4 wt.% (detail in later section). Variation of Ca/(Ca+Mg+Fe*) is due to their Ca-Tschermak (CaTs) contents, showing that clinopyroxenes of SGC have higher CaTs content than those of GW, although both compositional fields are overlapped. On the other hand, clinopyroxenes of garnet clinopyroxenite (GC) and garnet orthopyroxenite (GO) are homogeneous in composition and similar to those of megacrystalline subcalcic diopsides (MSD), suggesting they have higher equilibrium temperature than those of GW-SGC and relevance to megacryst suites. Orthopyroxenes of GW and SGC (one sample) are Ca-poor enstatite (Mg#= 0.894-0.923, CaO = 0.31–0.67 wt.%), while orthopyroxenes of GC and GO are Ca-rich bronzite (Mg#=0.845-0.876, CaO=1.24–1.64 wt.%) and similar to those of megacrystalline bronzites (MB). This difference shows consistency with the interpretation that GW-SGC and GC-GO equilibrated on different temperature. It is noted that significant difference in Mg# of both pyroxenes between GW-SGC and GC-GO indicates they have different rock compositions about Mg#. One sample from GW (SAE134) is originally clinopyroxenite based on petrographic observation and bulk rock composition determined by XRF may give original clinopyroxene composition before exsolution reaction. It is plotted near Mg-rich side of compositional field of MSD, indicating that original temperature and/or clinopyroxene composition may be similar to those of megacryst and GC-GO.

Variation of Mg# and minor elements such as Na, Ti and Cr in both pyroxenes are plotted in Figs. 3-2 and 3-3. Clinopyroxenes of megacryst suites ranging from subcalcic diopsides (MSD), clinopyroxene-ilmenite intergrowths (MCI) to megacrystalline augites (MA) illustrate regular chemical trends (Nixon and Boyd, 1979). With decreasing Mg#, there is an increase of Na and Ti and decrease of Cr. Clinopyroxene in SAX107 which has mica-amphibole-ilmenite-clinopyroxene

assemblage is plotted in Fe-rich end of MA compositional field, indicating that this rock crystallized from extremely fractionated megacryst magma. While, these contents in both pyroxenes from GC-GO also support genetic link with those of MSD, however some of them tend to plot outside the regular compositions of MSD. Particularly, clinopyroxene in quartz-garnet clinopyroxenite (QGC) has lower Na, Ti and Cr contents than those of megacrysts and other GC-GO. Although both pyroxenes in SAE141 (GC) have also lower Ti contents, most conspicuous feature is that orthopyroxene retains complex chemical zoning in single grain scale. Core and rim of most orthopyroxene grains are Mg and Cr-rich, while lowest Mg# and Cr content generally found in mantle of orthopyroxene grains. Pyroxenes from GW and SGC are characterized by their restricted Mg# and relatively large variation in Na, Ti and Cr contents, but their variations overlap for those of peridotite suites. Highest Mg# among clinopyroxenes in pyroxenite suites are found in SGC but they tend to be lower Cr content (Cr_2O_3 < 0.68 wt.%). On the other hand, lowest Na content is remarked in post-exsolution clinopyroxenes from SAE134 that was originally clinopyroxenite (Na_2O=0.25-0.37 wt.%). This means pre-exsolution clinopyroxene is very depleted in Na content and is consistent with the primary nature of crystallization process as suggested by textural observation.

Peridotite suites

Both pyroxenes of peridotite suites can also be divided them into two types on Ca-Mg-Fe* diagram, suggesting their different equilibrium temperatures. Those of garnet-spinel lherzolites (GSL) are Mg-rich diopside and enstatite, restricted in GW fields. While two pyroxenes in garnet lherzolites (GL) deviate from compositional ranges of GSL toward Ca-poor clinopyroxene and Ca-rich orthopyroxene (CaO=1.12-1.45 wt.%). Two samples of GL (SAG21 and SAG27) that have lower Ca in clinopyroxene and higher Ca in orthopyroxene tend to be lower Mg# (clinopyroxene; 0.868 and 0.861, orthopyroxene; 0.883 and 0.877), bearing resemblance to those of megacryst suites and GC-GO in pyroxenite suites. Similar to GL, six samples from spinel peridotite have subcalcic clinopyroxene and Ca-rich orthopyroxene (CaO=1.17-1.54 wt.%). It is interesting to note that these six samples are harzburgite based on thin section observation. Although harzburgites with relatively higher-Ca diopside and lower-Ca enstatite are present, no continuous

relationship has been observed. Particularly, there is a significant discrepancy for Ca in orthopyroxene between both (Fig. 3-4). Based on above reason, these are sort out and referred to as high-temperature spinel harzburgite (HTSH). While other spinel harzburgites and lherzolite are referred to as spinel harzburgite (SH) and spinel lherzolite (SL), respectively. These evidences suggest that for the classification scheme of peridotite suites, difference in equilibrium temperature is more significant than garnet appearance.

Minor elements variations of both pyroxenes from peridotite suites are also plotted in Figs 3-2 and 3-3 for comparison with pyroxenes in pyroxenite and megacryst suites. Those of GSL and SL are nearly identical with GW and SGC, but both pyroxenes tend to be higher Cr content than those of GW. While those in GL and HTSH show peculiar and complex variation. Important feature may be revealed in their complex behavior of compatible element such as Cr and incompatible element such as Na and Ti. HTSH pyroxenes have distinctly higher Cr content than other studied samples (clinopyroxene: ~ 2.0 wt.%; orthopyroxene: ~ 1.0 wt.%). This feature is consistent with their refractory character. Cr contents in GL tend to be rich in both pyroxenes. On the other hand, Na and Ti contents in HTSH and GL are variable and almost covered with whole range of studied xenoliths. Na and Ti contents in three HTSH give highest abundance and inconsistent with their refractory nature. But these values are equivalent with those of MB, suggesting their abundance have been controlled by enrichment process from magma that crystallized megacryst suites. This interpretation may be supported that two HTSH sample (SAS21 and SAS46) still remains highly depleted in Na and Ti as a result of relieving from the enrichment process.

In Fig. 3-4, pyroxene compositions are compared with abyssal peridotite samples whose trends are thought to have representative composition formed by partial melting event (e.g. Johnson et al., 1990). Although Mg# of pyroxenes overlaps for the abyssal peridotites, Na contents of most clinopyroxenes deviate from the abyssal peridotite field to greater extent than Ti content toward high abundances. Cr-rich HTSH clinopyroxenes tend to plot outside the compositional field defined by the abyssal peridotites. It is noted that highest Mg# (~ 0.952) from SL-SH is harzburgite (SAS22), their refractory composition may correlate with clinopyroxene modal abundance. One of the important differences between SL-SH and abyssal

peridotites are exhibited Ca content in orthopyroxene, which reflects equilibrated temperature in clinopyroxene-bearing assemblage. Most of orthopyroxene from abyssal peridotite has been reported as a high relatively uniform CaO content around 2.0 wt % in contrast to lower uniform ranges of those in Malaitan xenoliths. High-Ca content of orthopyroxene have been interpreted that they retain the compositions at nearly igneous temperature because they usually recovered from rift mountains and fracture zones locating near active mid-oceanic ridge (Dick and Fisher, 1989). Actually, most of these high values were obtained by specific analytical technique using defocused beam of microprobe analyses, XRF analyses of separate or fused single grain because orthopyroxene retain variable abundances of clinopyroxene exsolution lamellae. The orthopyroxene composition from Atlantis II fracture zone which were reported as present compositions without correction exhibits large Ca variation between 2.0~0.5 wt%. These values are best explained by variable low temperature re-equilibration accompanying clinopyroxene exsolution. Uniform CaO ranges through not only single sample but also each rock types in studied xenoliths may be accounted that low-temperature equilibration were attained well in orthopyroxene. Al contents in orthopyroxenes from spinel lherzolite assemblage also have been regarded as temperature dependence, not only bulk composition. Al content in both pyroxenes from peridotite suites are relatively homogeneous in contrast to very heterogeneous nature of GW-GC. Those of SL-SH are plotted in the field of abyssal peridotites and decreased with increasing Mg# in spite that some samples deviate from the trends toward lower Al contents and Mg#. Variations of Al content in orthopyroxene from GSL and GL are restricted around 2.5 wt.% and 3.3~3.6 wt.%, respectively. They show the consistency with garnet equilibration and depend on equilibrium conditions. However significant variations for temperature and/or pressure estimation are detectable in several samples. Especially, GSL with low modal garnet tends to have larger Al variation in both pyroxenes. This evidence indicates that garnet forming reaction was incomplete similar to GW and SGC in several samples. While all grains of both pyroxenes in GL and HTSH are remarkably homogeneous and there is no heterogeneity throughout individual specimens.

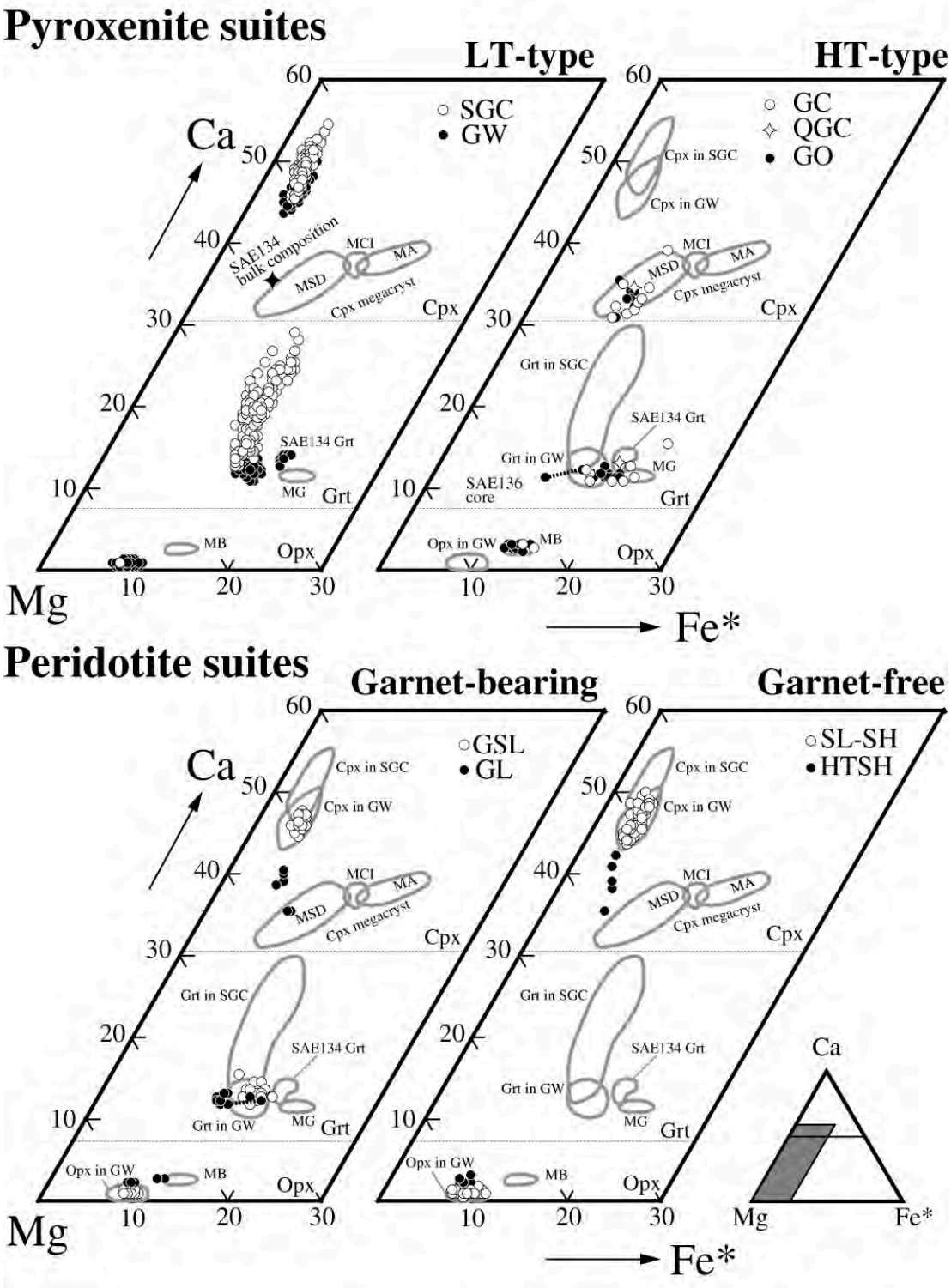

Fig. 3-1. Compositions of clinopyroxenes (Cpx), orthopyroxenes (Opx) and garnets (Grt) in several types of studied xenoliths represented on Ca-Mg-Fe* diagrams. Compositional fields for megacryst suites are from Neal and Davidson (1989).

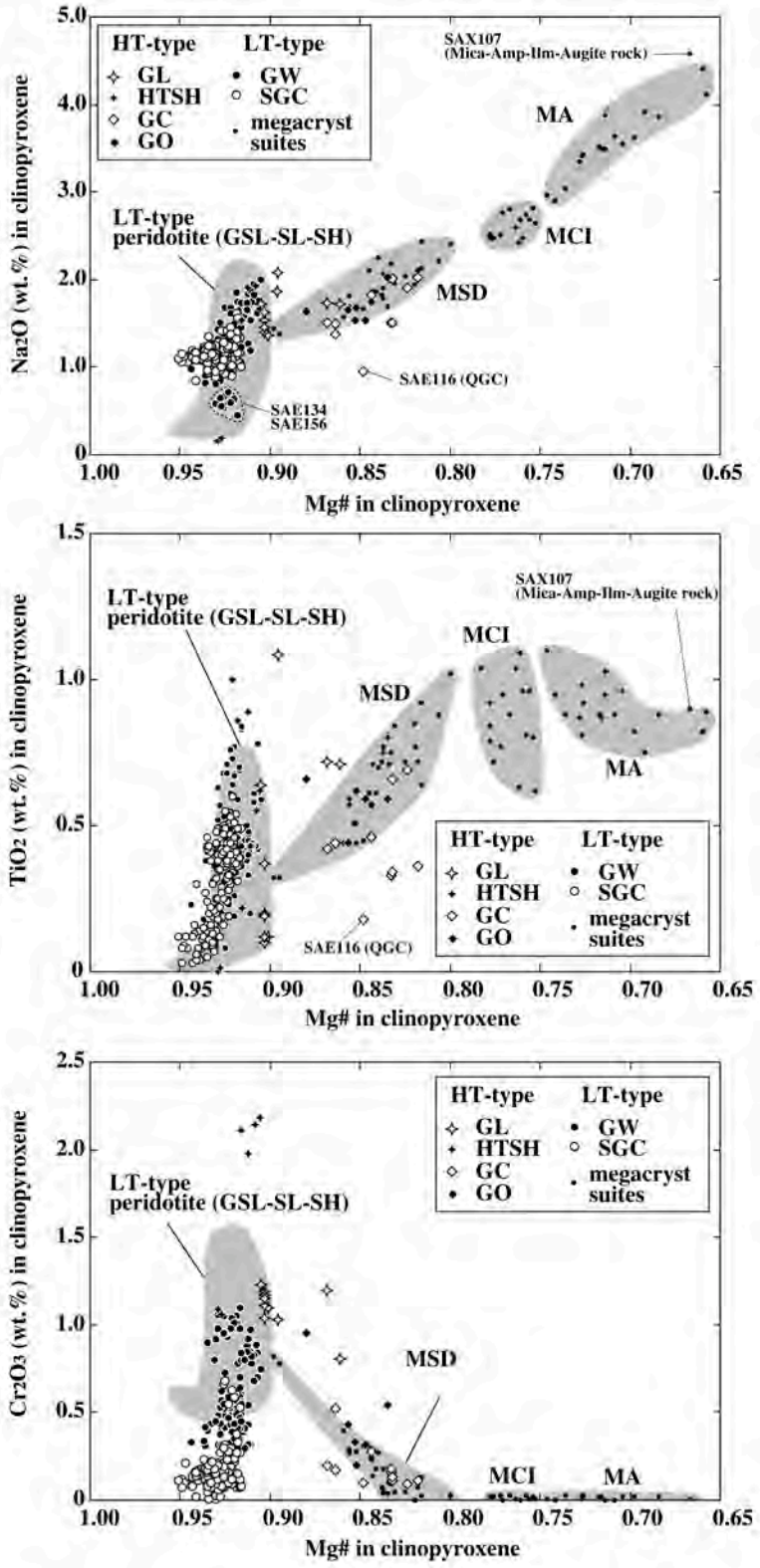

Fig. 3-2. Mg# = Mg/(Mg+Fe*) against abundances of minor element oxides (wt.%) in clinopyroxenes. Some plots for megacryst suites were compiled from Nixon and Boyd (1979) and Neal and Davidson (1989).

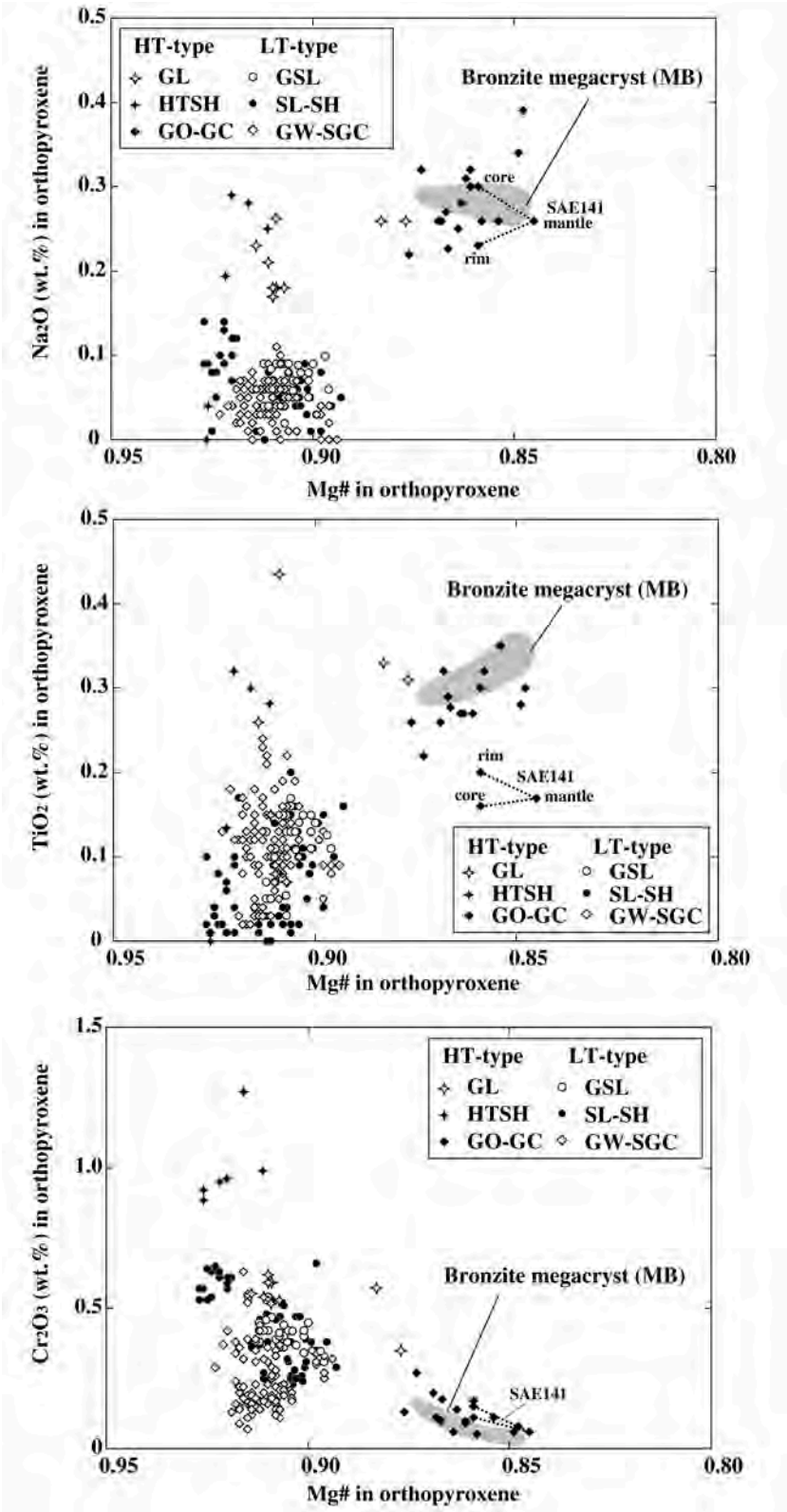

Fig. 3-3. Mg# = Mg/(Mg+Fe*) against abundances of minor element oxides (wt.%) in orthopyroxenes. The compositional fields for bronzite megacryst (MB) are obtained from Nixon and Boyd (1979) and Neal and Davidson (1989).

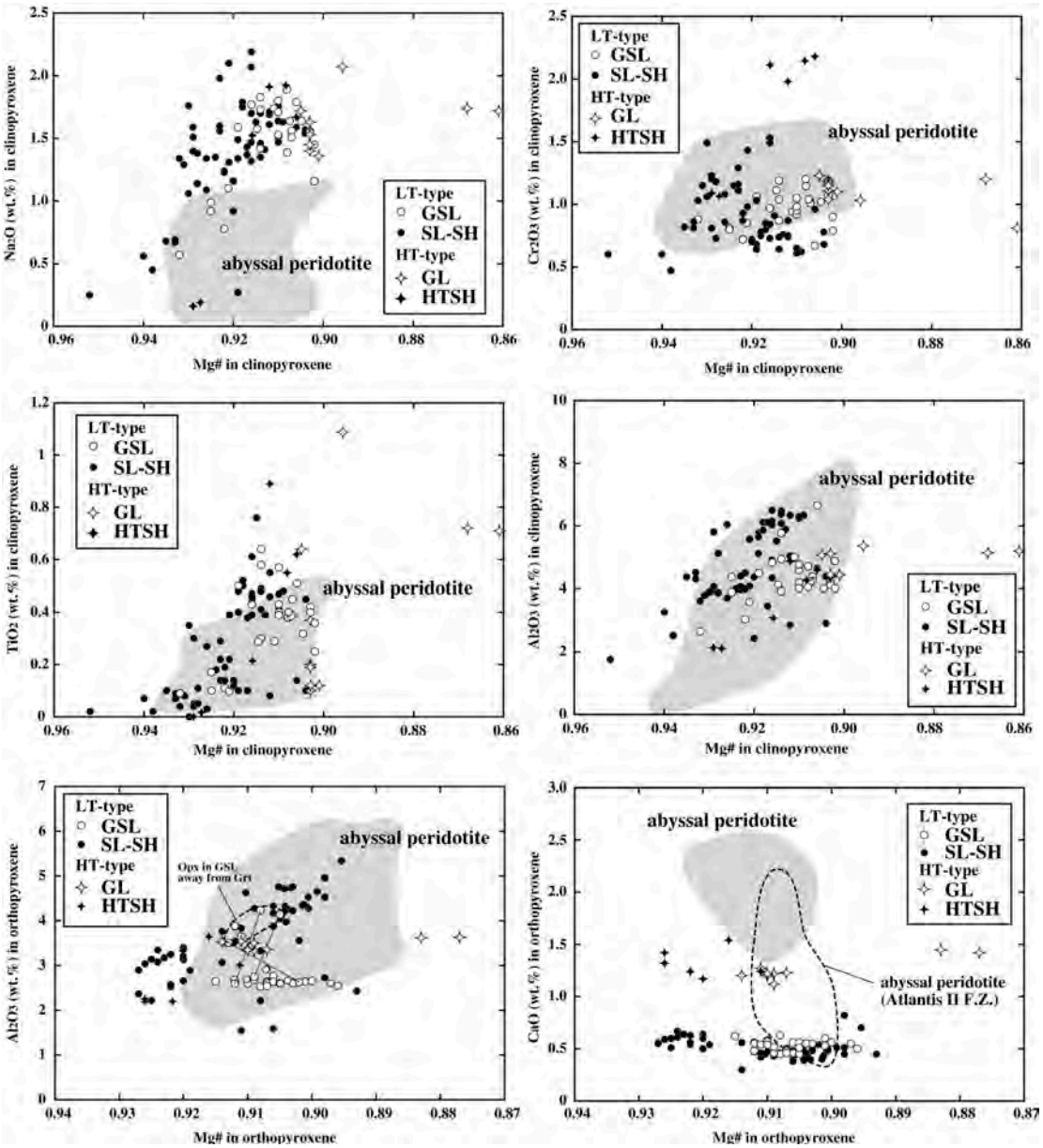

Fig. 3-4. Mg# = Mg/(Mg+Fe*) against abundances of other element oxides (wt.%) in clinopyroxenes and orthopyroxenes from Malaita peridotite suites. Representative values from heterogeneous orthopyroxenes are tied by thin lines. Abyssal peridotite fields are obtained from the compilation by Ross and Elthon (1997). Data for abyssal peridotites from Johnson et al. (1990), Johnson and Dick (1992), Bonatti et al. (1992), Dick and Fisher (1984), Michael and Bonatti (1985), Shibata and Thompson (1986), Arai and Fujii (1979), Hamlyn and Bonatti (1980), and Sinton (1979).

3-2 Garnet

Pyroxenite suites

Largest variation in terms of XCa=Ca/(Ca+Mg+Fe*+Mn) is observed in GW-SGC of pyroxenite suites. Similar to pyroxenes, garnet retains chemical zoning that is closely related with Al zoning in pyroxenes from GW-SGC. Therefore, all analyzed compositions are plotted in Fig. 3-1. XCa of SGC garnets vary from 0.125-0.288, whereas those of GW have restricted range from 0.113-0.142. In the most GW-SGC samples, XCa in garnet increase from core to rim. In the case of GW, observed heterogeneity of Ca content in single sample restricted about 1 wt.%. While, SGC garnets tend to have larger variation (~ 2 wt.%) in single sample. This evidence suggests that primary variation of XCa in GW-SGC modified by subsolidus cooling reaction and this reaction was incomplete. In contrast to XCa, regulated variation of Mg# was not detected in individual samples. Mg# in GW garnets usually ranges from 0.801-0.839. Mg# in SGC garnets overlaps for those of GW but highest Mg# is generally found in SGC (Mg#=0.804-0.857). Garnet in SAE134, which originated as clinopyroxenite displays distinctive lower Mg# (0.771-0.784). This means SAE134 has different K_D value (K_D= $(Fe/Mg)^{Grt}/(Fe/Mg)^{Cpx}$), indicating equilibrium condition was different from other GW-SGC samples.

Most of garnets from GC-GO pyroxenites are homogeneous in compositions and their compositions overlap for compositional field of megacrystalline garnet (MG) on Ca-Mg-Fe* diagram. However, some of GO garnets retain marked compositional zoning at grain scale. Mg# of homogeneous GO vary from 0.773 to 0.808 but largest garnet in SAE136 has high Mg# core (~ 0.864) and the rim and other anhedral small garnets show normal Mg# (~ 0.794). XCa in GO (including heterogeneous garnets) remains nearly constant from 0.108 to 0.125. There is no heterogeneity in GC garnet and their Mg# vary from 0.730-0.813. Although XCa in most of GC garnet overlaps the XCa range of GO and MG (XCa=0.106-0.123), SAE152 which has lowest Mg# remarks highest XCa (~ 0.153) among GC-GO garnets. Garnets in SAE116 (QGC) also have higher XCa (~ 0.132) among others.

Significant difference between the GW-SGC garnets and GO-GC is revealed by the minor elements such as Ti and Cr (Fig. 3-5). There is the compositional gap between GW-SGC and GC-GO-MG in terms Ti concentration. GW-SGC garnets have lower Ti contents (< 0.23 wt.%), whereas GC-GO-MG garnets have higher Ti

contents (> 0.32 wt.%). One exception is SAE116 (QGC), in which garnets contain equivalent amounts of TiO_2 (~0.17 wt.%) in those of GW-SGC. In terms of Ti contents there is no difference between GW and SGC garnets, however GW garnets tend to have higher Cr content than SGC garnets (GW 0.36-1.36 wt.%, SGC < 0.83 wt.%).

The covariation relationship between Mg# and Ti contents is well defined in MG similar to the case of MSD, implying that they track the crystallization trends of megacryst magma. Most of GO garnets are plotted near the Mg-rich side of MG field. Also three GC garnets have higher Mg# than Mg-rich MG with equivalent Ti contents, however low Mg# GC garnets (including SAE116) tend to plot below the MG trend. The deviation is also observed in clinopyroxene compositions, indicating that compositions of GC were not directly controlled by magma that crystallized megacrysts in spite of their overall similarity. Most of Cr contents of GC-GO garnets relatively settle on low concentration and correlate with Mg#. Highest Cr concentration usually remark in core of heterogeneous garnets from GO (up to 2.85 wt.%). Whereas, large heterogeneous garnet in SAE136 shows complex zoning, highest Cr content appears in mantle of the grain (up to 2.41 wt%). But Cr contents in their rims decrease to equivalent values with MG, GC and homogeneous GO.

Peridotite suites

Similar to pyroxenes, garnet compositions of GSL and GL are distinctive. Usually, Mg# in GL garnets is higher than those of GSL (GL: 0.845-886, GSL: 0.789-0.825). SAG21 and SAG27 with low Mg# pyroxenes have also low Mg# garnet, showing they have Fe-rich rock compositions. However, garnet in SAG21 retains high Mg# core, indicating that their Fe-rich compositions were attained by enrichment process (discussed in later section). XCa variation in GL garnets are quite restricted (XCa=0.115-0.130), while GSL garnets have relatively large variation (XCa=0.119-0.155). This variation may also formed by imperfect cooling reaction similar to garnets from GW, because these observed ranges are comparable. But lesser variations were detected in individual GSL samples compared with GW garnets.

The differences of Ti and Cr concentration between both types are not so significant. But four samples (including two Fe-rich sample) of GL tend to have

high-Ti garnets and they are similar to those in GC-GO. Ti contents in other GL and GSL garnets overlap for those in GW-SGC. On the other hand, Cr concentrations of most of garnets in peridotite suites are relatively higher than those in pyroxenite suites. Excluding one sample (SAG26), GSL garnets have restricted range in Cr contents (1.02-1.93 wt.%). It is noted that the SAG26 has highest XCa and Mg# garnet among GSL and it is petrographicaly anomalous (highly carbonated and garnet concentration). GL tends to have high Cr garnets (1.96-2.30 wt.%) than normal GSL, excepting one Fe-rich sample (SAG21). Also this is not simple variation because high Mg# core have lower Cr concentration than Fe-rich rim (core ~1.10 wt.%, rim ~1.47 wt.%). Previous studies reported some garnet bearing lherzolites (two samples are also spinel bearing) have much higher Cr garnets up to 5.46 wt.% (Nixon and Boyd, 1979; Neal 1985). Two of their garnets are depleted in Ti, whereas one spinel-bearing sample has high Ti garnet. These garnets coexist with Ca-rich orthopyroxenes (CaO=1.19-1.74 wt.%) and Ca-poor clinopyroxenes (Ca/(Ca+Mg+Fe*)= 0.343-0.413), indicating they originate higher equilibrium temperature (Nixon and Boyd, 1979; Neal 1985) and may belong to GL in spite that two of them are spinel-bearing lherzolite.

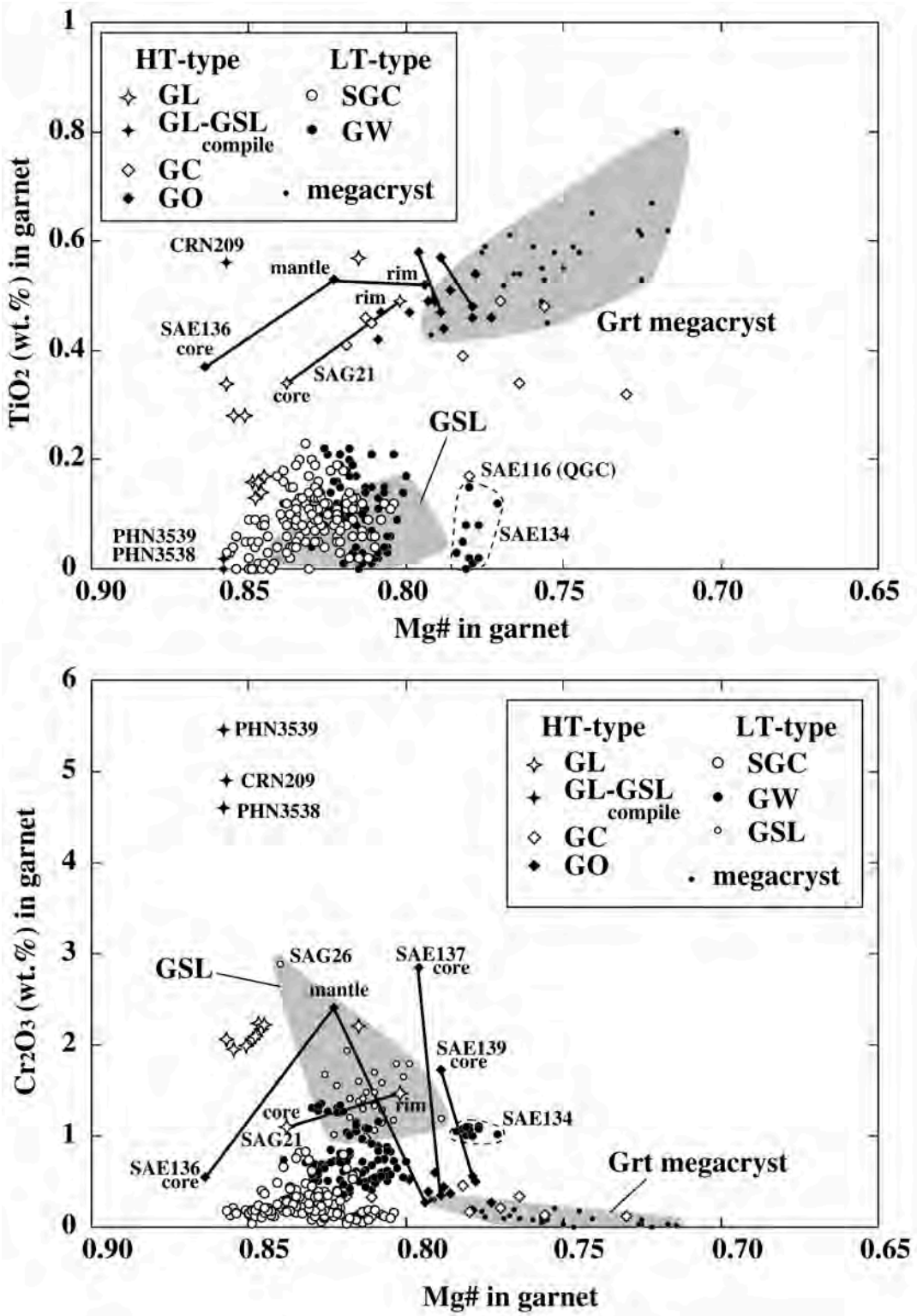

Fig. 3-5. Mg# = Mg/(Mg+Fe*) against abundances of minor element oxides (wt.%) in garnets. The compositional fields for garnet megacryst (MG) are obtained from Nixon and Boyd (1979) and Neal and Davidson (1989). Data for Cr-rich garnets (filled stars) in garnet-bearing peridotites from Nixon and Boyd (1979) and Neal (1985).

3-3 Olivine

Olivine in pyroxenite suites is very minor. In some GW-SGC olivine occur as products of garnet forming reaction based on thin section observation. On the other hand, olivine occurs as small inclusion in some GO. There is no olivine in GC samples. Olivine compositions were obtained from two GW, two SGC and three GO samples among pyroxenite suites. Although olivine in peridotite suites was highly altered, fresh olivine compositions were usually obtained in most of samples.

The olivines in GSL and SL are very similar in Mg#, varying from 0.886-0.912 (Fig. 3-6). Mg# in GW and SGC olivines overlaps for the range of SL-GSL in spite of their metamorphic origin. Although most of olivines in GL have overlaps for their Mg#, olivines in SAS21 and SAS27 have Fe-rich compositions similar to other phases (Mg#=0.870, 0.876). GO olivines also have Fe-rich compositions consistent with other minerals. Except for one sample (SAS23), SH and HTSH olivines tend to be Mg-rich (Mg#=0.919-0.923, SAS23 0.894). The systematic difference between lherzolite and harzburgite implies that Mg# of olivine correlates with modal abundance of clinopyroxene similar to other mantle-derived tectonic peridotites and melting experiments (e.g. Jaques and Green, 1980; Hirose and Kushiro, 1993).

Olivines from all types of peridotite suites and GO have limited variation in NiO and MnO (NiO: 0.27-0.52 wt.%, MnO: 0.06-0.19 wt.%). NiO and MnO contents in GW-SGC olivines show slight deviation, NiO contents are higher, whereas MnO contents are lower than those in olivines from other types. Significant difference between high-temperature and low-temperature types is revealed by the Ca contents in spite of their limited amounts. HTSH, GL and GO olivines that coexist with high-Ca orthopyroxenes contain around 0.1 wt.% CaO, whereas GSL, SL-SH and GW-SGC olivines coexisting with low-Ca orthopyroxene contain below 0.05 wt.% CaO. CaO content in olivine has been found to be correlated with equilibration temperature in other mantle-derived xenolith (Xu et al., 1998; Hauri and Hart, 1994). Furthermore, several experimental results demonstrated a slight pressure dependency, which can be used as geobarometer for spinel lherzolite (Köhler and Brey, 1990). In order to estimate equilibrium pressure, geobarometer of Köhler and Brey (1990) was attempted using CaO content in olivine, which were determined by another analytical conditions (see later section).

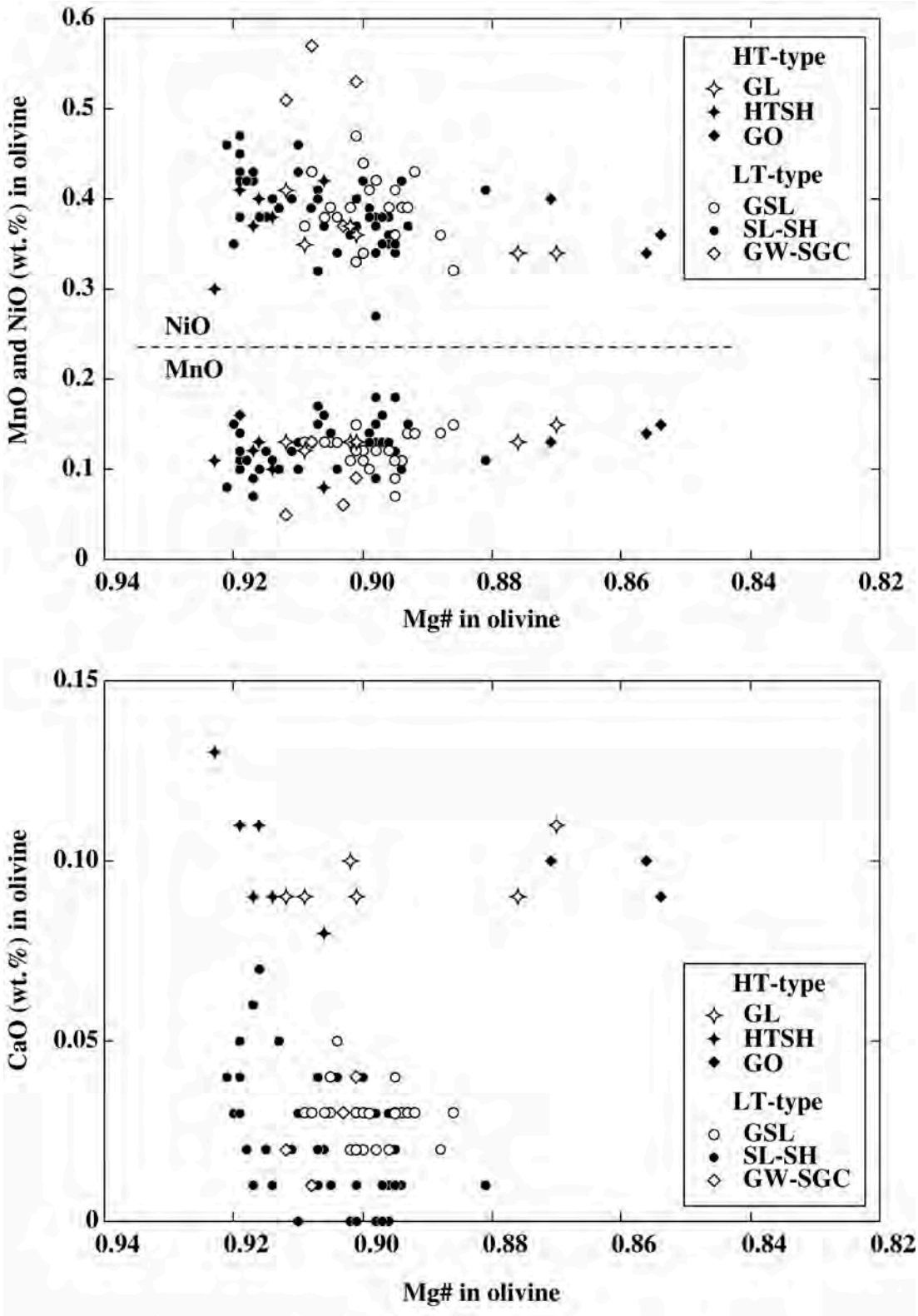

Fig. 3-6. Mg# = Mg/(Mg+Fe*) against abundances of minor element oxides (wt.%) in olivines.

3-4 Spinel

Spinels in each type of peridotites and pyroxenites have distinctive compositions (Fig. 3-7). Usually, their Cr# in peridotite are used to monitor their degree of depletion similar to Mg# of olivines (Arai 1994). Cr# of spinel in abyssal peridotites are well studied and they vary up to Cr# ~ 0.6 (Dick and Bullen 1984). The differences between SL and SH-HTSH spinels are significant in terms of Cr#. SH-HTSH tend to have higher Cr# spinels (Cr#=0.206-0.640) than SL (Cr#=0.084-0.224). Some exceptions of high Cr# spinel in lherzolite (e.g. SAS27, Cr#=0.616) were found in amphibole-rich samples and may have been affected by amphibole formation because they are totally surrounded by interstitial amphibole. They also characterized by lower Mg# than others. Most of SH-HTSH spinels with high Cr# composition tend to have high Mg# but still lower than Mg# of SL spinels and plot outside the compositional field of abyssal peridotite. It may display their difference of equilibrium temperatures between abyssal peridotite and studied xenoliths based on Kd values between olivine and spinel (Fabrie, 1971; Sack and Ghiorso, 1991). It is noted that spinels with maximum Cr# (0.497 and 0.610) are found in HTSH and they also have higher Mg# than those of abyssal peridotites. Two samples (PHN3539 and CRN209) which were reported by previous studies, have comparable Cr# and Mg# with those of HTSH. These two samples also contain high Cr garnet and show high equilibrium temperature, implying that they have strong relevance to HTSH samples. Whereas, Cr# of spinels in GSL are similar to SH rather than SL in terms of their high Cr# (0.270-0.431, one exception 0.147). Although spinel compositions in our GSL samples focused around Cr# ~0.35, compiled compositions of spinel in GSL samples are scattered from Cr# ~0.1-0.45. High Cr# nature of GSL spinels may have been attained by the garnet-forming and spinel-consuming reaction. In three samples from GW, spinel compositions are determined and they have equivalent Cr# and Mg# with those of SL (Cr#=0.071-0.138, Mg#=0.793-0.823), whereas most of SGC spinels tend to have lower Cr# and higher Mg# than SL and GW (Cr# < 0.105, Mg#=0.803-0.887).

Ti concentration in spinels exhibits relatively systematic variations but their interpretations may be not simple. In the case of abyssal peridotites, there is a distinctive difference between plagioclase-bearing spinel peridotite (TiO_2 < 0.5 wt.%) and plagioclase-free spinel peridotite (TiO_2 < 1.5 wt.%). High Ti concentration

of plagioclase bearing peridotites have been explained that they do not have simple nature of restite but resulted as the reaction products with infiltrated and/or trapped melt which crystallized plagioclase (Dick and Natland, 1996; Arai and Matsukage, 1996). GSL spinels tend to have higher Ti contents than SL and some SH and their Cr# and Ti concentration are broadly correlated. Although some high Cr# spinel in SH also have higher Ti contents, there is no correlation with Cr#. In the case of HTSH, two Cr-rich spinels are characterized by their opposite behaviors. TiO_2 is almost free in SAS21 and SAS46 spinel, while SAS1 and SAS63 spinel has very high TiO_2 over than 2.0 wt%. Similar characteristics are observed in the compiled compositions of spinels that were defined as high temperature GSL (Nixon and Boyd, 1979; Neal 1985). Observed Ti enrichment and depletion in spinels are consistent with the compositions of coexisting other phase, for example both pyroxenes and garnet in SAS21 and PHN3539 have very low Ti contents, whereas those in SAS1 and CRN209 have very high Ti contents. These enrichment characteristics “depleted rock types tend to have enriched compositions” may occur and be one predominant process forming the observed variation in Malaita xenoliths.

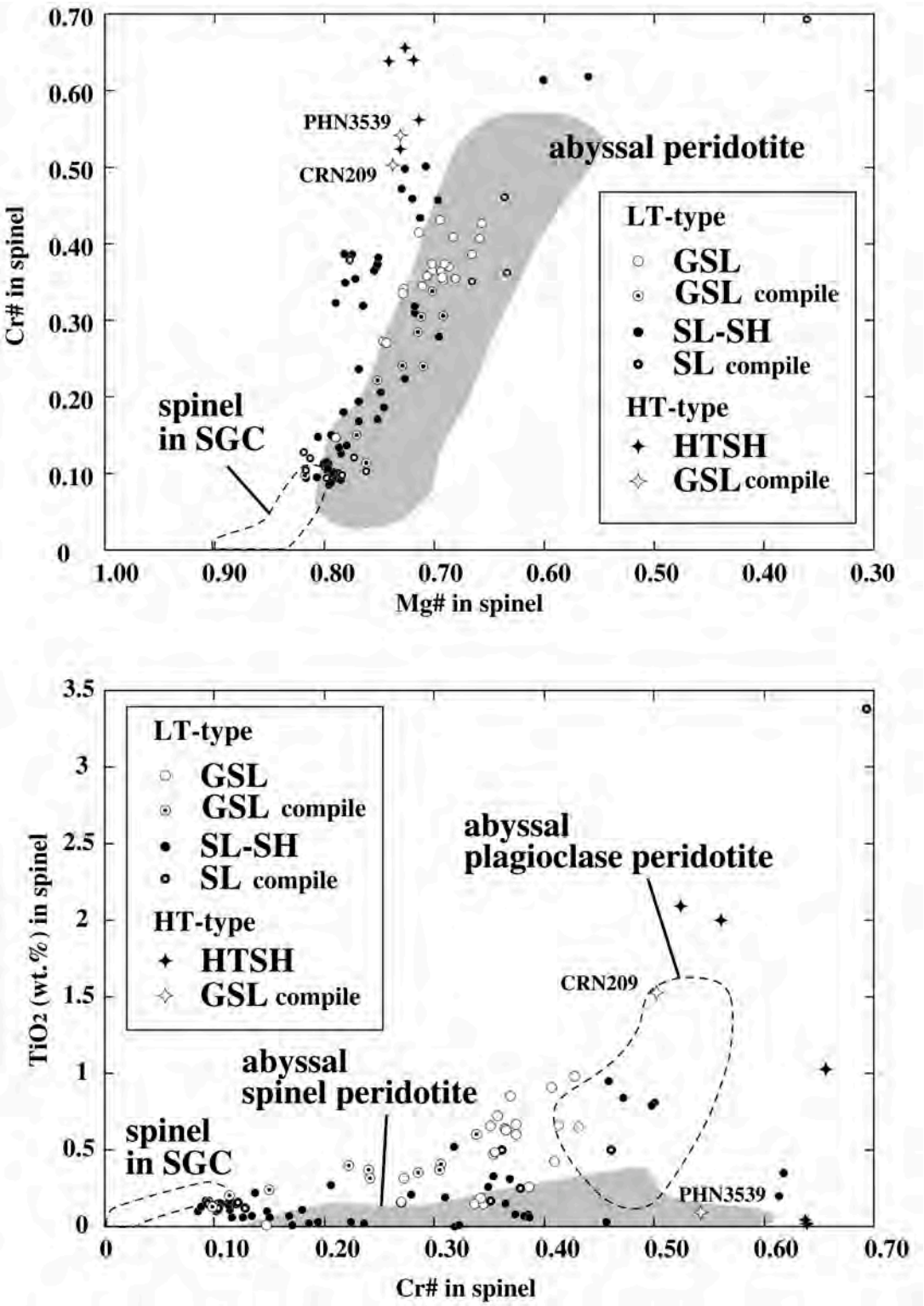

Fig. 3-7. Mg# = $Mg/(Mg+Fe^{2+})$ and TiO_2 (wt.%) against Cr# = Cr/(Cr+Al) in spinels. Abyssal peridotite fields are from the compilation of Dick and Bullen (1984). Some data for spinels in Malaita peridotite suites obtained from Nixon and Boyd (1979) and Neal (1985) are also plotted.

3-5 Compositional heterogeneity in individual samples

GW-SGC pyroxenite

Garnet and clinopyroxene from GW-SGC pyroxenites are characterized by significant compositional zoning, mainly Al in clinopyroxene and Ca in garnet. In Fig. 3-8, Al and Ca X-ray maps for representative GW (SAE117) and SGC (SAE125) are expressed. In SAE117, large clinopyroxene grains (light-blue) are surrounded by smaller garnet (yellow to red) and orthopyroxene (dark-blue). One largest grain retains exsolution plates of garnet. Al depletion is observed at rim of clinopyroxenes and near exsolution plates of garnet. This zoning pattern indicates that the garnets grew using Al of clinopyroxene and this reaction is incomplete. Similar Al zoning pattern is observed in clinopyroxenes of SGC (SAE125). Moreover, Ca concentration in rimwards of garnet is apparent in X-ray map of SAE125. These compositional changes are understood by considering phase relations between solid solutions of garnet, clinopyroxene and orthopyroxene in ACF diagram (Fig. 3-9). GW mainly consisted of liquidus clinopyroxene in higher temperature. With decreasing temperature, the compositional field of clinopyroxene shrinks, while three phases field of garnet, clinopyroxene and orthopyroxene extend continuously. Original clinopyroxene composition enters three phases field and clinopyroxene composition change with exsolving orthopyroxene and garnet. Further decreasing temperature, three phases field extend and exsolved garnet continuously changes its composition toward grossular-rich. Compositional changes of both pyroxenes are revealed as decreasing Al solubility following enlargement of pyroxene miscibility. In the case of SGC, all phases may have been crystallized from liquid and the bulk compositions are plotted in garnet and clinopyroxene two-phase field. With decreasing temperature, the tie-lines between garnet and clinopyroxene change their angles to stand following shrink of clinopyroxene compositional field, resulting that grossular rich garnet and CaTs poor clinopyroxene are stabilized.

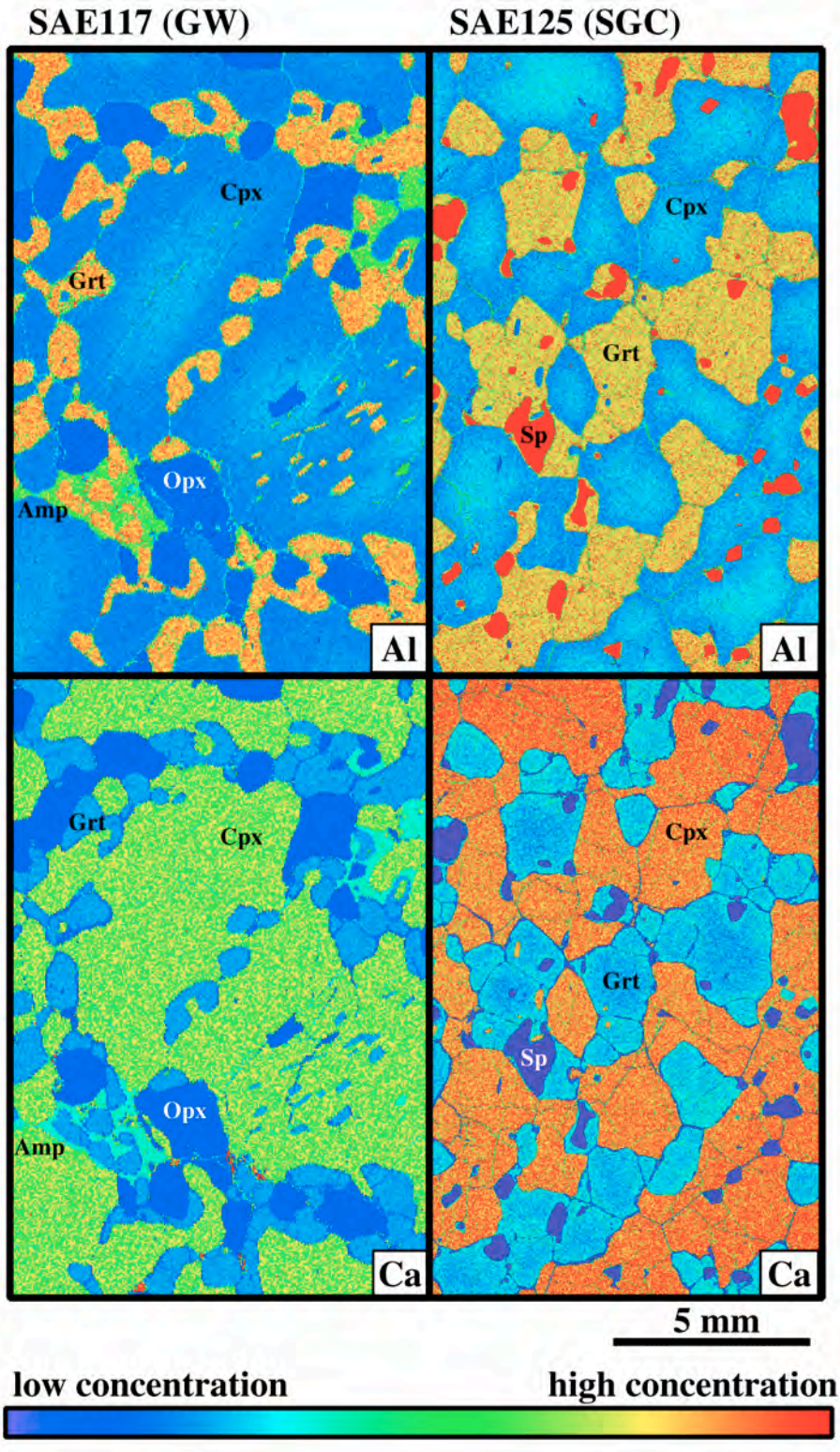

Fig. 3-8. Ca and Al X-ray concentration maps for polished thin sections of SAE117 (GW) and SAE125 (SGC). The scale bar represents 5.0 mm as stated.

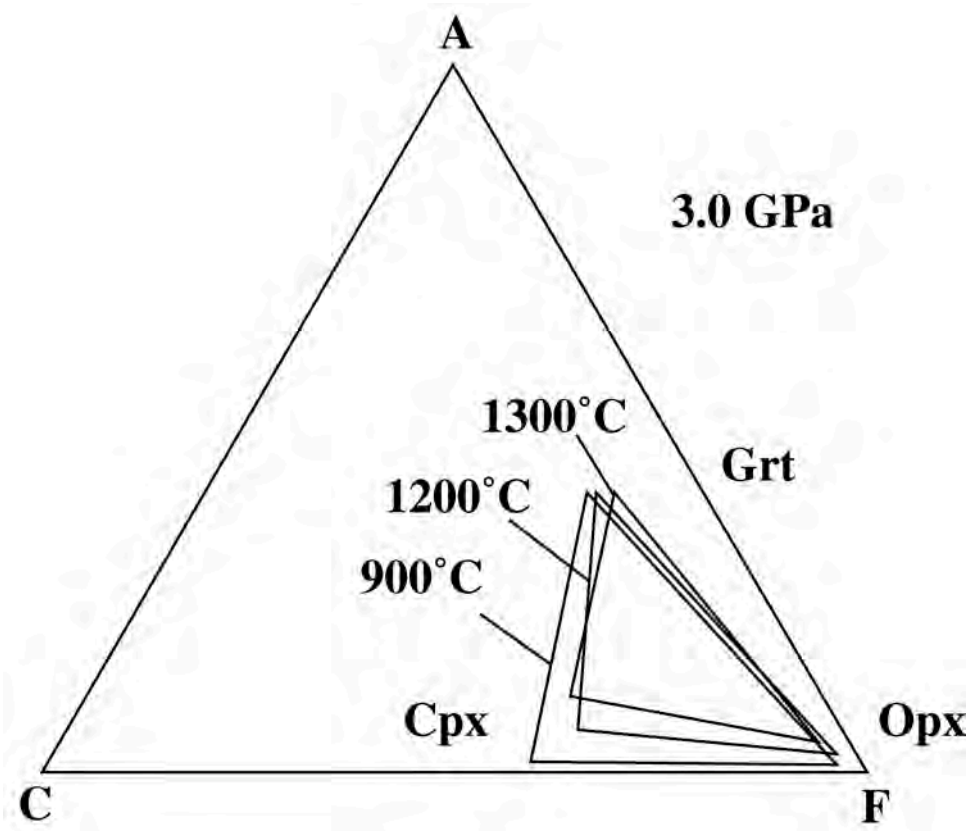

Fig. 3-9. ACF diagram showing the changes of three phase field Grt-Cpx-Opx with decreasing temperature at 3.0 GPa after Ellis and Green (1979). A=Al_2O_3-Na_2O; C=CaO; F=FeO+MgO, molecular proportions.

GO pyroxenite and GL peridotite

Most of studied samples from GO, GC pyroxenites and GL peridotites are characterized by their remarkable homogeneous compositions in single sample scale similar to general feature of megacryst suites from Malaita alnöite and other kimberlites (e.g. Dawson, 1980). However, some garnets have preserved chemical heterogeneities that are unaccountable by simple metamorphic reaction. In other constituent minerals with zoned garnet, any heterogeneity was detected, indicating that rock compositions were modified by infiltrating metasomatic melts or fluids. Only some garnets may preserve their former information. Evidences of garnet zoning resulting from metasomatic processes were described in numerous studies of peridotite suites of kimberlite xenolith (e.g. Smyth and Boyd, 1987; Griffin et al., 1989; Shimizu, 1997; Burgess and Harte, 1999). In order to identify nature of the process, garnets from two GO (SAE136 and SAE139) and four GL (SAG1, SAG7, SAG9 and SAG21) were investigated strictly by using x-ray maps and line traverses. In one sample from GC (SAE141), zoned orthopyroxene and clinopyroxene (garnets are homogeneous) were found and also investigated.

Thin section photograph and Cr X-ray map for SAE139 display that larger garnets have preserved Cr-rich composition and other anhedral garnets are not (Fig. 3-10). Line profile of largest garnet shows complex Cr zoning accompanying Ca concentration (Fig. 3-15), showing that maximum Cr concentration region (~ 3 wt.%) surrounds the core with less Cr contents (~ 2.2 wt.%). This pattern may be formed by three steps: original two garnets with Cr poor composition were annealed by growth of Cr-rich garnet, then Cr-poor matrix garnets were overgrown around that. Mg# of the garnet is slightly higher than matrix garnets but there is not large difference. Same complex history is also implied by the line profile and x-ray maps of largest garnet in SAE136 (Figs. 3-11 and 3-15). Overall texture is same with SAE139 except for containing unusual size of garnets (~ 3 cm). The garnet has strongly concaved grain boundary and the texture continues to small anhedral garnets in matrix. Cr-rich composition appears in rim of large grain not in outermost rim and anhedral matrix garnets. It is noted that weak-Cr enrichment is also detected between core of the garnet and clinopyroxene inclusion. The grain boundary is filled with small grains of orthopyroxene and Ti-rich amphibole indicative of complex origin for Cr-enrichment. An important feature of this garnet is that the high Mg# equivalent to

those of GL is preserved in the core (Mg# ~ 0.88). Mg# decrease from core to rim independent of Cr contents, indicating homogenization of Mg# by diffusion effect is faster than those of Cr as general observation (Griffin et al., 1989; Shimizu, 1997; Burgess and Harte, 1999). Similar behavior of garnet has been identified in SAG21 represented as Fe-rich garnet lherzolite (Figs. 3-12 and 3-15). The core of garnet with 5 mm in long axis retains high Mg# which decreases to rim smoothly, while Cr concentration is characterized by M-shaped zoning. Ti contents may also display similar zoning but remain unclear in due to low abundance. These evidences indicate that compositional variability observed in GO and GL was controlled by a series of metasomatism. This implication will be made doubly sure by investigations of REE abundances in later section. In garnets from other GL (SAG1, SAG7 and SAG9; Figs. 3-12, 3-13 and 3-15) with Mg# ~ 0.85, no marked heterogeneities have been observed in major element compositions but is not true in REE abundances.

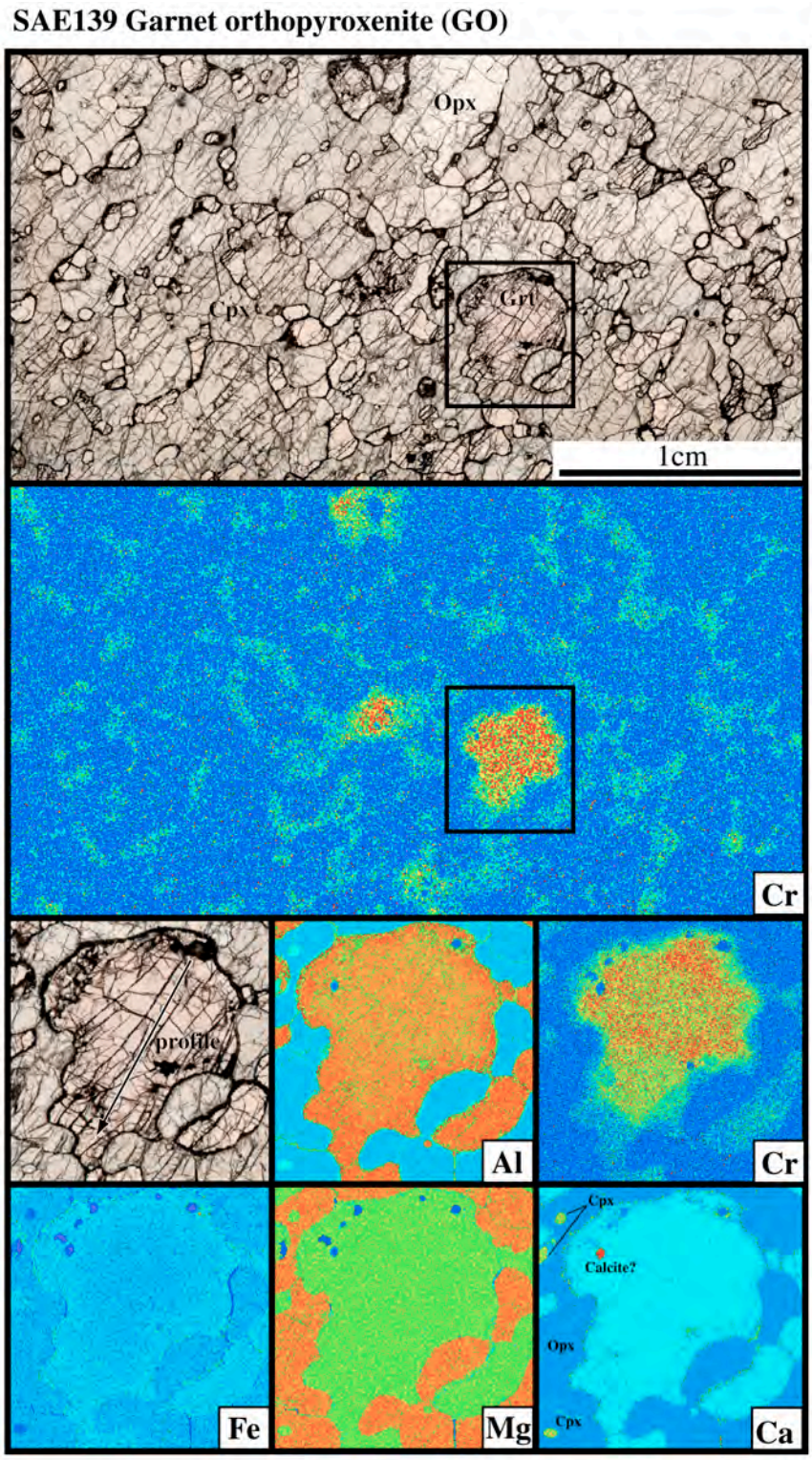

Fig. 3-10. Photomicrograph and Cr X-ray concentration map for polished thin section of SAE139 (GO), showing higher concentration of Cr in larger garnets. Lower maps represent X-ray maps for compositional variations of Al, Cr, Fe, Mg, and Ca in the largest garnet. The location of line profiles are expressed as arrow.

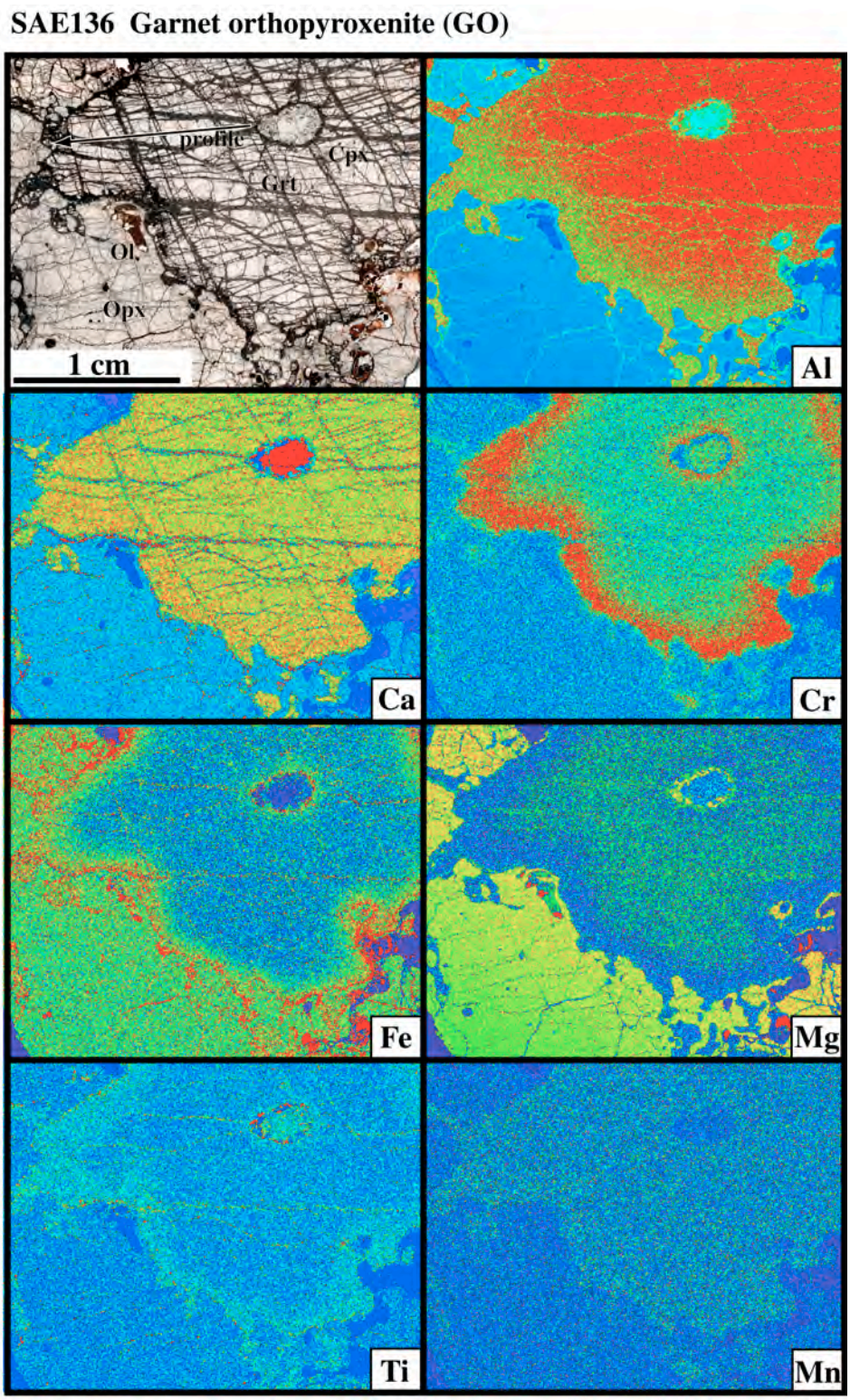

Fig. 3-11. Photomicrograph and Al, Ca, Cr, Fe, Mg, Ti and Mn X-ray concentration maps for polished thin section of SAE136 (GO), showing rimward concentration of Cr in largest garnet. Noted that anhedral garnets in matrix show lowest Cr concentration. The location of line profiles is expressed as arrow.

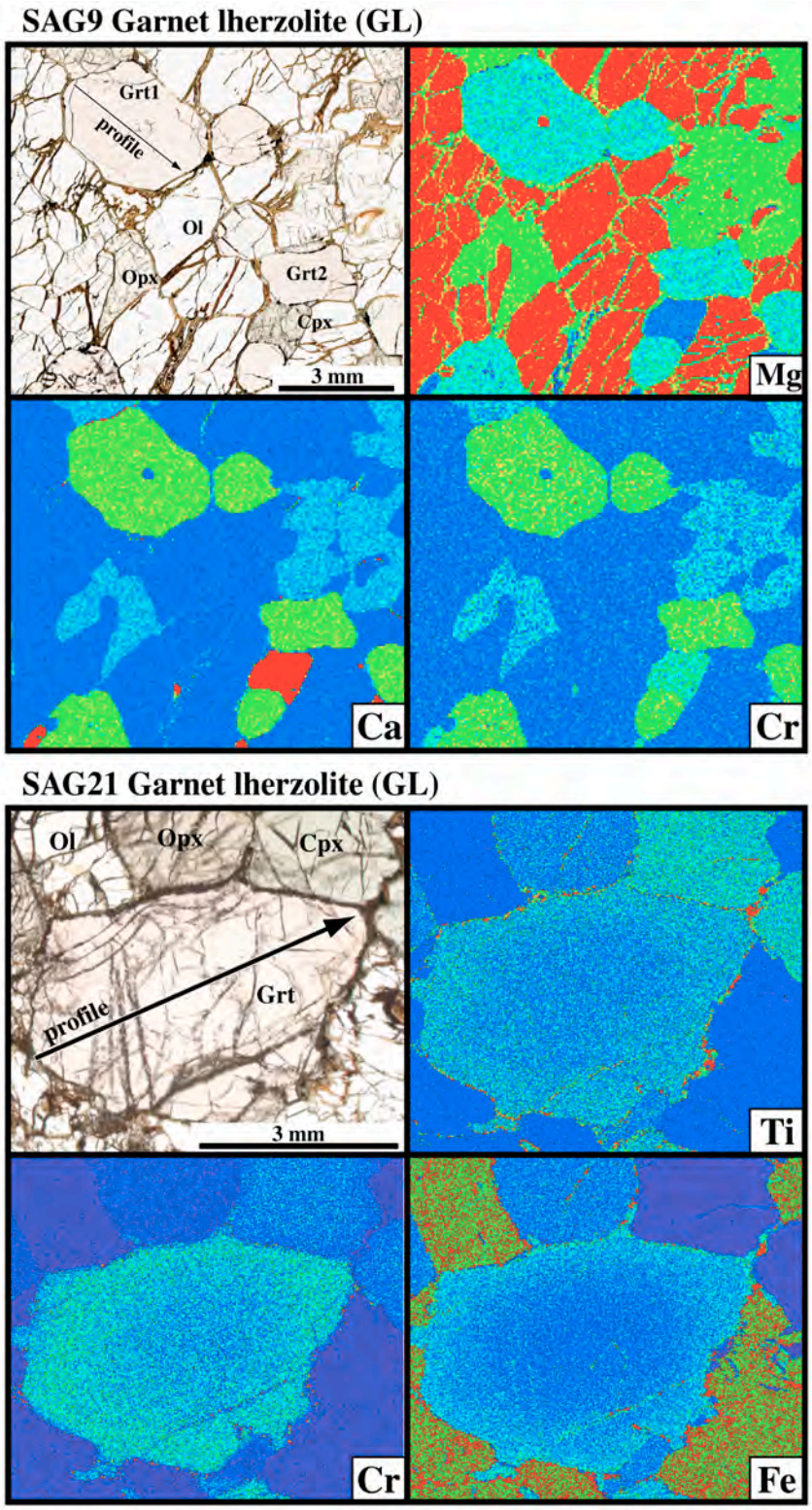

Fig. 3-12. Photomicrographs and X-ray concentration maps for polished thin section of SAG9 and SAG21 (GL). In garnet in SAG21, Fe/Mg zoning is accompanied with Cr and Ti concentrations. The locations of line profiles are expressed as arrows.

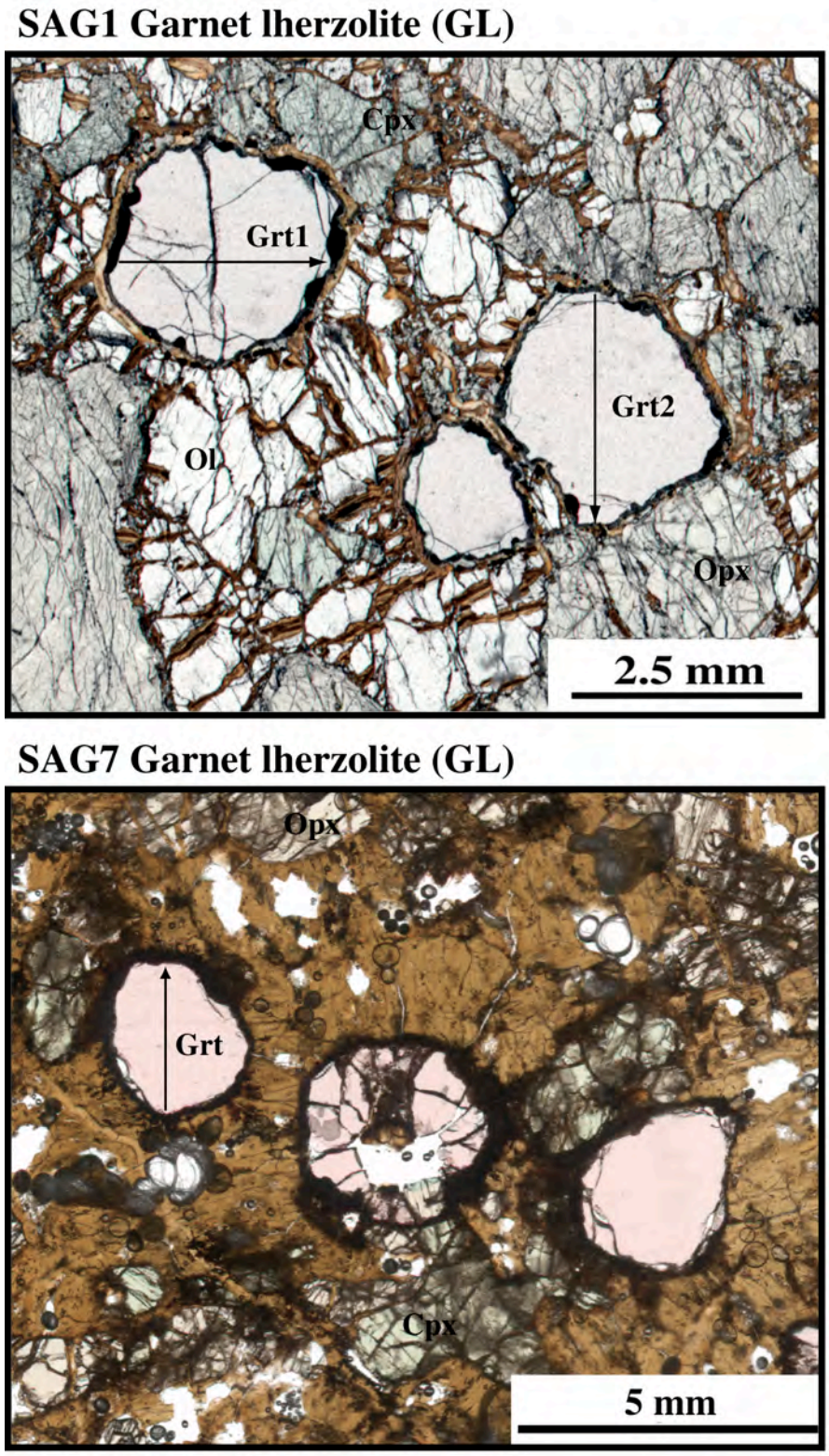

Fig. 3-13. Photomicrographs of SAG1 and SAG7 (GL). Arrows indicate the locations of line profiles in Fig. 3-15.

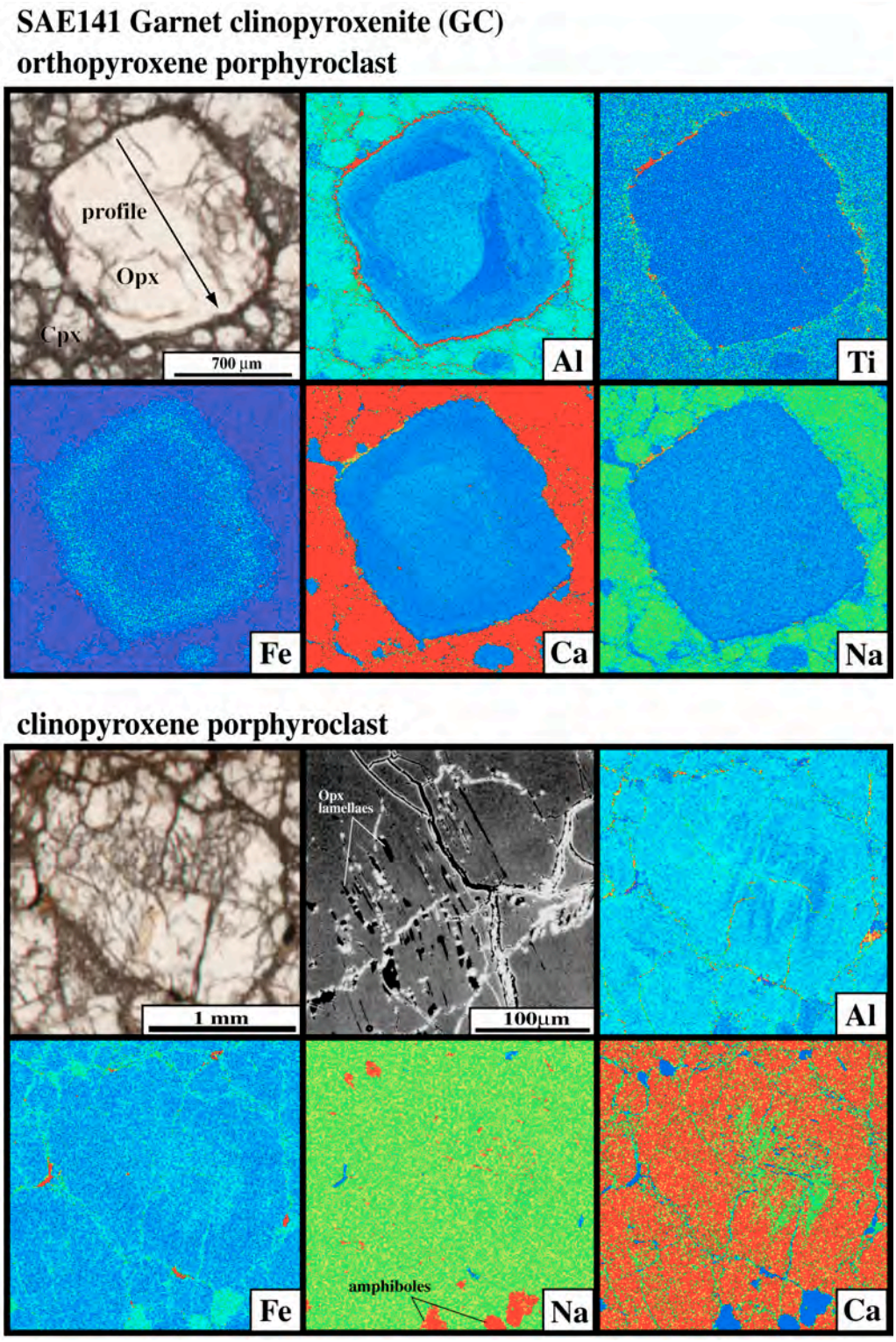

Fig. 3-14. Photomicrographs and X-ray concentration maps for orthopyroxene (upper) and clinopyroxene (lower) porphyroclasts in SAE141 (GC), showing apparent heterogeneity in both pyroxenes. Noted that high Ca in core of orthopyroxene and the presence of orthopyroxene lamellae indicate higher temperature origin. The location of line profile is expressed as arrow.

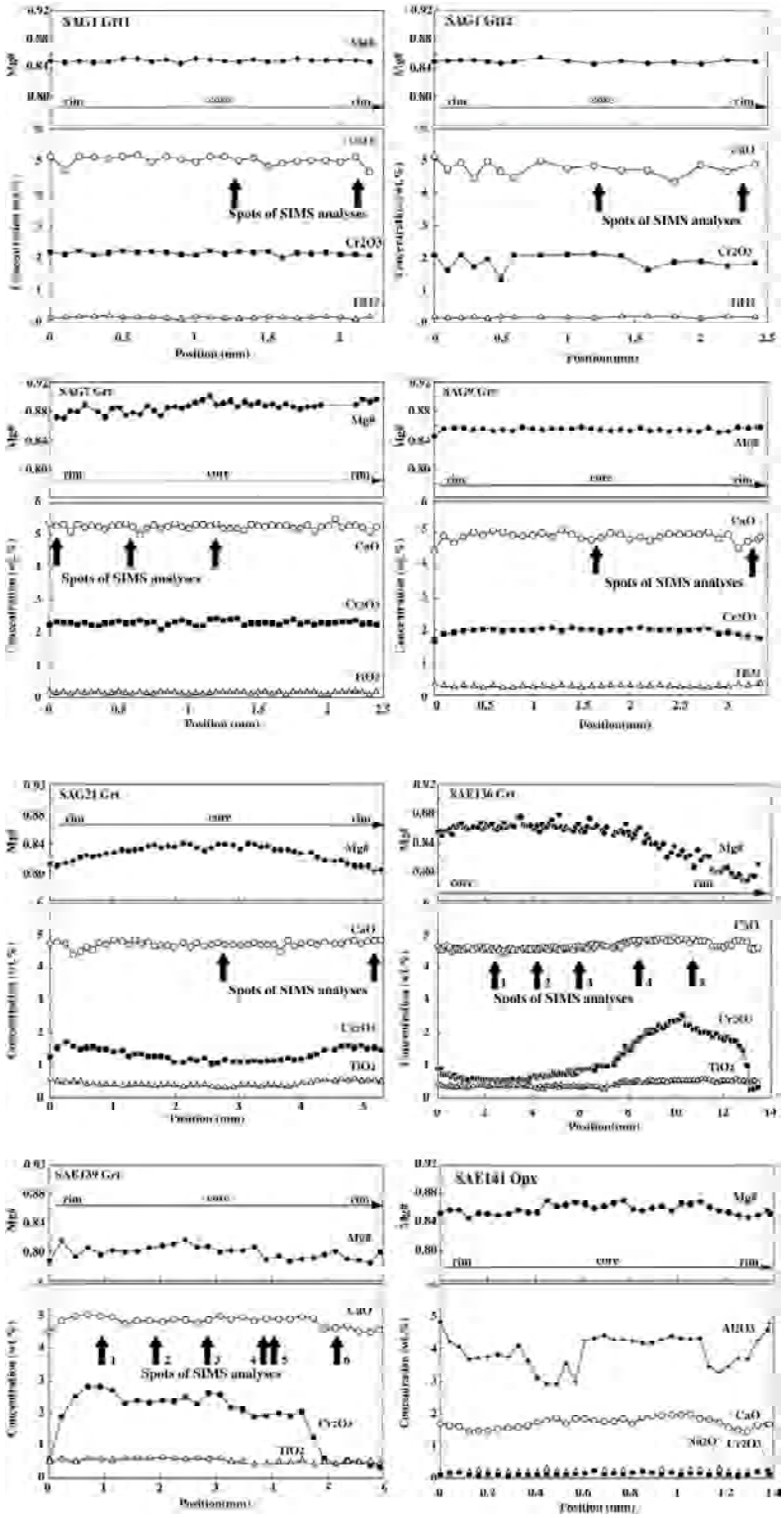

Fig. 3-15. Line profiles of variation of Mg#=Mg/(Mg+Fe*) and in wt.% of: CaO, Cr_2O_3 and TiO_2 (garnets): Al_2O_3, CaO, Na_2O and Cr_2O_3 (orthopyroxene) in representative HT-type samples. The directions of thin arrows correspond to those in photomicrographs. Spots of SIMS analyses are shown as thick arrows.

3-6 Equilibrium conditions

Estimations of equilibrium temperature and pressure of mantle-derived xenoliths from kimberlite and other volcanic rocks from worldwide localities have been applied to investigate at which depth they stabilized prior to be incorporated into their host volcanic rocks (e.g. Boyd, 1973; MacGregor, 1974; Finnerty and Boyd, 1984; Kawasaki, 1987). The common results from such xenolith investigations were that the variations of estimated equilibrium temperature and pressure obtained reflect the local geotherm when host volcanic rocks erupted (paleogeotherms). For assemblages of garnet, clinopyroxene and orthopyroxene, Al in orthopyroxene barometer (e.g. Wood and Banno, 1973; Nickel and Green, 1985; Kawasaki, 1987; Brey and Köhler, 1990) and two-pyroxene thermometer (e.g. Wells, 1977; Bertrand and Mercier, 1985; Brey and Köhler, 1990) have been widely used for P-T estimations. On the other hand, for a garnet-free assemblage such as spinel peridotite, there is no reliable barometer in spite of being a significant component of the shallower mantle. Ca exchange between olivine and clinopyroxene has been suggested as pressure estimations for spinel peridotites (e.g. Köhler and Brey, 1990). Similar to spinel peridotite, it is difficult to estimate the equilibrated pressure of the orthopyroxene free assemblage of garnet clinopyroxenite although some equations have been suggested (e.g. Mukhopadhyay, 1991; Simakov 1999). Temperature estimations can be made using Fe/Mg exchange reaction which have been applied for eclogite and garnet clinopyroxenite from wide variety of geological environment (e.g. Raheim and Green, 1974; Ellis and Grren, 1979; Powell, 1985; Krogh, 1988; Ravna, 2000).

The estimation of pressures of xenoliths studied that have garnet, clinopyroxene and orthopyroxene assemblage (GW, some GO, GSL and GL), Al in orthopyroxene geobarometer of Brey and Köhler (1990) (PBK90) were used. Then, temperatures were estimated using two-pyroxene thermometer of Brey and Köhler (1990) (TBK90). For some samples (SGC and GC) that do not include orthopyroxene, the Fe/Mg exchange between garnet and clinopyroxene thermometer of Ellis and Green (1979) (TEG79) were also used and compared with the estimation by two-pyroxene thermometer of Brey and Köhler (1990). In an effort to estimate the equilibrated pressures of garnet-free peridotite, precise analysis for trace amounts of Ca in olivines were carried out by electron microprobe (table 3-10) and the

barometer of Köhler and Brey (1990) were applied.

Most of the studied xenoliths belonging to GW, SGC and some GSL have the marked compositional zoning at single grain scale as described in the former section. Particularly, the Al contents of both pyroxenes and the Ca contents in garnet are significantly zoned. Because the heterogeneity of the Al content in orthopyroxene is directly related to their pressure estimation, care should be taken. For pressure estimation of GW and GSL, Al minimum orthopyroxenes and XCa maximum garnet in observed ranges were selected as pair of last equilibrated compositions. Similar to pressure estimation, Al minimum pyroxenes pair were used for temperature estimation. Although Al contents in clinopyroxene are also related to their Na contents, Na variation is limited in single sample and their contributions for temperature estimations may be small. Although no systematic variations were observed in Mg# of constituent minerals, XCa in garnet is directly related to temperature estimation using garnet and clinopyroxene thermometer. In that case, XCa maximum garnet and Al minimum pairs in single sample were selected as last equilibrated pairs. While, for pressure and temperature estimations of GO and GL with heterogeneous garnets, rim compositions of zoned garnets were chosen.

The results of calculations are listed in Table 3-10 and plotted in Fig. 3-16. The combination of TBK(90) and PBK(90), all garnet bearing peridotites (GSL and GL) are plotted in garnet lherzolite stability field determined by pyrolite III experiments (Green and Ringwood, 1970). The P-T points for GSL yield a systematic variation forming a line in low temperature side of the oceanic geotherm of Clark and Ringwood (1964). As well the interpretation of previous studies (Nixon and Boyd, 1979; Kawasaki, 1987), Malaitan geotherm are affected by relatively high heat flow and different from those of subcontinental mantle calculated by using kimberlite xenoliths. There is a significant temperature and pressure gaps between GSL and GL, showing the agreement with their discontinuous compositions of clinopyroxene and orthopyroxene. The result of temperature estimations for spinel peridotite (SL, SH and HTSH) is expressed by the lines with pressure variation in the figure. T lines of six HTSH samples lie at higher temperature than those of SH-SL and overlay P-T plots of GL, indicating their equilibrated conditions were close to those of GL. On the other hand, estimated temperatures for SH and SL are broad and covered with whole range of GSL. It is well known that spinel to garnet peridotite

transition depends on their degree of depletion (e.g. O'Neil, 1981; Robinson and Wood, 1998). The spinel-garnet reaction boundary continuously shifts to higher pressures with increasing of depletion. These evidences indicate that some of spinel peridotites were derived from garnet lherzolite field of pyrolite III composition and variations in garnet appearance may reflect their different bulk compositions. Actually, most of spinel peridotite with calculated temperature over 1000˚C is harzburgite with Cr-rich spinels and consistent with the bulk chemical effect of spinel-garnet transition.

The results of pressure estimations on spinel peridotite are given in Fig. 3-17, displaying pressure isopleths in the field of temperature and ln DCa between clinopyroxene and olivine. TBK90 were given as equilibrated temperature for pressure calculation. HTSH and one GL have restricted range of ln DCa between –5.0 ~ -6.0 and yield pressures over 30 kb. These values are clearly overestimated in compared with the results of PBK90 for GL. Furthermore, the results for SL-SH gave unrealistic pressures (up to 40 kb) in spite of their lower equilibrated temperature. The problems may be associated with lower CaO content in olivine than expected amounts. Usually, these phenomena have been observed in the application of this method to natural rock (e.g. Xu, 1998; Yang et al., 1998) and interpreted as Ca-disequilibria between olivine and clinopyroxene because equilibrium of adjustment pyroxenes ceased much higher temperatures than in olivines during a cooling process (Köhler and Brey, 1990).

The fact as the equilibrium ceasing temperature of pyroxenes is relatively high may be provided the comparison with other equilibrated temperatures calculated by Fe/Mg exchange between constituent minerals, particularly the difference is enhanced by the results of spinel and olivine thermometer. The spinel-olivine temperatures using the method of Sack and Ghiorso (1991) are systematically lower than the results of two-pyroxene temperature and the deviation reaches to about 300 ˚C (Fig. 3-18). These deviations were also caused by differential rates of diffusion and recrystallization for absolute temperature change (Fabries, 1977; Ozawa,1983). Fig. 3-18 give another indication that the degree of deviations are nearly constant in whole temperature range recorded by spinel peridotite (averaged value –212˚C). They consist well-correlated line parallel to 1:1 line. This evidence may be accounted that these peridotites placed under the conditions with relatively equivalent cooling

rate.

The estimated temperatures and pressures of pyroxenite suites (GW, SGC, GO and GC) using the combination of TBK(90) and PBK(90) display that they derived from two different equilibrium conditions, high P-T (GC and GO) and low P-T (GW and SGC) similar to peridotite suites. P-T plots of GO and GC are plotted in higher P-T extension of GL field excluding one GC sample (SAE132) which display higher pressure. Most of the P-T plots for GW and one SGC are plotted in narrow GSL fields, indicating that equilibrated conditions of GSL and GW were controlled by nearly same geotherm. However six of them are deviate toward lower T and/or higher P side than GSL fields. Origin of this deviation is not unclear but may be due to failure of temperature estimations in due to heterogeneous nature. In case that average composition pairs are used for estimation of temperatures, only deviated six samples give higher temperature and fall into GSL fields in spite that others are almost unchanged.

Compared to the combination of PBK(90) and TBK(90), those of PBK(90) and TEG(79) give higher pressures and temperatures for all calculated samples. In Fig. 3-16, TEG(79) at pressure values estimated by TBK(90) + PBK(90) are plotted. In that case, the maximum temperature deviation is +127˚C in GSL. Although the P-T plots of GL tend to have smaller deviations, significant temperature difference are observed (< +64˚C). It is noted that calculated temperatures using TEG(79) are strongly affected by the presence of Fe^{3+} in clinopyroxene and/or garnet. Because all Fe were assumed as Fe^{2+} and no correction for Fe^{3+} were applied for temperature estimations, the deviations in temperature calculated TEG(79) may be due to the presence of Fe^{3+}. It is evident that temperature estimations of SGC and GC calculated using TEG(90) must be compared with those of other samples using same method. Temperature lines for GC and SGC lie at comparable range for those of GW and GO, respectively. It can be safely said that SGC-GW and GC-GO were derived from equivalent depths as shown by resemblance of major element compositions. On the other hand, T lines of two SGC samples (SAE115 and SAE125) show much higher temperatures than other SGC and GW. Because both samples have the highest XCa in garnet and Al in clinopyroxene, it may be possible to differ their Fe^{3+} distributions between garnet and clinopyroxene from others. But it is meaningless discussion about errors of Kd values determined in each samples at the present state.

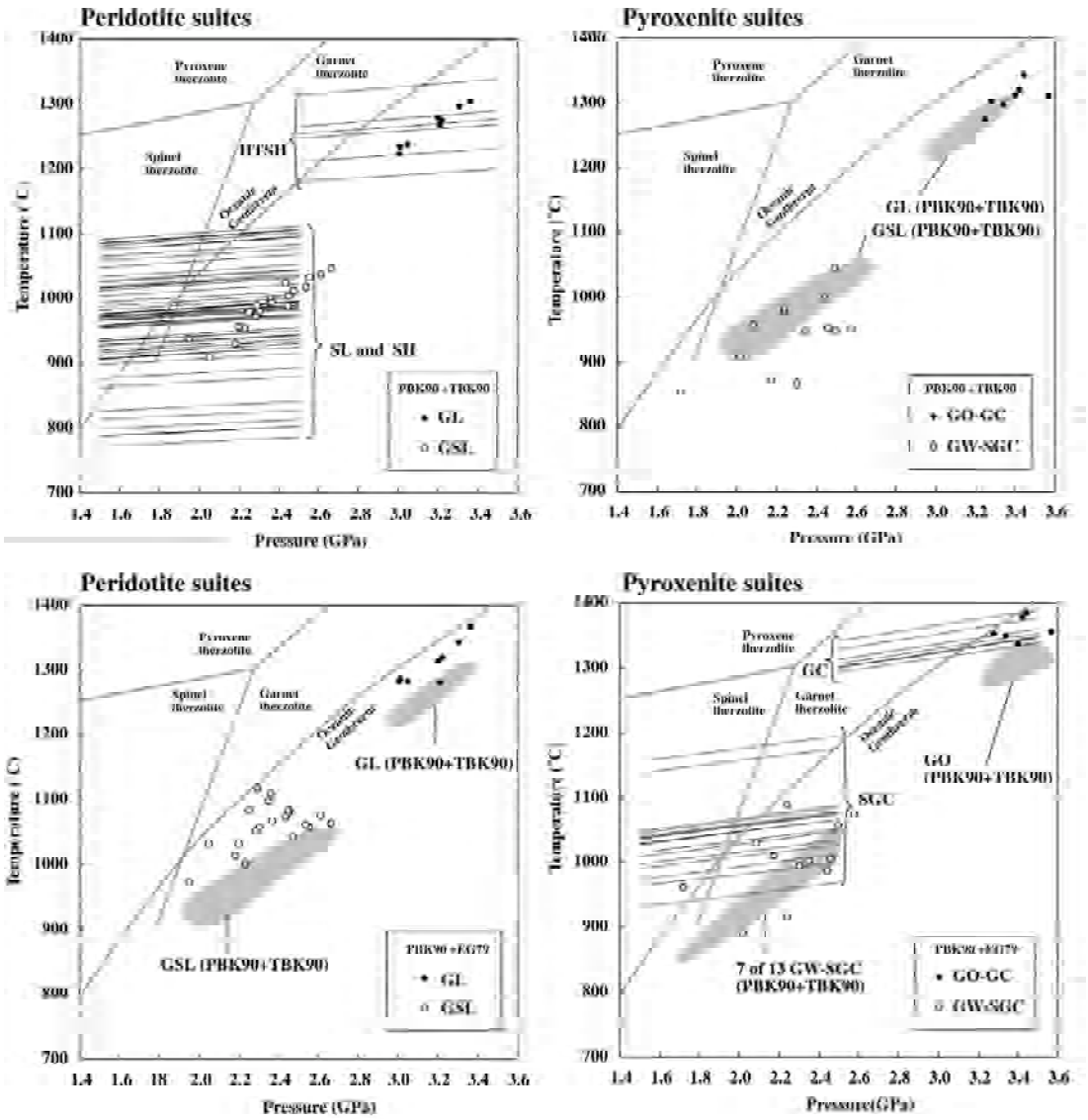

Fig. 3-16. P-T estimates for peridotite (left) and pyroxenite suites (right) of Malaitan xenoliths using upper: the combination of Al in orthopyroxene barometer (PBK90) and two-pyroxene thermometer (TBK90) of Brey and Köhler (1990), lower; Fe/Mg exchange between clinopyroxene and garnet thermometer (TEG79) of Ellis and Green (1979) at pressure values estimated by the combination of TBK(90) and PBK(90). T estimates for spinel peridotite and spinel-garnet clinopyroxenite are used TBK(90) and TEG(79), respectively. They are expressed as thin lines with pressure dependence. The line of oceanic geotherm is taken from Clark and Ringwood (1964). The P-T fields of the different mineral assemblages in pyrolite III compositions (Green and Ringwood, 1970) are illustrated. Most plots using TEG(79) are given higher T than TBK(90). Note both peridotite and pyroxenite suites are divided into two types; higher P-T (> 1200˚C, > 3.0 GPa) and lower P-T (< 1100˚C, < 2.7 GPa) types.

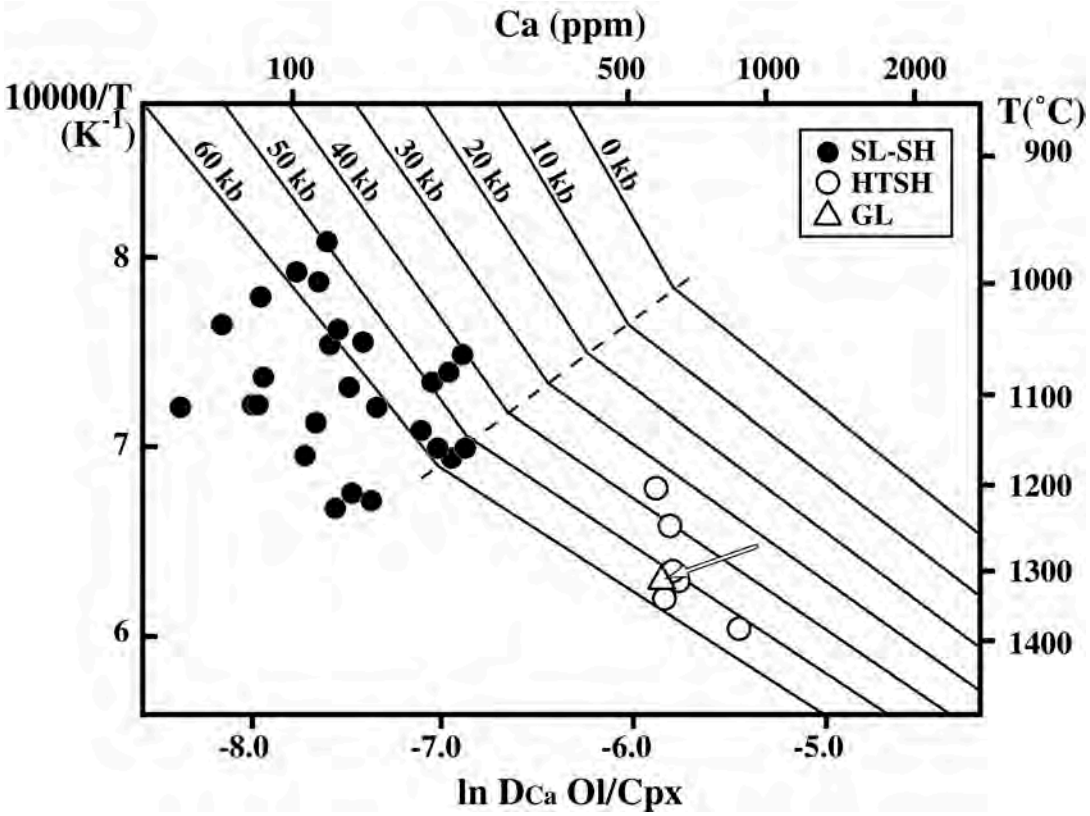

Fig. 3-17. P-T estimates for spinel peridotites using the combination of Ca exchange between olivine and clinopyroxene barometer (Köhler and Brey, 1990) and two-pyroxene thermometer (Brey and Köhler, 1990). Solid lines are isobars calculated from Eqs. (5) and (6) of Köhler and Brey (1990). Arrow indicates the deviation from P-T estimates using conjunction between PBK90 and TBK90 for garnet lherzolite (SAG30), showing that both pressure and temperature are overestimated owing to lower Ca content in olivine than expected value and the degree of deviations may be different between SL-SH and HTSH.

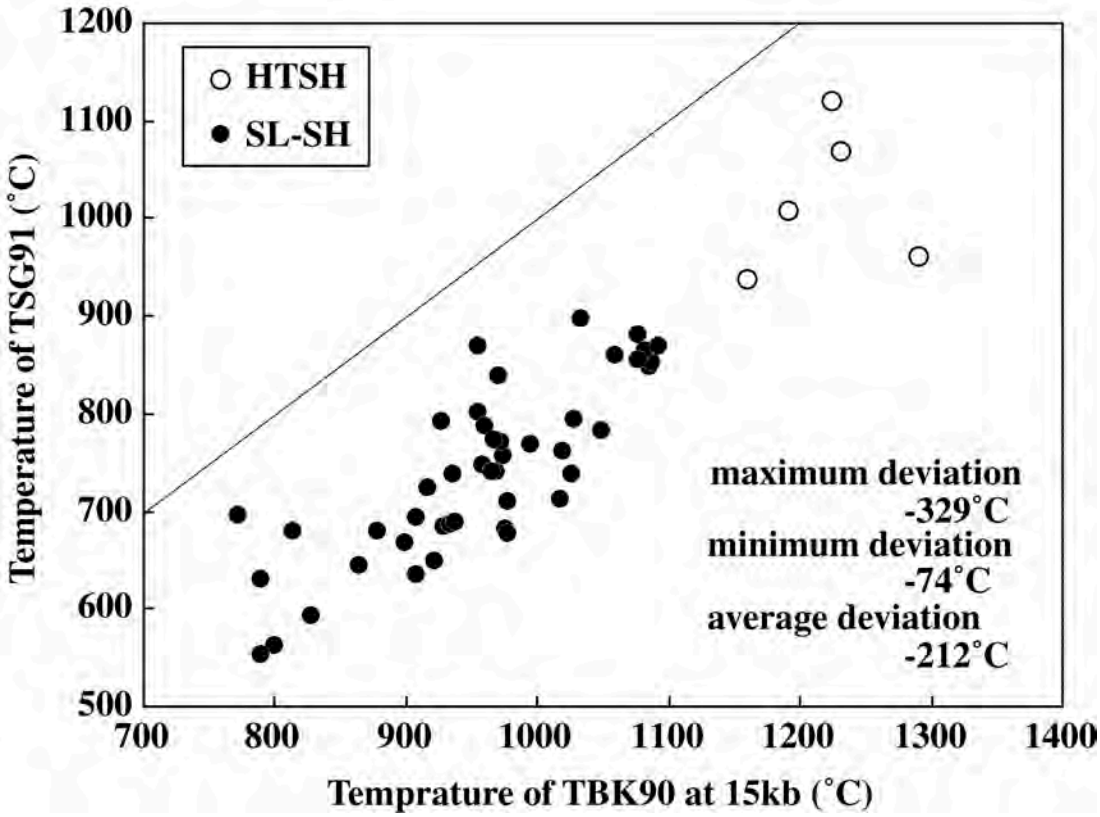

Fig. 3-18. Comparison of T estimations for spinel peridotites using the two-pyroxene thermometer (Brey and Köhler, 1990) and olivine-spinel thermometer (Sack and Ghiorso, 1991). Olivine-spinel thermometer yields systematically lower temperature than those using two-pyroxene thermometer.

Table 3-1. Major element compositions of garnets, clinopyroxenes and orthopyroxenes in LT-type garnet websterite and garnet clinopyroxenite.

	Garnet websterite (GW)														
	SAE134			SAE138			SAE122			SAE117			SAE111		
Garnets	avg.	XCa max.	XCa min.	avg.	XCa max.	XCa min.	avg.	XCa max.	XCa min.	avg.	XCa max.	XCa min.	avg.	XCa max.	XCa min.
SiO_2	41.25	41.36	41.49	41.60	41.44	41.77	41.57	41.50	41.71	41.80	41.51	41.99	41.59	42.11	41.69
TiO_2	0.06	0.02	0.15	0.05	0.01	0.04	0.04	0.01	0.00	0.11	0.12	0.11	0.16	0.22	0.19
Al_2O_3	23.35	23.41	23.15	23.03	23.31	23.64	23.89	23.85	23.90	23.85	23.80	23.91	23.67	23.90	23.95
Cr_2O_3	1.06	1.10	1.07	0.64	0.72	0.61	0.49	0.47	0.50	0.66	0.74	0.69	0.77	0.83	0.76
FeO^{*}	9.76	9.64	9.67	8.17	8.07	8.11	8.38	7.87	8.38	7.67	7.04	7.58	7.91	8.05	7.99
MnO	0.34	0.34	0.34	0.27	0.29	0.28	0.34	0.37	0.36	0.30	0.30	0.30	0.32	0.32	0.32
MgO	19.33	19.19	19.26	19.63	19.74	20.14	20.47	20.13	20.70	20.56	20.51	20.66	19.90	20.33	20.51
CaO	5.45	5.71	5.05	5.26	5.38	4.39	5.12	5.42	4.66	5.19	5.33	4.89	5.16	5.41	5.23
Na_2O	0.01	0.03	0.00	0.01	0.01	0.00	0.01	0.01	0.00	0.02	0.04	0.03	0.01	0.03	0.01
Total	100.61	100.81	100.18	98.65	98.97	98.98	100.31	99.62	100.21	100.17	99.37	100.15	99.49	101.18	100.64
Mg#	0.779	0.780	0.780	0.811	0.814	0.816	0.813	0.820	0.815	0.827	0.839	0.829	0.817	0.818	0.821
XCa	0.136	0.142	0.127	0.134	0.137	0.113	0.127	0.136	0.116	0.130	0.135	0.123	0.131	0.135	0.130
Clinopyroxenes	avg.	Al max.	Al min.	avg.	Al max.	Al min.	avg.	Al max.	Al min.	avg.	Al max.	Al min.	avg.	Al max.	Al min.
SiO_2	53.30	52.93	53.59	53.57	53.05	54.47	53.55	52.49	54.27	53.96	53.23	54.47	53.68	53.51	53.54
TiO_2	0.32	0.30	0.30	0.18	0.20	0.13	0.17	0.20	0.17	0.40	0.48	0.31	0.48	0.52	0.44
Al_2O_3	3.52	4.09	2.93	4.24	5.58	2.84	4.36	6.53	2.86	4.43	5.69	3.79	3.96	4.80	3.40
Cr_2O_3	0.56	0.63	0.57	0.41	0.32	0.42	0.34	0.32	0.28	0.48	0.59	0.47	0.46	0.46	0.41
FeO^{*}	2.39	2.45	2.38	2.14	2.15	2.04	2.29	2.58	2.34	2.54	2.47	2.55	2.35	2.49	2.29
MnO	0.07	0.04	0.09	0.04	0.01	0.06	0.05	0.09	0.10	0.07	0.07	0.07	0.06	0.07	0.03
MgO	16.62	16.33	16.82	16.03	15.24	16.69	16.01	14.75	16.98	16.04	15.29	16.68	16.10	16.00	16.39
CaO	22.86	22.28	22.64	21.82	21.00	21.74	22.39	22.55	22.74	21.39	21.43	21.46	21.19	21.08	21.14
Na_2O	0.62	0.59	0.56	1.01	1.05	0.82	1.09	1.19	0.85	1.36	1.41	1.24	1.10	1.31	1.02
K_2O	0.00	0.00	0.01	0.01	0.00	0.02	0.00	0.00	0.01	0.01	0.00	0.01	0.00	0.00	0.00
Total	100.25	99.63	99.88	99.46	98.61	99.22	100.25	100.70	100.60	100.67	100.66	101.04	99.37	100.23	98.66
Mg#	0.925	0.922	0.927	0.930	0.927	0.936	0.926	0.911	0.928	0.918	0.917	0.921	0.924	0.920	0.927
Orthopyroxenes	avg.	Al max.	Al min.	avg.	Al max.	Al min.	avg.	Al max.	Al min.	avg.	Al max.	Al min.	avg.	Al max.	Al min.
SiO_2	56.34	56.35	56.07	56.62	56.10	56.92	56.57	54.53	57.12	57.26	57.02	57.04	56.41	56.25	56.78
TiO_2	0.09	0.08	0.09	0.05	0.03	0.10	0.05	0.03	0.05	0.12	0.10	0.15	0.15	0.16	0.16
Al_2O_3	2.59	3.15	2.11	2.70	3.63	2.32	3.11	4.86	2.39	2.59	3.05	2.46	2.30	2.45	2.19
Cr_2O_3	0.29	0.27	0.25	0.21	0.31	0.18	0.15	0.13	0.07	0.18	0.17	0.14	0.20	0.22	0.21
FeO^{*}	6.83	6.98	7.04	5.61	5.77	5.59	5.78	5.26	5.80	5.94	5.82	5.89	5.87	5.54	6.05
MnO	0.13	0.15	0.09	0.07	0.14	0.03	0.07	0.06	0.06	0.07	0.07	0.07	0.10	0.11	0.08
NiO	0.09	0.12	0.05	0.13	0.13	0.10	0.15	0.11	0.19	0.12	0.10	0.12	0.08	0.07	0.09
MgO	33.86	33.77	34.14	34.21	34.14	34.34	34.54	33.56	35.13	33.96	33.63	34.30	33.74	34.59	33.24
CaO	0.40	0.39	0.41	0.36	0.36	0.36	0.40	0.46	0.47	0.55	0.53	0.54	0.54	0.55	0.51
Na_2O	0.02	0.02	0.00	0.02	0.03	0.01	0.03	0.02	0.02	0.07	0.07	0.07	0.05	0.07	0.04
Total	100.64	101.27	100.26	99.97	100.63	99.94	100.84	99.01	101.29	100.84	100.56	100.77	99.45	100.01	99.35
Mg#	0.898	0.896	0.896	0.916	0.913	0.916	0.914	0.919	0.915	0.911	0.912	0.912	0.911	0.917	0.907

Table 3-1. Continued

	Garnet websterite (GW)														
	SAE103			SAE106			SAE128			SAE144			SAE102		
Garnets	avg.	XCa max.	XCa min.	avg.	XCa max.	XCa min.	avg.	XCa max.	XCa min.	avg.	XCa max.	XCa min.	avg.	XCa max.	XCa min.
SiO_2	41.74	41.67	41.73	41.61	41.75	41.80	41.61	41.55	41.64	42.18	42.49	41.65	42.00	42.11	41.95
TiO_2	0.12	0.15	0.11	0.11	0.04	0.14	0.07	0.09	0.09	0.12	0.14	0.11	0.15	0.14	0.15
Al_2O_3	23.10	23.10	22.71	23.18	22.72	23.56	23.74	23.91	24.07	23.22	23.50	22.94	23.09	22.92	23.08
Cr_2O_3	1.28	1.33	1.26	0.87	0.88	0.85	0.62	0.60	0.65	1.06	1.09	1.16	1.30	1.36	1.34
FeO*	7.90	7.62	7.95	8.41	8.70	7.82	8.73	8.53	8.92	8.30	8.37	8.47	7.78	7.69	7.90
MnO	0.31	0.30	0.33	0.35	0.37	0.41	0.33	0.32	0.36	0.36	0.37	0.36	0.37	0.35	0.40
MgO	20.62	20.59	20.55	20.28	20.24	20.52	20.37	20.17	20.45	20.30	20.37	20.11	20.58	20.70	20.28
CaO	5.54	5.68	5.43	5.02	5.19	4.87	4.99	5.09	4.76	4.80	4.95	4.58	5.12	5.40	4.58
Na_2O	0.01	0.00	0.02	0.01	0.02	0.00	0.01	0.01	0.00	0.02	0.00	0.00	0.01	0.03	0.00
Total	100.62	100.44	100.10	99.84	99.92	99.96	100.47	100.25	100.93	100.36	101.27	99.39	100.41	100.69	99.67
Mg#	0.136	0.140	0.134	0.125	0.128	0.122	0.124	0.127	0.118	0.121	0.123	0.116	0.128	0.133	0.117
XCa	0.823	0.828	0.822	0.811	0.806	0.824	0.806	0.808	0.803	0.813	0.813	0.809	0.825	0.827	0.821
Clinopyroxenes	avg.	Al max.	Al min.	avg.	Al max.	Al min.	avg.	Al max.	Al min.	avg.	Al max.	Al min.	avg.	Al max.	Al min.
SiO_2	53.28	52.54	53.08	52.97	52.98	54.31	53.03	52.36	53.78	53.06	52.26	52.79	53.39	53.24	53.09
TiO_2	0.44	0.49	0.43	0.44	0.55	0.41	0.49	0.47	0.41	0.46	0.59	0.45	0.69	0.70	0.63
Al_2O_3	4.45	5.56	3.85	5.80	6.05	4.13	5.80	6.68	4.48	4.88	6.17	4.22	4.41	4.85	3.97
Cr_2O_3	0.92	0.98	0.92	0.63	0.73	0.70	0.41	0.32	0.55	0.82	0.75	0.79	1.02	0.98	1.06
FeO*	2.14	2.07	2.16	2.42	2.17	2.52	2.42	2.56	2.59	2.74	2.78	2.68	2.38	2.49	2.13
MnO	0.05	0.08	0.03	0.06	0.05	0.09	0.06	0.07	0.04	0.07	0.06	0.09	0.07	0.07	0.07
MgO	15.85	15.24	16.13	15.28	15.08	15.67	15.28	14.88	15.86	15.48	14.92	15.52	15.74	15.46	15.75
CaO	21.07	20.29	21.29	20.73	21.06	21.48	20.91	20.89	21.73	20.06	19.75	20.42	21.34	21.37	21.68
Na_2O	1.23	1.43	1.20	1.60	1.68	1.30	1.66	1.84	1.45	1.77	2.00	1.65	1.37	1.43	1.33
K_2O	0.01	0.00	0.02	0.01	0.01	0.00	0.00	0.00	0.00	0.02	0.03	0.00	0.00	0.00	0.01
Total	99.45	98.68	99.11	99.94	100.35	100.62	100.06	100.07	100.90	99.36	99.29	98.62	100.41	100.60	99.72
Mg#	0.930	0.929	0.930	0.918	0.925	0.917	0.918	0.912	0.916	0.910	0.905	0.912	0.922	0.917	0.929
Orthopyroxenes	avg.	Al max.	Al min.	avg.	Al max.	Al min.	avg.	Al max.	Al min.	avg.	Al max.	Al min.	avg.	Al max.	Al min.
SiO_2	56.38	55.16	56.90	56.36	55.76	55.93	56.72	54.98	56.92	55.57	55.03	56.11	56.77	56.42	56.84
TiO_2	0.13	0.10	0.12	0.09	0.08	0.10	0.12	0.09	0.16	0.13	0.12	0.15	0.19	0.21	0.22
Al_2O_3	3.44	5.41	2.43	3.03	3.96	2.27	2.68	5.10	2.40	2.49	2.58	2.40	2.68	3.09	2.55
Cr_2O_3	0.43	0.63	0.34	0.27	0.33	0.16	0.19	0.21	0.17	0.29	0.28	0.29	0.39	0.44	0.42
FeO*	5.43	5.47	5.49	5.97	6.02	6.07	6.18	6.11	6.22	6.11	6.13	6.08	5.86	5.78	5.94
MnO	0.10	0.07	0.09	0.13	0.12	0.13	0.09	0.12	0.03	0.12	0.11	0.12	0.12	0.08	0.08
NiO	0.13	0.14	0.17	0.11	0.18	0.13	0.11	0.14	0.07	0.09	0.09	0.10	0.11	0.11	0.07
MgO	34.15	33.28	34.67	33.81	33.32	33.70	34.38	33.01	34.44	33.94	33.94	33.95	34.34	33.78	34.40
CaO	0.41	0.31	0.42	0.42	0.45	0.43	0.43	0.43	0.37	0.50	0.49	0.51	0.50	0.53	0.47
Na_2O	0.05	0.03	0.05	0.05	0.07	0.06	0.03	0.05	0.10	0.09	0.06	0.11	0.04	0.06	0.03
Total	100.64	100.60	100.66	100.24	100.29	98.96	100.94	100.25	100.87	99.32	98.82	99.82	101.00	100.50	101.02
Mg#	0.918	0.916	0.918	0.910	0.908	0.908	0.908	0.906	0.908	0.908	0.908	0.909	0.913	0.912	0.912

Table 3-1. Continued

	Garnet websterite (GW)						Garnet clinopyroxenite			Olivine bearing			Rutile bearing		
	SAE143			SAE145			SAE105			SAE148			SAE156		
Garnets	avg.	XCa max.	XCa min.	avg.	XCa max.	XCa min.	avg.	XCa max.	XCa min.	avg.	XCa max.	XCa min.	avg.	XCa max.	XCa min.
SiO2	41.39	41.02	41.42	41.49	41.39	40.87	41.53	41.78	41.06	42.17	42.16	41.40	42.16	41.75	42.64
TiO2	0.14	0.14	0.13	0.14	0.12	0.17	0.09	0.04	0.15	0.15	0.15	0.21	0.15	0.14	0.10
Al2O3	23.59	23.51	23.63	22.95	23.26	23.20	23.59	23.64	23.52	23.60	23.50	23.67	23.13	22.87	23.52
Cr2O3	0.68	0.66	0.69	1.07	1.04	1.05	0.51	0.50	0.52	0.75	0.74	0.68	0.56	0.37	0.79
FeO*	7.62	7.68	7.73	8.13	7.99	8.19	7.69	7.57	7.73	8.60	8.49	8.50	7.90	7.58	8.17
MnO	0.32	0.33	0.30	0.37	0.35	0.39	0.26	0.27	0.27	0.39	0.39	0.36	0.38	0.39	0.35
MgO	20.46	20.55	20.69	20.26	20.27	20.40	20.86	20.81	21.07	20.19	19.87	20.49	20.22	20.46	20.66
CaO	5.01	5.09	4.94	4.92	5.00	4.83	5.00	5.26	4.83	4.63	5.17	4.32	5.24	5.18	4.71
Na2O	0.02	0.03	0.04	0.02	0.05	0.00	0.01	0.00	0.02	0.03	0.03	0.05	0.01	0.03	0.03
Total	99.22	99.00	99.56	99.35	99.45	99.10	99.54	99.87	99.16	100.52	100.50	99.70	99.75	98.77	101.06
Mg#	0.126	0.127	0.124	0.124	0.126	0.121	0.12	0.13	0.12	0.117	0.130	0.109	0.132	0.130	0.117
XCa	0.827	0.827	0.827	0.816	0.819	0.816	0.83	0.83	0.83	0.807	0.807	0.811	0.820	0.828	0.818
Clinopyroxenes	avg.	Al max.	Al min.	avg.	Al max.	Al min.	avg.	Al max.	Al min.	avg.	Al max.	Al min.	avg.	Al max.	Al min.
SiO2	53.57	53.68	53.99	53.38	53.01	53.16	53.97	53.66	54.00	53.39	53.80	53.55	53.58	53.30	54.05
TiO2	0.40	0.48	0.42	0.46	0.61	0.38	0.33	0.39	0.34	0.85	1.00	0.84	0.55	0.77	0.44
Al2O3	4.11	5.41	3.64	4.91	6.55	3.79	3.94	4.77	3.49	4.70	4.88	4.60	3.20	4.11	2.82
Cr2O3	0.49	0.84	0.39	0.84	0.83	0.88	0.28	0.35	0.23	0.65	0.60	0.65	0.42	0.39	0.48
FeO*	2.56	2.65	2.53	2.64	2.60	2.64	2.28	2.53	2.51	2.47	2.37	2.54	2.44	2.55	2.34
MnO	0.06	0.06	0.02	0.10	0.11	0.13	0.05	0.07	0.03	0.05	0.06	0.07	0.07	0.10	0.05
MgO	16.01	15.47	16.61	15.28	14.58	15.56	16.68	16.31	17.22	15.39	15.63	15.49	16.78	16.41	16.86
CaO	20.89	19.83	21.39	20.03	19.14	20.30	20.18	19.57	20.20	20.09	19.50	20.07	21.82	21.52	22.17
Na2O	1.32	1.92	1.26	1.71	1.94	1.73	0.99	1.07	1.00	1.44	1.39	1.44	0.58	0.63	0.57
K2O	0.02	0.01	0.01	0.02	0.02	0.02	0.00	0.00	0.01	0.01	0.00	0.01	0.00	0.00	0.00
Total	99.42	100.34	100.26	99.36	99.37	98.59	98.71	98.72	99.03	99.03	99.33	99.33	99.45	99.88	99.88
Mg#	0.918	0.912	0.921	0.912	0.909	0.913	0.929	0.920	0.924	0.917	0.921	0.916	0.925	0.920	0.928
Orthopyroxenes	avg.	Al max.	Al min.	avg.	Al max.	Al min.	avg.	Al max.	Al min.						
SiO2	56.15	-	-	56.13	55.86	57.00	56.61	56.30	57.05						
TiO2	0.13	-	-	0.13	0.11	0.18	0.11	0.13	0.16						
Al2O3	3.09	-	-	3.07	3.74	2.55	2.90	3.53	2.49						
Cr2O3	0.18	-	-	0.33	0.37	0.31	0.14	0.15	0.20						
FeO*	5.64	-	-	5.91	6.03	5.96	5.64	5.53	5.59						
MnO	0.10	-	-	0.13	0.15	0.12	0.09	0.08	0.10						
NiO	0.04	-	-	0.09	0.13	0.13	0.10	0.10	0.08						
MgO	33.16	-	-	32.97	33.01	33.73	34.43	34.12	34.54						
CaO	0.60	-	-	0.49	0.49	0.48	0.55	0.67	0.49						
Na2O	0.05	-	-	0.07	0.07	0.07	0.06	0.06	0.04						
Total	99.15	-	-	99.33	99.97	100.52	100.64	100.67	100.74						
Mg#	0.913	-	-	0.909	0.907	0.910	0.916	0.917	0.917						

Total Fe as FeO; Mg#=Mg/(Mg+Fe); XCa=Ca/(Ca+Mg+Fe*+Mn)

Table 3-2. Major element compositions of garnets, clinopyroxenes and spinels in LT-type spinel-garnet clinopyroxenite.

	Spinel garnet clinopyroxenite (SGC) group1														
	SAE101			SAE109			SAE112			SAE124			SAE140		
Garnets	avg.	XCa max.	XCa min.	avg.	XCa max.	XCa min.	avg.	XCa max.	XCa min.	avg.	XCa max.	XCa min.	avg.	XCa max.	XCa min.
SiO_2	41.45	41.39	41.44	41.57	41.38	41.51	41.65	41.46	42.21	41.54	41.72	41.43	41.68	41.96	41.87
TiO_2	0.19	0.20	0.19	0.13	0.13	0.11	0.08	0.06	0.12	0.10	0.09	0.11	0.11	0.13	0.13
Al_2O_3	23.29	23.30	23.60	23.36	23.18	23.37	24.39	24.38	23.68	23.86	24.06	23.78	23.61	23.59	23.90
Cr_2O_3	0.75	0.82	0.76	0.63	0.53	0.57	0.26	0.21	0.37	0.39	0.31	0.32	0.24	0.23	0.15
FeO*	7.31	7.25	7.23	7.86	7.78	7.89	7.50	7.64	7.45	7.32	7.28	7.29	7.15	7.31	7.14
MnO	0.19	0.13	0.18	0.26	0.19	0.30	0.22	0.16	0.26	0.23	0.25	0.22	0.21	0.22	0.17
MgO	20.66	20.48	20.57	19.74	19.46	19.74	19.86	19.74	21.18	20.96	20.89	20.64	19.76	19.61	20.01
CaO	5.29	5.63	5.07	5.63	5.93	5.38	5.87	6.40	5.07	5.52	5.88	5.23	6.15	6.35	5.74
Na_2O	0.02	0.01	0.02	0.01	0.01	0.02	0.02	0.01	0.01	0.01	0.00	0.02	0.01	0.02	0.00
Total	99.14	99.21	99.05	99.19	98.59	98.90	99.86	100.05	100.34	99.94	100.47	99.03	98.92	99.42	99.09
Mg#	0.834	0.834	0.835	0.817	0.817	0.817	0.825	0.822	0.835	0.836	0.837	0.835	0.831	0.827	0.833
XCa	0.133	0.141	0.128	0.143	0.151	0.137	0.149	0.160	0.125	0.136	0.144	0.131	0.156	0.161	0.146
Clinopyroxenes	avg.	Al max.	Al min.	avg.	Al max.	Al min.	avg.	Al max.	Al min.	avg.	Al max.	Al min.	avg.	Al max.	Al min.
SiO_2	53.10	52.09	53.48	52.80	52.62	52.74	54.23	54.45	53.93	52.97	52.24	53.42	53.02	52.60	52.98
TiO_2	0.50	0.54	0.50	0.47	0.60	0.39	0.33	0.36	0.31	0.44	0.41	0.41	0.45	0.49	0.60
Al_2O_3	4.55	5.67	3.89	4.41	5.15	3.60	4.65	5.15	3.93	4.81	5.75	4.13	4.96	5.74	4.64
Cr_2O_3	0.61	0.60	0.66	0.53	0.48	0.53	0.34	0.33	0.35	0.26	0.25	0.32	0.18	0.15	0.12
FeO*	2.40	2.45	2.35	2.50	2.37	2.39	2.50	2.48	2.60	2.37	2.39	2.36	2.39	2.54	2.44
MnO	0.05	0.02	0.09	0.05	0.06	0.05	0.05	0.00	0.07	0.04	0.05	0.00	0.04	0.05	0.01
MgO	16.03	15.64	16.45	15.72	15.56	15.45	15.47	15.52	16.35	16.13	15.61	16.24	15.97	16.04	16.05
CaO	20.51	20.82	20.61	21.19	20.43	22.18	20.32	19.67	21.22	21.93	21.83	21.87	21.27	21.09	21.19
Na_2O	1.25	1.42	1.19	1.08	1.15	1.01	1.46	1.56	1.38	1.21	1.27	1.22	1.06	1.17	1.02
K_2O	0.01	0.01	0.01	0.01	0.00	0.00	0.01	0.00	0.00	0.00	0.00	0.00	0.00	0.00	0.00
Total	99.03	99.25	99.23	98.76	98.42	98.34	99.35	99.53	100.13	100.15	99.81	99.96	99.35	99.86	99.04
Mg#	0.922	0.919	0.926	0.918	0.921	0.920	0.917	0.918	0.918	0.924	0.921	0.925	0.923	0.918	0.921
Spinels	avg.	Cr# max	Cr# min	avg.	Cr# max	Cr# min	avg.	Cr# max	Cr# min	avg.	Cr# max	Cr# min	avg.	Cr# max	Cr# min
SiO_2	0.03	0.04	0.03	0.04	0.05	0.04	0.04	-	-	0.03	0.00	0.04	0.04	0.04	0.05
TiO_2	0.22	0.22	0.22	0.23	0.34	0.16	0.10	-	-	0.19	0.25	0.19	0.11	0.12	0.11
Al_2O_3	56.59	55.38	57.81	58.44	54.64	63.38	62.17	-	-	60.91	58.54	63.28	65.42	65.12	65.80
Cr_2O_3	9.86	11.22	8.50	8.39	11.81	4.05	4.75	-	-	6.81	9.44	4.39	2.11	2.28	1.83
Fe_2O_3	1.65	1.69	1.61	2.71	3.20	2.16	1.41	-	-	2.70	2.86	2.26	2.01	2.10	2.15
FeO	8.61	8.84	8.38	9.12	9.80	8.43	8.35	-	-	7.74	8.26	7.51	7.47	7.49	7.31
MnO	0.06	0.06	0.07	0.09	0.10	0.05	0.04	-	-	0.07	0.09	0.03	0.04	0.04	0.07
NiO	0.51	0.55	0.48	0.40	0.27	0.43	0.47	-	-	0.60	0.61	0.57	0.45	0.38	0.48
MgO	20.53	20.28	20.78	20.92	20.25	21.90	21.39	-	-	22.10	21.60	22.46	22.64	22.62	22.81
Total	98.08	98.29	97.87	100.34	100.46	100.59	98.72	-	-	101.14	101.65	100.72	100.29	100.20	100.61
Mg#	0.784	0.777	0.790	0.763	0.740	0.790	0.798	-	-	0.795	0.781	0.807	0.813	0.811	0.815
Cr#	0.105	0.120	0.090	0.088	0.127	0.041	0.049	-	-	0.070	0.098	0.044	0.021	0.023	0.018

Table 3-2. Continued

	Spinel garnet clinopyroxenite (SGC)														
	group2												group3		
	SAE115			SAE118			SAE130			SAE146			SAE108		
Garnets	avg.	XCa max.	XCa min.	avg.	XCa max.	XCa min.	avg.	XCa max.	XCa min.	avg.	XCa max.	XCa min.	avg.	XCa max.	XCa min.
SiO_2	41.39	41.42	41.62	41.54	41.76	41.80	41.54	41.92	41.28	42.33	42.19	41.98	41.89	41.66	42.05
TiO_2	0.10	0.04	0.14	0.10	0.09	0.07	0.11	0.07	0.16	0.11	0.12	0.10	0.02	0.01	0.03
Al_2O_3	23.84	23.77	23.96	24.09	24.24	24.25	24.08	24.46	24.05	23.64	23.61	23.88	23.40	22.99	23.71
Cr_2O_3	0.15	0.30	0.10	0.20	0.21	0.22	0.23	0.29	0.20	0.38	0.39	0.35	0.15	0.12	0.13
FeO*	6.80	6.60	7.32	7.14	6.79	7.24	7.05	7.14	7.23	7.36	7.36	7.57	5.66	5.79	5.66
MnO	0.23	0.23	0.23	0.22	0.26	0.20	0.21	0.22	0.23	0.21	0.20	0.21	0.16	0.14	0.14
MgO	18.09	17.53	18.46	19.47	18.45	20.06	19.31	18.35	19.49	19.96	19.56	20.07	18.16	17.36	18.92
CaO	9.30	9.84	8.48	7.32	7.78	6.79	7.87	8.10	7.35	5.83	6.23	5.70	9.38	10.44	8.31
Na_2O	0.01	0.00	0.02	0.01	0.00	0.00	0.01	0.00	0.02	0.01	0.01	0.03	0.01	0.02	0.01
Total	99.90	99.74	100.31	100.09	99.57	100.63	100.42	100.55	100.01	99.82	99.67	99.88	98.81	98.55	98.95
Mg#	0.826	0.826	0.818	0.829	0.829	0.832	0.830	0.821	0.828	0.829	0.826	0.825	0.851	0.842	0.856
XCa	0.233	0.249	0.212	0.182	0.200	0.168	0.195	0.206	0.182	0.148	0.158	0.143	0.239	0.266	0.212
Clinopyroxenes	avg.	Al max.	Al min.	avg.	Al max.	Al min.	avg.	Al max.	Al min.	avg.	Al max.	Al min.	avg.	Al max.	Al min.
SiO_2	51.61	50.79	52.14	52.85	52.39	53.33	52.19	51.16	51.97	53.09	52.43	53.29	52.30	51.25	53.58
TiO_2	0.41	0.49	0.40	0.39	0.39	0.35	0.43	0.49	0.41	0.39	0.40	0.33	0.08	0.03	0.12
Al_2O_3	7.34	7.96	6.87	5.63	6.64	4.82	6.17	8.20	5.36	5.15	6.64	4.22	7.51	9.52	6.31
Cr_2O_3	0.12	0.08	0.17	0.13	0.12	0.17	0.14	0.17	0.11	0.27	0.28	0.28	0.11	0.08	0.21
FeO*	2.26	2.34	2.25	2.34	2.41	2.21	2.07	2.12	2.02	2.29	2.20	2.34	1.45	1.49	1.53
MnO	0.00	0.00	0.00	0.02	0.00	0.00	0.04	0.05	0.03	0.03	0.01	0.02	0.02	0.00	0.01
MgO	14.68	14.38	14.79	15.84	14.98	16.33	15.38	14.61	15.79	15.49	14.69	15.74	14.79	13.77	15.43
CaO	22.90	21.94	22.98	22.76	22.43	22.91	22.44	22.38	22.01	21.26	21.16	21.46	22.25	22.36	22.34
Na_2O	1.08	1.01	1.08	1.02	1.16	0.98	1.06	1.16	0.97	1.31	1.45	1.25	1.12	1.19	1.13
K_2O	0.00	0.02	0.00	0.00	0.02	0.00	0.00	0.00	0.01	0.00	0.00	0.01	0.01	0.01	0.00
Total	100.41	98.99	100.68	101.00	100.54	101.10	99.92	100.32	98.67	99.29	99.27	98.94	99.64	99.71	100.66
Mg#	0.920	0.916	0.921	0.923	0.917	0.929	0.930	0.925	0.933	0.923	0.922	0.923	0.948	0.943	0.947
Spinels	avg.	Cr# max	Cr# min	avg.	Cr# max	Cr# min	avg.	Cr# max	Cr# min		Cr# max	Cr# min	avg.	Cr# max	Cr# min
SiO_2	0.04	0.06	0.04	0.03	0.03	0.06	0.03	0.02	0.04	-	0.06	0.02	0.05	0.07	0.07
TiO_2	0.05	0.04	0.04	0.10	0.13	0.13	0.08	0.03	0.10	-	0.18	0.14	0.01	0.00	0.03
Al_2O_3	66.18	65.36	66.84	65.16	63.33	66.34	65.81	65.31	66.57	-	59.69	63.26	67.27	68.10	66.52
Cr_2O_3	1.59	2.16	0.92	2.57	3.67	1.72	2.48	2.77	1.96	-	6.85	4.16	1.37	1.46	1.13
Fe_2O_3	1.55	0.97	1.47	2.42	1.96	2.56	1.21	1.02	0.81	-	2.58	0.58	0.95	0.35	1.44
FeO	7.69	7.87	7.43	7.83	8.07	7.55	7.57	7.24	7.91	-	8.86	8.52	5.48	5.94	5.08
MnO	0.07	0.07	0.07	0.04	0.11	0.00	0.03	0.02	0.00	-	0.07	0.09	0.05	0.02	0.08
NiO	0.44	0.47	0.47	0.49	0.49	0.46	0.43	0.48	0.47	-	0.69	0.00	0.28	0.32	0.30
MgO	22.49	22.07	22.68	22.51	21.82	23.05	22.60	22.54	22.50	-	20.93	21.59	24.02	23.98	24.02
Total	100.10	99.07	99.95	101.14	99.61	101.85	100.23	99.43	100.36	-	99.89	98.37	99.49	100.24	98.65
Mg#	0.815	0.818	0.822	0.800	0.798	0.807	0.823	0.831	0.823	-	0.769	0.810	0.871	0.872	0.870
Cr#	0.016	0.022	0.009	0.026	0.037	0.017	0.025	0.028	0.019	-	0.071	0.042	0.013	0.014	0.011

Table 3-2. Continued

	Spinel garnet clinopyroxenite (SGC) group3														
	SAE110			SAE142			SAE153			SAE104			SAE125		
Garnets	avg.	XCa max.	XCa min.	avg.	XCa max.	XCa min.	avg.	XCa max.	XCa min.	avg.	XCa max.	XCa min.	avg.	XCa max.	XCa min.
SiO_2	40.97	42.36	40.19	42.22	42.46	42.50	42.54	42.92	42.51	41.36	41.12	41.25	41.12	41.29	41.15
TiO_2	0.02	0.04	0.06	0.07	0.06	0.09	0.04	0.04	0.08	0.09	0.12	0.13	0.08	0.05	0.06
Al_2O_3	25.05	24.28	25.57	23.91	23.82	24.01	23.84	24.08	24.03	23.83	23.94	23.79	23.78	23.59	23.92
Cr_2O_3	0.16	0.12	0.16	0.17	0.18	0.19	0.23	0.34	0.21	0.08	0.10	0.04	0.14	0.14	0.12
FeO*	6.06	5.78	6.07	6.28	6.32	6.24	6.86	6.82	6.76	7.10	6.99	7.33	7.15	6.56	7.34
MnO	0.19	0.21	0.22	0.15	0.19	0.13	0.17	0.14	0.16	0.22	0.18	0.23	0.23	0.20	0.23
MgO	18.95	18.11	19.94	19.45	19.26	19.54	19.83	19.43	20.65	18.03	17.42	18.64	17.26	16.87	17.63
CaO	8.02	8.50	6.92	7.67	7.75	7.71	6.84	7.18	6.10	8.54	9.29	8.00	10.10	11.63	9.23
Na_2O	0.01	0.02	0.00	0.01	0.03	0.00	0.01	0.03	0.01	0.02	0.00	0.01	0.01	0.02	0.00
Total	99.45	99.42	99.12	99.92	100.07	100.40	100.37	100.98	100.50	99.26	99.16	99.42	99.87	100.33	99.69
Mg#	0.848	0.848	0.854	0.847	0.844	0.848	0.837	0.835	0.845	0.819	0.816	0.819	0.811	0.821	0.811
XCa	0.204	0.221	0.175	0.193	0.196	0.193	0.171	0.181	0.152	0.217	0.238	0.201	0.253	0.288	0.233
Clinopyroxenes	avg.	Al max.	Al min.	avg.	Al max.	Al min.	avg.	Al max.	Al min.	avg.	Al max.	Al min.	avg.	Al max.	Al min.
SiO_2	52.65	52.43	53.67	51.69	51.90	51.76	53.21	52.45	54.14	52.22	51.58	53.00	50.89	49.95	51.73
TiO_2	0.09	0.12	0.13	0.23	0.24	0.27	0.12	0.16	0.15	0.19	0.19	0.30	0.28	0.30	0.28
Al_2O_3	6.76	8.03	5.05	6.36	7.40	5.59	5.67	6.52	4.81	7.02	8.84	5.51	8.85	10.74	7.03
Cr_2O_3	0.14	0.17	0.13	0.14	0.08	0.18	0.18	0.22	0.23	0.06	0.12	0.02	0.12	0.19	0.14
FeO*	1.76	1.74	1.73	1.96	1.84	1.93	1.98	1.93	1.94	1.95	2.05	1.71	1.99	1.91	2.24
MnO	0.03	0.08	0.02	0.03	0.08	0.00	0.03	0.01	0.06	0.03	0.04	0.09	0.02	0.02	0.00
MgO	14.87	14.58	15.93	15.20	14.92	15.92	15.44	15.10	16.12	14.84	14.42	15.23	14.02	12.63	14.97
CaO	22.37	22.41	22.29	22.33	22.57	22.64	22.00	21.65	21.96	22.60	22.46	22.30	22.30	22.82	23.08
Na_2O	1.13	1.23	1.17	1.13	1.11	1.19	1.21	1.25	1.13	1.02	1.16	0.85	1.24	1.25	1.21
K_2O	0.01	0.01	0.01	0.02	0.00	0.01	0.01	0.00	0.02	0.00	0.01	0.00	0.01	0.00	0.00
Total	99.81	100.78	100.13	99.07	100.13	99.48	99.86	99.28	100.55	99.93	100.88	99.01	99.70	99.81	100.66
Mg#	0.938	0.937	0.942	0.933	0.935	0.936	0.933	0.933	0.937	0.931	0.926	0.941	0.926	0.922	0.923
Spinels	avg.	Cr# max	Cr# min	avg.	Cr# max	Cr# min	avg.	Cr# max	Cr# min	avg.	Cr# max	Cr# min	avg.	Cr# max	Cr# min
SiO_2	0.04	0.04	0.04	0.04	0.03	0.01	0.03	0.02	0.04	0.03	0.02	0.03	0.02	0.02	0.06
TiO_2	0.03	0.00	0.04	0.05	0.02	0.08	0.06	0.05	0.04	0.01	0.00	0.03	0.00	0.02	0.00
Al_2O_3	67.41	67.58	67.48	66.42	66.06	66.62	65.55	65.77	66.08	67.62	67.93	68.12	67.18	67.22	67.56
Cr_2O_3	1.51	2.03	0.98	2.48	2.53	0.84	1.98	2.09	1.70	0.77	1.06	0.80	1.34	1.58	1.11
Fe_2O_3	0.48	0.50	0.47	1.22	1.61	1.54	2.09	1.76	1.86	0.65	1.04	0.48	1.16	0.53	1.15
FeO	6.89	6.92	6.65	6.85	6.73	5.90	6.49	6.73	6.55	7.74	7.42	7.99	7.50	7.92	7.47
MnO	0.04	0.02	0.05	0.04	0.03	0.03	0.04	0.06	0.01	0.06	0.11	0.05	0.05	0.01	0.07
NiO	0.30	0.34	0.29	0.56	0.47	0.67	0.45	0.45	0.39	0.37	0.34	0.40	0.36	0.34	0.41
MgO	23.20	23.36	23.23	23.15	23.21	23.36	23.17	23.03	23.25	22.58	23.01	22.60	22.81	22.54	22.92
Total	99.90	100.79	99.22	100.81	100.70	99.04	99.86	99.96	99.93	99.83	100.92	100.48	100.42	100.17	100.75
Mg#	0.850	0.850	0.854	0.838	0.835	0.851	0.831	0.832	0.834	0.829	0.831	0.827	0.826	0.827	0.828
Cr#	0.015	0.020	0.010	0.024	0.025	0.008	0.020	0.021	0.017	0.008	0.010	0.008	0.013	0.016	0.011

Total Fe as FeO; Mg#=Mg/(Mg+Fe), Fe^{3+} in spinel estimated from the stoichiometric method; Cr#=Cr/(Cr+Al); XCa=Ca/(Ca+Mg+Fe*+Mn)

Table 3-3. Major element compositions of garnets, clinopyroxenes, orthopyroxenes and olivines in HT-type garnet clinopyroxenite (GC) and garnet orthopyroxenite (GO).

	Garnet clinopyroxenite										Garnet orthopyroxenite		
	SAE116	SAE107	SAE113	SAE120	SAE147	SAE152	SAE154	SAE132	SAE141		SAX37	SAE135	SAE157
Garnets													
SiO_2	41.22	41.35	41.41	41.53	41.95	41.44	42.21	41.27	40.98		41.00	41.39	42.04
TiO_2	0.17	0.46	0.39	0.41	0.48	0.32	0.45	0.49	0.34		0.46	0.42	0.47
Al_2O_3	23.72	22.15	23.36	23.38	23.19	22.53	22.98	23.46	22.50		23.27	22.66	23.21
Cr_2O_3	0.17	0.98	0.46	0.34	0.13	0.12	0.33	0.21	0.34		0.27	0.89	0.52
FeO*	9.69	8.25	9.94	8.27	10.98	11.47	8.52	10.73	10.38		10.36	8.61	9.06
MnO	0.30	0.23	0.28	0.28	0.31	0.32	0.26	0.26	0.28		0.26	0.24	0.25
MgO	19.27	20.13	20.06	20.93	19.14	17.42	20.48	20.10	18.81		19.83	20.42	20.16
CaO	5.24	4.56	4.35	5.01	4.52	6.03	4.40	4.34	4.92		4.48	4.29	4.70
Na_2O	0.02	0.04	0.04	0.04	0.05	0.04	0.03	0.04	0.03		0.06	0.04	0.04
Total	99.80	98.15	100.28	100.19	100.74	99.69	99.66	100.90	98.58		99.99	98.95	100.46
Mg#	0.780	0.813	0.782	0.819	0.756	0.730	0.811	0.770	0.764		0.773	0.809	0.799
Clinopyroxenes													
SiO_2	54.35	53.80	53.70	53.71	53.75	53.10	54.36	53.50	53.52		53.59	53.81	53.83
TiO_2	0.18	0.44	0.46	0.42	0.69	0.36	0.44	0.66	0.33		0.59	0.44	0.51
Al_2O_3	5.79	5.01	6.01	5.39	5.44	7.19	4.85	5.77	5.41		5.77	5.31	5.14
Cr_2O_3	0.10	0.52	0.28	0.20	0.09	0.11	0.17	0.11	0.16		0.54	0.43	0.33
FeO*	5.69	5.28	5.87	4.99	6.41	5.88	5.28	6.39	6.37		6.26	5.50	5.64
MnO	0.15	0.11	0.14	0.11	0.14	0.11	0.13	0.12	0.14		0.11	0.12	0.14
MgO	17.82	18.90	17.81	18.42	16.82	14.83	18.83	17.81	17.79		17.84	18.55	18.30
CaO	15.36	13.72	13.48	15.76	14.89	16.31	14.41	13.85	14.53		14.08	13.60	14.72
Na_2O	0.95	1.49	1.82	1.51	1.91	2.03	1.37	2.01	1.51		2.03	1.66	1.54
K_2O	0.01	0.01	0.01	0.01	0.01	0.02	0.01	0.01	0.00		0.02	0.01	0.01
Total	100.38	99.29	99.57	100.53	100.15	99.92	99.84	100.23	99.76		100.82	99.42	100.15
Mg#	0.848	0.864	0.844	0.868	0.824	0.818	0.864	0.832	0.833		0.835	0.857	0.853
Orthopyroxenes									core	mantle	rim			
SiO_2								54.95	55.23	55.17	55.09	55.22	55.18	55.62
TiO_2								0.30	0.16	0.17	0.20	0.28	0.22	0.26
Al_2O_3								3.68	3.71	3.79	4.51	3.69	3.94	3.73
Cr_2O_3								0.08	0.11	0.06	0.15	0.06	0.27	0.20
FeO*								9.82	8.80	9.79	8.72	9.64	7.94	8.26
MnO								0.13	0.15	0.14	0.14	0.13	0.14	0.15
NiO								0.09	0.07	0.11	0.04	0.10	0.12	0.14
MgO								30.13	29.99	29.93	29.76	30.35	30.66	30.70
CaO								1.44	1.64	1.42	1.48	1.52	1.60	1.62
Na_2O								0.39	0.30	0.26	0.23	0.34	0.32	0.26
Total								101.00	100.16	100.84	100.31	101.33	100.39	100.93
Mg#								0.848	0.859	0.845	0.859	0.849	0.873	0.869

	Garnet orthopyroxenite													
	SAE126	SAE127	SAG19	SAE114	SAE149	SAE151	SAE155	SAE136			SAE137		SAE139	
								Mg-rich core	Cr-rich mantle	Fe-rich rim	Cr-rich core	small avg.	Cr-rich core	small avg.
Garnets														
SiO_2	41.19	41.14	41.65	41.45	42.06	42.15	41.97	42.00	41.33	41.63	40.89	41.16	40.83	41.08
TiO_2	0.49	0.49	0.47	0.44	0.51	0.54	0.46	0.37	0.53	0.52	0.57	0.47	0.58	0.48
Al_2O_3	23.25	23.13	23.21	23.20	23.25	22.74	23.00	23.46	21.70	23.18	22.07	23.15	21.12	22.63
Cr_2O_3	0.39	0.60	0.58	0.44	0.37	0.50	0.19	0.55	2.41	0.27	1.73	0.35	2.85	0.56
FeO*	9.40	9.58	8.62	9.67	9.72	9.97	10.03	6.25	7.90	9.26	9.27	9.36	9.10	9.82
MnO	0.28	0.25	0.21	0.27	0.28	0.26	0.27	0.25	0.31	0.26	0.23	0.23	0.29	0.24
MgO	20.26	20.39	20.37	20.12	20.05	19.61	19.88	22.29	20.59	20.02	19.45	19.60	19.89	19.47
CaO	4.65	4.61	4.48	4.66	4.57	4.67	4.52	4.59	4.86	4.57	4.81	4.34	5.00	4.50
Na_2O	0.04	0.05	0.03	0.05	0.03	0.05	0.04	0.03	0.07	0.06	0.08	0.03	0.06	0.05
Total	99.93	100.25	99.62	100.30	100.83	100.49	100.36	99.79	99.69	99.77	99.09	98.69	99.72	98.83
Mg#	0.793	0.791	0.808	0.788	0.786	0.778	0.779	0.864	0.823	0.794	0.789	0.789	0.796	0.779
Clinopyroxenes														
SiO_2	53.07									53.14		53.09		53.57
TiO_2	0.62									0.66		0.59		0.57
Al_2O_3	5.24									5.18		5.21		5.54
Cr_2O_3	0.20									0.95		0.32		0.24
FeO*	5.52									4.36		5.67		5.81
MnO	0.12									0.11		0.13		0.11
MgO	17.87									17.90		17.54		17.66
CaO	15.07									15.52		14.81		14.31
Na_2O	1.68									1.64		1.53		1.75
K_2O	0.01									0.01		0.01		0.01
Total	99.40									99.47		98.90		99.58
Mg#	0.852									0.880		0.847		0.844
Orthopyroxenes														
SiO_2	55.27	55.29	55.08	55.79	55.76	55.33	55.83			54.97		54.75		55.02
TiO_2	0.29	0.27	0.26	0.27	0.30	0.35	0.32			0.32		0.27		0.28
Al_2O_3	3.61	3.71	3.89	3.74	3.65	3.64	3.29			3.59		3.74		3.76
Cr_2O_3	0.10	0.14	0.13	0.09	0.17	0.11	0.05			0.11		0.06		0.09
FeO*	8.43	8.69	7.84	8.70	8.81	9.20	8.98			8.60		8.50		8.70
MnO	0.13	0.14	0.11	0.15	0.14	0.15	0.11			0.11		0.11		0.11
NiO	0.09	0.10	0.11	0.09	0.12	0.08	0.06			0.09		0.11		0.08
MgO	30.94	30.67	31.00	30.36	30.11	30.24	30.41			30.43		30.19		30.12
CaO	1.40	1.52	1.43	1.49	1.51	1.24	1.50			1.45		1.34		1.50
Na_2O	0.27	0.28	0.22	0.30	0.30	0.26	0.26			0.26		0.25		0.32
Total	100.52	100.81	100.08	100.98	100.85	100.58	100.81			99.92		99.30		99.97
Mg#	0.867	0.863	0.876	0.861	0.859	0.854	0.858			0.868		0.864		0.861
Olivines														
SiO_2			40.13							40.41		39.97		
FeO			12.52							13.81		13.74		
MnO			0.13							0.15		0.14		
NiO			0.40							0.36		0.34		
MgO			47.25							45.49		45.83		
CaO			0.10							0.09		0.10		
Total			100.53							100.30		100.11		
Mg#			0.871							0.854		0.856		

Total Fe as FeO; Mg#=Mg/(Mg+Fe)

Table 3-4. Major element compositions of garnets, clinopyroxenes in megacryst suites.

	Subcalcic Diopsides (MSD)										Inclusion in Grt
	SAX40 fine	SAX40 coarse	SAX51	SAX39J	SAX44	SAX39B	SAX39D	SAX39F	SAX39I	SAX39C	SAE133
Clinopyroxenes											
SiO_2	54.54	54.24	53.26	53.79	53.32	53.37	52.95	53.56	53.91	53.78	52.37
TiO_2	0.44	0.45	0.61	0.72	0.75	0.80	0.72	0.85	0.77	0.72	0.51
Al_2O_3	5.34	5.50	5.53	5.44	5.45	5.35	5.55	5.57	5.60	5.72	5.76
Cr_2O_3	0.28	0.31	0.18	0.07	0.04	0.04	0.05	0.00	0.00	0.07	0.20
FeO*	5.86	5.84	5.93	5.95	5.89	5.80	6.38	6.45	6.62	6.67	6.51
MnO	0.16	0.15	0.10	0.13	0.13	0.17	0.13	0.13	0.16	0.12	0.17
MgO	18.94	18.34	17.57	17.24	16.92	16.50	16.89	16.46	16.83	16.84	18.22
CaO	13.81	13.86	14.35	15.41	15.50	15.52	14.92	15.45	14.71	14.33	13.40
Na_2O	1.66	1.67	1.86	1.83	1.79	1.69	2.04	1.94	2.04	2.10	1.95
K_2O	0.01	0.01	0.00	0.04	0.01	0.00	0.01	0.01	0.02	0.00	0.03
Total	101.03	100.37	99.39	100.61	99.80	99.25	99.64	100.42	100.64	100.35	99.10
Mg#	0.852	0.848	0.841	0.838	0.837	0.835	0.825	0.820	0.819	0.818	0.832998

	Cpx-Ilm (MCI)		Augites (MA)						Cpx-Rt (MCR)	Mica-Amp--Ilm-Augite (MAIA)
	SAX36	SAX39E	SAX35	SAX47	SAX45	SAX49	SAX48	SAX32A	SAX34	SAX107
Clinopyroxenes										
SiO_2	53.37	53.74	53.32	52.90	53.22	53.18	53.15	53.98	53.49	53.52
TiO_2	1.04	1.09	1.10	0.95	0.88	0.98	0.95	0.88	0.96	0.90
Al_2O_3	5.12	5.39	5.46	5.33	4.93	5.62	5.47	5.50	5.71	8.68
Cr_2O_3	0.01	0.00	0.01	0.00	0.03	0.01	0.00	0.00	0.02	0.01
FeO*	7.83	7.99	8.17	8.25	8.41	8.55	8.86	8.81	8.91	8.51
MnO	0.14	0.12	0.19	0.16	0.19	0.14	0.15	0.20	0.15	0.13
MgO	14.24	14.28	13.47	13.29	13.13	12.76	12.43	12.02	11.92	9.55
CaO	15.68	15.24	14.68	15.17	15.23	14.76	14.78	14.60	14.45	13.47
Na_2O	2.59	2.68	2.96	2.90	3.04	3.41	3.49	3.64	3.54	4.58
K_2O	0.02	0.00	0.00	0.01	0.01	0.00	0.00	0.00	0.01	0.00
Total	100.03	100.54	99.36	98.94	99.08	99.41	99.29	99.62	99.15	99.35
Mg#	0.764	0.761	0.746	0.742	0.736	0.727	0.714	0.709	0.704	0.667

	Megacrystalline garnet (MG)										
	SAX19	SAE133	SAX22	SAX29	SAX9	SAX8-1	SAX8-2	SAX24	SAX21	SAX27	SAX23
Garnets											
SiO_2	41.48	41.19	41.79	41.05	41.38	41.00	40.83	41.34	39.79	40.28	41.05
TiO_2	0.43	0.50	0.59	0.52	0.61	0.42	0.48	0.55	0.53	0.55	0.59
Al_2O_3	23.24	23.47	23.16	23.20	23.12	23.39	23.30	23.08	23.17	23.23	23.15
Cr_2O_3	0.30	0.30	0.12	0.10	0.13	0.08	0.07	0.05	0.07	0.04	0.00
FeO*	9.49	9.56	10.21	10.50	10.73	10.95	10.97	10.93	11.19	11.38	11.37
MnO	0.21	0.25	0.33	0.33	0.30	0.31	0.28	0.31	0.36	0.26	0.29
MgO	20.21	20.34	19.77	19.61	19.77	19.11	18.78	19.08	19.43	19.13	18.79
CaO	4.79	4.79	4.78	4.82	4.74	4.54	4.07	4.71	4.52	4.66	4.60
Na_2O	0.03	0.04	0.05	0.03	0.05	0.05	0.04	0.04	0.04	0.01	0.02
Total	100.17	100.44	100.78	100.18	100.83	99.85	98.81	100.07	99.09	99.55	99.86
Mg#	0.792	0.791	0.775	0.769	0.767	0.757	0.753	0.757	0.756	0.750	0.747

	SAX17	SAX30	SAX16	SAX3	SAX11	SAX10
Garnets						
SiO_2	40.33	40.95	40.63	40.85	41.45	40.48
TiO_2	0.58	0.62	0.61	0.53	0.67	0.80
Al_2O_3	22.68	23.15	23.13	23.08	23.24	22.31
Cr_2O_3	0.00	0.03	0.08	0.03	0.00	0.01
FeO*	11.78	12.41	12.47	12.25	12.57	12.82
MnO	0.30	0.32	0.32	0.32	0.35	0.32
MgO	18.13	18.44	18.42	18.08	18.33	17.93
CaO	4.54	4.38	4.45	4.51	4.57	4.75
Na_2O	0.07	0.09	0.07	0.05	0.11	0.08
Total	98.41	100.39	100.17	99.72	101.29	99.49
Mg#	0.733	0.726	0.725	0.725	0.722	0.714

Table 3-5. Major element compositions of olivines, orthopyroxenes, clinopyroxenes, garnets and spinels in HT-type garnet lherzolite (GL) and spinel harzburgite(SH).

	Garnet lherzolite (GL)										Spinel harzburgite (HTSH)					
	SAG1	SAG15	SAG9	SAG21		SAG27	SAG7	SAG13	SAG16	SAG2	SAG30	SAS1	SAS8	SAS21	SAS46	SAS63	SAS69
Olivines																	
SiO_2	41.51	41.40	41.39	40.61		40.99	-	-	-	-	40.78	40.88	40.98	41.42	40.88	40.48	41.14
FeO	9.45	8.64	8.88	12.53		11.94	-	-	-	-	9.47	8.28	8.08	7.49	7.91	9.02	8.19
MnO	0.13	0.13	0.12	0.15		0.13	-	-	-	-	0.13	0.13	0.12	0.11	0.16	0.08	0.10
NiO	0.37	0.41	0.35	0.34		0.34	-	-	-	-	0.36	0.40	0.37	0.30	0.41	0.42	0.38
MgO	49.02	50.13	49.57	47.13		47.35	-	-	-	-	48.62	50.90	50.32	50.32	50.09	48.74	49.09
CaO	0.10	0.09	0.09	0.11		0.09	-	-	-	-	0.09	0.11	0.09	0.13	0.11	0.08	0.09
Total	100.59	100.79	100.39	100.86		100.85	-	-	-	-	99.45	100.69	99.95	99.78	99.56	98.81	98.98
Mg#	0.902	0.912	0.909	0.870		0.876	-	-	-	-	0.901	0.916	0.917	0.923	0.919	0.906	0.914
Orthopyroxenes																	
SiO_2	56.22	55.99	56.22	55.17		55.57	56.45	56.30	56.40	-	56.08	55.30	55.99	56.59	56.82	56.22	56.89
TiO_2	0.07	0.26	0.15	0.31		0.33	0.08	0.09	0.08	-	0.44	0.30	0.32	0.01	0.00	0.28	0.14
Al_2O_3	3.36	3.53	3.54	3.63		3.62	3.33	3.37	3.35	-	3.50	3.64	3.33	2.19	2.25	3.02	2.21
Cr_2O_3	0.53	0.55	0.54	0.35		0.57	0.59	0.59	0.62	-	0.52	1.27	0.96	0.92	0.88	0.99	0.95
FeO*	5.89	5.46	5.64	7.77		7.36	5.89	5.80	5.77	-	5.85	5.30	5.07	4.71	4.81	5.64	5.03
MnO	0.15	0.12	0.11	0.12		0.12	0.13	0.13	0.12	-	0.06	0.14	0.09	0.12	0.10	0.09	0.11
NiO	0.12	0.09	0.11	0.12		0.09	0.13	0.12	0.13	-	0.07	0.14	0.12	0.09	0.12	0.13	0.11
MgO	32.36	32.70	32.41	31.04		31.29	33.09	33.04	32.82	-	32.75	32.44	32.86	32.91	33.80	32.53	33.24
CaO	1.23	1.20	1.27	1.42		1.45	1.22	1.20	1.22	-	1.12	1.54	1.17	1.42	1.32	1.24	1.24
Na_2O	0.18	0.23	0.21	0.26		0.26	0.18	0.18	0.17	-	0.26	0.28	0.29	0.04	0.00	0.25	0.19
Total	100.10	100.14	100.19	100.20		100.66	101.09	100.82	100.67	-	100.65	100.34	100.19	99.00	100.10	100.39	100.12
Mg#	0.907	0.914	0.911	0.877		0.883	0.909	0.910	0.910	-	0.909	0.916	0.920	0.926	0.926	0.911	0.922
Clinopyroxenes																	
SiO_2	53.71	53.44	53.70	53.18		53.18	53.61	53.79	53.46	53.11	53.54	53.05	53.02	54.16	54.32	54.03	54.00
TiO_2	0.12	0.64	0.37	0.71		0.72	0.20	0.19	0.12	0.10	1.09	0.62	0.89	0.00	0.01	0.55	0.22
Al_2O_3	4.44	5.07	5.11	5.20		5.14	4.38	4.40	4.45	4.39	5.38	4.60	4.87	2.13	2.10	4.25	3.06
Cr_2O_3	1.10	1.23	1.04	0.81		1.20	1.19	1.17	1.15	1.11	1.03	2.18	1.98	1.09	1.06	2.14	2.11
FeO*	3.41	3.26	3.32	4.96		4.70	3.35	3.37	3.35	3.34	3.46	3.38	2.89	2.56	2.69	3.19	2.93
MnO	0.05	0.10	0.10	0.11		0.12	0.09	0.10	0.06	0.11	0.11	0.10	0.09	0.10	0.09	0.13	0.09
MgO	17.40	17.38	17.45	17.31		17.39	17.39	17.49	17.40	17.48	16.69	18.20	16.87	18.91	19.26	17.68	17.86
CaO	17.92	16.86	16.79	15.36		15.43	18.16	17.95	17.05	18.12	16.63	15.39	16.39	20.79	20.18	16.74	17.41
Na_2O	1.36	1.72	1.63	1.72		1.74	1.40	1.40	1.45	1.53	2.07	1.67	1.91	0.16	0.19	1.92	1.52
K_2O	0.01	0.02	0.02	0.01		0.02	0.01	0.01	0.01	0.02	0.01	0.01	0.02	0.05	0.04	0.01	0.00
Total	99.53	99.72	99.52	99.37		99.64	99.79	99.86	98.48	99.31	100.00	99.20	98.92	99.96	99.95	100.64	99.20
Mg#	0.901	0.905	0.903	0.861		0.868	0.903	0.903	0.903	0.903	0.896	0.906	0.912	0.929	0.927	0.908	0.916
Garnets				core	rim												
SiO_2	42.49	41.86	41.52	42.46	42.40	41.23	42.18	42.13	42.09	42.51	42.33						
TiO_2	0.14	0.34	0.28	0.34	0.49	0.57	0.16	0.16	0.17	0.13	0.28						
Al_2O_3	22.14	21.86	22.39	23.01	22.39	21.32	21.91	22.04	22.22	22.32	22.34						
Cr_2O_3	2.17	2.07	1.96	1.10	1.47	2.21	2.24	2.24	2.22	2.10	1.98						
FeO*	6.84	6.31	6.47	7.32	8.83	8.18	6.74	6.78	6.77	6.77	6.82						
MnO	0.19	0.24	0.27	0.23	0.28	0.26	0.29	0.28	0.27	0.25	0.26						
MgO	21.09	21.15	21.36	21.28	20.08	20.24	20.98	21.00	20.71	21.13	21.84						
CaO	5.14	4.98	4.88	4.61	4.86	4.96	5.16	5.16	5.12	5.23	4.89						
Na_2O	0.02	0.03	0.02	0.03	0.03	0.03	0.02	0.02	0.01	0.02	0.05						
Total	100.22	98.83	99.15	100.35	100.80	99.01	99.66	99.80	99.59	100.45	100.78						
Mg#	0.846	0.857	0.855	0.838	0.802	0.815	0.847	0.847	0.845	0.848	0.851						
Spinels																	
SiO_2												0.21	-	0.11	0.14	0.14	0.12
TiO_2												2.09	-	0.02	0.04	2.01	1.03
Al_2O_3												24.61	-	19.09	18.95	21.77	17.05
Cr_2O_3												40.41	-	50.51	49.67	41.42	48.63
Fe_2O_3												4.49	-	4.10	5.61	6.58	6.29
FeO												11.39	-	10.98	10.14	11.85	10.78
MnO												0.22	-	0.20	0.25	0.26	0.25
NiO												0.22	-	0.18	0.22	0.22	0.23
MgO												17.33	-	15.78	16.36	16.55	16.11
Total												100.96	-	100.98	101.37	100.79	100.50
Mg#												0.731	-	0.719	0.742	0.713	0.727
Cr#												0.524		0.640	0.637	0.561	0.657

Total Fe as FeO; Mg#=Mg/(Mg+Fe), Fe^{3+} in spinel estimated from the stoichiometric method; Cr#=Cr/(Cr+Al)

Table 3-6. Major element compositions of olivines, orthopyroxenes, clinopyroxenes, garnets and spinels in LT-type garnet-spinel lherzolite (GSL).

	Garnet-Spinel lherzolite (GSL)											
	SAG3	SAG10	SAG12	SAG14	SAG17	SAG20	SAG24		SAS7		SAS9	SAS11
Olivines												
SiO_2	40.87	40.94	-	41.06	41.38	41.26	40.96		41.50		40.85	41.24
FeO	9.76	9.69	-	9.90	9.32	9.82	8.95		10.08		9.25	8.98
MnO	0.11	0.15	-	0.12	0.13	0.12	0.13		0.12		0.13	0.13
NiO	0.44	0.47	-	0.42	0.39	0.34	0.37		0.39		0.38	0.43
MgO	49.39	49.31	-	48.93	49.58	49.44	50.08		48.83		49.81	49.96
CaO	0.02	0.03	-	0.02	0.03	0.03	0.03		0.02		0.03	0.03
Total	100.59	100.58	-	100.47	100.82	101.01	100.51		100.94		100.45	100.77
Mg#	0.900	0.901		0.898	0.905	0.900	0.909		0.896		0.906	0.908
Orthopyroxenes							core	rim	core	rim	core	core
SiO_2	56.65	56.01	56.75	56.15	55.87	56.36	55.49	56.41	56.987	57.686	55.65	55.55
TiO_2	0.17	0.15	0.13	0.13	0.13	0.13	0.00	0.19	0.10	0.12	0.05	0.05
Al_2O_3	2.77	2.53	2.61	2.64	2.68	2.61	3.51	2.63	4.24	2.60	3.89	3.65
Cr_2O_3	0.40	0.39	0.40	0.36	0.45	0.42	0.47	0.38	0.24	0.33	0.38	0.42
FeO*	6.13	6.10	6.14	6.21	5.88	6.29	5.71	6.41	5.90	5.69	5.73	5.88
MnO	0.14	0.12	0.14	0.13	0.12	0.14	0.16	0.11	0.10	0.09	0.13	0.13
NiO	0.08	0.08	0.13	0.12	0.10	0.11	0.07	0.07	0.10	0.00	0.13	0.15
MgO	33.21	33.81	33.73	33.50	34.04	33.81	33.76	33.14	32.66	33.14	33.40	33.69
CaO	0.46	0.45	0.49	0.56	0.48	0.56	0.56	0.59	0.58	0.54	0.55	0.54
Na_2O	0.06	0.09	0.06	0.08	0.06	0.07	0.04	0.06	0.10	0.11	0.04	0.04
Total	100.07	99.74	100.58	99.89	99.80	100.51	99.76	99.99	101.01	100.30	99.96	100.10
Mg#	0.906	0.908	0.907	0.906	0.912	0.905	0.9134	0.9021	0.908	0.912	0.912	0.911
Clinopyroxenes												
SiO_2	52.84	52.82	53.40	53.65	53.09	52.90	51.97		52.54		53.70	53.72
TiO_2	0.64	0.43	0.57	0.39	0.50	0.43	0.36		0.51		0.10	0.17
Al_2O_3	4.94	4.83	4.77	4.19	4.50	4.02	4.88		6.66		4.38	3.89
Cr_2O_3	1.04	0.97	0.92	0.95	1.06	0.98	0.90		0.67		0.81	0.80
FeO*	2.53	2.49	2.71	2.82	2.44	2.77	3.09		2.71		2.30	2.34
MnO	0.05	0.06	0.08	0.08	0.08	0.10	0.14		0.13		0.08	0.06
MgO	15.01	15.31	15.32	15.95	15.61	15.78	15.98		14.59		15.90	16.23
CaO	20.47	20.42	20.51	20.57	20.43	20.53	20.46		20.23		21.79	22.02
Na_2O	1.73	1.77	1.80	1.52	1.59	1.53	1.16		1.79		0.99	0.92
K_2O	0.00	0.00	0.00	0.01	0.01	0.01	0.00		0.00		0.00	0.00
Total	99.26	99.09	100.08	100.14	99.30	99.03	98.95		99.82		100.06	100.14
Mg#	0.914	0.916	0.910	0.910	0.919	0.910	0.902		0.906		0.925	0.925
Garnets												
SiO_2	41.58	42.33	41.92	41.70	41.19	41.72	41.65		42.41		41.50	41.47
TiO_2	0.11	0.09	0.12	0.13	0.12	0.11	0.09		0.14		0.03	0.04
Al_2O_3	22.85	22.75	22.51	22.83	22.73	22.53	22.46		22.74		23.40	23.37
Cr_2O_3	1.18	1.38	1.29	1.31	1.42	1.60	1.56		1.07		1.02	1.20
FeO*	8.55	8.23	8.42	8.19	7.99	8.18	7.77		8.41		7.74	7.78
MnO	0.41	0.34	0.36	0.35	0.41	0.35	0.41		0.35		0.42	0.45
MgO	19.66	20.35	19.89	20.08	20.12	20.25	20.18		20.11		20.20	19.59
CaO	5.05	4.71	4.83	4.99	5.06	5.14	5.41		4.89		5.33	5.57
Na_2O	0.01	0.02	0.01	0.01	0.02	0.03	0.02		0.04		0.02	0.01
Total	99.39	100.20	99.35	99.59	99.07	99.91	99.55		100.15		99.65	99.48
Mg#	0.804	0.815	0.808	0.814	0.818	0.815	0.822		0.810		0.823	0.818
Spinels												
SiO_2	0.04	0.01	0.05	0.03	0.03	-	0.03		0.02		0.04	0.05
TiO_2	0.85	0.63	0.72	0.67	0.66	-	0.19		0.60		0.01	0.16
Al_2O_3	35.06	35.91	35.91	34.92	36.88	-	37.10		34.67		53.60	43.39
Cr_2O_3	30.65	30.80	29.86	31.11	29.88	-	28.72		30.93		13.79	23.95
Fe_2O_3	4.38	3.57	4.76	5.19	3.01	-	4.64		4.57		2.36	3.66
FeO	13.26	12.58	12.46	12.64	13.02	-	11.35		12.90		9.45	11.11
MnO	0.18	0.19	0.23	0.20	0.21	-	0.23		0.25		0.14	0.16
NiO	0.24	0.23	0.25	0.30	0.24	-	0.27		0.23		0.29	0.30
MgO	16.33	16.63	16.85	16.71	16.42	-	17.05		16.19		19.97	18.16
Total	101.01	100.54	101.09	101.75	100.34	-	99.57		100.36		99.65	100.94
Mg#	0.687	0.702	0.707	0.702	0.692	-	0.728		0.691		0.790	0.744
Cr#	0.370	0.365	0.358	0.374	0.352		0.342		0.374		0.147	0.270

Table 3-6. Continued

	Garnet-Spinel lherzolite (GSL)												
	Amphibole-rich						Carbonatized						
	SAG4	SAG5	SAG6	SAG8	SAG22	SAE131	SAG11		SAG18	SAG23	SAG25	SAG26	SAE123
Olivines													
SiO_2	41.40	-	41.52	41.14	41.00	40.75	41.91		41.65	41.64	-	-	-
FeO	10.26	-	10.48	10.48	11.07	10.39	9.63		9.35	9.65	-	-	-
MnO	0.11	-	0.14	0.14	0.15	0.11	0.11		0.13	0.12	-	-	-
NiO	0.36	-	0.39	0.43	0.32	0.39	0.39		0.39	0.33	-	-	-
MgO	48.85	-	49.26	48.37	48.48	49.37	49.54		50.10	49.27	-	-	-
CaO	0.03	-	0.03	0.03	0.03	0.03	0.02		0.04	0.02	-	-	-
Total	101.02	-	101.81	100.58	101.05	101.03	101.59		101.66	101.03	-	-	-
	0.895		0.893	0.892	0.886	0.894	0.902		0.905	0.901			
Orthopyroxenes							core	rim					
SiO_2	56.75	56.80	56.48	56.36	56.01	56.47	55.89	57.00	56.57	56.64	56.32	56.45	57.22
TiO_2	0.15	0.15	0.15	0.14	0.11	0.11	0.17	0.14	0.11	0.03	0.10	0.04	0.07
Al_2O_3	2.61	2.64	2.64	2.66	2.55	2.64	4.14	2.75	2.60	2.55	2.68	2.65	2.64
Cr_2O_3	0.37	0.37	0.42	0.45	0.31	0.40	0.45	0.44	0.54	0.36	0.47	0.54	0.42
FeO*	6.35	6.11	6.59	6.54	6.84	6.52	6.17	6.00	5.92	6.11	6.04	5.63	5.78
MnO	0.12	0.14	0.14	0.13	0.16	0.14	0.11	0.12	0.08	0.15	0.11	0.13	0.13
NiO	0.06	0.11	0.08	0.10	0.06	0.08	0.13	0.08	0.08	0.13	0.13	0.12	0.07
MgO	33.33	33.37	33.50	33.08	33.22	33.45	32.93	33.45	33.57	33.55	33.92	33.85	33.58
CaO	0.55	0.50	0.60	0.56	0.50	0.53	0.45	0.46	0.58	0.46	0.52	0.62	0.56
Na_2O	0.08	0.09	0.08	0.09	0.06	0.05	0.09	0.08	0.07	0.04	0.09	0.06	0.09
Total	100.38	100.29	100.67	100.10	99.82	100.38	100.53	100.53	100.11	100.02	100.38	100.08	100.55
Mg#	0.903	0.907	0.901	0.900	0.896	0.901	0.9049	0.9086	0.910	0.907	0.909	0.915	0.912
Clinopyroxenes													
SiO_2	53.76	53.53	53.69	53.46	53.48	53.44	53.15		53.45	54.31	53.62	54.00	53.72
TiO_2	0.39	0.40	0.42	0.40	0.25	0.45	0.58		0.30	0.11	0.38	0.09	0.29
Al_2O_3	4.24	4.59	4.20	4.12	4.02	4.39	5.77		3.92	3.04	4.71	2.65	5.01
Cr_2O_3	1.01	1.05	1.07	1.19	0.79	1.02	0.87		1.19	0.72	1.20	0.88	0.94
FeO*	2.87	2.73	3.05	2.99	3.06	2.85	2.48		2.67	2.52	2.72	2.27	2.70
MnO	0.08	0.07	0.10	0.09	0.10	0.07	0.08		0.09	0.10	0.09	0.08	0.07
MgO	15.77	15.44	15.84	15.62	15.77	15.53	14.88		15.96	16.68	15.03	17.37	15.49
CaO	20.56	20.42	20.56	20.33	20.34	20.36	20.24		20.50	22.41	20.09	22.03	20.13
Na_2O	1.51	1.71	1.56	1.55	1.45	1.56	1.83		1.42	0.78	1.89	0.57	1.74
K_2O	0.00	0.01	0.01	0.00	0.00	0.01	0.01		0.00	0.00	0.00	0.02	0.02
Total	100.18	99.96	100.49	99.75	99.24	99.66	99.90		99.50	100.66	99.75	99.95	100.10
Mg#	0.907	0.910	0.903	0.903	0.902	0.907	0.914		0.914	0.922	0.908	0.932	0.911
Garnets													
SiO_2	41.92	42.06	41.74	41.55	42.18	41.62	42.16		41.54	41.78	41.82	41.24	41.32
TiO_2	0.11	0.09	0.11	0.15	0.04	0.09	0.09		0.09	0.02	0.11	0.04	0.08
Al_2O_3	22.79	23.02	22.52	21.89	22.94	22.75	23.21		21.89	22.54	22.75	21.65	22.88
Cr_2O_3	1.48	1.33	1.79	1.79	1.19	1.33	1.14		1.93	1.59	1.41	2.89	1.42
FeO*	8.61	8.27	8.68	8.61	9.25	8.46	8.41		7.87	8.31	8.25	6.84	7.72
MnO	0.39	0.37	0.42	0.40	0.56	0.40	0.41		0.37	0.42	0.42	0.38	0.38
MgO	19.62	19.77	19.80	19.22	19.42	19.65	19.83		19.91	19.62	20.33	20.10	20.35
CaO	5.18	5.06	5.35	5.24	5.07	5.03	4.86		5.31	5.73	5.05	6.16	5.02
Na_2O	0.02	0.03	0.01	0.01	0.02	0.01	0.02		0.02	0.01	0.02	0.01	0.02
Total	100.14	100.00	100.42	98.86	100.67	99.34	100.12		98.92	100.03	100.17	99.31	99.18
Mg#	0.802	0.810	0.803	0.799	0.789	0.806	0.808		0.819	0.808	0.814	0.840	0.825
Spinels													
SiO_2	0.05	0.04	-	0.04	0.01	0.06	-		0.05	0.03	0.03	-	0.08
TiO_2	0.91	0.64	-	0.98	0.26	0.47	-		0.65	0.15	0.32	-	0.43
Al_2O_3	32.13	35.64	-	30.16	33.52	36.18	-		30.54	36.63	42.42	-	32.41
Cr_2O_3	32.92	30.40	-	33.51	31.42	29.55	-		34.55	28.80	23.74	-	33.37
Fe_2O_3	4.44	4.70	-	5.98	5.96	5.17	-		5.21	5.68	4.03	-	4.10
FeO	14.17	12.98	-	14.11	13.80	13.50	-		12.52	12.09	10.90	-	13.00
MnO	0.22	0.22	-	0.26	0.22	0.24	-		0.22	0.21	0.19	-	0.26
NiO	0.20	0.19	-	0.22	0.16	0.25	-		0.21	0.26	0.29	-	0.23
MgO	15.34	16.52	-	15.18	15.41	16.16	-		16.02	16.70	18.07	-	15.68
Total	100.39	101.32	-	100.43	100.77	101.58	-		99.98	100.55	99.99	-	99.57
Mg#	0.659	0.694	-	0.657	0.666	0.681	-		0.695	0.711	0.747	-	0.683
	0.407	0.364		0.427	0.386	0.354			0.431	0.345	0.273		0.409

Total Fe as FeO; Mg#=Mg/(Mg+Fe), Fe^{3+} in spinel estimated from the stoichiometric method; Cr#=Cr/(Cr+Al)

Table 3-7. Major element compositions of olivines, orthopyroxenes, clinopyroxenes and spinels in LT-type spinel lherzolite and harzburgite (SL-SH).

	Spinel lherzolite-harzburgite (SL-SH)																									
	SAS2	SAS3	SAS4	SAS5	SAS6	SAS10	SAS13	SAS14	SAS15	SAS16	SAS17	SAS18	SAS19	SAS20	SAS22	SAS23	SAS24	SAS25	SAS26	SAS27	SAS28	SAS29	SAS30	SAS31	SAS32	SAS33	SAS34
Olivines																											
SiO2	40.92	40.59	40.87	-	-	-	40.14	41.19	40.94	41.83	40.97	41.17	41.06	41.16	41.04	41.15	41.05	41.38	40.81	40.38	40.50	40.11	40.94	41.25	41.38	41.21	41.08
FeO	8.28	8.17	9.79	-	-	-	9.93	7.88	8.95	7.89	9.85	9.68	9.10	7.80	8.01	10.45	9.04	8.02	8.92	10.45	8.89	8.75	7.84	10.05	9.91	9.64	9.96
MnO	0.12	0.09	0.14	-	-	-	0.13	0.10	0.10	0.16	0.12	0.15	0.15	0.15	0.11	0.15	0.17	0.14	0.13	0.15	0.13	0.12	0.12	0.15	0.09	0.11	0.12
NiO	0.38	0.42	0.39	-	-	-	0.38	0.38	0.43	0.47	0.42	0.40	0.41	0.35	0.45	0.37	0.32	0.43	0.39	0.37	0.46	0.40	0.42	0.34	0.37	0.36	0.38
MgO	50.31	50.87	48.96	-	-	-	49.09	50.46	50.52	50.51	49.47	49.40	49.87	50.60	50.97	48.74	49.74	51.05	49.16	48.81	50.60	50.00	50.14	49.56	49.13	49.57	49.09
CaO	0.02	0.01	0.03	-	-	-	0.03	0.04	0.03	0.05	0.04	0.00	0.01	0.03	0.03	0.03	0.04	0.04	0.01	0.03	0.00	0.02	0.04	0.03	0.00	0.00	0.00
Total	100.03	100.15	100.18	-	-	-	99.70	100.04	100.96	100.91	100.88	100.80	100.59	100.09	100.60	100.89	100.36	101.06	99.43	100.18	100.58	99.40	99.50	101.38	100.88	100.89	100.62
Mg#	0.915	0.917	0.899	-	-	-	0.898	0.919	0.910	0.919	0.900	0.901	0.907	0.920	0.919	0.893	0.907	0.919	0.908	0.893	0.910	0.911	0.919	0.898	0.898	0.902	0.898
Orthopyroxenes																											
SiO2	56.00	56.60	56.16	55.27	55.50	55.72	55.32	56.63	55.91	56.82	55.82	55.21	55.73	57.31	56.52	55.69	56.46	56.30	55.41	56.05	55.86	55.40	55.87	55.56	55.05	54.94	55.35
TiO2	0.17	0.09	0.16	0.10	0.13	0.20	0.09	0.08	0.03	0.04	0.15	0.10	0.00	0.10	0.03	0.05	0.02	0.02	0.03	0.05	0.02	0.01	0.02	0.11	0.13	0.11	0.11
Al2O3	2.89	3.13	4.04	4.33	4.32	3.88	4.26	3.08	3.86	3.14	4.33	4.75	4.21	2.37	2.22	3.56	3.84	3.35	4.28	2.73	3.07	3.76	3.17	4.21	4.72	4.74	4.76
Cr2O3	0.61	0.59	0.31	0.26	0.29	0.44	0.23	0.54	0.37	0.64	0.41	0.48	0.54	0.57	0.53	0.47	0.25	0.63	0.53	0.35	0.37	0.36	0.65	0.25	0.38	0.28	0.32
FeO*	5.30	5.28	6.23	6.21	6.43	6.15	6.28	5.03	5.75	4.94	6.06	6.08	5.96	4.80	5.02	6.40	5.93	4.97	5.93	6.67	5.77	5.67	5.00	6.32	6.23	6.34	6.17
MnO	0.15	0.13	0.12	0.15	0.17	0.15	0.08	0.10	0.17	0.08	0.16	0.13	0.18	0.12	0.13	0.14	0.18	0.15	0.14	0.16	0.15	0.22	0.12	0.17	0.14	0.14	0.18
NiO	0.06	0.08	0.06	0.05	0.11	0.09	0.07	0.10	0.09	0.14	0.10	0.06	0.04	0.03	0.09	0.08	0.05	0.14	0.09	0.07	0.08	0.04	0.10	0.04	0.10	0.05	0.10
MgO	33.90	34.23	33.26	32.89	32.75	33.14	33.10	34.12	33.55	33.92	32.96	33.14	33.02	34.16	34.98	32.98	33.87	33.93	33.33	32.89	34.25	33.72	33.63	33.50	33.04	33.19	33.05
CaO	0.54	0.60	0.45	0.46	0.47	0.48	0.45	0.61	0.49	0.60	0.48	0.62	0.40	0.56	0.51	0.54	0.42	0.67	0.43	0.45	0.30	0.56	0.64	0.39	0.48	0.40	0.45
Na2O	0.12	0.07	0.05	0.05	0.05	0.06	0.06	0.08	0.09	0.08	0.09	0.01	0.01	0.14	0.01	0.09	0.03	0.05	0.01	0.08	0.01	0.03	0.10	0.04	0.06	0.05	0.05
Total	99.72	100.81	100.82	99.78	100.21	100.31	99.95	100.35	100.31	100.39	100.57	100.59	100.08	100.16	100.02	100.01	101.05	100.19	100.19	99.50	99.87	99.77	99.31	100.59	100.34	100.24	100.54
Mg#	0.919	0.920	0.905	0.904	0.901	0.906	0.904	0.924	0.912	0.925	0.906	0.907	0.908	0.927	0.925	0.902	0.911	0.924	0.909	0.898	0.914	0.914	0.923	0.904	0.904	0.903	0.905
Clinopyroxenes																											
SiO2	53.05	53.59	52.69	53.24	52.69	52.70	52.14	53.11	52.78	53.82	52.99	52.63	52.80	54.00	54.37	53.33	52.52	53.65	52.42	54.06	53.40	53.04	53.64	52.66	52.30	52.60	51.88
TiO2	0.61	0.18	0.50	0.48	0.49	0.76	0.41	0.08	0.22	0.04	0.52	0.27	0.10	0.35	0.02	0.14	0.11	0.00	0.07	0.10	0.07	0.12	0.05	0.48	0.45	0.47	0.48
Al2O3	4.92	4.00	6.12	5.76	6.48	5.52	6.27	3.80	5.58	4.07	5.87	6.05	4.37	3.89	1.75	4.65	5.13	3.91	4.52	2.92	3.26	4.37	3.87	6.34	6.50	6.15	6.37
Cr2O3	1.53	1.15	0.78	0.68	0.74	0.91	0.65	1.15	0.98	1.20	0.75	0.86	0.82	1.49	0.60	0.96	0.73	1.06	0.86	0.78	0.60	0.72	1.18	0.62	0.84	0.73	0.64
FeO*	2.48	2.37	2.34	2.35	2.45	2.45	2.61	2.18	2.38	2.21	2.33	2.12	1.95	2.14	1.56	2.83	2.18	2.25	1.99	3.02	1.88	2.49	2.23	2.57	2.41	2.38	2.45
MnO	0.10	0.08	0.08	0.08	0.10	0.07	0.09	0.08	0.10	0.06	0.06	0.08	0.07	0.10	0.08	0.08	0.08	0.09	0.08	0.10	0.07	0.08	0.08	0.09	0.10	0.09	0.11
MgO	15.29	16.27	14.61	14.96	14.60	14.88	14.79	16.52	15.60	16.29	14.76	14.77	15.78	15.94	17.48	15.36	15.66	16.71	15.66	15.88	16.43	16.12	16.24	14.37	14.64	14.58	14.64
CaO	18.99	20.78	20.53	21.04	20.91	20.85	20.15	21.04	20.96	20.44	20.57	21.65	23.04	19.86	24.11	20.31	21.55	21.08	23.01	20.37	23.06	21.88	20.41	20.77	20.51	21.19	21.23
Na2O	2.07	1.35	1.79	1.49	1.70	1.63	1.64	1.29	1.31	1.40	1.75	1.34	0.68	1.76	0.25	1.59	1.14	1.06	0.67	1.57	0.56	0.92	1.38	1.63	1.70	1.47	1.46
K2O	0.01	0.00	0.01	0.01	0.00	0.02	0.01	0.01	0.00	0.01	0.00	0.02	0.02	0.00	0.01	0.01	0.00	0.00	0.01	0.00	0.01	0.01	0.01	0.01	0.00	0.02	0.02
Total	99.04	99.76	99.43	100.10	100.17	99.78	98.76	99.26	99.91	99.53	99.61	99.78	99.62	99.52	100.22	99.25	99.09	99.80	99.32	98.81	99.33	99.76	99.10	99.54	99.44	99.66	99.28
Mg#	0.916	0.924	0.918	0.919	0.914	0.915	0.910	0.931	0.921	0.929	0.918	0.926	0.935	0.930	0.952	0.906	0.928	0.930	0.933	0.904	0.940	0.920	0.928	0.909	0.916	0.916	0.914
Spinels																											
SiO2	0.05	0.03	0.03	0.05	0.02	0.03	0.05	0.09	0.00	0.04	0.05	0.03	0.01	0.05	0.03	0.06	0.04	0.05	0.02	0.04	0.01	0.04	0.06	0.03	0.03	0.03	0.00
TiO2	1.10	0.31	0.15	0.14	0.13	0.27	0.15	0.15	0.06	0.08	0.22	0.06	0.02	0.81	0.03	0.21	0.07	0.00	0.01	0.35	0.07	0.11	0.07	0.17	0.10	0.12	0.10
Al2O3	30.94	36.31	56.78	58.04	57.85	48.59	58.15	36.86	53.31	36.47	54.94	56.36	50.83	26.71	30.93	42.00	55.15	40.61	52.54	18.63	51.83	49.83	35.54	58.91	57.89	57.38	59.25
Cr2O3	35.35	31.64	10.68	9.25	9.69	18.76	9.00	31.60	14.07	32.50	12.97	12.08	17.28	39.99	38.72	24.18	12.74	28.41	16.10	45.01	15.65	16.33	32.81	8.93	9.80	9.53	8.23
Fe2O3	4.40	4.18	1.91	1.77	1.77	2.88	2.03	3.31	2.95	2.94	1.48	1.22	1.24	4.38	1.90	4.11	1.89	2.96	1.06	7.28	2.07	3.52	3.75	1.70	1.72	1.90	1.58
FeO	12.08	10.51	9.34	9.63	9.73	11.18	9.67	10.38	9.31	10.45	9.98	9.82	11.24	11.89	12.32	13.04	9.71	10.11	11.11	16.68	10.29	9.58	10.49	9.94	9.55	9.43	9.39
MnO	0.23	0.27	0.14	0.10	0.12	0.14	0.15	0.23	0.18	0.22	0.19	0.13	0.14	0.31	0.23	0.20	0.14	0.19	0.14	0.34	0.15	0.18	0.20	0.15	0.13	0.09	0.09
NiO	0.24	0.31	0.28	0.42	0.39	0.30	0.32	0.23	0.37	0.21	0.41	0.32	0.28	0.29	0.17	0.29	0.30	0.24	0.31	0.11	0.26	0.35	0.23	0.46	0.36	0.38	0.41
MgO	16.86	17.93	20.48	20.36	20.31	18.71	20.43	17.98	20.08	17.82	19.91	20.13	18.50	16.16	15.91	16.77	20.10	18.50	18.87	11.92	19.25	19.42	17.72	20.39	20.43	20.32	20.57
Total	101.26	101.48	99.79	99.77	100.04	100.85	99.94	100.81	100.34	100.72	100.14	100.15	99.52	100.58	100.23	100.86	100.14	101.06	100.16	100.35	99.57	99.35	100.86	100.69	100.02	99.19	99.64
Mg#	0.713	0.753	0.796	0.790	0.788	0.749	0.790	0.755	0.794	0.752	0.780	0.785	0.746	0.708	0.697	0.696	0.787	0.765	0.752	0.560	0.769	0.783	0.751	0.785	0.792	0.794	0.796
Cr#	0.434	0.369	0.112	0.097	0.101	0.206	0.094	0.365	0.150	0.374	0.137	0.126	0.186	0.501	0.457	0.279	0.134	0.319	0.171	0.618	0.168	0.180	0.382	0.092	0.102	0.100	0.085

Table 3-7. Continued

	Spinel lherzolite-harzburgite (SL-SH)																										
	SAS35	SAS36	SAS40	SAS41	SAS42	SAS43	SAS45	SAS47	SAS48	SAS49	SAS50	SAS51	SAS52	SAS53	SAS54	SAS56	SAS58	SAS59	SAS61	SAS62	SAS64	SAS65	SAS66	SAS67	SAS68	SAS70	SAS71
Olivines																											
SiO2	41.36	40.56	-	40.71	40.66	40.45	40.80	40.09	40.89	41.16	41.08	40.91	40.58	40.44	40.77	40.51	40.59	40.97	40.72	40.81	41.07	40.92	40.94	40.61	40.63	41.07	-
FeO	9.80	9.13	-	9.02	10.07	9.99	10.00	10.02	9.11	8.13	8.31	9.71	9.98	11.36	9.03	9.92	9.73	8.33	10.13	7.98	9.59	7.64	7.88	9.99	10.08	7.88	-
MnO	0.13	0.10	-	0.16	0.18	0.12	0.13	0.13	0.14	0.10	0.10	0.13	0.13	0.11	0.17	0.16	0.18	0.11	0.10	0.07	0.13	0.08	0.11	0.12	0.05	0.11	-
NiO	0.27	0.34	-	0.37	0.34	0.38	0.35	0.36	0.39	0.38	0.39	0.38	0.38	0.41	0.40	0.35	0.37	0.40	0.42	0.43	0.37	0.46	0.38	0.35	0.36	0.42	-
MgO	48.54	48.10	-	49.03	48.15	48.29	48.36	48.50	48.43	49.67	48.72	48.63	48.58	47.01	49.26	48.38	48.30	49.85	47.94	49.67	48.99	50.29	50.23	47.89	47.94	49.39	-
CaO	0.00	0.04	-	0.02	0.03	0.00	0.03	0.01	0.01	0.07	0.05	0.03	0.00	0.01	0.02	0.01	0.02	0.01	0.01	0.06	0.01	0.04	0.03	0.01	0.02	0.02	-
Total	100.10	98.26	-	99.32	99.43	99.23	99.69	99.11	98.97	99.49	98.64	99.79	99.64	99.32	99.64	99.33	99.19	99.66	99.31	99.02	100.16	99.43	99.56	98.96	99.08	98.89	-
Mg#	0.898	0.904	-	0.906	0.895	0.896	0.896	0.896	0.905	0.916	0.913	0.899	0.897	0.881	0.907	0.897	0.898	0.914	0.894	0.917	0.901	0.921	0.919	0.895	0.895	0.918	-
Orthopyroxenes																											
SiO2	55.25	56.55	56.68	55.84	55.76	55.87	57.45	55.55	55.76	56.62	56.95	57.05	55.01	55.93	55.67	57.82	55.36	55.96	54.77	55.81	55.00	57.00	55.66	56.16	54.87	56.81	54.93
TiO2	0.08	0.14	0.01	0.09	0.14	0.09	0.02	0.15	0.02	0.04	0.06	0.04	0.11	0.16	0.00	0.00	0.04	0.10	0.10	0.01	0.04	0.02	0.01	0.02	0.08	0.07	0.11
Al2O3	4.34	2.60	3.40	4.63	4.66	4.53	2.22	4.96	3.98	3.21	2.53	2.93	4.28	2.43	3.54	1.55	3.33	2.66	5.34	3.25	4.53	2.90	3.04	1.59	4.36	2.57	4.23
Cr2O3	0.26	0.38	0.61	0.48	0.38	0.39	0.33	0.34	0.42	0.57	0.61	0.47	0.31	0.29	0.46	0.27	0.46	0.59	0.38	0.61	0.66	0.53	0.57	0.23	0.24	0.63	0.25
FeO*	6.36	5.93	5.21	5.81	6.50	6.42	6.09	6.55	6.24	5.27	5.15	6.11	6.52	7.11	5.76	5.96	6.10	5.31	6.68	5.14	6.57	4.80	4.94	6.34	6.44	5.05	6.30
MnO	0.16	0.08	0.13	0.17	0.16	0.19	0.14	0.18	0.13	0.12	0.14	0.14	0.15	0.11	0.11	0.13	0.17	0.12	0.09	0.13	0.14	0.10	0.13	0.16	0.15	0.06	0.15
NiO	0.14	0.07	0.10	0.06	0.11	0.09	0.06	0.06	0.06	0.12	0.10	0.08	0.09	0.10	0.10	0.10	0.13	0.10	0.09	0.12	0.09	0.08	0.10	0.10	0.12	0.10	0.14
MgO	32.67	33.57	33.58	33.09	32.54	32.65	33.78	32.37	33.01	33.77	34.15	33.37	33.11	33.32	33.59	34.16	33.59	34.09	32.08	34.03	32.32	34.40	34.64	34.38	33.02	33.65	32.93
CaO	0.40	0.47	0.64	0.45	0.51	0.53	0.46	0.51	0.46	0.60	0.54	0.48	0.49	0.45	0.47	0.46	0.46	0.50	0.70	0.63	0.82	0.55	0.59	0.38	0.43	0.56	0.48
Na2O	0.03	0.05	0.07	0.04	0.03	0.05	0.09	0.04	0.01	0.10	0.14	0.05	0.01	0.05	0.00	0.08	0.05	0.12	0.04	0.09	0.01	0.09	0.09	0.05	0.06	0.13	0.07
Total	99.71	99.84	100.44	100.66	100.78	100.80	100.63	100.71	100.09	100.42	100.38	100.72	100.07	99.95	99.70	100.53	99.69	99.55	100.28	99.82	100.19	100.47	99.77	99.39	99.77	99.62	99.59
Mg#	0.901	0.910	0.920	0.910	0.899	0.901	0.908	0.898	0.904	0.920	0.922	0.907	0.901	0.893	0.912	0.911	0.908	0.920	0.895	0.922	0.898	0.927	0.926	0.906	0.901	0.922	0.903
Clinopyroxenes																											
SiO2	52.28	53.27	54.10	52.98	53.05	52.92	55.09	53.61	53.01	54.57	55.07	53.03	53.26	53.59	54.53	55.51	54.33	54.65	53.21	54.29	51.66	54.72	54.90	55.35	53.23	55.38	53.40
TiO2	0.47	0.55	0.03	0.30	0.39	0.41	0.10	0.40	0.09	0.14	0.39	0.19	0.38	0.45	0.02	0.08	0.14	0.39	0.46	0.22	0.10	0.04	0.05	0.14	0.46	0.29	0.47
Al2O3	6.24	5.04	3.71	5.81	5.89	6.08	3.46	5.65	4.31	3.98	4.08	4.50	6.12	4.39	2.52	2.86	4.00	4.34	6.04	4.40	5.12	3.62	3.94	2.43	6.34	4.07	6.30
Cr2O3	0.61	0.87	1.08	0.81	0.76	0.74	0.85	0.64	0.81	1.11	1.43	0.93	0.80	0.68	0.47	0.75	0.87	1.49	0.73	1.16	1.03	1.03	1.23	0.70	0.74	1.29	0.65
FeO*	2.62	2.59	2.39	2.08	2.53	2.51	2.63	2.41	2.06	2.50	2.45	2.45	2.44	2.98	2.02	2.79	2.45	2.56	2.46	2.44	2.43	2.19	2.29	2.61	2.58	2.44	2.68
MnO	0.09	0.06	0.12	0.08	0.10	0.12	0.10	0.08	0.07	0.09	0.08	0.09	0.08	0.07	0.09	0.08	0.07	0.10	0.04	0.07	0.09	0.07	0.07	0.11	0.08	0.08	0.10
MgO	14.82	15.04	16.90	15.25	14.95	14.96	16.33	15.38	15.96	16.82	16.13	16.20	15.17	15.72	17.06	16.31	16.28	15.72	15.14	16.46	15.56	16.85	16.84	16.92	15.07	16.30	15.14
CaO	21.11	20.28	20.56	20.49	21.23	20.91	20.59	21.26	23.04	19.75	19.00	21.08	21.18	20.40	22.72	20.06	20.94	18.84	21.12	19.72	23.75	20.42	20.10	21.25	20.56	19.22	20.06
Na2O	1.47	1.71	1.09	1.59	1.41	1.35	1.43	1.34	0.69	1.56	2.10	1.24	1.37	1.54	0.45	1.61	1.23	2.19	1.32	1.60	0.27	1.34	1.51	1.16	1.69	1.98	1.76
K2O	0.01	0.00	0.00	0.01	0.00	0.00	0.01	0.01	0.01	0.00	0.00	0.01	0.01	0.00	0.00	0.00	0.00	0.01	0.01	0.01	0.01	0.00	0.01	0.01	0.00	0.02	0.00
Total	99.72	99.41	99.97	99.39	100.30	100.00	100.58	100.78	100.03	100.51	100.74	99.71	100.80	99.81	99.89	100.05	100.30	100.28	100.54	100.37	100.02	100.27	100.94	100.68	100.77	101.07	100.57
Mg#	0.910	0.912	0.926	0.929	0.913	0.914	0.917	0.919	0.933	0.923	0.921	0.922	0.917	0.904	0.938	0.912	0.922	0.916	0.916	0.923	0.919	0.932	0.929	0.920	0.912	0.923	0.910
Spinels																											
SiO2	0.02	0.05	0.06	0.01	0.03	0.01	-	0.02	0.00	0.07	0.05	0.03	0.02	-	0.02	0.02	-	0.04	0.00	0.08	0.00	0.04	0.06	-	0.04	0.05	0.04
TiO2	0.13	0.52	0.01	0.10	0.06	0.11	-	0.14	0.03	0.33	0.95	0.19	0.16	-	0.02	0.20	-	0.84	0.15	0.26	0.03	0.06	0.08	-	0.17	0.79	0.16
Al2O3	58.79	39.26	39.31	54.05	56.10	56.42	-	56.32	50.07	36.95	29.17	40.50	56.05	-	46.26	19.18	-	28.36	57.26	37.23	47.01	34.83	35.09	-	57.64	26.72	57.49
Cr2O3	8.42	27.29	28.01	13.98	11.00	10.83	-	10.74	17.99	30.24	36.84	27.10	10.86	-	21.27	45.54	-	37.80	10.11	29.81	20.23	32.78	32.85	-	9.01	39.58	8.90
Fe2O3	2.57	4.38	4.87	2.10	2.77	2.71	-	2.90	2.46	4.71	5.03	3.61	2.92	-	3.70	7.18	-	5.44	2.42	4.99	2.99	4.85	4.71	-	3.11	5.46	3.61
FeO	9.55	12.18	9.03	8.80	9.25	9.30	-	9.11	10.26	9.76	11.62	12.09	9.23	-	10.15	15.26	-	11.21	9.34	9.36	11.93	9.16	9.48	-	8.91	11.22	8.48
MnO	0.11	0.18	0.19	0.12	0.11	0.14	-	0.13	0.16	0.20	0.26	0.20	0.10	-	0.15	0.33	-	0.25	0.15	0.20	0.24	0.21	0.21	-	0.10	0.25	0.09
NiO	0.40	0.21	0.22	0.36	0.34	0.41	-	0.43	0.36	0.22	0.28	0.26	0.34	-	0.27	0.15	-	0.21	0.41	0.28	0.23	0.23	0.24	-	0.36	0.22	0.42
MgO	20.65	17.40	19.00	20.52	20.46	20.46	-	20.59	19.19	18.54	16.78	17.30	20.55	-	18.99	12.87	-	16.97	20.54	18.73	17.79	18.43	18.36	-	20.94	16.74	21.18
Total	100.64	101.46	100.70	100.03	100.10	100.38	-	100.38	100.50	101.04	100.97	101.28	100.23	-	100.83	100.73	-	101.13	100.38	100.93	100.45	100.58	101.06	-	100.28	101.03	100.37
Mg#	0.794	0.718	0.790	0.806	0.798	0.797	-	0.801	0.769	0.772	0.720	0.718	0.799	-	0.769	0.601	-	0.730	0.797	0.781	0.727	0.782	0.775	-	0.807	0.727	0.817
Cr#	0.088	0.318	0.323	0.148	0.116	0.114	-	0.113	0.194	0.354	0.459	0.310	0.115	-	0.236	0.614	-	0.472	0.106	0.349	0.224	0.387	0.386	-	0.095	0.498	0.094

Total Fe as FeO; Mg#=Mg/(Mg+Fe), Fe^{3+} in spinel estimated from the stoichiometric method; Cr#=Cr/(Cr+Al)

Table 3-8. Bulk rock major and trace element compositions of analyzed xenoliths.

	LT-type garnet pyroxenite					HT-type garnet pyroxenite			Garnet peridotite	
	GW1	GW1	SGC1	SGC2	SGC3	GC	QGC	GO	GL	GL
Sample	SAE134	SAE111	SAE112	SAE115	SAE110	SAE113	SAE116	SAE114	SAG1	SAG2
SiO_2	49.53	50.06	46.45	40.72	45.28	46.17	50.01	49.11	44.71	45.41
TiO_2	0.26	0.38	0.25	0.32	0.07	0.47	0.20	0.44	0.21	0.21
Al_2O_3	7.77	8.47	13.52	14.20	16.77	14.62	10.12	8.39	2.99	3.08
Fe_2O_3	4.54	4.37	5.67	4.58	4.39	8.93	7.42	11.01	8.97	9.06
MnO	0.12	0.12	0.13	0.09	0.11	0.20	0.16	0.18	0.13	0.13
MgO	19.15	19.69	18.66	16.14	18.25	18.84	17.61	27.89	36.56	36.58
CaO	16.40	15.55	13.18	15.94	14.63	9.46	11.66	2.39	4.09	3.60
Na_2O	0.23	0.53	0.61	0.49	0.37	0.74	0.45	0.05	0.03	0.03
K_2O	0.05	n.d.	n.d.	n.d.	n.d.	n.d.	n.d.	n.d.	0.01	0.01
P_2O_5	0.04	0.05	0.07	0.08	0.05	0.05	0.05	0.05	0.07	0.06
total	98.10	99.20	98.54	92.55	99.92	99.50	97.69	99.51	97.78	98.17
Sr	104	60	66	77	36	47	174	21	42	50
Rb	3.0	0.9	0.2	n.d.	0.3	0.6	0.3	0.7	1.8	1.7
Ba	234	61	84	181	154	51	398	265	71	87
Y	6.4	10.1	4.2	10.4	2.3	23.4	7.5	11.0	2.1	2.4
Zr	5.9	18.9	15.1	31.5	0.2	28.0	11.9	13.8	9.1	9.8
Nb	1.1	1.5	0.9	3.8	1.6	0.1	0.1	0.7	2.7	2.8
Ni	320	310	427	294	296	363	121	544	1595	1622

oxides in wt.%; other trace elements in ppm

Table 3-9. Equilibrium pressure and temperature estimates for Malaitan xenoliths.

Peridotite suites	PBK90	TBK90	TEG79
Garnet lherzolite (GL)			
SAG1	30.1	1235	1287
SAG7	30.0	1223	1282
SAG9	32.0	1279	1314
SAG13	30.5	1237	1282
SAG15	32.2	1275	1320
SAG16	32.1	1269	1281
SAG21	33.1	1297	1344
SAG27	33.6	1303	1367
SAG30	33.0	1264	1353
Garnet-spinel lherzolite (GSL)			
SAE123	26.1	1036	1075
SAE131	23.5	993	1098
SAG3	21.8	930	1013
SAG4	25.5	1033	1056
SAG5	25.4	1019	1061
SAG6	23.6	999	1110
SAG8	24.4	1024	1073
SAG10	20.5	910	1031
SAG11	22.3	955	1001
SAG12	22.9	973	1052
SAG14	23.7	993	1068
SAG17	24.7	1012	1043
SAG18	22.5	979	1083
SAG20	23.0	982	1057
SAG22	26.6	1047	1063
SAG23	19.5	938	973
SAG24	22.0	956	1032
SAG25	22.9	990	1117
SAG26	24.5	1003	1083
SAS7	24.5	990	1082
SAS9	-	-	-
SAS11	-	-	-
SAG31	-	-	-
SAS44	-	-	-
SAS55	-	-	-
SAS57	-	-	-
SAS60	-	-	-
PHN3538*	34.3	1186	1172
PHN3539*	30.3	1192	1178
CRN209*	32.4	1341	1411

	TBK90 at 15kb	TBK90 at 25kb	TBK90 at 35kb	TSG91
Spinel harzburgite (HTSH)				
SAS1	1291	1314	1338	962
SAS8	1244	1266	1289	-
SAS21	1160	1180	1200	938
SAS46	1191	1211	1232	1008
SAS63	1231	1254	1277	1068
SAS69	1225	1247	1269	1121
PHN3549B*	1128	1147	1167	-

	TBK90 at 15kb	TBK90 at 25kb	TBK90 at 35kb	TSG91
Spinel lherzolite-harzburgite (SL-SH)				
SAS2	1048	1068	1087	784
SAS3	994	1012	1030	770
SAS4	917	934	951	725
SAS5	934	951	969	-
SAS6	899	916	934	-
SAS10	913	930	948	-
SAS13	976	994	1013	683
SAS14	958	975	992	747
SAS15	976	995	1013	678
SAS16	1025	1043	1062	739
SAS17	928	945	963	686
SAS18	864	880	896	645
SAS19	799	813	828	564
SAS20	1027	1045	1064	795
SAS22	772	786	799	698
SAS23	977	996	1015	710
SAS24	908	925	941	635
SAS25	1017	1035	1053	714
SAS26	789	803	818	553
SAS27	955	974	992	870
SAS28	827	841	856	595
SAS29	934	951	969	686
SAS30	1019	1038	1056	761
SAS31	920	938	956	649
SAS32	938	955	973	690
SAS33	899	916	934	670
SAS34	877	894	911	681
SAS35	907	925	942	694
SAS36	968	987	1005	740
SAS40	1065	1084	1103	-
SAS41	973	990	1008	758
SAS42	926	944	962	794
SAS43	972	990	1009	772
SAS45	1016	1035	1054	-
SAS47	954	971	989	802
SAS48	813	828	843	681
SAS49	1085	1105	1124	848
SAS50	1086	1106	1125	854
SAS51	965	983	1001	742
SAS52	959	977	995	788
SAS53	982	1001	1021	-
SAS54	935	951	968	739
SAS56	1033	1053	1072	897
SAS58	1004	1023	1041	-
SAS59	1076	1096	1115	882
SAS61	966	985	1003	773
SAS62	1082	1101	1120	866
SAS64	788	803	819	631
SAS65	1058	1077	1095	859
SAS66	1076	1095	1113	856
SAS67	988	1006	1024	-
SAS68	970	989	1007	839
SAS70	1091	1111	1130	870
SAS71	1013	1032	1052	-

Pyroxenite suites	PBK90	TBK90	TEG79
Garnet websterite (GW)			
SAE111	24.4	999	987
SAE117	22.4	979	1088
SAE122	17.2	855	963
SAE134	20.1	908	890
SAE138	22.4	982	916
SAE103	24.6	953	1005
SAE106	23.5	947	1003
SAE128	21.7	873	1010
SAE144	25.0	950	1058
SAE102	23.0	867	994
SAE143	20.8	956	1030
SAE145	25.8	951	1075
Spinel-garnet clinoyroxenite (SGC)			
SAE101	24.9	1045	1057
Garnet orthopyroxenite (GO)			
SAE135	34.4	1344	1385
SAE157	34.2	1321	1379
SAE126	33.4	1299	1350
SAE136	32.5	1275	1196
SAE137	32.8	1303	1353
SAE139	34.0	1314	1337
SAX37	34.7	1306	1357
Garnet clinopyroxenite (GC)			
SAE132	35.7	1312	1356

	TEG79 at 15kb	TEG79 at 25kb	TEG79 at 35kb
Olivine-garnet clinopyroxenite			
SAE148	974	1012	1051
Rutile-garnet clinopyroxenite			
SAE156	931	969	1006
Spinel-garnet clinoyroxenite (SGC)			
SAE109	1009	1047	1086
SAE112	1048	1087	1126
SAE124	1037	1076	1115
SAE140	1045	1084	1122
SAE115	1138	1176	1215
SAE118	1040	1077	1115
SAE130	998	1034	1070
SAE146	1028	1067	1105
SAE108	1016	1051	1086
SAE110	1030	1066	1103
SAE142	1037	1074	1111
SAE153	990	1027	1063
SAE104	965	999	1033
SAE125	1156	1194	1232
Garnet-clinopyroxenite (GC)			
SAE107	1281	1329	1376
SAE113	1254	1301	1348
SAE120	1294	1342	1390
SAE147	1259	1306	1353
SAE152	1248	1293	1338
SAE154	1266	1313	1360
SAE133 (MG-MSD inc)	1361	1411	1461
Quartz-garnet clinopyroxenite (QGC)			
SAE116	1254	1300	1346

PBK90 (kb): Brey and Köhler (1990) Al in orthopyroxene barometer
TBK90 (˚C): Brey and Köhler (1990) two-pyroxene solvus thermometer
TEG79 (˚C): Ellis and Green (1979) Fe/Mg exchange between garnet and clinopyroxene thermometer
SG91 (˚C): Sack and Ghiorso (1991) Fe/Mg exchange between spinel and olivine thermometer
* Data sources for PHN and CRN samples are from Nixon and Boyd (1979) and Neal (1985), respectively.

Table 3-10. Microprobe analyses of Ca, Al and Cr contents (ppm) in olivines from representative spinel peridotites from Malaitan xenoliths.

	spinel harzburgite (HTSH)						garnet lherzolite(GL)
	SAS46	SAS63	SAS69	SAS1	SAS8	SAS21	SAG30
No. of analysis	3	3	3	3	3	3	3
Ca (ppm)	632	543	560	706	507	615	493
SD (%)	1	1	3	1	2	4	2
Al (ppm)	56	83	49	108	70	57	61
SD (%)	8	10	3	3	11	14	15
Cr (ppm)	139	164	113	382	95	180	29
SD (%)	34	42	33	9	45	4	102

	spinel lherzoltie-harzburgite (SL-SH)									
	SAS41	SAS42	SAS43	SAS44	SAS45	SAS51	SAS50	SAS49	SAS48	SAS47
No. of analysis	3	3	3	3	3	3	3	3	3	3
Ca (ppm)	50	38	31	132	101	117	103	196	10	34
SD (%)	14	29	71	11	7	9	4	8	43	25
Al (ppm)	4	2	6	10	4	12	18	22	1	1
SD (%)	115	87	65	57	115	33	17	7	173	173
Cr (ppm)	-	-	-	-	-	-	49	35	-	-
SD (%)	-	-	-	-	-	-	46	45	-	-

	SAS52	SAS53	SAS54	SAS55	SAS56	SAS57	SAS64	SAS62	SAS61	SAS60
No. of analysis	3	3	3	3	3	3	3	3	3	3
Ca (ppm)	36	72	69	156	93	151	-	211	29	110
SD (%)	0	10	12	12	13	10	-	7	43	8
Al (ppm)	2	4	2	7	3	7	1	18	5	9
SD (%)	87	87	87	22	100	57	173	17	50	105
Cr (ppm)	-	-	-	-	-	5	-	2	-	-
SD (%)	-	-	-	-	-	173	-	173	-	-

	SAS59	SAS58	SAS65	SAS66	SAS67	SAS68	SAS70	SAG31	SAS22	SAS20
No. of analysis	3	3	3	3	3	3	3	3	2	2
Ca (ppm)	112	122	175	187	77	77	124	146	61	136
SD (%)	10	10	6	7	14	14	12	6	25	15
Al (ppm)	15	3	16	16	6	8	19	10	-	16
SD (%)	10	100	17	76	25	67	21	16	-	24
Cr (ppm)	34	-	18	26	-	-	76	34	-	-
SD (%)	111	-	103	121	-	-	50	92	-	-

	SAS36	SAS31	SAS16	SAS25	SAS17	SAS4	SAS13	SAS24	SAS30
No. of analysis	2	2	2	2	2	2	2	2	2
Ca (ppm)	108	79	190	230	104	93	129	115	205
SD (%)	0	0	3	4	5	11	16	94	2
Al (ppm)	11	4	25	22	3	7	16	4	17
SD (%)	71	47	7	8	141	28	0	50	11
Cr (ppm)	7	-	53	24	36	-	-	-	-
SD (%)	141	-	14	121	61	-	-	-	-

4. REE abundances in clinopyroxene and garnet

Selected REE abundances in clinopyroxenes and garnets (amphiboles in some samples) were analyzed by using Cameca IMS 3f ion mass spectrometer (SIMS) at the Tokyo Institute of Technology. The primary beam of negatively charged oxygen ions with a current of approximately 20 nA and a net energy of 12.5 keV was focused to a spot about 20 micron in diameter. An energy filtering technique with offset voltage of –60 V was achieved to eliminate possible molecular interferences. As a standard material, well-calibrated augite megacryst from alkali basalt in Japan were used for all analyses. Analytical uncertainities originate mainly from counting statistics and are 10-20 %; the details was presented elsewhere (e.g. Wang and Yurimoto, 1994). Most of SIMS analyses were conducted in polished thin sections and separated grain mounts after checking major element chemistry. The results of analyses are shown in Table 4. C1 chondrite normalization values of Sun and McDonough (1989) are used for all REE patterns illustrated in figures.

4-1 LT-type pyroxenites (GW-SGC)

In the case of the major elements, most of clinopyroxene and garnet in GW-SGC are heterogeneous as a result of incomplete metamorphic reactions. This evidence suggests behavior of REE contents accompanying major element zoning must be checked. In representative samples from GW (SAE117) and SGC (SAE104 and SAE125) leaving large heterogeneity, detail investigations have been conducted. Their results are shown as chondrite normalized patterns in Fig. 4-1 and Fig. 4-3. In SAE117, Al-rich core, intermediate mantle and Al-poor rim of single clinopyroxene have essentially same patterns with HREE depletion and difference of concentration is within analytical error. It means that even Al-rich core of clinopyroxene could not preserve their original REE contents before exsolution of garnet with the normal preferential partitioning of HREE. Similar to GW, there are no marked differences between core and rim in heterogeneous clinopyroxenes of SGC (SAE104 and SAE125). In contrast to clinopyroxene, rim compositions of garnets are depleted in HREE relative to those in cores as expected that modal garnet increased with proceeding of metamorphic reaction. However their differences are much smaller than variations of different samples, suggesting that REE homogenizations of GW

and GSL pyroxenites may have been obtained well in single sample scale. They can be verified by comparing their partition coefficients between clinopyroxene and garnet ($D^{clinopyroxene/garnet}$ = D values).

Chondrite-normalized patterns of clinopyroxenes and garnets in GW are shown in Fig 4-1 and their D values are shown in Fig 4-2. Several patterns of clinopyroxenes were obtained but all are characterized by HREE depletions relative to MREE. Their patterns of D values illustrate well-coincidence independent of abundances and pattern-shapes in both phases, indicating that all clinopyroxenes were equilibrated with garnets and different patterns and abundances may reflect difference of bulk concentrations and/or modal proportions of clinopyroxene and garnet between samples. REE patterns of clinopyroxene in GW samples were divided into three groups: lower LREE/HREE group (group1 or GW1), higher LREE/HREE group (group3 or GW3) and selective LREE enrichment group (group2 or GW2). It is noted that each differences may be reflected by their textural variations. GW1 tends to have typical garnet exsolution textures with homogeneous specimens. Their parallel REE patterns observed for both clinopyroxenes and garnets indicate that variation of concentration would be made under garnet-free condition and controlled by original crystallization process before metamorphic process. One of three low concentration samples was originally clinopyroxenite determined by textural observation (SAE134) and consistent with the primary nature of the crystallization process. On the other hand, GW2 and GW3 are characterized by the irregularity of garnet morphology. It is difficult to decide whether garnet is metamorphic origin by textural evidences in most of GW2 and GW3. Highest LREE/HREE ratio and abundances among this group is obtained from clinopyroxene and garnet in rutile bearing garnet clinopyroxenite, showing their unusual nature. Also selected LREE enriched group tends to have irregular morphology of garnets. SAE106 shows obvious modification of original texture and the presence of spinel touching with clinopyroxene against general observation. Their REE characteristics might be invoked by secondary modification.

Chondrite-normalized REE patterns of clinopyroxenes and garnets in SGC are shown in Fig 4-3 and their D values are shown in Fig. 4-4. D values of HREE have relatively large errors associated with low concentrations. Some samples display substantial lowering of D values approximately one order of magnitude for

most elements. Main cause of the changes in the partition coefficients can be attributed to changes of major element compositions. Fig 4-5 shows the correlation between partition coefficients of Nd, Dy and observed ranges of XCa in garnet, Al(4)-fold coordination in clinopyroxenes. These correlations were generally found in the studies of natural garnet and clinopyroxene pairs. Harte and Kirkley (1997) investigated REE concentrations in clinopyroxenes and garnets from Roberts Victor eclogites with a wide range of major element compositions. They suggested that REE incorporates into their structures by YAG-type coupled substitution expressed as $REE^{3+}Al^{[4]}Ca_{-1}Si_{-1}$. Observed systematic changes in partitioning of REE may not be due to temperature differences but changes in Ca abundances similar to those of Roberts Victor eclogite.

The overall characteristics in REE patterns of SGC are revealed by lower HREE abundances than those of GW. Similar to those of GW, REE patterns in garnets and clinopyroxenes correlate with their textures and major element chemistries. SGC has been divided into three groups based on the textural variation: group1 (SGC1) spinel always mounted by garnet, group2 (SGC2) spinel occurs both in garnets and clinopyroxenes and group3 (SGC3) with typical granoblastic texture. SGC1 have higher LREE/HRRE ratios relative to those of GW1 in both garnet and clinopyroxene. While, SGC1 and SGC2 in clinopyroxene display nearly equivalent abundances, however SGC2 garnets tend to represent higher abundances of LREE than SGC1. It is noted that D values of SGC2 tend to be lower than SGC1 according to their major element compositions. Same behavior of LREE/HREE ratios in garnets and clinopyroxenes from single sample means that inferred bulk compositions must have same variations. In Fig 4-6, Ce_N/Er_N are plotted for major element variations (Al_2O_3 in clinopyroxene: CaO in garnet), which reflect bulk chemistries in spite that they modified by subsequent metamorphic reactions. Although observed ranges of Al_2O_3 in clinopyroxenes are very wide in each samples, if only lowest values are attracted from GW1 to SGC2, weak correlation can be detectable (but not from SGC1 to SGC2). Ce_N/Er_N in garnets display strong correlation with observed ranges of CaO. One favorable explanation for their continuous changes of LREE/HREE ratios is that bulk REE abundances of SGC1 and SGC2 were controlled by garnet crystallizing melt. This interpretation is supported by restricted amount of olivine relative to garnet in SGC.

On the other hand, REE patterns and concentrations of SGC3 are problematic because both LREE and HREE abundances are highly depleted in spite of their fractionated mineral assemblages and compositions. In particular, low abundances of LREE cannot be accounted for one sequence of fractionation and later metamorphic reaction unless the presence of LREE-preferred phase is reminded. However, possible candidate such as apatite was never found in SGC3 in spite of detailed investigation. On the other hand, there are significant differences in minor element chemistry between SGC2 and SGC3. Fig. 4-7 illustrates correlations between Mg# and Ti concentrations in garnets and clinopyroxenes. Ti concentrations are significantly different between SGC2 and SGC3, suggesting resemblance of Ti and REE behaviors. Presumably, the process that formed their granoblastic textures may have lowered REE and Ti abundances in SGC3.

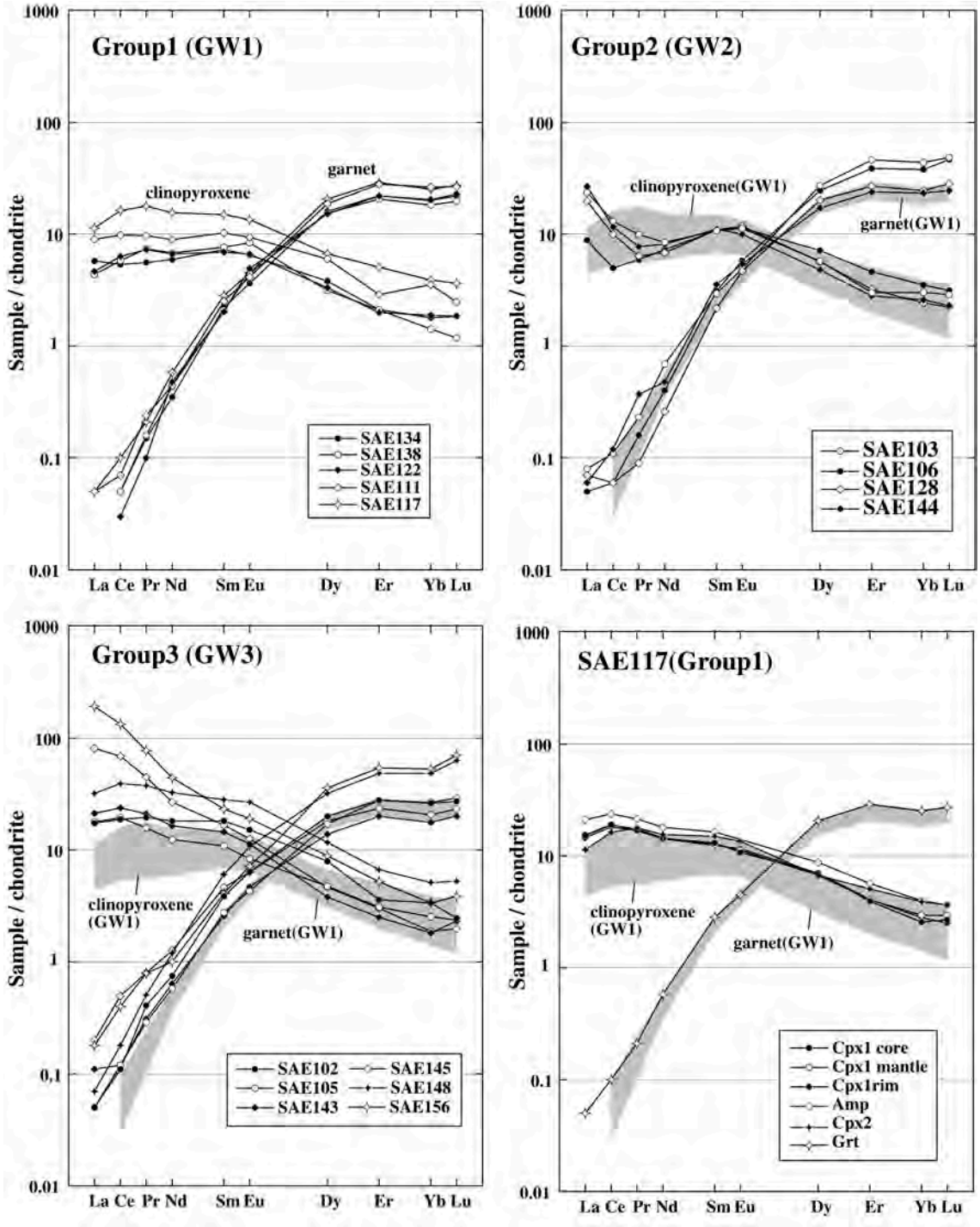

Fig. 4-1. Chondrite-normalized REE patterns of garnets, clinopyroxenes and amphibole (SAE117) from LT-type garnet websterites and garnet clinopyroxenites (GW).

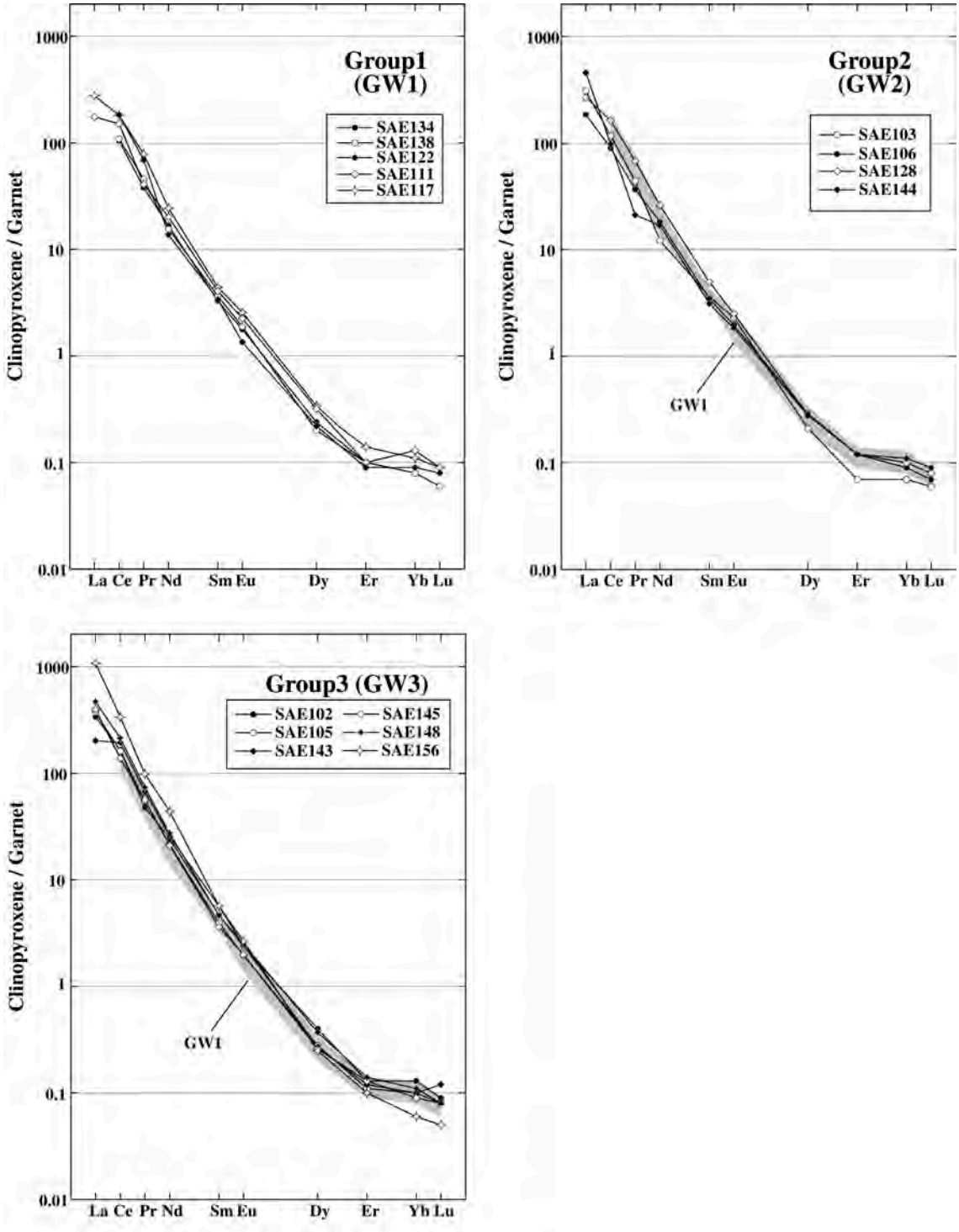

Fig. 4-2. Partitioning of REE between clinopyroxene and garnet (D values) from LT-type garnet websterites and garnet clinopyroxenites (GW).

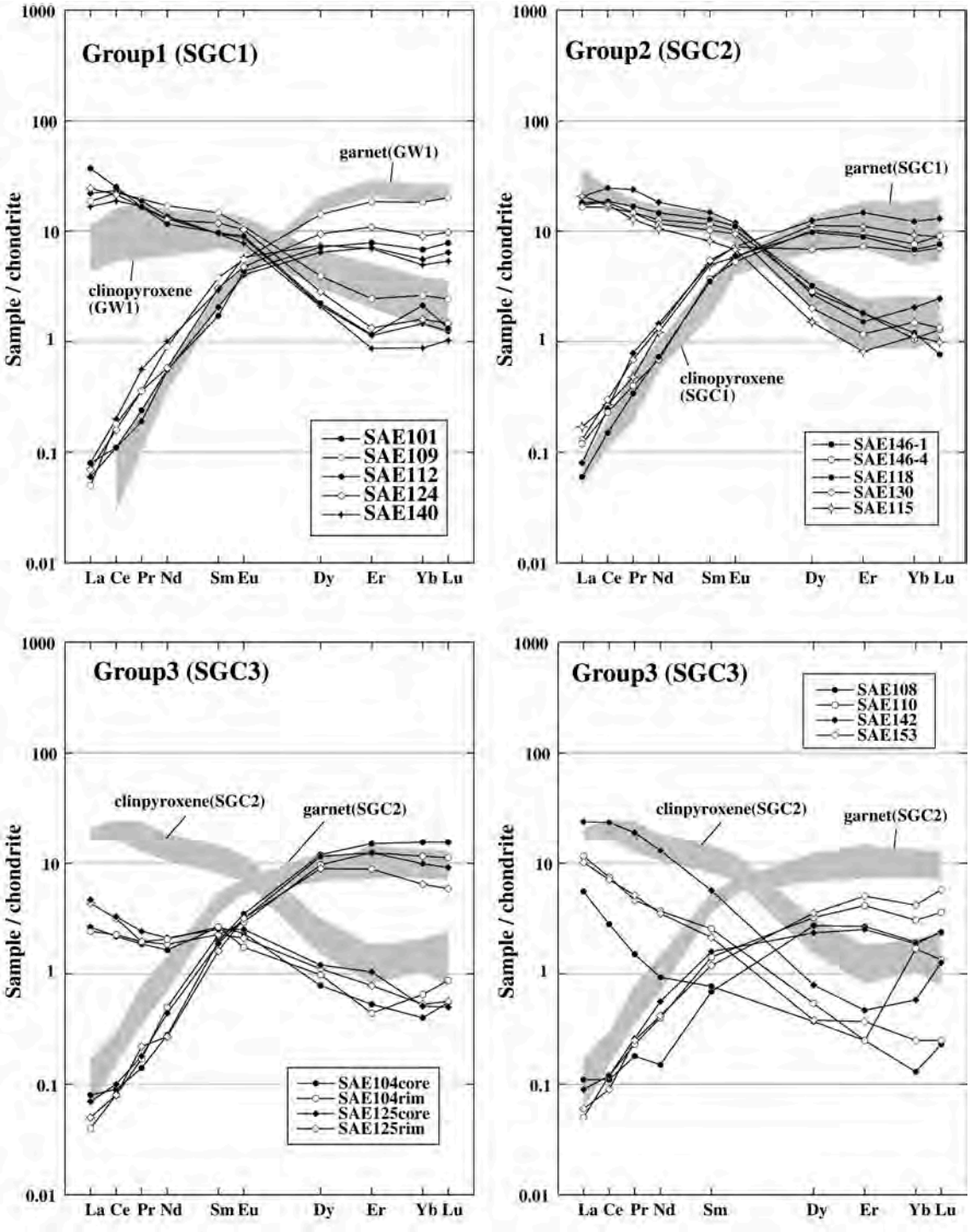

Fig. 4-3. Chondrite-normalized REE patterns of garnets and clinopyroxenes from LT-type spinel garnet clinopyroxenites (SGC).

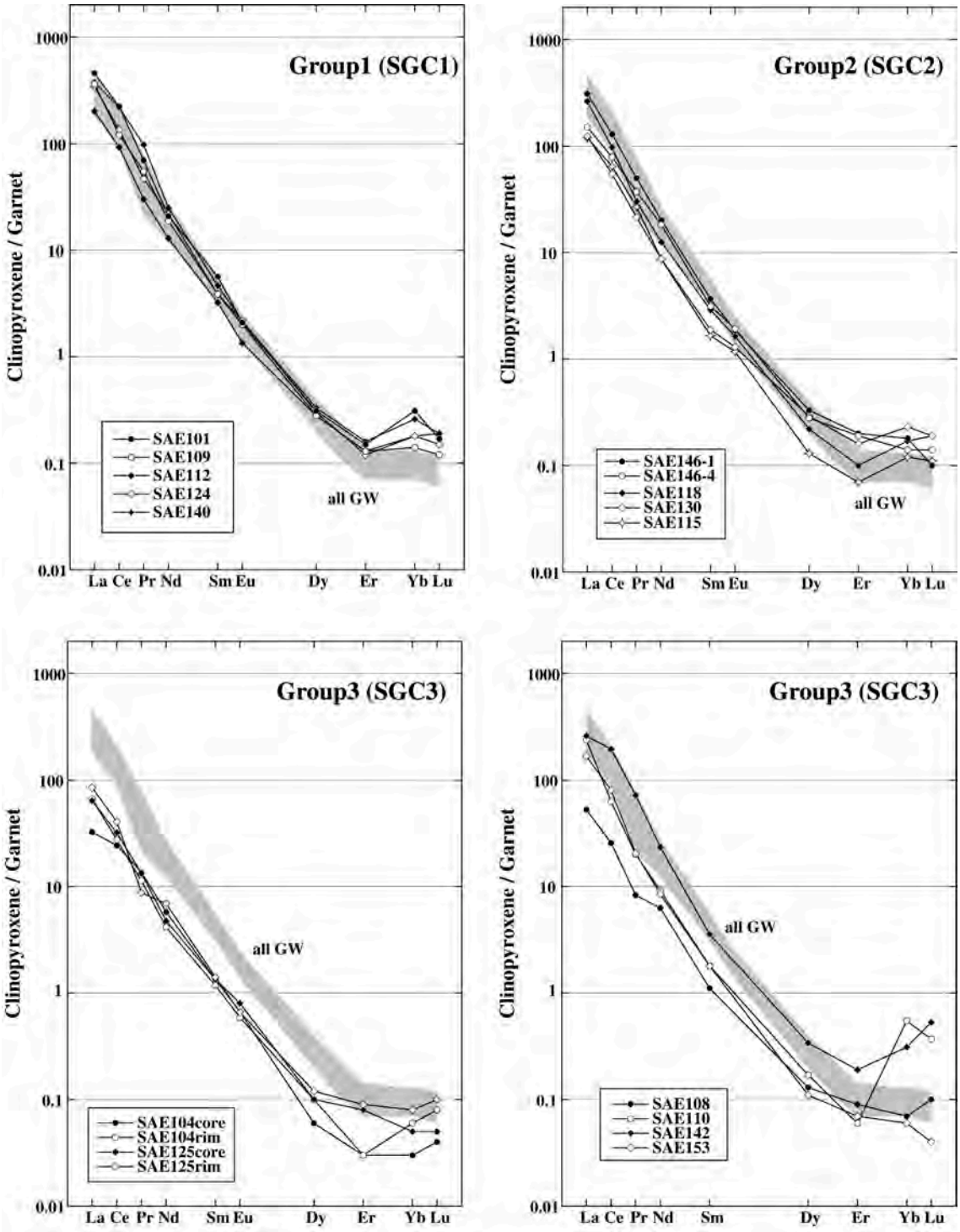

Fig. 4-4. Partitioning of REE between clinopyroxene and garnet (D values) from LT-type spinel garnet clinopyroxenites (GW).

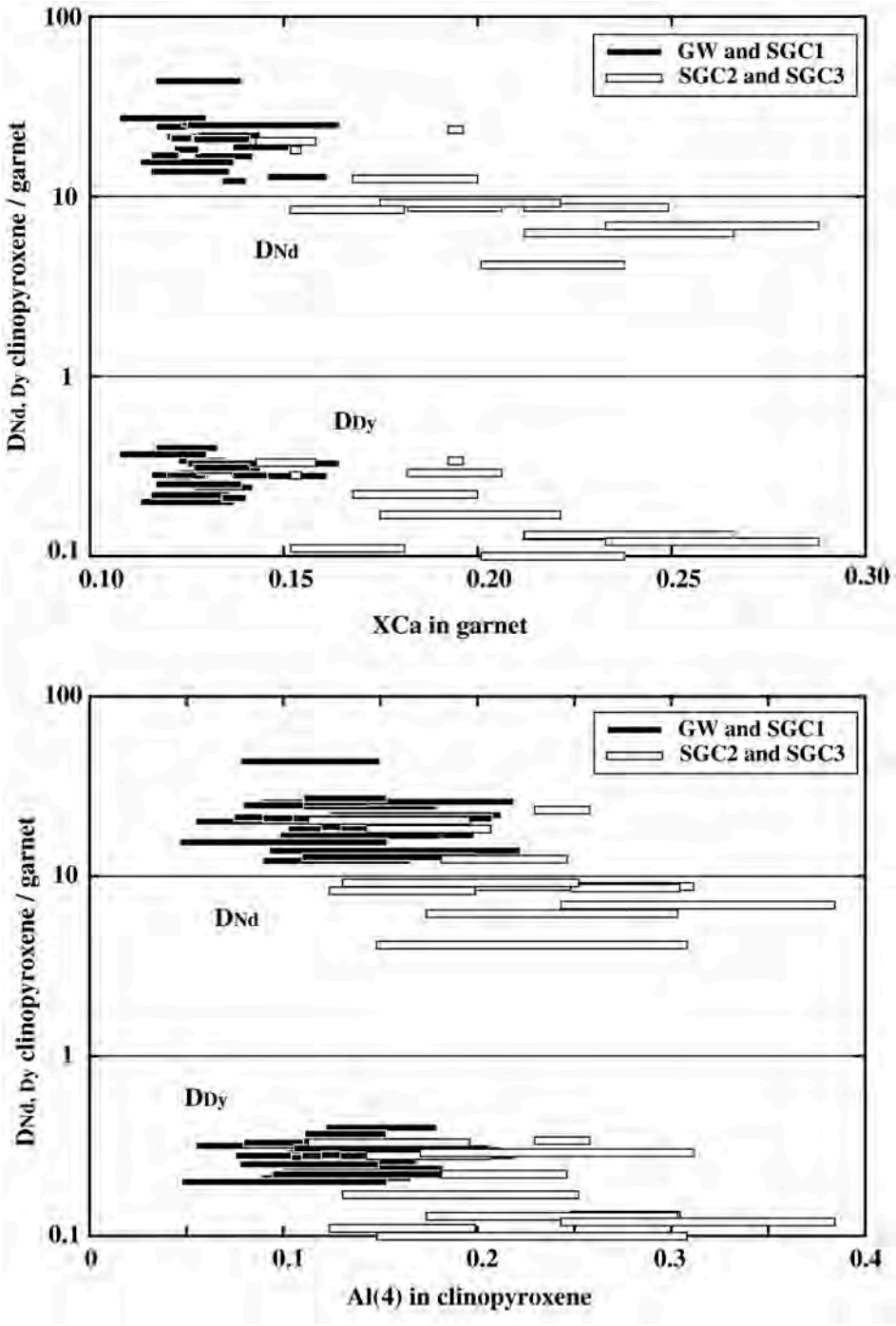

Fig. 4-5. Covariations between $D_{Nd, Dy}$ clinopyroxene / garnet and XCa in garnets (upper), Al(4) in clinopyroxenes (lower) from LT-type garnet websterites (GW) and spinel-garnet clinopyroxenites (SGC).

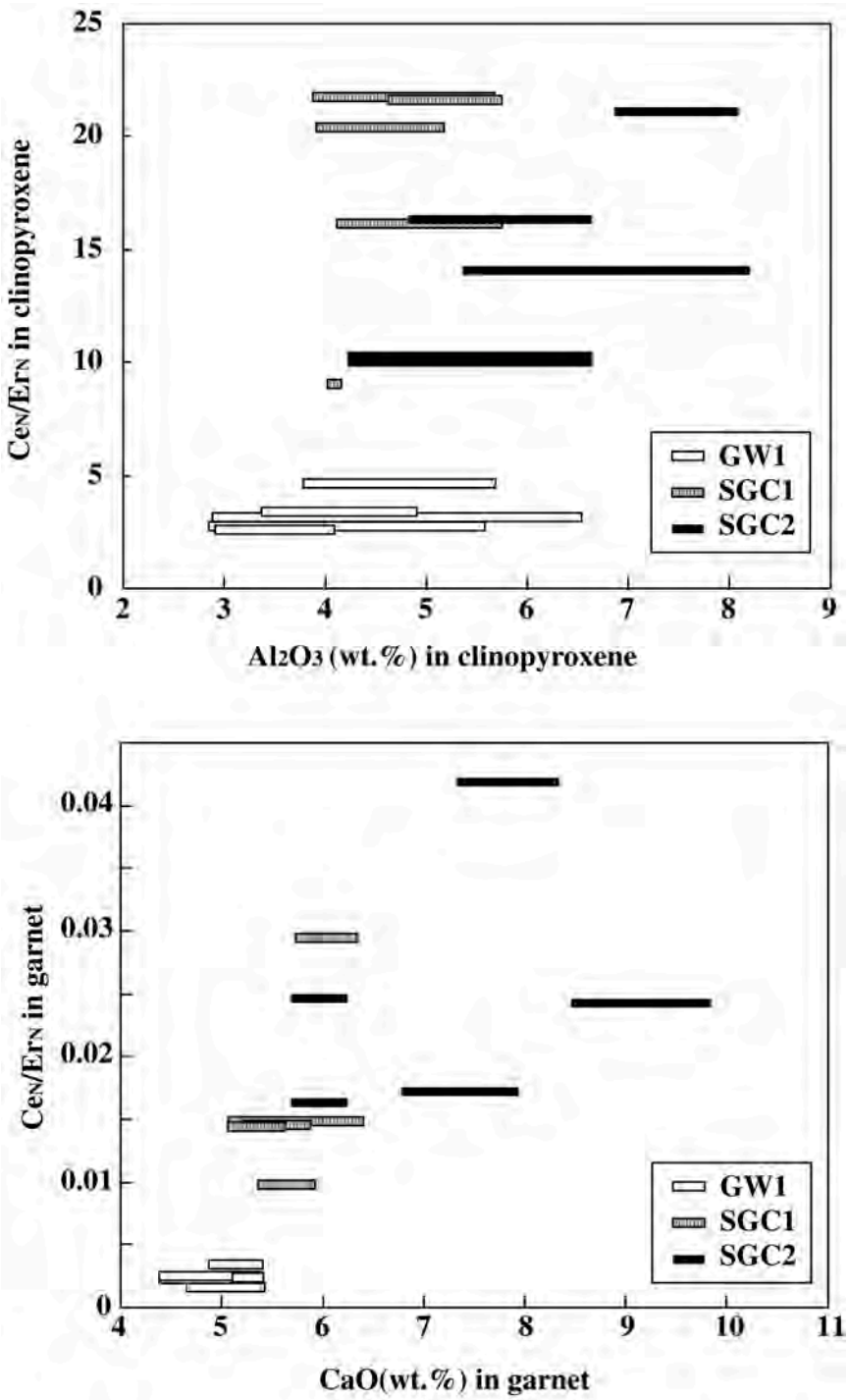

Fig. 4-6. Covariations between Ce_N/Er_N and Al_2O_3 (wt.%) in clinopyroxenes (upper) and Ce_N/Er_N and CaO (wt.%) in garnets (lower) from LT-type garnet websterites (GW) and spinel-garnet clinopyroxenites (SGC).

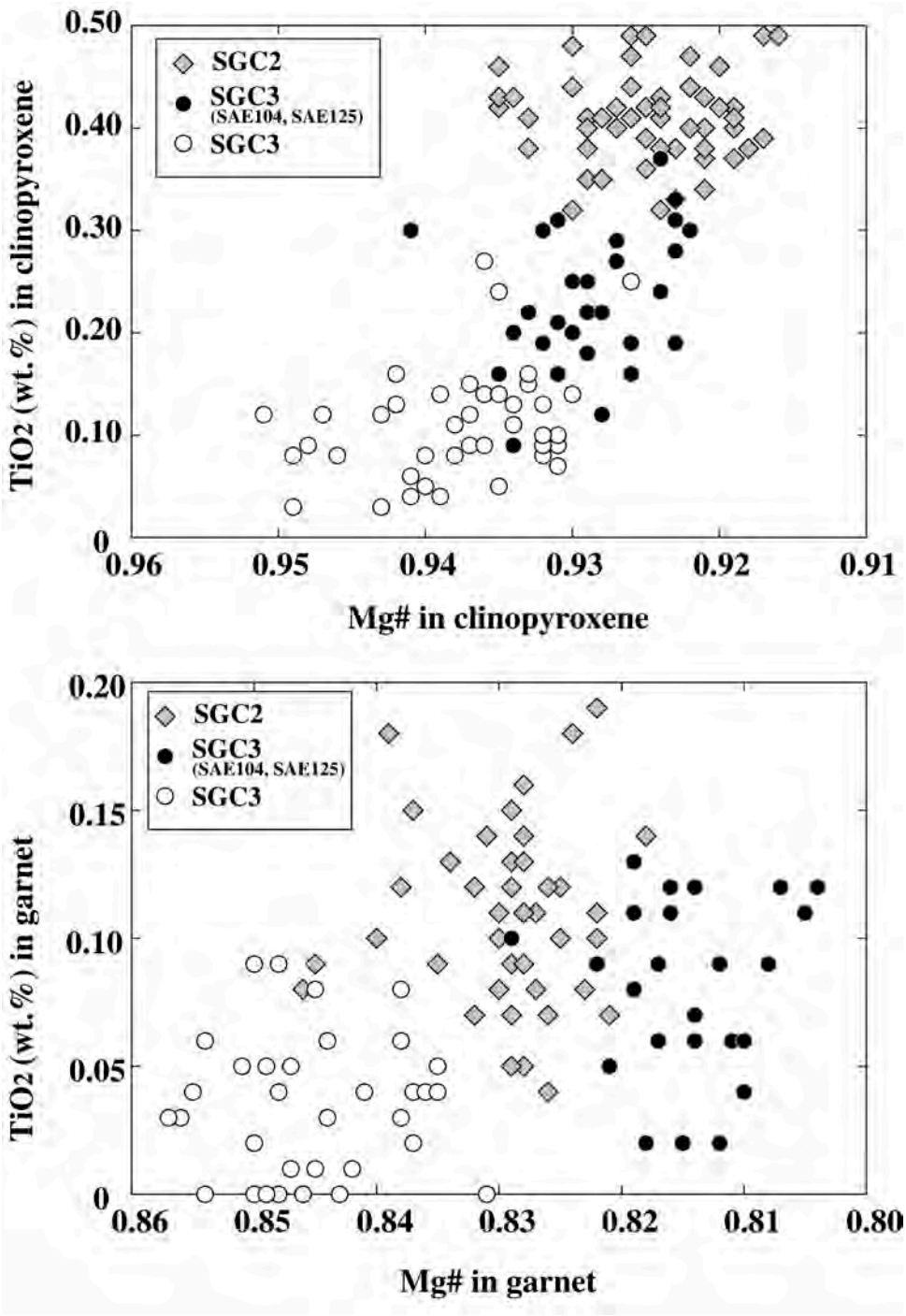

Fig. 4-7. Covariations between Mg#=Mg/(Mg+Fe*) and TiO_2 (wt.%) in clinopyroxenes (upper) and garnets (lower) from LT-type spinel-garnet clinopyroxenite (SGC).

4-2 LT-type peridotites (GSL and SL-SH)

Chondrite-normalized patterns of clinopyroxenes and garnets in GSL are shown in Fig. 4-8 and their D values are shown in Fig. 4-9. They are divided into four subgroups based on petrographical differences: amphibole-free group, amphibole-rich group, carbonate-rich group and garnet-poor group. D values of most GSL display good accordance with those of GW and consistent with their similar mineral chemistries and calculated temperatures. Some D values of carbonated and garnet-poor samples show significant deviation from range of GW. In the case of garnet-poor group, the deviation may be attributed by the presence of substantial heterogeneity. Two analyzed clinopyroxenes from SAS7 have obvious disparity of HREE abundances and suggest that HREE-rich clinopyroxene did not distribute the REE into garnet. SAS9 clinopyroxene without HREE depletions is also owing to imperfect reequilibration with garnet in sample scale. The two patterns without HREE depletions are similar to REE patterns of clinopyroxenes from SL, indicating that they were originally equilibrated in garnet-free assemblage. On the other hand, the deviation observed in D values of SAG26 is very similar to those of SGC, lowering all REE partition coefficients. SAG26 contains unusual Ca-rich garnets. This evidence supports that D values depend on XCa in garnet. Origin of the D value deviations observed in SAE123 and SAG25 remain unknown but may be due to the presence of substantial heterogeneity.

REE patterns of garnets and clinopyroxenes in amphibole-free GSL and amphibole-rich GSL display no systematic difference. Most of garnet and clinopyroxene in both groups have higher LREE abundances and LREE/HREE ratios than those of GW1. However, SAG22 with highest abundance of amphibole (~ 18%), have remarkable high REE concentrations both in garnet and clinopyroxene. SAG23 from carbonate-rich group have also remarkable LREE-enriched patterns and Ce abundance in clinopyroxene exceeds in two orders of magnitude of chondrite abundance. On the other hand, clinopyroxene in carbonate-rich SAG26 is highly depleted in MREE and HREE. Unusual REE behaviors of carbonate-rich GSL are difficult to understand and carbonatization process may have been significantly contributed to change the REE contents of original clinopyroxene and garnet.

REE patterns of clinopyroxenes in SL-SH peridotites are plotted in Fig. 4-10 and compared with the field of abyssal peridotite clinopyroxenes (Johnson et al.

1990). They are divided into mainly three groups based on their Yb abundances and shape of patterns. First group (group1) has clinopyroxene with Yb_N > 11. These patterns are characterized by regulated abundances from Sm to Lu in contrast to variable abundances of LREE. Particularly, La varied from X1 to X100 chondrite. Second group (group2) has clinopyroxene with Yb_N from 12 to 4.8 and can be further subdivided into two subgroups. One subgroup has enriched in LREE and is characterized by typically inflected patterns with minimum Nd_N. Two samples (SAS27 and SAS51) of this subgroup contain the clinopyroxene with the straight patterns, which are constantly elevated from Yb to Ce. Another subgroup has distinctly depleted in LREE and lower Nd/Sm ratio than those in group1. Third group (group3) has clinopyroxene with Yb_N from 4.8 to 2.0 and characterized by high LREE/HREE ratios with typically concave downward shape in the LREE (La_N/Ce_N <1). This group also may be classified into two subgroup based on the difference of Ce/Er ratio. Although they are bounded by factor of 5 for the present, it is not so clear because the difference of Ce/Er ratio and shape of patterns are consecutive. Other six samples (SAS17, SAS36, SAS53, SAS56 and SAS58) have clinopyroxenes with HREE depletion in compared with MREE. These clinopyroxenes may have been affected by crystallization of garnet, which were not found in sample observation. Judging from patterns formed LREE to MREE, these two patterns are similar to group1 clinopyroxenes with higher Yb_N. It is interesting to note that all samples of group3 with lowest Yb_N are harzburgite (modal clinopyroxene < 5%) and most of samples from other two groups are lherzolite (one exception is SAS28). This evidence strongly suggests that HREE abundances reflect their depletion of basaltic components in spite that LREE enrichment processes occurred apparently. Compared with abyssal peridotite clinopyroxenes, their Yb abundances are covered with the fields and some of lowest LREE/HREE samples have very similar patterns. Strong LREE depletions observed in abyssal peridotite clinopyroxenes have referred as the evidence that abyssal peridotites are the residues of near-fractional melting, not batch melting. In Fig. 4-11, the results of model calculations (equations after Johnson et al., 1990) are expressed as chondrite-normalized patterns of residual clinopyroxenes. Partition coefficients, source compositions, mineral proportions in the source and those entering the melts are needed for model calculations. Selected values are listed in table 4-9 and they have

been used for studies of abyssal peridotites recovered from Southwest Indian and American-Antarctic Ridge far from hot spots (Johnson et al., 1990, Johnson and Dick, 1992) and LREE-depleted Hawaiian xenoliths (Yang et al., 1998). The results clearly demonstrate that samples with lower LREE/HREE clinopyroxenes must be formed by near-fractional melting similar to formation of abyssal peridotites. Although the abundances of LREE enriched clinopyroxenes is relatively scarce in abyssal peridotites (Johnson et al. 1990), similar LREE-enriched patterns have been usually found in spinel peridotites obtained as xenolith and from alpine-type peridotites. They have been interpreted as the products resulting from chromatographic-type melt-rock reaction processes (e.g. Navon and Stolper, 1987; Bodinier et al., 1990; Takazawa et al., 1992; Hauri and Hart, 1994; Bedini et al., 1997). In Fig. 4-11, the results of model calculations by Bedini et al. (1997) are illustrated. Bedini et al. (1997) calculated chromatographic fractionation in clinopyroxene of lherzolite and harzburgite in the same parameters except for modal and REE compositions. They suggested that original REE and modal composition of matrix peridotite highly effects whether rocks equilibrate with infiltrating LREE-enriched melt or not. This means that harzburgites easily reach equilibrium with infiltrated melt at lower melt/rock ratio than lherzolite, indicating it is difficult for harzburgite to keep original LREE/HREE ratios under the condition where melt migrates. Group3 harzburgites with higher Ce/Er ratios may represent equilibrium with infiltrated melt. On the other hand, group3 harzburgites with lower Ce/Er ratio were relatively relieved of melt affection and the clinopyroxenes may preserve original HREE abundance formed by former partial melting event.

In Fig. 4-12, Yb_N are plotted with variable chemical parameters, which should reflect the degree of depletion. The covariations with Cr# in spinels, Al content in orthopyroxene and Mg# in olivine display good correlation and make the melting trend as expectation in spite that several samples deviate from the trends. It is noted that two group2 samples with Cr-rich spinel are characterized by high-amphibole abundance, indicating that Cr# in spinels are modified by amphibole formation. The deviations may tend to be strong in Mg#, Na content and Ti content in clinopyroxenes. SAS22 with lowest affection of REE pattern by migrated melt, has highest Mg# and lowest Na content in clinopyroxene. The plots of SAS22 tend to be near the extension of the trend formed by most of group1 and 2. This evidence

suggests that most of Mg#, Na content and some of Ti content of clinopyroxene in harzburgites were modified by later melt percolating process same as REE abundances. Yb abundances in clinopyroxenes may also correlate with temperatures calculated by pyroxene thermometry (Brey and Köhler, 1990). Fig. 4-13 shows the covariation relationships between Yb_N and calculated temperatures at 1.5 GPa. Group1 has the intermediate equilibration temperatures at 900-1000˚C. Group2 is separated into higher temperatures (> 900˚C) and lower temperatures (< 900˚C). This difference corresponds to subdivision determined by LREE enrichment of clinopyroxenes. Most of group3 have the higher equilibration temperatures (from 900 to 1100˚C), however the lowest temperature (< 800˚C) is found in SAS22 harzburgite which has lowest REE abundances, Na content and highest Mg# in clinopyroxene. These evidences indicate that equilibrated temperatures were highly concerned in both depletion and enrichment event.

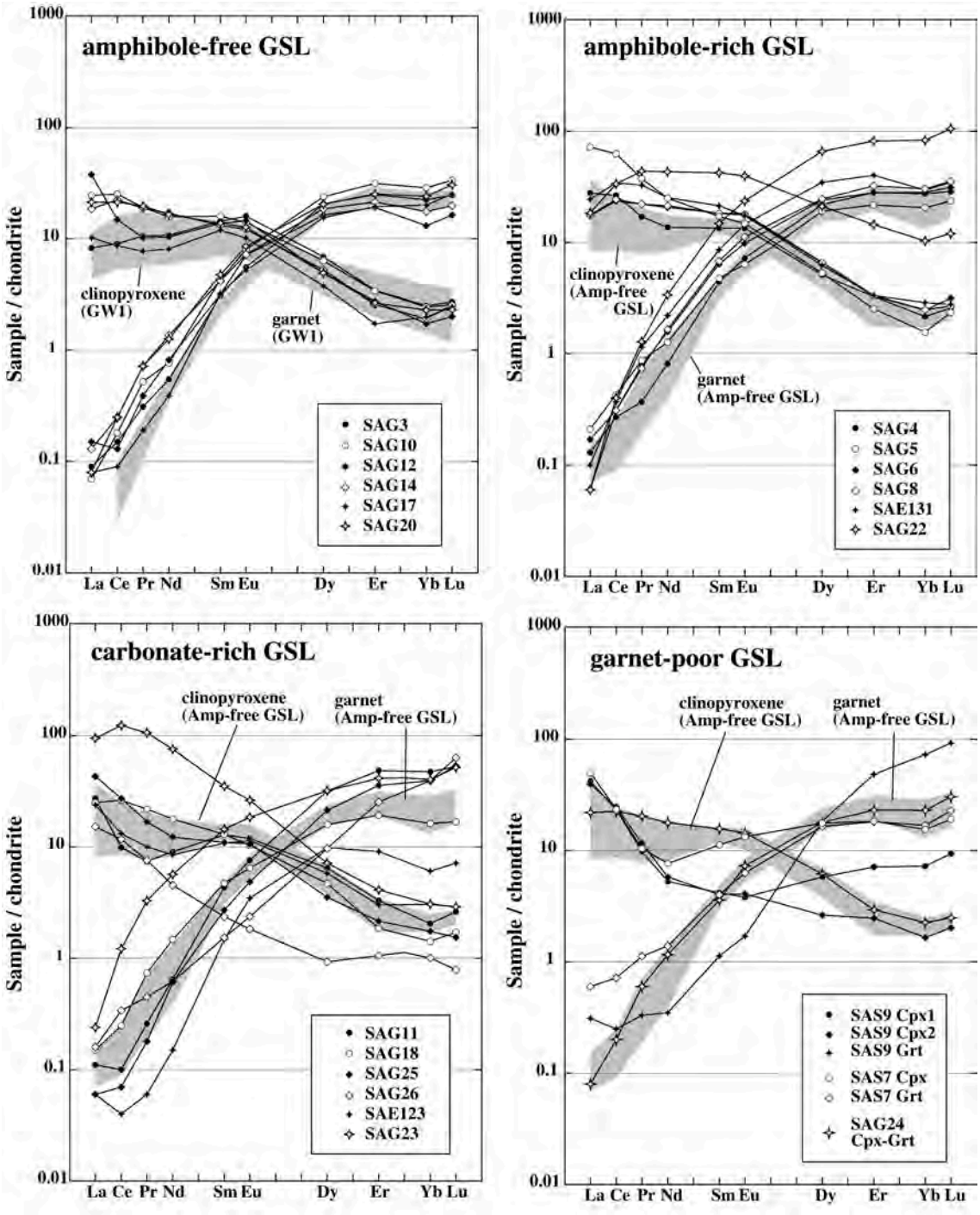

Fig. 4-8. Chondrite-normalized REE patterns of garnets and clinopyroxenes from LT-type garnet-spinel lherzolites (GSL).

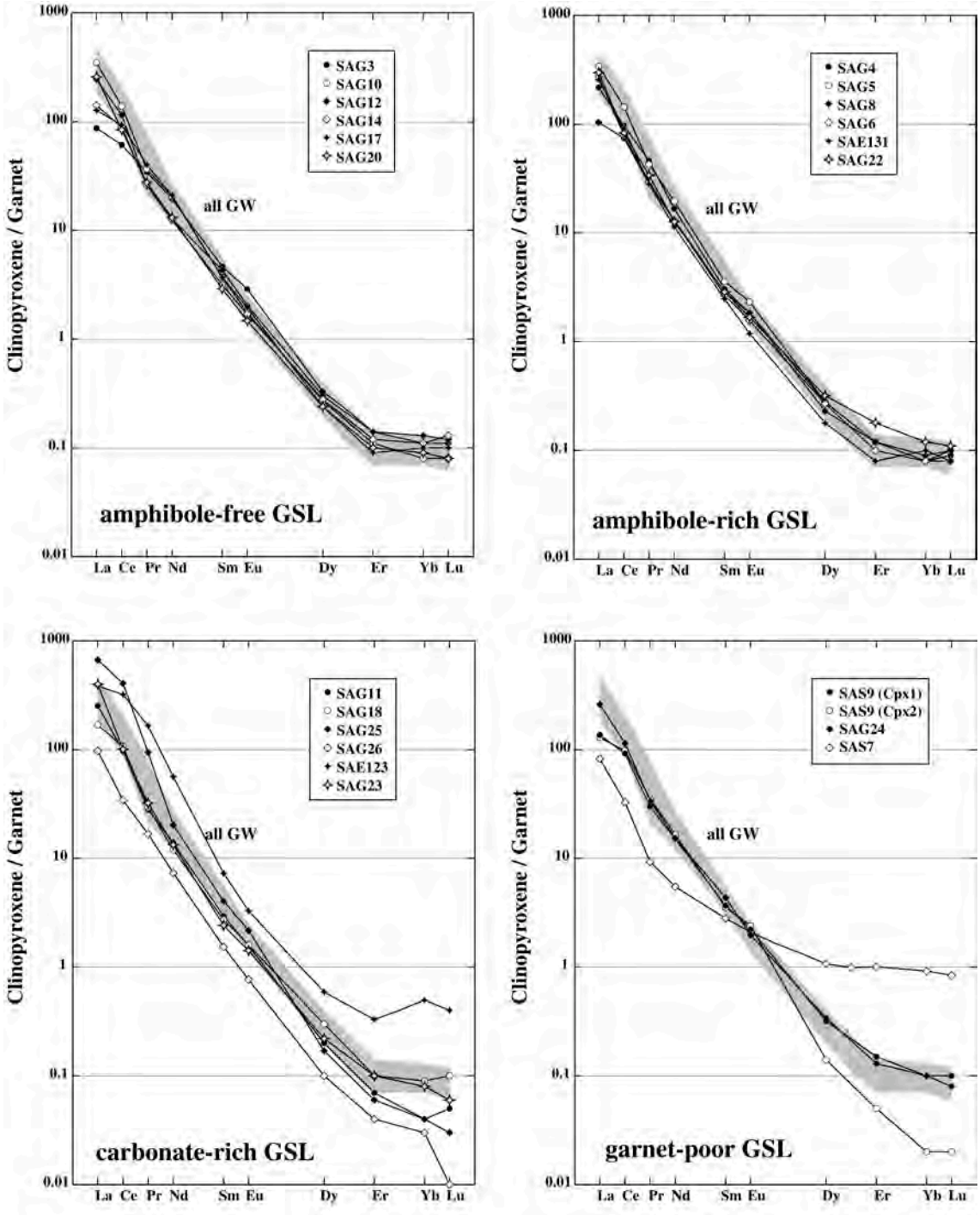

Fig. 4-9. Partitioning of REE between clinopyroxene and garnet (D values) from LT-type garnet-spinel lherzolites (GSL).

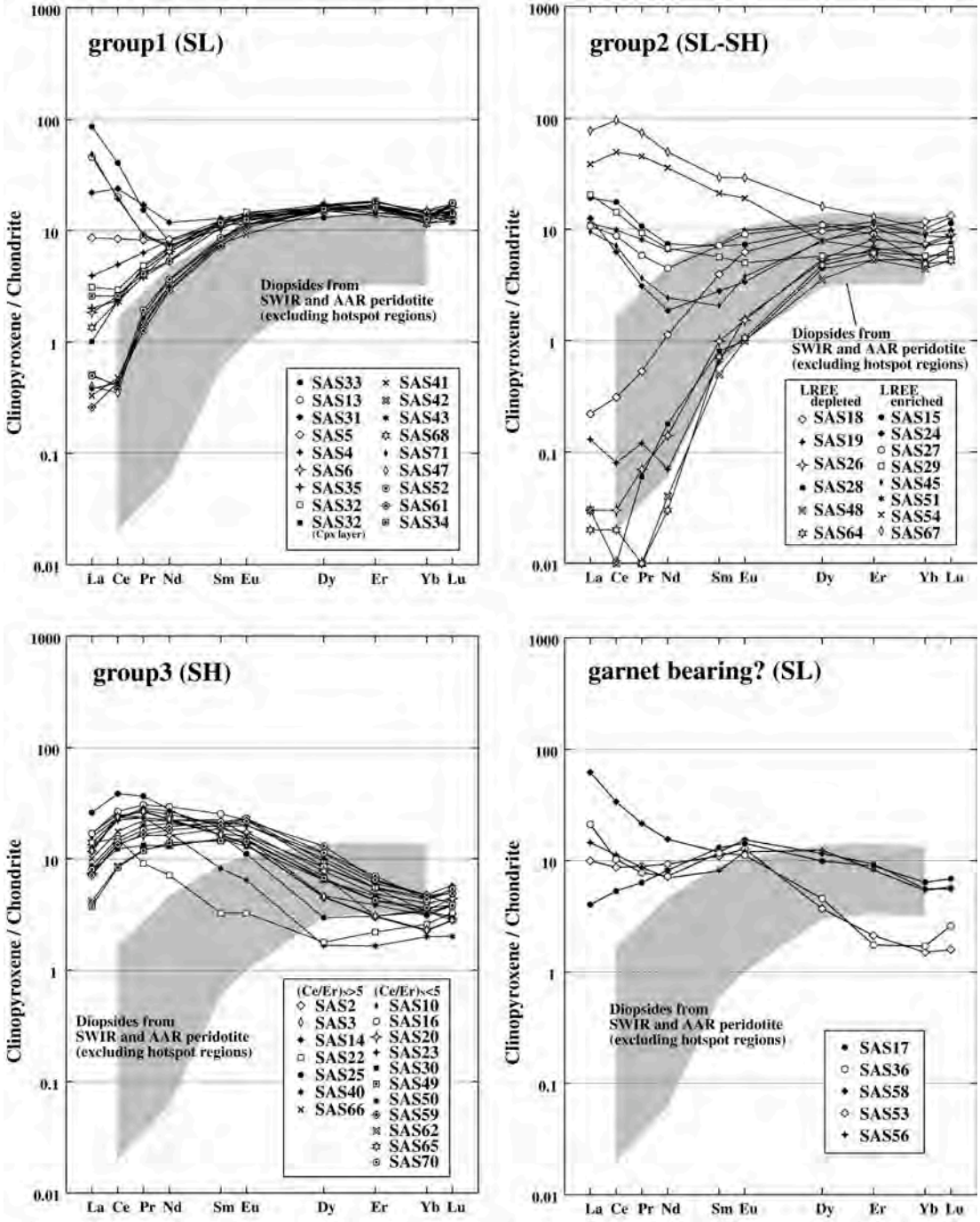

Fig. 4-10. Chondrite-normalized REE patterns of clinopyroxenes from LT-type spinel lherzolites and harzburgite (SL-SH). The fields of abyssal peridotite diopsides (Southwest Indian and American-Antarctic Ridge far from hot spots) are from Johnson et al. (1990) and Johnson and Dick (1992).

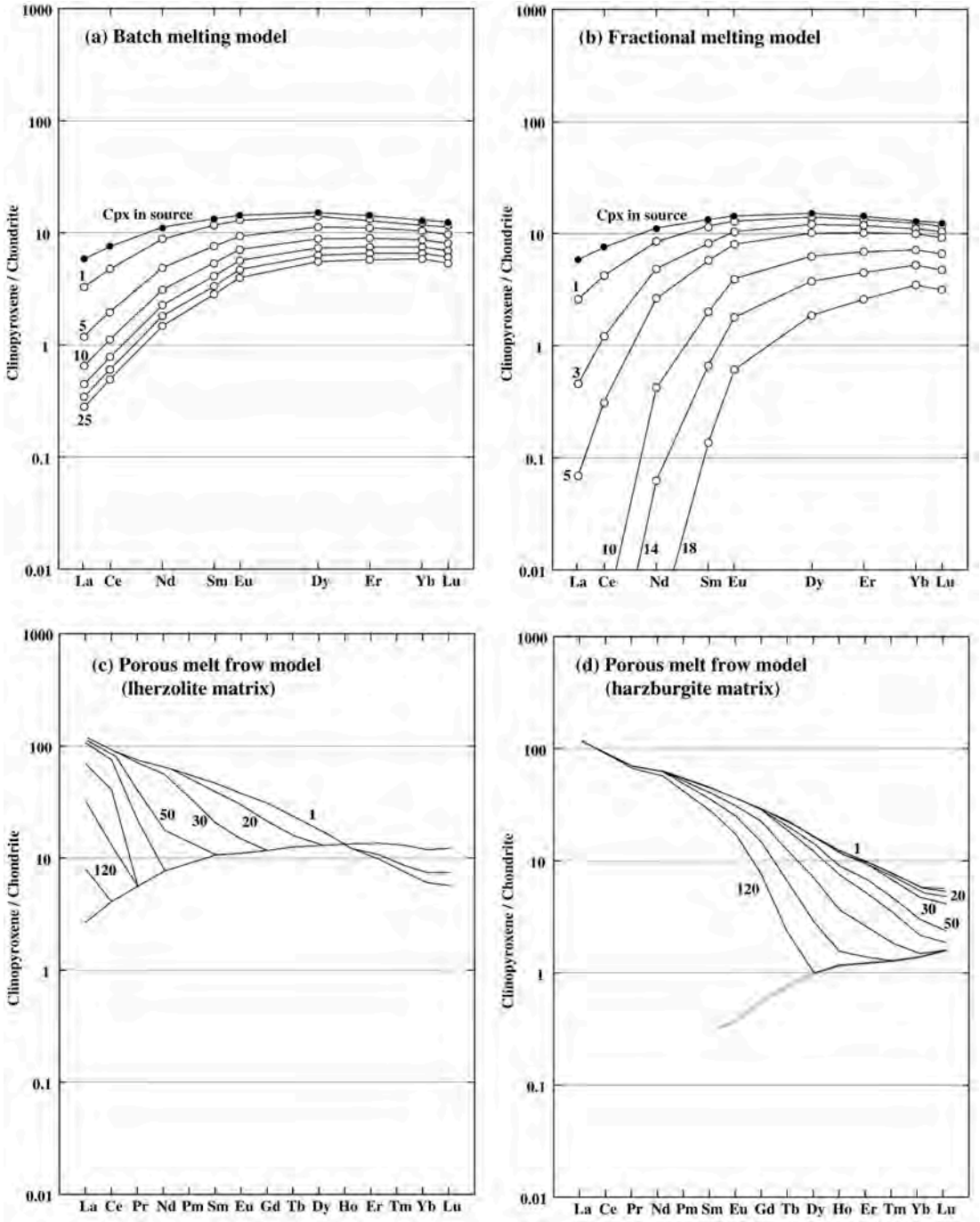

Fig. 4-11. Upper: Model batch (a) and fractional (b) melting residues of a depleted source mantle calculated for spinel peridotite assemblage. Partition coefficients, melting mode, initial mode and source compositions are listed in table 4-9. Lower: 1D numerical simulation of porous melt flow on chromatographic fractionation of REE in clinopyroxenes, showing the effects that LREE-rich melt percolated through the different matrix peridotites (from Bedini et al., 1997). Lherzolite (c) and harzburgite (d) matrix models have been calculated with identical parameters, except for modal and REE composition of peridotite. Numbers with patterns indicate each distanses (m) in 200 m of column height. Parameters used calculations are found in Vernieres et al. (1997) and Bedini et al. (1997).

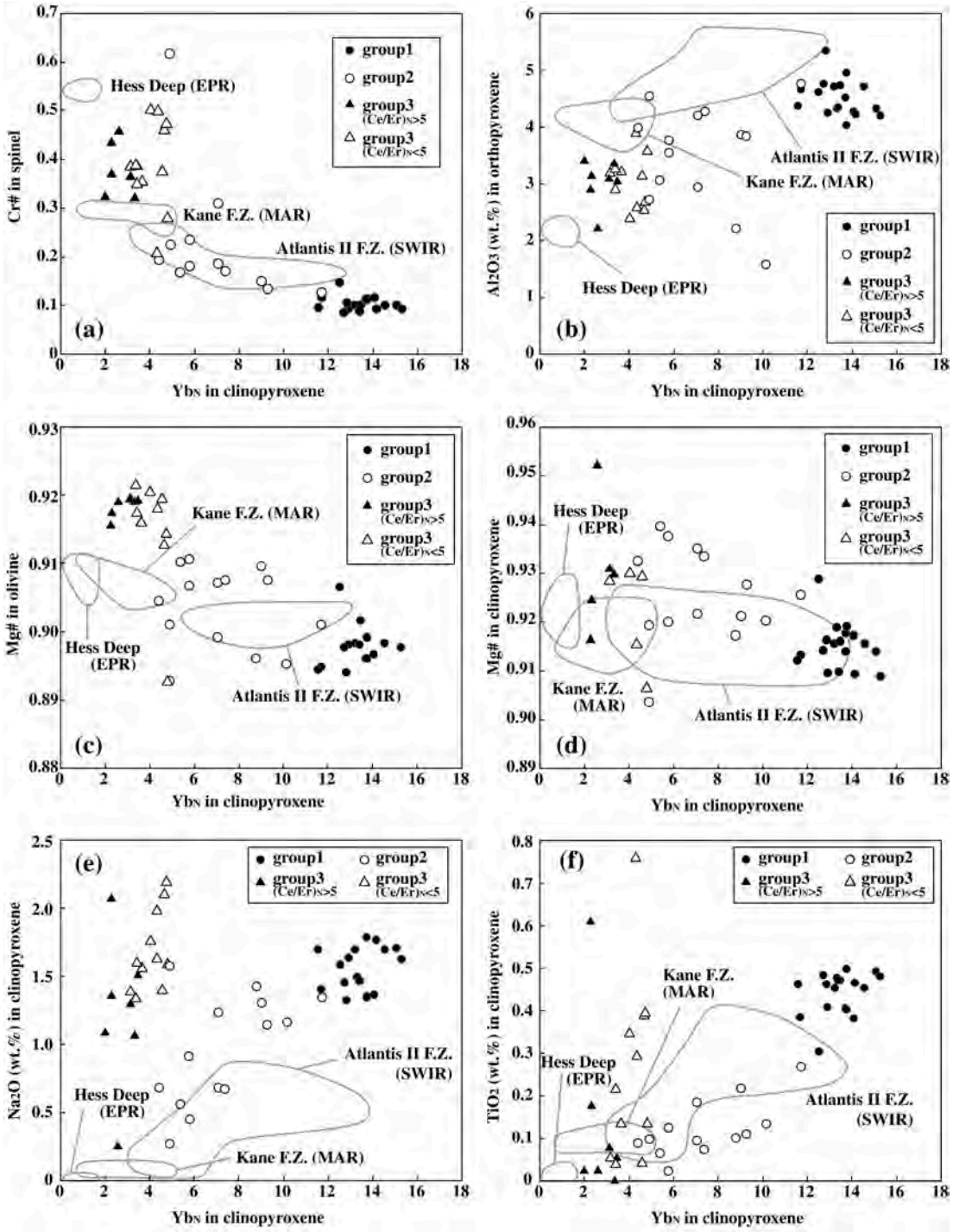

Fig. 4-12. Yb_N in clinopyroxene against variable depletion indicators: (a) Cr# = Cr/(Cr+Al) in spinel, (b) Al_2O_3 wt.% in orthopyroxene, (c) Mg# = Mg/(Mg+Fe*) in olivine, (d) Mg# = Mg/(Mg+Fe*) in clinopyroxene, (e) Na_2O wt.% in clinopyroxene and (f) TiO_2 in clinopyroxene from LT-type spinel lherzolites and harzburgites (SL-SH). The fields for abyssal peridotites from Hess Deep (Dick and Natland, 1996), Kane Fracture Zone (Ross and Elthon, 1997) and Atlantis II Fracture Zone (Johnson, 1990 and Johnson and Dick, 1992) are shown for comparison.

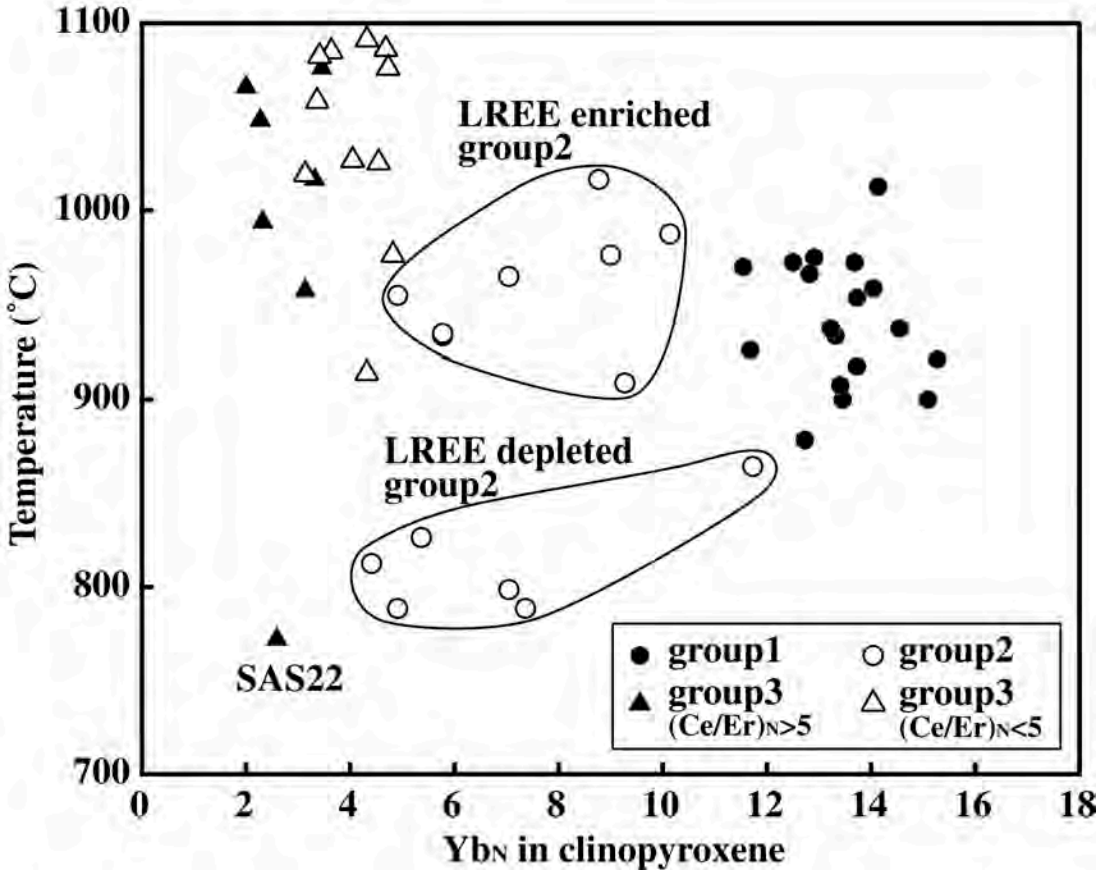

Fig. 4-13. Yb_N in clinopyroxenes against T estimates (at 1.5 GPa) using two-pyroxene thermometer (Brey and Köhler, 1990) from LT-type spinel lherzolite and harzburgite (SL-SH). Note that LREE depleted group2 and least modified group3 (SAS22) show the lower temperatures than those of LREE-enriched group2 and most group3 with concave downward "equilibrated" patterns.

4-3 Megacryst suites

Chondrite-normalized patterns of clinopyroxenes and garnets in megacryst suites are shown in Fig. 4-14. The garnets from megacryst suites (MG) show restricted variation in REE abundances and profiles with depleted in LREE. Similar to garnet, clinopyroxenes from megacryst suites (MSD, MCI and MA) have limited variation in abundances and profiles with humped shape in spite of wide range of Mg#. One analysis from subcalcic diopside inclusion in garnet megacryst shows minimum LREE and MREE abundances (La_N =4.95, Nd_N =9.34). On the other hand, clinopyroxene from mica-amphibole-ilmenite-augite rock (MAIA; SAX107) has distinctly high abundances in all REE with similar humped shape (La_N =20.5, Nd_N =25.2).

In Fig. 4-15, their REE abundances are plotted with Mg# in spite of limited REE variations. Dy, Er and Yb for garnet, La and for clinopyroxene are selected, because their high concentrations lower error of analyses (one sigma around 10%). In garnet, systematic variation could not be observed, however lowest Mg# of garnet has highest abundances of Dy, Er and Yb. In MSD, systematic variation could not be detected, however La and Ce abundances in other megacrysts (MCI, MA and MRI) show systematic decreasing with Mg#. Highest La and Ce remarked in MCI with high Mg#, while lowest La and Ce remarked in MRI with low Mg#. Origin of this variation is not accountable for simple fractionation scheme between melt and minerals and other evidences may be required for decipherment.

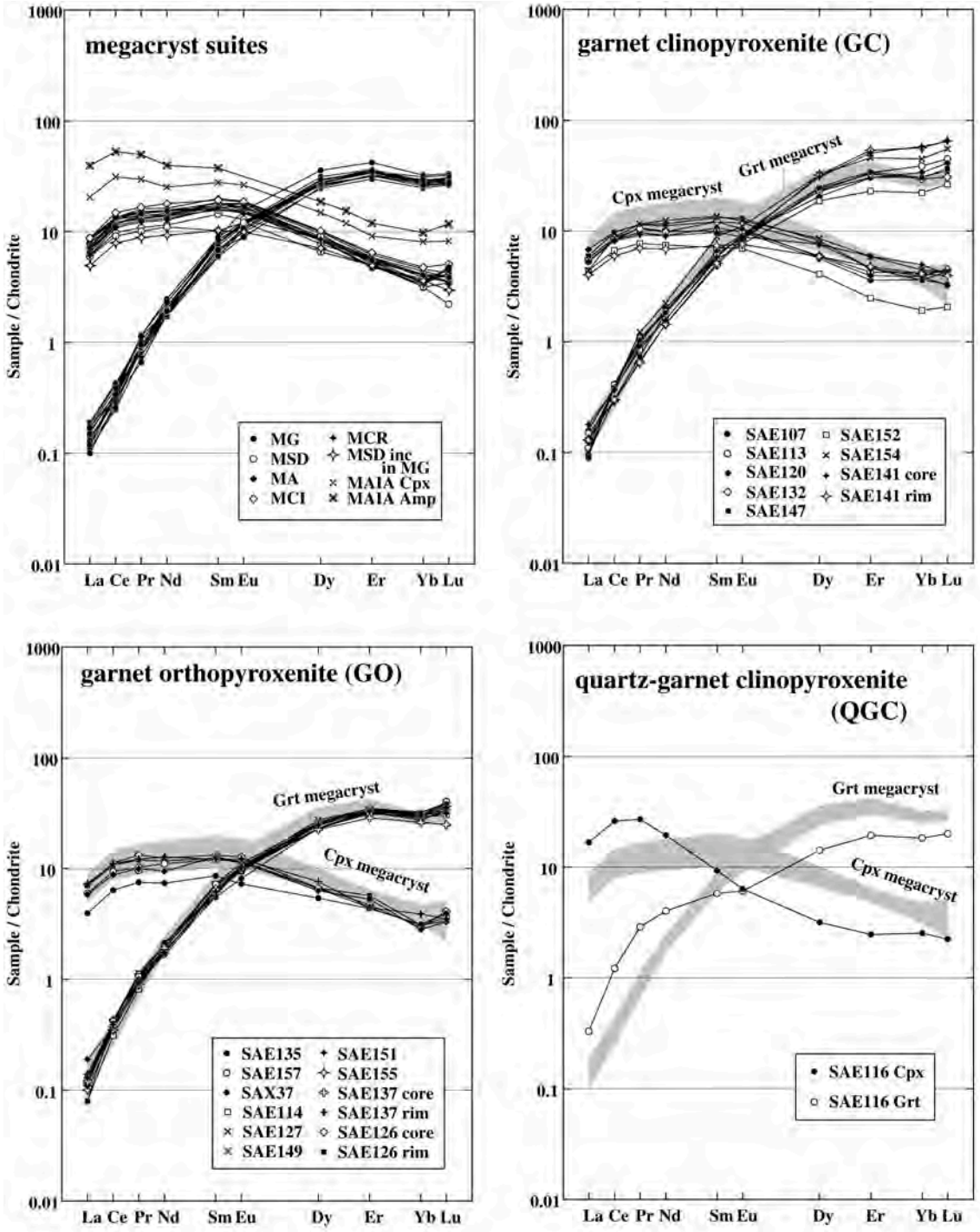

Fig. 4-14. Chondrite-normalized REE patterns of garnets, clinopyroxenes and amphibole (MAIA; SAX107) from megacryst suites, HT-type garnet clinopyroxenites (GC-QGC) and garnet orthopyroxenites (GO).

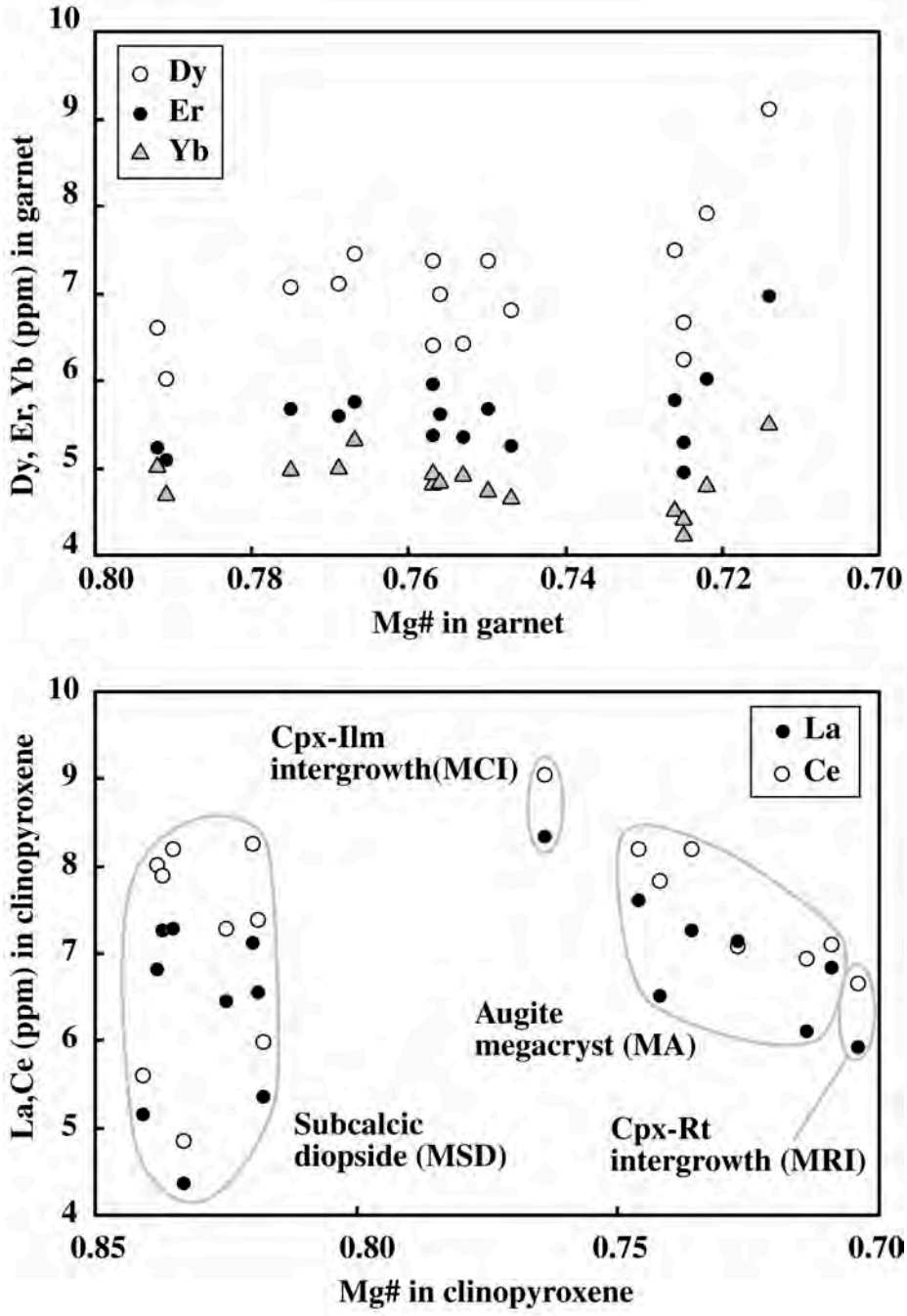

Fig. 4-15. Mg#=Mg/(Mg+Fe*) against several REE abundances (ppm) in clinopyroxenes and garnets from megacryst suites

4-4 HT-type pyroxenites (GC-GO)

Chondrite-normalized patterns of clinopyroxenes and garnets in GC and GO are shown in Fig. 4-14. Their D value profiles are shown in Fig. 4-16. Heterogeneous GO are described in next section together with those of HT-type peridotites. Similar to major element, their REE patterns exhibit well homogeneity in individual sample and grain scale. In two samples of GO (SAE126 and SAE137), no significant differences were observed in core-rim variations of both garnets and clinopyroxenes. Whereas, in SAE141 (GC) which contains zoned orthopyroxenes, substantial heterogeneity were observed between core and rim of clinopyroxene and not in garnet. The core has higher HREE than the rim. LREE/HREE ratios in both core of clinopyroxene, rim of clinopyroxene and garnet tend to be higher than other GC-GO. Origin of this patterns remain unknown similar to their texture and mineral chemistry. On the other hand, their D values including SAE141 (pair of rim compositions) have good accordance among all samples. D values determined by MG host and MSD inclusion pair is also same with D profiles of GC and GO. Compared to D values of LT-type (GW), they are characterized by lower D_{LREE} (D_{La}=30.2-85.1) and D_{LREE}/D_{HREE} (D_{Ce}/D_{Yb}=153-275) than those of LT-type. These systematic differences can be explained by distinct equilibrium temperature and/or clinopyroxene chemistry. Because both are usually dependent in natural system, it may be difficult to determine which effects are significant for observed values. However, effect of changes in ionic radius may be smaller in higher temperature conditions and observed lower D_{LREE}/D_{HREE} ratios for GC-GO might be consistent with expected changes by temperature effect. Their D profiles are compared with those determined by several experiments, which have been conducted for deciphering coexisting melts (Fig. 4-17). Excluding the ‘’Hauri et al.’’ data, four D profiles show relatively similar patterns. It is important to note that garnets in all experiments have higher XCa (0.186-0.262) than those of GC-GO, indicating deviation between experimental D and observed D may be due to compositional effect similar to the difference between GW and SGC.

REE profiles in GC and GO highly resemble with those of megacrysts; similar humped shapes of clinopyroxenes and LREE depleted garnets, and they tend to be plotted in lower ranges of megacrysts. However, samples with lowest total REE contents of clinopyroxenes in both GC and GO show substantial lowering from

observed range of megacrysts. They have particular characteristics in major element chemistries. In the case of GC, SAE152 with lowest Mg# of clinopyroxene and garnet have lowest REE abundances of clinopyroxene and garnet (excluding SAE141). In contrast, SAE135 with highest Mg# of clinopyroxene and garnet among homogeneous GO display lowest REE abundances of clinopyroxene but not about garnet. These evidences show that their Mg# and REE abundances do not correlate each other in the case of GC-GO similar to other minor elements such Ti and Na.

SAE116, which contains quartz displays a considerable difference in REE profiles of both garnet and clinopyroxene: LREE enriched and HREE depleted clinopyroxene and garnet with highest LREE/HREE ratio among others. These sinusoidal patterns often observed in clinopyroxenes and garnets in GL and their origin will be discussed in later section.

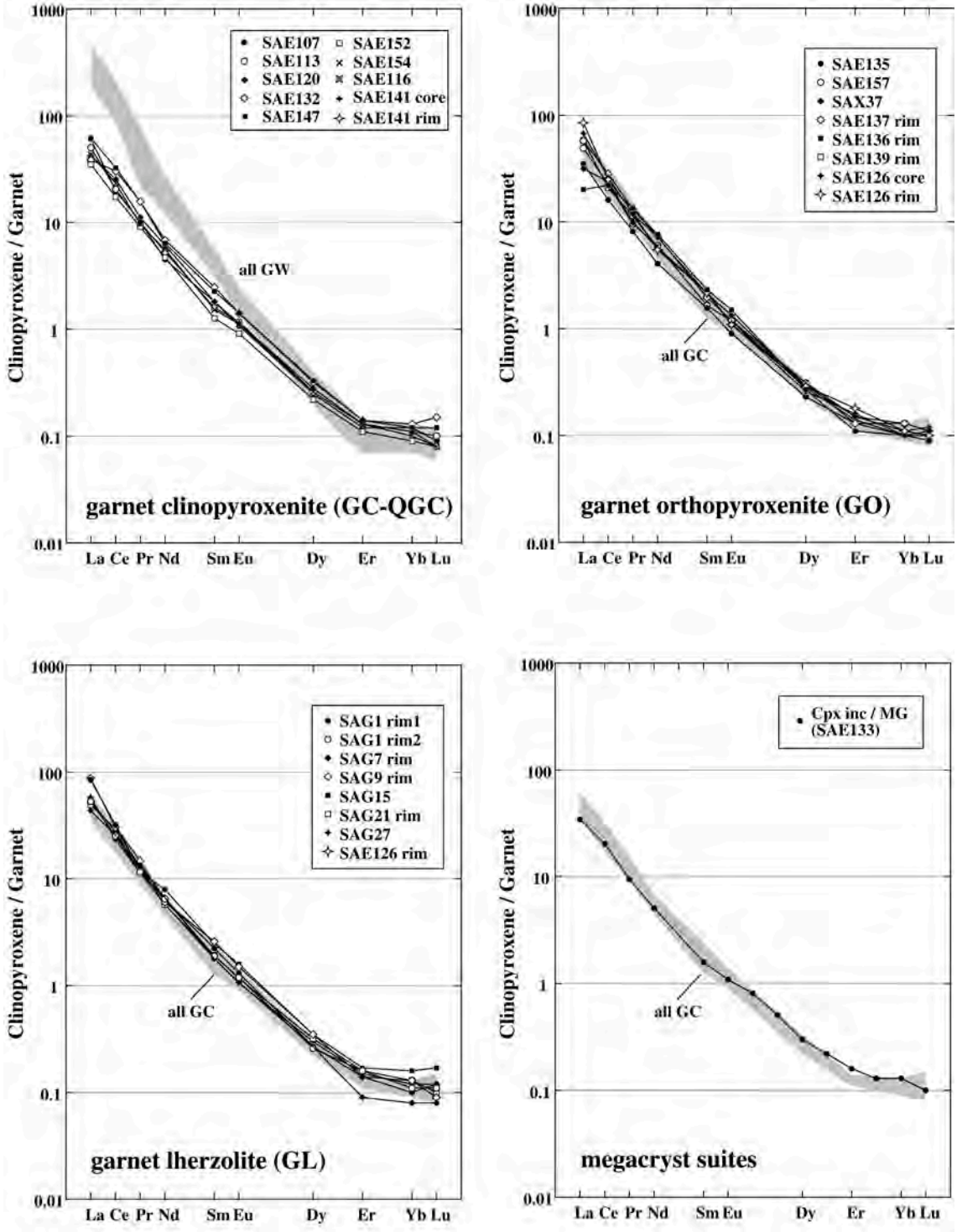

Fig. 4-16. Partitioning of REE between clinopyroxene and garnet (D values) from megacryst suites, HT-type garnet clinopyroxenites (GC-QGC), garnet orthopyroxenites and garnet lherzolites.

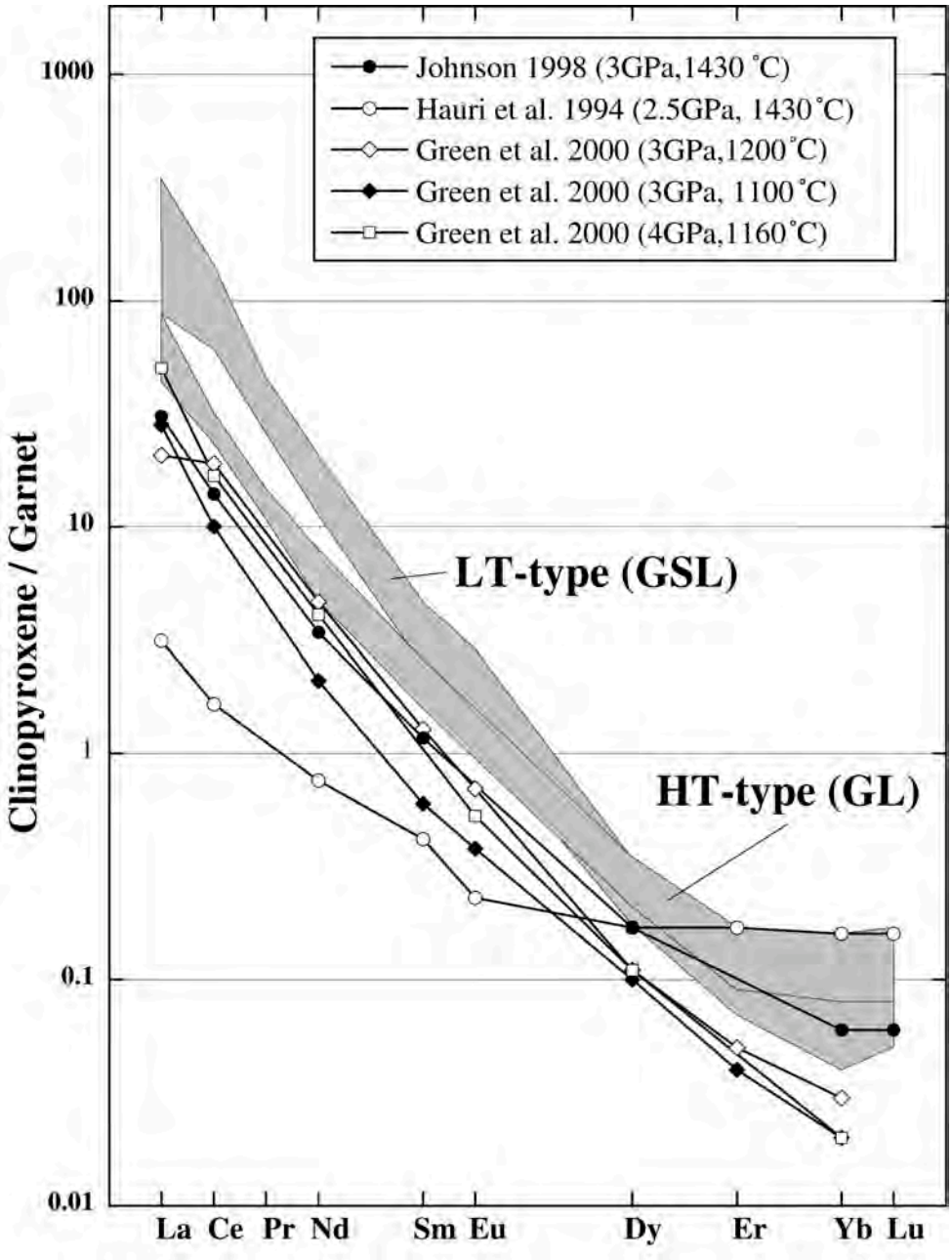

Fig. 4-17. Partitioning of REE between clinopyroxene and garnet calculated from several experimental results (Hauri et al., 1994; Johnson, 1998; Green et al., 2000). Note that garnets in all experiments have higher XCa values than those in studied garnets.

4-5 HT-type peridotites (GL-HTSH) and heterogeneous GO

Similar to major elements, REE heterogeneity was usually observed in the garnets from GL and GO. In contrast to garnets, REE heterogeneity of clinopyroxenes could not be detected in studied samples, implying that clinopyroxenes have well-homogenized REE compositions similar with major elements in single sample scale. Fig. 4-16 displays the D values determined by using rim compositions are compared with D values of GC. Systematic difference could not be observed between both, supporting that distribution of clinopyroxene and garnet rim is consistent with equilibrium partitioning.

Fig. 4-18 illustrates chondrite-normalized REE patterns for each samples, and analyzed spots of heterogeneous garnets are expressed on major elements zoning profiles in Fig. 3-15. One of the important results is that greater LREE heterogeneity was obtained from homogeneous garnets in terms of major element chemistry. REE patterns of single garnet in SAG7 display the Nd anomaly, which tends to diminish from core to rim. One grain of garnet (Grt1) from SAG1 has similar Nd behavior. Core of another neighbor grain (Grt2) have similar Sm-Lu abundances to core of Grt1, however the pattern inflects in Sm rather than Nd. Both grains display good accordance in rim compositions. REE patterns of clinopyroxenes from both samples show higher LREE and lower HREE compared to those of megacryst. It is interesting to note that same patterns were observed in QGC (SAE116), suggesting that similar process occurred in both peridotites and pyroxenites. These sinusoidal patterns were reported from the analyses of cratonic garnet peridotite xenolith and interpreted as the result of various stages of infiltrated melt-garnet interaction (e.g. Shimizu et al., 1997; Shimizu, 1999). Shimizu (1999) explained how garnet REE patterns change during infiltrated melt and garnet reaction in similar manner with clinopyroxene-melt interaction (Fig. 4-19). In the case that initial garnet becomes to equilibrate with infiltrated melt which is not in equilibrium with initial garnet, LREEs reach to equilibrium value faster than HREEs due to their lower partition coefficients. If this chromatographic reaction continues, REE patterns in garnet are progressively changed from 1 to 5 with a continuous sweeping from LREE to HREE. REE patterns obtained from SAG1, SAG7 and SAE116 qualitatively represent early stages of modification and core of garnets may leave former stages of modification. Fig. 4-20 displays reconstructed bulk compositions using the garnet REE patterns,

present mode determined by thin-section observation and partition coefficients listed in table 4-9. Simply assumed that whole-rock major element compositions and REE abundances in garnet were not modified by later metamorphism and metasomatism, REE abundance (except for LREE) in SAG1 and SAG7 are significantly depleted compared to those in depleted MORB source mantle which constructed after removing 2 % melt generated by non-modal batch melting in the garnet stability field from the primitive mantle composition (McDonough and Sun, 1995; Hirschmann and Stolper, 1996; Yang et al., 1998). Although extent of depletion can not be estimated from these evidences, it can be safely said that these samples experienced extensive degree of melting from fertile source mantle before metasomatism.

REE patterns of garnets and clinopyroxenes in SAG9, SAG15 and SAG30 bear a remote resemblance to those of megacryst, however they are notably higher LREE and lower HREE than the field of megacrysts. These patterns may represent “intermediate” between SAG7, SAG1 and megacryst. Core of garnet in SAG9 shows slight inflection about Nd and have lower concentrations than rim of same grain excluding La and Ce. It is noted that La abundance of garnet core exceed rim of same grain, indicating that progressive changes of REE patterns cannot be expressed as simple additions of REE like Fig. 4-19.

REE patterns of Fe-rich SAG21 and SAG27 resemble those of megacrysts similar to major elements. Garnet with Mg# zoning in SAG21 also show the difference between core and rim about HREE and MREE. Larger HREE variations in single garnets were also observed in heterogeneous GO. Significant REE variations from core to mantle of garnet in SAE136 were obtained. Because the rim is highly fractured, SIMS analyses were not conducted. Cr-rich mantle (spot 5) shows similar abundance with those of megacryst except for enriched La and Ce. Spot 4 about 2 mm toward the core reveals drastic deviations of HREE abundances from spot 5. Although difference between spot 4 and spot 3 is relatively limited, Eu and Dy abundances are significantly lower in spot 4. It is difficult to discuss about the differences between spot 1, spot 2 and spot 3. This drastic change about HREE abundances between spot 5 and spot 4 implies that they correspond to Cr variation rather than Mg#. Garnet with complex Cr zoning in SAE139 support the interpretation that REE abundances correspond to Cr content. However, the opposite variation was observed in SAE139. HREE depletions were obtained from Cr-rich

mantles (spot 1 and spot 3). Possible original cores of garnets (spot 2, spot 4 and spot 5) yield similar patterns with Cr-poor rim (spot 6) and other anhedral garnet (Grt2). Although it is difficult to understand for origin of these variations, either case reveals that HREE in garnets are easy to leave behind the modification.

REE patterns of clinopyroxenes in HTSH also can be interpreted as result of melt-rock reaction. Clinopyroxenes in SAS1, SAS8, SAS63 and SAS69 represent good accordance with the ranges of megacryst clinopyroxenes and as a fully equilibrated final stage. Clinopyroxenes in these samples have equivalent Ti and Na contents to those of MCD in spite of their depleted nature (high Cr# in spinel and high Mg# in olivine), indicating that high Na and Ti contents have also reactive origin. On the other hand, SAS21 and SAS46 clinopyroxene has significant depletion in HREE and equivalent LREE to megacryst, showing as earlier stage of melt-rock reaction. Distinct depletions of HREE ($Yb_N < 1$) might have been produced by high-degree of melting, which is represented by major element chemistry (both Na and Ti contents are almost zero) and later metasomatic event modified LREE in clinopyroxene selectively.

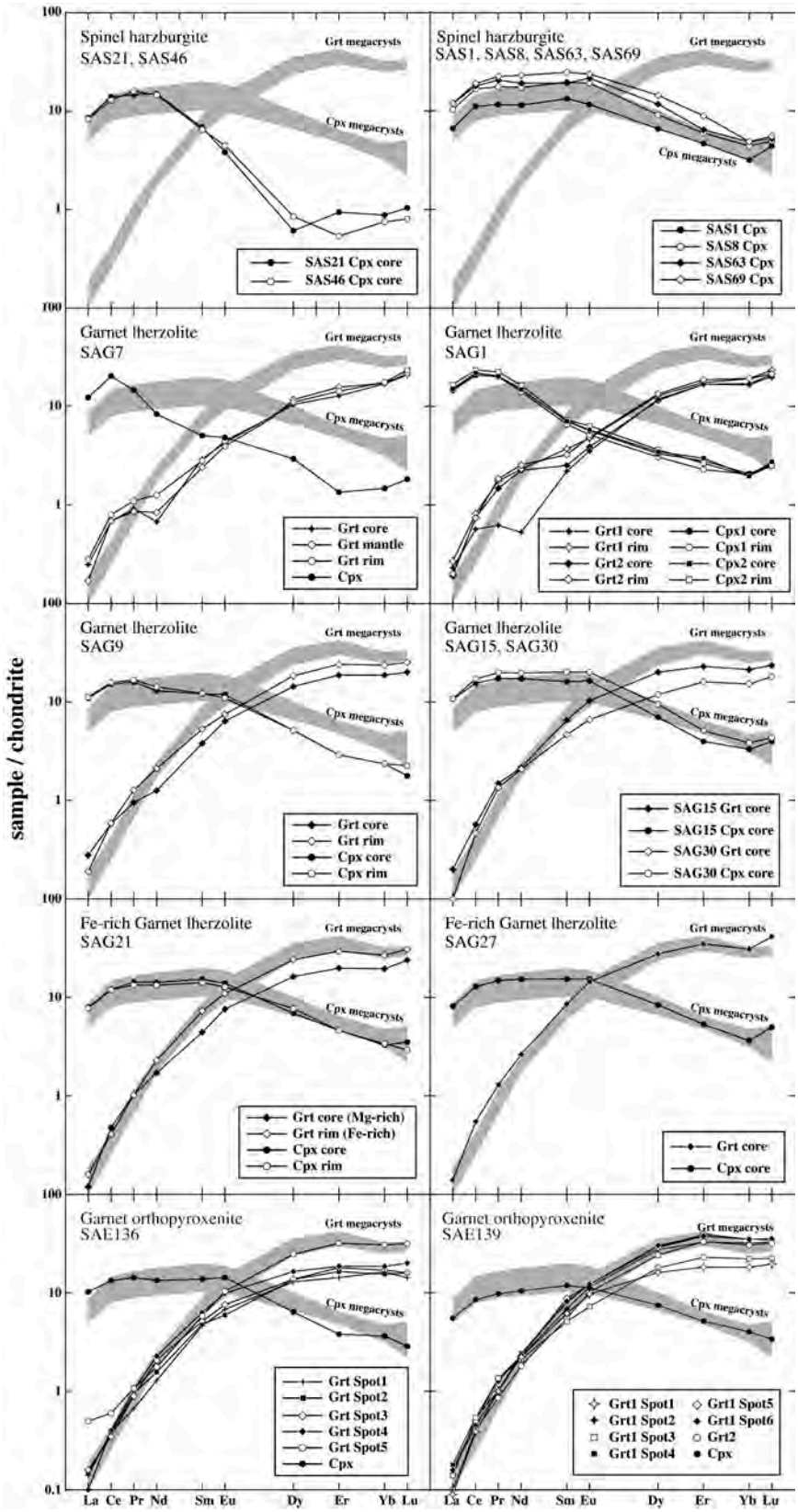

Fig. 4-18. Chondrite-normalized REE patterns of garnets and clinopyroxenes from megacryst suites, HT-type spinel harzburgites (HTSH), garnet lherzolites (GL) and heterogeneous garnet orthopyroxenites (GO).

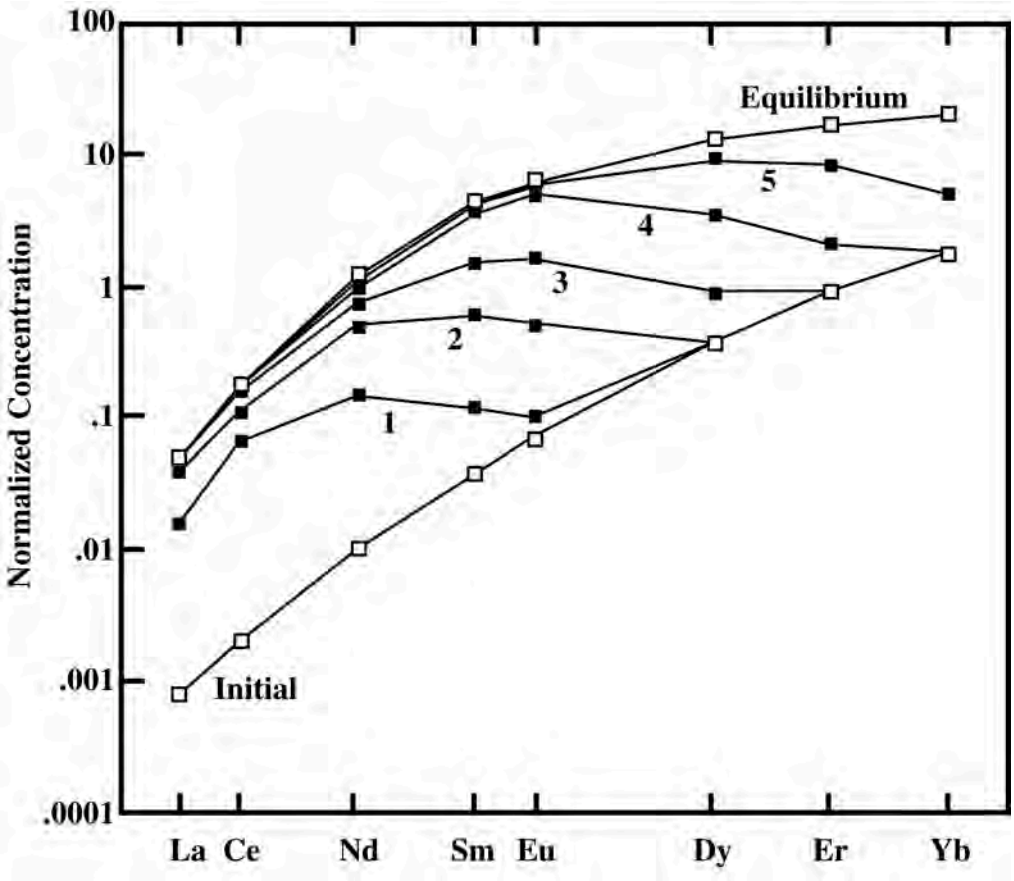

Fig. 4-19. Schematic REE variations in garnets at various stages of melt/rock reaction process proposed by Shimizu (1999). A series of progressive change from initial to equilibrium garnet is shown (early stage as 1, advanced stage as 5).

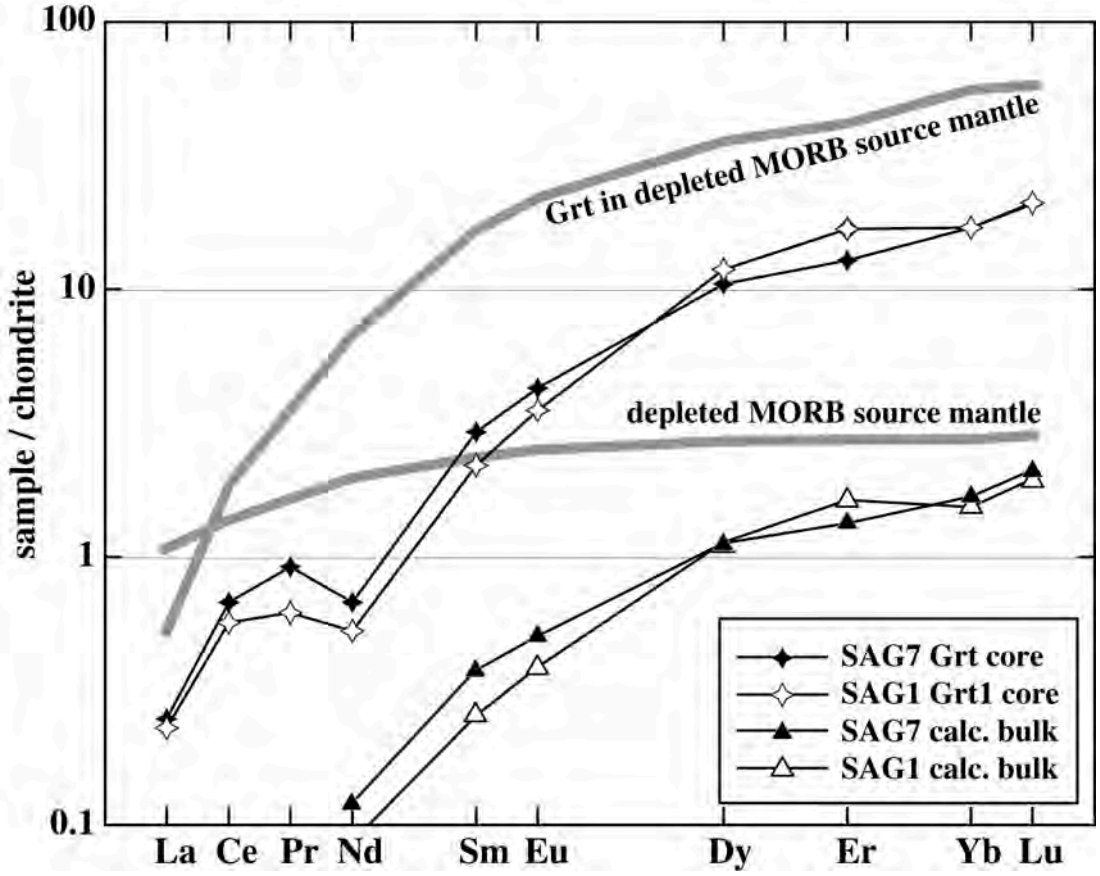

Fig. 4-20. Reconstructed bulk REE contents (from Nd to Lu) in SAG1 and SAG7 based on present modal abundances of consisting phase. REE contents in each phase were calculated using partition coefficients from the literature (listed in table 4-9) assuming that they equilibrated with core of garnets. Gray thick lines indicate REE abundances of MORB source mantle (Yang et al., 1998) and consisted garnet. Mineral proportions were obtained from Walter (1998), which experimentally determined the mineral compositions and modes of fertile peridotite at pressure of 3 GPa. Note that reconstructed bulk REE patterns display significantly low concentrations about all REEs and fractionate from MREE to HREE.

Table 4-1. REE abundances in clinopyroxenes and garnets from LT-type garnet websterites and clinopyroxenites (GW)

	garnet websterite (GW)							
	Group1							
	SAE134	SAE138	SAE122	SAE111	SAE117			
					rim	mantle	core	Cpx2
Clinopyroxenes								
La	5.77	4.37	4.67	9.00	14.5	15.1	15.4	11.4
Ce	5.36	5.81	6.29	9.80	18.1	18.9	19.0	16.3
Pr	5.60	7.37	7.25	9.66	16.8	17.3	16.8	17.8
Nd	5.92	6.79	6.64	8.94	14.2	14.4	14.3	15.5
Sm	7.27	7.64	6.92	10.2	12.4	12.7	13.1	15.0
Eu	6.48	8.35	6.64	9.36	11.6	11.2	10.7	13.5
Dy	3.81	3.14	3.33	6.01	7.01	6.72	7.02	6.67
Er	2.12	2.11	1.99	2.88	4.10	4.05	3.92	5.06
Yb	1.79	1.42	1.88	3.53	2.80	2.96	2.56	3.90
Lu	1.84	1.18	1.86	2.48	2.51	2.94	2.68	3.64
Garnets								
La	-	-	-	0.05	0.05			
Ce	0.05	0.05	0.03	0.07	0.10			
Pr	0.15	0.16	0.10	0.24	0.21			
Nd	0.35	0.44	0.48	0.44	0.58			
Sm	2.22	2.09	2.03	2.52	2.82			
Eu	3.64	4.45	4.92	4.15	4.50			
Dy	16.0	15.4	15.2	18.7	20.6			
Er	22.1	20.6	21.9	27.8	28.8			
Yb	19.9	18.1	20.4	26.3	25.2			
Lu	22.1	19.7	22.8	26.5	27.2			

	garnet websterite (GW)							garnet clinopyroxenite		
	Group2				Group3					
	SAE103	SAE106	SAE128	SAE144	SAE102	SAE143	SAE145	SAE105	SAE148	SAE156
Clinopyroxenes										
La	23.7	8.83	19.7	26.7	17.4	21.3	80.8	17.9	32.1	192
Ce	13.1	5.00	9.96	11.6	18.8	23.9	68.9	19.4	39.3	134
Pr	9.93	5.92	6.41	7.75	19.6	21.1	44.8	15.8	37.6	77.6
Nd	8.45	7.26	6.84	8.14	18.2	16.5	26.8	12.4	32.7	44.3
Sm	10.7	10.8	10.9	11.1	18.2	14.5	16.7	10.9	28.2	23.2
Eu	11.3	11.4	11.8	9.96	15.2	11.3	12.6	8.40	26.8	19.2
Dy	5.74	7.15	5.68	4.79	7.98	3.80	4.67	4.77	11.7	8.89
Er	3.00	4.60	3.22	2.81	3.60	2.50	3.03	3.09	6.69	5.22
Yb	3.03	3.51	2.43	2.60	3.37	1.82	1.88	2.54	5.12	3.38
Lu	2.88	3.14	2.24	2.31	2.46	2.32	1.98	2.38	5.27	3.84
Garnets										
La	0.08	0.05	0.07	0.06	0.05	0.11	0.20	0.05	0.07	0.18
Ce	0.11	0.06	0.06	0.12	0.11	0.12	0.50	0.12	0.18	0.40
Pr	0.23	0.16	0.09	0.37	0.41	0.31	0.80	0.29	0.51	0.79
Nd	0.69	0.40	0.26	0.48	0.75	0.64	1.27	0.58	1.20	1.01
Sm	2.95	3.11	2.18	3.56	3.88	2.58	4.63	2.76	6.09	4.09
Eu	4.92	5.79	4.69	5.41	6.40	4.68	6.35	4.29	10.7	7.19
Dy	27.1	24.6	20.2	17.1	20.0	13.9	18.2	17.1	32.1	35.9
Er	46.2	38.6	26.9	23.9	27.8	20.1	23.6	28.0	48.5	54.3
Yb	43.8	38.0	24.5	23.2	26.3	17.7	20.7	26.7	48.6	53.0
Lu	48.5	46.2	28.3	24.5	27.2	20.2	23.3	29.1	63.1	70.2

Table 4-2. REE abundances in clinopyroxenes and garnets from LT-type spinel-garnet clinopyroxenites (SGC)

	spinel garnet clinopyroxenite (SGC)									
	Group1					Group2				
	SAE101	SAE109	SAE112	SAE124	SAE140	SAE115	SAE118	SAE130	SAE146-1	SAE146-4
Clinopyroxenes										
La	37.1	18.6	22.1	24.3	16.7	20.8	20.6	16.6	18.2	17.6
Ce	25.1	22.2	23.3	21.4	18.9	17.4	24.7	16.6	18.7	18.2
Pr	16.7	19.6	18.8	16.7	16.8	12.9	23.8	14.7	16.9	14.9
Nd	11.6	17.0	13.6	12.7	13.0	10.5	18.3	11.6	14.7	12.6
Sm	9.68	14.7	9.49	11.8	9.48	8.19	14.9	10.3	12.9	11.6
Eu	9.07	11.1	8.75	10.3	7.77	6.84	11.9	9.44	11.1	10.2
Dy	2.23	3.93	2.13	2.85	2.08	1.51	2.70	2.02	3.21	2.86
Er	1.16	2.45	1.14	1.33	0.87	0.82	1.52	1.18	1.82	1.82
Yb	2.13	2.62	1.46	1.60	0.88	1.13	2.04	1.50	1.21	1.06
Lu	1.32	2.44	1.25	1.46	1.03	0.99	2.46	1.34	0.77	1.29
Garnets										
La	0.08	0.05	0.06	0.07	0.08	0.17	0.08	0.13	0.06	0.12
Ce	0.11	0.18	0.11	0.16	0.20	0.27	0.25	0.30	0.15	0.23
Pr	0.24	0.36	0.19	0.36	0.56	0.48	0.79	0.69	0.34	0.40
Nd	0.56	0.90	0.55	0.58	1.01	1.22	1.46	1.34	0.73	0.69
Sm	1.72	3.80	2.04	3.05	2.92	4.97	5.15	5.47	3.51	3.70
Eu	4.34	5.54	4.06	4.77	5.81	5.84	7.31	7.24	5.98	5.30
Dy	7.19	14.2	6.47	9.44	7.48	11.3	12.5	6.88	9.81	10.3
Er	7.87	18.5	7.12	10.9	6.96	11.1	14.8	7.25	8.92	9.38
Yb	6.82	18.3	5.58	9.00	4.96	9.23	12.3	6.52	6.82	7.68
Lu	7.82	20.1	6.42	9.82	5.37	8.96	13.1	7.13	7.67	9.11

	Group3							
	SAE108	SAE110	SAE142	SAE153	SAE104		SAE125	
					core	rim	core	rim
Clinopyroxenes								
La	5.55	11.6	23.7	10.2	2.65	2.42	4.69	4.35
Ce	2.81	7.48	23.4	7.09	2.18	2.25	3.28	3.16
Pr	1.50	4.63	19.0	5.12	1.86	1.96	2.42	1.95
Nd	0.93	3.69	13.0	3.51	1.64	2.06	2.12	1.85
Sm	0.77	2.55	5.66	2.13	2.64	2.65	2.52	2.27
Eu	-	-	-	-	2.33	1.74	2.53	2.11
Dy	0.37	0.54	0.79	0.38	0.78	0.98	1.20	1.11
Er	0.25	0.25	0.47	0.37	0.53	0.44	1.04	0.78
Yb	0.13	1.69	0.58	0.25	0.40	0.65	0.51	0.53
Lu	0.23	1.33	1.26	0.25	0.55	0.87	0.50	0.56
Garnets								
La	0.11	0.05	0.09	0.06	0.08	0.04	0.07	0.05
Ce	0.11	0.12	0.12	0.09	0.09	0.08	0.10	0.08
Pr	0.18	0.23	0.26	0.25	0.14	0.17	0.18	0.22
Nd	0.15	0.40	0.56	0.42	0.28	0.50	0.44	0.27
Sm	0.69	1.42	1.59	1.19	1.95	2.24	1.88	1.61
Eu	-	-	-	-	3.49	2.94	3.14	3.19
Dy	2.73	3.24	2.35	3.54	12.0	9.67	11.6	8.98
Er	2.69	4.14	2.52	5.03	15.1	12.5	12.5	8.83
Yb	1.94	3.05	1.87	4.19	15.6	11.6	9.92	6.45
Lu	2.36	3.59	2.40	5.78	15.5	11.3	9.17	5.89

Table 4-3. REE abundances in clinopyroxenes and garnets from LT-type garnet-spinel lherzolites (GSL)

	garnet-spinel lherzolite (GSL)											
							amphibole-rich					
	SAG3	SAG10	SAG12	SAG14	SAG17	SAG20	SAG4	SAG5	SAG6	SAG8	SAE131	SAG22
Clinopyroxenes												
La	1.96	5.80	8.93	4.42	2.44	5.05	6.57	17.0	4.13	4.17	5.79	4.37
Ce	5.55	15.5	9.07	13.7	5.28	13.0	16.2	38.3	14.3	14.8	20.9	20.4
Pr	1.00	1.82	0.97	1.79	0.74	1.87	1.62	3.55	2.10	2.09	3.10	4.14
Nd	5.04	7.35	4.88	7.92	3.79	7.73	6.39	11.7	9.66	9.97	11.8	20.1
Sm	2.20	2.44	2.10	2.02	1.83	2.11	2.05	2.61	2.80	2.79	3.27	6.46
Eu	0.93	0.82	0.84	0.71	0.59	0.74	0.78	0.86	1.05	1.02	1.01	2.30
Dy	1.75	1.61	1.26	1.34	0.96	1.25	1.29	1.35	1.67	1.67	1.57	5.36
Er	0.57	0.57	0.46	0.42	0.29	0.44	0.54	0.42	0.55	0.54	0.55	2.39
Yb	0.43	0.41	0.29	0.32	0.34	0.39	0.37	0.27	0.42	0.42	0.49	1.75
Lu	0.07	0.06	0.05	0.06	0.06	0.06	0.07	0.06	0.08	0.07	0.07	0.30
Garnets												
La	0.02	0.02	0.04	0.03	0.02	0.02	0.03	0.05	0.04	0.02	0.02	0.01
Ce	0.09	0.11	0.08	0.15	0.06	0.15	0.17	0.27	0.19	0.19	0.23	0.24
Pr	0.03	0.05	0.04	0.07	0.02	0.07	0.03	0.08	0.07	0.07	0.11	0.12
Nd	0.26	0.36	0.38	0.64	0.18	0.59	0.38	0.60	0.74	0.77	1.03	1.58
Sm	0.47	0.66	0.49	0.64	0.49	0.73	0.67	0.73	0.98	1.04	1.31	2.26
Eu	0.32	0.46	0.41	0.42	0.30	0.50	0.42	0.37	0.57	0.65	0.84	1.37
Dy	5.25	6.07	4.15	4.71	3.93	5.22	5.52	4.84	6.08	6.25	8.80	16.7
Er	4.11	5.21	3.17	3.55	3.23	4.19	4.64	3.58	4.61	5.32	6.61	13.5
Yb	3.80	4.88	2.24	3.00	3.43	4.11	4.62	3.48	4.78	5.15	5.03	14.0
Lu	0.63	0.85	0.42	0.50	0.64	0.77	0.73	0.60	0.79	0.90	0.87	2.67

	carbonate-rich						garnet-poor			
	SAG11	SAG18	SAG23	SAE123	SAG25	SAG26	SAS7	SAG24	SAS9 Cpx1	SAS9 Cpx2
Clinopyroxenes										
La	6.45	5.93	22.4	5.66	10.2	3.59	11.7	5.21	9.93	9.34
Ce	6.08	16.1	75.3	8.08	16.7	7.17	14.4	13.7	14.2	15.0
Pr	0.71	2.08	10.1	0.95	1.59	0.72	0.99	1.94	0.93	1.10
Nd	4.22	8.30	35.2	3.98	5.73	2.11	3.58	8.31	2.46	2.69
Sm	1.96	1.98	5.37	1.66	1.68	0.36	1.72	2.40	0.64	0.61
Eu	0.69	0.60	1.53	0.66	0.62	0.11	0.77	0.83	0.22	0.24
Dy	1.64	1.19	1.82	1.47	0.90	0.24	4.48	1.56	1.46	0.67
Er	0.55	0.31	0.68	0.50	0.36	0.18	3.04	0.48	1.18	0.41
Yb	0.35	0.24	0.52	0.52	0.30	0.17	2.63	0.38	1.23	0.28
Lu	0.07	0.04	0.07	0.07	0.04	0.02	0.48	0.06	0.24	0.05
Garnets										
La	0.03	0.04	0.06	0.01	0.02	0.04	0.14	0.02	0.07	
Ce	0.06	0.15	0.75	0.03	0.04	0.21	0.44	0.12	0.15	
Pr	0.03	0.07	0.31	0.01	0.02	0.04	0.11	0.06	0.03	
Nd	0.30	0.69	2.64	0.07	0.28	0.29	0.65	0.54	0.16	
Sm	0.66	0.73	2.21	0.23	0.41	0.24	0.61	0.55	0.17	
Eu	0.44	0.37	1.07	0.20	0.28	0.14	0.36	0.42	0.10	
Dy	8.08	4.02	8.09	2.50	5.40	2.46	4.19	4.55	4.64	
Er	8.03	3.18	6.84	1.50	5.92	4.19	3.00	3.81	7.98	
Yb	8.08	2.76	6.84	1.03	6.70	6.69	2.87	3.89	12.4	
Lu	1.33	0.43	1.32	0.18	1.36	1.61	0.58	0.77	2.34	

Table 4-4. REE abundances in clinopyroxenes from LT-type spinel lherzolites and harzburgites. (SL-SH)

	spinel lherzolite and harzburgite (SL-SH)											
	Group1											
	SAS4	SAS5	SAS6	SAS13	SAS31	SAS32	SAS32	SAS33	SAS34	SAS35	SAS41	SAS42
Clinopyroxenes												
La	0.93	2.04	0.44	10.8	5.21	0.24	0.74	20.3	0.61	0.48	0.08	0.12
Ce	3.03	5.16	1.58	12.3	14.5	1.43	1.80	24.7	1.58	1.45	0.29	0.24
Pr	0.61	0.78	0.42	0.86	1.62	0.45	0.46	1.46	0.39	0.37	0.13	0.14
Nd	3.83	3.92	3.02	3.32	5.54	3.20	3.35	3.72	2.50	2.45	1.39	1.51
Sm	1.89	1.74	1.80	1.83	1.96	1.86	1.85	1.73	1.80	1.63	1.17	1.19
Eu	0.76	0.80	0.76	0.72	0.82	0.76	0.85	0.67	0.73	0.72	0.54	0.65
Dy	3.93	4.00	4.25	3.91	4.36	3.76	4.07	3.35	3.98	3.97	3.84	3.85
Er	2.56	2.84	2.97	2.70	2.60	2.58	2.78	2.39	2.69	2.68	2.25	2.83
Yb	2.33	2.26	2.56	2.19	2.60	2.25	2.47	2.29	2.16	2.28	2.13	1.99
Lu	0.37	0.45	0.41	0.43	0.44	0.38	0.36	0.41	0.45	0.44	0.34	0.31

	Group 1						Group 2 (LREE depleted)					
	SAS43	SAS47	SAS52	SAS61	SAS68	SAS71	SAS18	SAS19	SAS26	SAS28	SAS48	SAS64
Clinopyroxenes												
La	0.09	0.09	0.12	0.06	0.32	11.54	0.05	0.03	0.01	0.00	0.01	0.00
Ce	0.26	0.22	0.25	0.27	1.41	11.86	0.19	0.05	0.02	0.01	0.01	0.01
Pr	0.15	0.17	0.18	0.12	0.37	0.87	0.05	0.01	0.01	0.01	0.00	0.00
Nd	1.47	1.66	1.71	1.35	3.01	3.48	0.53	0.03	0.07	0.08	0.02	0.01
Sm	1.26	1.27	1.32	1.11	1.73	1.57	0.60	0.10	0.15	0.12	0.08	0.11
Eu	0.67	0.71	0.66	0.62	0.79	0.79	0.36	0.09	0.09	0.06	0.06	0.06
Dy	3.90	3.99	4.35	3.84	4.03	4.14	2.44	1.30	1.38	1.13	0.91	1.21
Er	2.70	2.40	3.06	2.78	2.62	3.06	1.75	1.08	1.34	0.88	0.88	1.01
Yb	2.33	2.34	2.39	2.18	1.96	2.40	1.99	1.20	1.26	0.91	0.75	0.83
Lu	0.30	0.35	0.34	0.37	0.34	0.38	0.34	0.22	0.23	0.17	0.13	0.13

	Group2 (LREE enriched)								garnet-bearing?		
	SAS15	SAS24	SAS27	SAS29	SAS45	SAS51	SAS54	SAS67	SAS17	SAS36	SAS53
Clinopyroxenes											
La	4.55	2.98	2.55	4.85	2.25	2.67	9.11	18.2	0.95	5.02	2.37
Ce	10.8	3.84	5.37	8.74	4.35	6.04	30.2	58.5	3.26	6.27	5.33
Pr	1.01	0.30	0.55	0.88	0.35	0.77	4.30	6.97	0.60	0.74	0.85
Nd	3.46	0.87	2.09	3.17	1.13	3.04	16.7	23.2	3.83	3.38	4.34
Sm	1.08	0.43	1.10	0.86	0.32	1.13	3.23	4.48	1.99	1.79	1.68
Eu	0.42	0.20	0.52	0.29	0.22	0.57	1.10	1.69	0.83	0.65	0.74
Dy	2.62	2.03	2.76	1.46	1.98	2.87	1.99	4.10	2.51	1.16	0.94
Er	1.93	1.57	1.49	1.03	1.82	1.72	1.13	2.14	1.48	0.29	0.35
Yb	1.53	1.58	0.83	0.98	1.49	1.20	0.98	1.72	1.09	0.29	0.26
Lu	0.29	0.25	0.17	0.15	0.22	0.19	0.15	0.33	0.17	0.07	0.04

	Group3 $(Ce/Er)_N$>5							garnet-bearing?	
	SAS3	SAS14	SAS22	SAS25	SAS2	SAS40	SAS66	SAS56	SAS58
Clinopyroxenes									
La	2.80	2.75	3.34	6.18	2.77	4.04	2.39	3.45	14.8
Ce	14.7	14.2	9.31	23.5	14.6	15.3	10.8	6.89	20.7
Pr	2.55	2.70	0.86	3.47	2.52	2.24	2.11	0.82	2.05
Nd	10.6	12.6	3.33	13.0	10.5	7.99	10.2	3.26	7.26
Sm	2.53	2.93	0.50	2.46	2.51	1.25	2.54	1.23	1.83
Eu	0.79	0.88	0.19	0.64	0.78	0.37	0.93	0.70	0.89
Dy	1.16	1.18	0.45	0.75	1.15	0.43	1.78	3.14	2.94
Er	0.51	0.64	0.36	0.51	0.50	0.28	0.51	1.36	1.54
Yb	0.39	0.53	0.44	0.57	0.39	0.34	0.59	0.91	0.95
Lu	0.07	0.10	0.08	0.10	0.07	0.05	0.11	0.15	0.14

	Group3 $(Ce/Er)_N$<5										
	SAS10	SAS16	SAS20	SAS23	SAS30	SAS49	SAS50	SAS59	SAS62	SAS65	SAS70
Clinopyroxenes											
La	3.72	4.01	1.76	2.99	1.87	0.89	2.06	1.69	0.99	3.28	1.91
Ce	14.3	16.3	8.33	13.6	7.51	5.12	9.34	8.15	5.20	14.1	8.73
Pr	2.22	2.90	1.54	2.21	1.26	1.13	1.89	1.58	1.15	2.60	1.72
Nd	10.4	13.7	7.58	10.4	6.07	6.51	9.66	8.47	6.20	11.7	9.08
Sm	3.43	3.88	2.86	3.30	2.32	2.23	2.96	3.04	2.29	3.11	3.27
Eu	0.94	1.29	1.01	1.17	0.75	0.83	1.16	1.27	0.87	1.32	1.34
Dy	2.14	2.17	1.98	2.56	1.64	1.70	2.83	3.32	1.64	2.40	2.88
Er	0.90	0.92	0.80	0.99	0.77	0.71	1.05	1.07	0.70	0.91	1.16
Yb	0.73	0.78	0.69	0.82	0.53	0.62	0.79	0.81	0.58	0.58	0.74
Lu	0.13	0.13	0.11	0.15	0.10	0.10	0.10	0.12	0.08	0.07	0.14

Table 4-5. REE abundances in clinopyroxenes, garnets and amphibole (MAIA; SAX107) from megacryst suites.

	subcalcic diopside (MSD)								MSD Inclusion in MG
	SAX51	SAX39J	SAX44	SAX39B	SAX39D	SAX39F	SAX39I	SAX39C	SAE133
Clinopyroxenes									
La	1.42	2.05	1.97	2.07	1.74	2.01	1.88	1.44	1.17
Ce	5.60	8.02	7.88	8.20	7.28	8.25	7.39	5.99	4.86
Pr	0.96	1.32	1.43	1.39	1.24	1.45	1.26	1.03	0.84
Nd	5.15	6.82	7.26	7.28	6.45	7.11	6.55	5.35	4.36
Sm	1.56	2.53	2.43	2.73	2.40	2.64	2.53	2.20	1.57
Eu	0.70	0.98	0.88	0.94	0.86	1.03	0.89	0.74	0.58
Dy	1.67	2.30	1.97	2.22	2.11	2.44	2.17	2.17	1.81
Er	0.82	0.95	0.90	0.96	0.78	0.83	0.88	0.92	0.82
Yb	0.54	0.70	0.53	0.65	0.64	0.59	0.58	0.70	0.62
Lu	0.06	0.10	0.09	0.09	0.09	0.11	0.11	0.09	0.08

	Cpx-Ilm (MCI)	augite (MA)						Cpx-Ri (MCR)	Mica-Amp-Ilm-Augite (MAIA)	
	SAX36	SAX35	SAX47	SAX45	SAX49	SAX48	SAX32A	SAX34	SAX107	
Clinopyroxenes										*Amphibole*
La	2.08	1.96	1.69	1.74	1.66	1.53	1.59	1.45	4.86	9.33
Ce	9.04	8.19	7.84	8.19	7.08	6.93	7.11	6.66	19.1	32.2
Pr	1.58	1.53	1.34	1.45	1.38	1.20	1.32	1.16	2.82	4.72
Nd	8.34	7.61	6.52	7.27	7.15	6.12	6.84	5.92	11.8	18.5
Sm	2.95	3.05	2.82	2.76	2.80	2.45	2.63	2.52	4.24	5.70
Eu	1.08	1.10	0.95	1.04	0.90	0.85	1.06	0.99	1.53	-
Dy	2.58	2.59	2.13	2.16	2.16	2.16	2.53	2.14	3.78	4.72
Er	1.07	1.02	0.95	0.89	0.91	0.79	0.96	0.81	1.51	1.97
Yb	0.81	0.78	0.69	0.69	0.59	0.61	0.74	0.57	1.37	1.67
Lu	0.13	0.11	0.09	0.10	0.12	0.11	0.10	0.12	0.21	0.30

	garnet (MG)							
	SAX19	SAE133	SAX22	SAX29	SAX9	SAX8-1	SAX8-2	SAX24
Garnets								
La	0.05	0.03	0.04	0.04	0.04	0.03	0.04	0.04
Ce	0.26	0.24	0.26	0.24	0.22	0.21	0.21	0.22
Pr	0.10	0.09	0.09	0.11	0.11	0.09	0.08	0.09
Nd	0.97	0.86	0.98	0.91	1.07	0.81	0.84	1.07
Sm	1.20	0.99	1.20	1.29	1.29	0.91	1.05	1.22
Eu	0.71	0.53	0.68	0.68	0.68	0.52	0.52	0.68
Dy	6.60	6.03	7.06	7.11	7.46	6.41	6.42	7.37
Er	5.23	5.09	5.68	5.60	5.76	5.38	5.34	5.96
Yb	5.01	4.68	4.97	4.98	5.31	4.80	4.90	4.92
Lu	0.77	0.74	0.70	0.72	0.81	0.73	0.78	0.78

	garnet (MG)							
	SAX21	SAX27	SAX23	SAX30	SAX16	SAX3	SAX11	SAX10
Garnets								
La	0.03	0.03	0.04	0.03	0.03	0.03	0.02	0.03
Ce	0.19	0.21	0.20	0.16	0.18	0.15	0.18	0.21
Pr	0.06	0.09	0.08	0.09	0.08	0.07	0.08	0.11
Nd	0.84	0.93	0.89	0.89	0.81	0.84	0.87	1.15
Sm	0.98	1.20	0.92	1.05	1.13	1.06	1.37	1.35
Eu	0.62	0.70	0.60	0.62	0.67	0.57	0.71	0.90
Dy	6.99	7.37	6.81	7.49	6.66	6.24	7.92	9.10
Er	5.61	5.69	5.25	5.77	5.29	4.95	6.03	6.96
Yb	4.83	4.73	4.65	4.50	4.40	4.22	4.80	5.50
Lu	0.76	0.70	0.67	0.69	0.69	0.67	0.74	0.85

Table 4-6. REE abundances in clinopyroxenes and garnets from HT-type garnet clinopyroxenites (GC-QGC).

	garnet clinopyroxenite (GC)									
	SAE116	SAE107	SAE113	SAE120	SAE147	SAE152	SAE154	SAE132	SAE141 core	SAE141 rim
Clinopyroxenes										
La	3.97	1.26	1.26	1.62	1.41	1.05	1.05	1.34	1.25	0.95
Ce	15.9	5.14	5.10	6.01	5.96	4.08	5.36	5.29	5.01	3.66
Pr	2.57	0.92	1.01	1.08	1.09	0.74	1.10	1.00	0.88	0.66
Nd	9.05	4.25	4.65	5.20	5.45	3.50	5.83	4.60	4.24	3.21
Sm	1.43	1.63	1.52	1.85	2.02	1.09	2.08	1.86	1.49	1.13
Eu	0.37	0.57	0.59	0.61	0.76	0.40	0.72	0.69	0.51	0.44
Dy	0.81	1.43	1.52	1.48	2.08	1.04	2.17	1.95	1.93	1.50
Er	0.41	0.59	0.71	0.65	0.76	0.41	0.98	0.76	0.98	0.79
Yb	0.43	0.62	0.71	0.66	0.61	0.33	0.76	0.67	0.85	0.70
Lu	0.06	0.08	0.11	0.08	0.11	0.05	0.11	0.11	0.10	0.10
Garnets										
La	0.08	0.02	0.03	0.04	0.02	0.03	0.02	0.03	0.04	0.03
Ce	0.75	0.26	0.25	0.24	0.18	0.24	0.23	0.17	0.22	0.18
Pr	0.27	0.09	0.10	0.10	0.07	0.08	0.12	0.06	0.09	0.06
Nd	1.88	0.94	0.87	0.85	0.85	0.74	1.04	0.67	0.73	0.68
Sm	0.89	0.90	0.95	1.02	0.89	0.85	1.36	0.75	0.89	0.78
Eu	0.35	0.53	0.50	0.53	0.53	0.44	0.64	0.49	0.53	0.50
Dy	3.61	5.78	5.86	5.20	6.28	4.74	8.20	6.12	7.81	8.10
Er	3.21	5.04	5.58	5.01	5.62	3.80	7.57	5.45	8.41	8.89
Yb	3.11	5.24	6.57	5.76	5.16	3.77	7.62	5.04	9.90	9.57
Lu	0.51	0.89	1.14	1.04	0.93	0.67	1.40	0.78	1.63	1.65

	garnet orthopyroxenite (GO)											
	SAX37	SAE135	SAE157	SAE127	SAE114	SAE149	SAE151	SAE155	SAE126 core	SAE126 rim	SAE137 core	SAE137 rim
Clinopyroxenes												
La	1.39	0.94	1.41						1.70	1.66	1.74	
Ce	5.38	3.91	5.77						6.87	6.56	6.74	
Pr	0.95	0.71	0.97						1.26	1.13	1.16	
Nd	4.42	3.45	5.19						5.83	5.47	5.98	
Sm	1.95	1.32	1.83						2.02	1.90	1.85	
Eu	0.66	0.42	0.68						0.74	0.65	0.71	
Dy	1.61	1.38	1.67						1.69	1.70	1.94	
Er	0.88	0.72	0.73						0.78	0.94	0.73	
Yb	0.48	0.53	0.53						0.50	0.52	0.66	
Lu	0.08	0.10	0.09						0.10	0.09	0.09	
Garnets												
La	0.04	0.03	0.03	0.03	0.02	0.03	0.03	0.02	0.03	0.02	0.03	0.03
Ce	0.23	0.24	0.26	0.25	0.19	0.22	0.25	0.21	0.26	0.26	0.24	0.24
Pr	0.10	0.09	0.10	0.11	0.08	0.08	0.10	0.09	0.11	0.09	0.09	0.09
Nd	0.77	0.84	0.86	0.96	0.89	0.94	0.95	0.81	0.81	1.00	0.90	0.81
Sm	0.88	0.84	1.10	1.06	0.97	1.08	1.12	0.94	0.95	0.87	1.00	0.95
Eu	0.60	0.47	0.58	0.60	0.55	0.59	0.65	0.58	0.56	0.60	0.59	0.59
Dy	6.23	5.92	5.90	6.96	6.26	6.55	6.63	6.40	5.77	5.83	5.72	6.32
Er	5.57	5.47	5.15	5.73	5.54	5.61	5.78	5.36	5.33	5.33	4.75	5.44
Yb	4.95	5.44	5.04	5.38	4.95	5.22	5.46	5.10	4.68	4.86	4.42	5.26
Lu	0.90	0.97	1.02	0.83	0.77	0.96	0.99	0.93	0.86	0.82	0.63	0.80

Table 4-7. REE abundances in clinopyroxenes and garnets from HT-type garnet orthopyroxenites (GO)

	garnet orthopyroxenite (GO)						
	SAE136						SAE139
	Cpx	Grt					Cpx
		Spot1	Spot2	Spot3	Spot4	Spot5	
La	2.43	0.03	0.04	0.04	0.02	0.12	1.31
Ce	8.13	0.24	0.23	0.22	0.24	0.37	5.20
Pr	1.36	0.06	0.09	0.09	0.10	0.10	0.93
Nd	6.25	0.60	0.73	0.96	1.06	0.83	4.89
Sm	2.10	0.71	0.74	0.79	0.96	0.89	1.82
Eu	0.83	0.39	0.34	0.44	0.57	0.60	0.65
Dy	1.62	3.28	3.48	3.49	4.17	6.26	1.90
Er	0.63	2.36	2.72	2.98	3.08	5.26	0.85
Yb	0.62	2.77	2.63	2.87	3.15	5.22	0.68
Lu	0.07	0.36	0.40	0.41	0.51	0.80	0.09

	SAE139						
	Grt1						Grt2
	Spot1	Spot2	Spot3	Spot4	Spot5	Spot6	
La	0.02	0.04	0.03	0.04	0.04	0.04	0.02
Ce	0.24	0.27	0.33	0.33	0.31	0.28	0.25
Pr	0.10	0.10	0.13	0.10	0.13	0.12	0.08
Nd	1.04	1.05	0.99	1.14	1.07	1.09	0.85
Sm	0.95	1.05	0.78	1.22	1.34	1.25	0.84
Eu	0.56	0.67	0.42	0.71	0.71	0.71	0.59
Dy	4.09	6.97	4.54	7.33	7.36	7.67	6.11
Er	3.02	5.41	3.79	6.19	6.51	6.21	5.49
Yb	3.08	5.44	3.77	5.97	5.93	5.90	5.19
Lu	0.50	0.84	0.56	0.87	0.90	0.90	0.81

Table 4-8. REE abundances in clinopyroxenes and garnets from HT-type garnet lherzolites (GL) and spinel harzburgite (HTSH).

	garnet lherzolite (GL)								
	SAG1				SAG7	SAG9		SAG15	SAG30
	Cpx1		Cpx2			core	rim		
	core	rim	core	rim					
Clinopyroxenes									
La	3.55	3.44	3.58	3.95	2.95	2.58	2.64	2.52	2.57
Ce	12.8	12.7	13.4	14.3	12.5	9.27	9.69	9.54	10.5
Pr	1.90	1.94	1.93	2.13	1.39	1.51	1.57	1.64	1.88
Nd	6.61	6.98	6.92	7.65	3.91	6.06	6.63	8.04	9.21
Sm	1.01	1.08	1.09	1.11	0.78	1.85	1.86	2.46	3.09
Eu	0.30	0.33	0.34	0.37	0.28	0.69	0.64	0.95	1.16
Dy	0.78	0.85	0.88	0.93	0.75	1.30	1.30	1.77	2.40
Er	0.38	0.47	0.49	0.44	0.22	0.48	0.48	0.66	0.85
Yb	0.35	0.35	0.33	0.33	0.25	0.40	0.40	0.56	0.65
Lu	0.07	0.07	0.07	0.06	0.05	0.05	0.06	0.10	0.11

	garnet lherzolite (GL)			spinel harzburgite (HTSH)					
	SAG21		SAG27	SAS1	SAS8	SAS21	SAS46	SAS63	SAS69
	core	rim							
Clinopyroxenes									
La	1.88	1.85	1.93	1.58	2.45	2.03	1.98	2.82	2.85
Ce	7.39	7.30	7.88	6.81	10.3	8.56	7.91	11.0	11.7
Pr	1.35	1.27	1.41	1.11	1.67	1.38	1.51	1.96	2.13
Nd	6.65	6.20	7.12	5.36	8.10	6.97	6.78	8.92	10.8
Sm	2.33	2.16	2.36	2.04	2.99	1.05	1.00	2.96	3.77
Eu	0.81	0.74	0.89	0.68	1.12	0.22	0.26	1.25	1.38
Dy	1.75	1.95	2.13	1.68	2.32	0.16	0.22	2.99	3.67
Er	0.76	0.76	0.88	0.77	0.99	0.16	0.09	1.07	1.48
Yb	0.56	0.57	0.62	0.54	0.75	0.15	0.13	0.83	0.83
Lu	0.09	0.07	0.13	0.11	0.13	0.03	0.02	0.13	0.14

	garnet lherzolite (GL)						
	SAG1				SAG7		
	Grt1		Grt2		core	mantle	rim
	core	rim	core	rim			
garnets							
La	0.05	0.04	0.04	0.05	0.06	0.04	0.07
Ce	0.35	0.40	0.46	0.45	0.41	0.42	0.49
Pr	0.06	0.10	0.14	0.18	0.09	0.08	0.10
Nd	0.25	0.41	1.05	1.19	0.32	0.39	0.59
Sm	0.34	0.32	0.39	0.50	0.45	0.37	0.43
Eu	0.21	0.22	0.23	0.28	0.25	0.23	0.26
Dy	3.00	2.98	2.92	3.41	2.66	2.99	2.81
Er	2.79	2.73	2.78	3.09	2.13	2.60	2.37
Yb	2.89	2.86	2.83	3.27	2.89	2.92	2.98
Lu	0.54	0.46	0.51	0.54	0.53	0.55	0.60

	garnet lherzolite (GL)						
	SAG9		SAG15	SAG21		SAG27	SAG30
	core	rim		core	rim		
garnets							
La	0.07	0.05	0.05	0.03	0.04	0.03	0.02
Ce	0.35	0.36	0.35	0.29	0.25	0.34	0.29
Pr	0.09	0.12	0.14	0.10	0.10	0.12	0.13
Nd	0.59	0.99	1.01	0.80	1.08	1.23	0.97
Sm	0.58	0.81	1.00	0.68	1.12	1.31	0.71
Eu	0.37	0.43	0.60	0.44	0.64	0.84	0.38
Dy	3.66	4.67	5.10	4.13	6.13	7.02	3.00
Er	3.09	3.99	3.80	3.28	4.87	5.77	2.65
Yb	3.18	4.02	3.63	3.31	4.55	5.26	2.58
Lu	0.51	0.64	0.59	0.61	0.78	1.05	0.46

Table 4-9. Depleted mantle source composition (ppm), partition coefficients, source mode and melting mode for modeling calculations

Element	La	Ce	Nd	Sm	Eu	Dy	Er	Yb	Lu
depleted source	0.256	0.837	0.923	0.362	0.147	0.687	0.453	0.470	0.072
ol/melt!	0.00004	0.00006	0.00031	0.00065	0.00075	0.0027	0.011	0.027	0.03
opx/melt!	0.0028	0.0032	0.0041	0.0058	0.0078	0.012	0.022	0.039	0.053
cpx/melt!	0.065	0.09	0.19	0.3	0.4	0.52	0.55	0.58	0.53
sp/melt!	0.00002	0.00003	0.00004	0.00009	0.00014	0.00021	0.00033	0.00046	0.0008
grt/melt!	0.009	0.035	0.19	0.67	1.15	2.6	3.35	5.94	5.92

mineral	Ol	Opx	Cpx	Sp	Grt
source mode1	0.516	0.292	0.170	0.022	
source mode2	0.513	0.341	0.131	0.015	
source mode3	0.531	0.177	0.273		0.019
melting mode1	-0.06	0.28	0.67	0.11	
melting mode2	-0.14	-0.05	1.08	0.11	

Depleted mantle source composition, all partition coefficients and source mode 1 after Yang et al. (1998). Source mode 2 and 3 are obtained from Niu (1997) and Walter (1998). Melting mode 1 and 2 are from Kinzler (1997).

5 Discussion

5-1 Petrogenesis of LT-type pyroxenite (GW-SGC)

In contrast to observed heterogeneity of single sample or grain scale, variation represented by whole samples cannot be accounted by only metamorphic reaction and must be controlled by magmatic differentiation process. Fig. 5-1 displays whole range of the variation of Al_2O_3 in clinopyroxenes and CaO in garnets from LT-type pyroxenites, showing the systematic variations from GW, SGC1 to SGC2. The LT-type pyroxenite suites may represent cumulates formed at various stages of crystal fractionation involving with clinopyroxene, orthopyroxene, spinel and garnet. Textural, major element and REE variations may give some constraints for inferred crystallization history. Equilibrated pressures of each samples determined by geothermobarometry is limited below 3.0 GPa, suggesting crystallization might have been occurred below 3.0 GPa except for the consideration that they crystallized in rapid upwelling diapir of mantle (e.g. Herzberg, 1978; Suen and Frey, 1987). However, polybaric crystallization process do not need for explaining observed variations. Furthermore, both pyroxenes, spinel and melt assemblage is difficult to obtain above 3.0 GPa as constraints from melting phase relation. Therefore, crystallization history of LT-type pyroxenites can be explained by melting phase relation in the CMAS system below 3.0 GPa and monotonic decreases in temperature.

5-1-1 High pressure (below 3.0 GPa) fractionation model

Figs. 5-2 and 5-3 illustrate the liquidus phase relations in the system $CaMgSi_2O_6$-$CaAl_2Si_2O_6$-Mg_2SiO_4-SiO_2 at a pressure slightly below 3.0 GPa and schairer diagram focused on important liquidus invariant points (Milholland and Presnall, 1998). A decrease in pressure, invariant points (Fo) and (Grt) take off each other and both move away from Mg_2SiO_4 apex. While, as a pressure increasing both points approach each other and meet at 3.0 GPa along the aluminous pyroxene plane. This means that garnet and spinel lherzolite transition presents along the solidus at 3.0 Gpa in the CMAS system. This phase relation will apply the cumulate model for LT-type pyroxenites, which can be summarized as follows:

(1) SAE134 (GW1, Fig. 5-4a) originated as clinopyroxenite based on textural

observation and characterized by significant depletion of incompatible elements such as Na, Ti and REE. This feature is consistent that this bulk chemistry represents as liquidus clinopyroxene composition and the near-primary melt placed in the clinopyroxene volume. This interpretation may be connected with denial of peridotitic source material because the primary melt of peridotite melting must have crystallized olivine as the expansion of olivine volume by the dropped pressure (e.g. Kushiro, 1968; Presnall et al., 1979; Sen and Presnall 1984, Gudfinnsson and Presnall, 1996). On the other hand, considering basaltic source material, the primary liquid composition located near garnet-clinopyroxene plane and as the shrinking garnet volume by dropped pressure, the liquid composition can be inside the clinopyroxene volume. The origin of disappearance of liquidus olivine will be further considered in the later section.

(2) Primary mineralogy inferred by other GW1 is the assemblage of clinopyroxene, orthopyroxene (Fig. 5-4b) and with trace amount of spinel (Fig. 5-4c). Parallel REE variations among GW1 negate the presence of garnet as major crystallizing phase in this stage. By crystallizing clinopyroxene, orthopyroxene and spinel, the liquid located along the univariant line (Fo)-(Grt). It is noted that olivine must be absent at this stage, indicating that trace amounts of olivine might have reacted with the liquid and orthopyroxene and disappeared at invariant point (Grt). However, there is no evident that olivine was present. On the other hand, higher LREE/HREE feature of GW3 indicates garnet appeared before spinel crystallization. This interpretation may be supported by the absence of spinel, olivine and apparent exsolution texture. In this case, there was another liquid along the univariant line by crystallizing clinopyroxene, orthopyroxene and garnet. The destination of this liquid will not follow in later.

(3) As the temperature decreased, evolved liquid reached invariant point (Fo). At this point, preexisting orthopyroxene began to react with the liquid and garnet newly crystallized. Even if the liquid were separated before orthopyroxene perfectly consumed, with further decreasing temperature, orthopyroxene reacted with spinel producing sub-solidus garnet and olivine. Three of SGC1 containing olivine could represent as this cumulate (Fig. 5-4d).

(4) With further reaction, orthopyroxene might have been perfectly consumed at invariant point (Fo). After that, the liquid moved to leave (Fo) by crystallization of

clinopyroxene, spinel and garnet. Two of SGC1 and all of SGC2 could represent as the cumulate in this later stage, because any form of olivine does not present, showing sub-solidus orthopyroxene consuming reaction could not take place in these samples (Fig. 5-4e). Evolved nature of olivine-free SGC is revealed by grossular-rich garnet, CaTs-rich clinopyroxene and high LREE/HREE ratios in both phases.

(5) There are varied amounts of amphibole coexisting with other primary phases in texture. Although evolved SGC2 tend to higher abundance of amphibole, primitive GW1 also contain interstitial amphibole. Amphibole might have crystallized from trace amounts of trapped melt.

It is noted that this cumulate model does not adequately explain all of the variations, texture, major element and REE chemistry. Specifically, limited variation in Mg# must be evaluated for this cumulate model. Also this cumulate model cannot account for the origin of SGC3. These incoherencies will be considered later.

5-1-2 Incoherencies for high-pressure cumulate model

Why liquidus olivine is absent ?

There are two basic considerations for absence of liquidus olivine; (1) the primary melt crystallized olivine but never observed in LT-type pyroxenites (2) the primary melt did not saturate in olivine. If LT-type pyroxenites formed as cumulate in lithospheric mantle, they might have precipitated along the walls of peridotite similar to ‘mafic layers’ in orogenic peridotites (e.g. Suen and Frey, 1987; Takazawa et al. 1999; Garrido and Bodinier,1999). Generally, mafic layers are found in wall peridotites with sharp-flatted boundaries. In some cases, harzburgite and dunite are dominated as the wallrocks and interpreted as reaction products of magma/wallrock interaction (e.g. Kelemen et al., 1992). If olivine selectively precipitates along the wall, olivine component in magma may be removed from the part of pyroxenite and used as forming dunite or harzburgite. There are varied metasomatic signatures in LT-type peridotites, which represent as possible wall rocks, indicating magma/wallrock interaction significantly occurred. Although clinopyroxenes in studied harzburgites reveal serious Na, Ti, Fe and REE enrichment relative to those of lherzolite, their modal compositions and other mineral chemistry such as Mg# in olivine and Cr# in spinel are comparable for other restitic harzburgites (e.g. Johnson et al. 1990), suggesting the metasomatic process might have unchanged modal

abundance of olivine severely. On the other hand, if the primary magma crystallized olivine firstly, they must reach on olivine-clinopyroxene divariant surface and crystallized both simultaneously along the olivine-clinopyroxene cotectic. If former olivine clinopyroxenite are present, they may appear as the assemblage with olivine, clinopyroxene, garnet and orthopyroxene after metamorphism. There is a candidate in studied samples as the olivine garnet clinopyroxenite (SAE148), however high REE contents in the garnet and clinopyroxene is far from primary composition, indicating this rock originated as spinel websterite and olivine and garnet appeared by later metamorphic reaction. These apparent lacks of dunite, olivine-rich harzburgite and former olivine clinopyroxenite in studied samples may support that the primary magma did not saturate in olivine component. When the source material of LT-type pyroxenites are considered, the material derived from higher pressures may give some important constraints. In samples belonging HT-type, significant amount of pyroxenites present and there are some possibilities that they represent as restites after extraction of the primary magma for LT-type pyroxenites.

Why Mg# are stabilized?

Generally, when the cumulate model are evaluated, Mg# of rocks and constituent minerals give importance to read the crystallization sequence as one of the useful guide (e.g. Suen and Frey, 1987). However, Mg# of all phases in LT-type pyroxenites are restricted in the range similar to those of LT-type peridotite, suggesting those of Mg# must be controlled by another process. If mafic layer in orogenic peridotite is analogous to LT-type pyroxenite, their variations of Mg# may drop a hint. Takazawa et al. (1999) reported the presence of interlayer variations of Mg# in mafic layer from Horoman complex, Japan. The centers of thick (>75 cm) layers have lower Mg# than the margins and thinner layers. Also Mg# of the centers decreases as the distance from mafic layer-peridotite contact increases. They resulted that some of Mg# in mafic layers were controlled by diffusion of Fe-Mg exchange between mafic layers and host peridotites. Although in the case of xenolith study, it is difficult to detect the change of Mg# owing to small sizes of the specimens, some studies of composite nodule reveal the diffusion-controlled change of Mg# as a function of distance from the contact (e.g. McGuire 1987; Goto and Yokoyama, 1988). These evidences may imply Mg# of LT-type pyroxenite modified by later

diffusion process and homogenized equivalent to those of wall peridotites in spite of their unknown scale lengths and spatial relations in peridotitic mantle.

Melting residue or crystallizing cumulate ?

Alternatively, observed variations might have been generated by partial melting process, inspired by compositional characteristics of MORB which suggest the presence of residual garnet in their source (Salters, 1996; Hirshmann and Stolper, 1996). Many researchers have been believed that garnet signatures were originated from garnet pyroxenite entrained in peridotite matrix rather than garnet peridotite in the source region because high mantle potential temperature required for the melting in the garnet peridotite makes greater volumes of partial melt than observed crustal thickness (e.g. McKenzie and Bickle, 1988; Iwamori et al., 1995; Hirscmann and Stolper, 1996). If Lt-type pyroxenite derived from oceanic lithosphere, they may represent as partial melting residue, which once contributed to MORB generation. For these arguments, I will consider which models (partial melting and crystal cumulate) are preferred for accounting the generation of observed trends.

Fig. 5-5 exhibits reconstructed bulk compositions of LT-type pyroxenites based on modal and average mineral compositions. They are compared with experimentally determined liquidus topologies at 3.0 GPa (Milholland and Presnall, 1998). Although reconstructed bulk compositions may be erroneous because of combinations of poor-quality mode and heterogeneous mineral composition, the bulk rock major element abundances of selected samples, which determined by XRF analyses support that these values are meaningful. Furthermore, their compositions make clear line in CaTs-Ol-Qz plane as expected by petrographic observation and mineral chemistry. The trend is understood as near-parallel line to aluminous pyroxene plane mainly controlled by the presence of orthopyroxene and the compositions of garnet and clinopyroxene. According to increasing of modal spinel from GW1 to SGC2, the plots deviate from aluminous pyroxene plane toward Qz-poor side. If partial melting model can account for this trend, SGC2 might have been near parental material, while GW1 represents near liquidus compositions. For melting of SGC1, the initial melt occurs on the univaliant line in the coexisting spinel, garnet and clinopyroxene, which located in Qz-rich side of the plane. In the consideration that near-fractional melting are reasonable process worked in natural

system, solid residual trend is constructed along opposite way from the liquid compositions until one phase eliminate from the source. Therefore, residual trend formed by SGC2 melting is predicted to be away from aluminous pyroxene plane with decreasing in CaTs component of the bulk rock, however opposite trends are observed in the reconstructed bulk compositions such that Qz-poor rock (spinel-rich rock) have CaTs-rich bulk composition. Furthermore, fractional melting may fail to account for the presence of orthopyroxene-rich GW1. In Fig 5-5, the reconstructed bulk compositions are plotted along the aluminous pyroxene plane projected from Ol apex. Two samples from GW1 are distinctively rich in Opx component and they must plot in Opx volume as contrasted with others in Cpx volume. Compared to the three-phase field (dashed line), defined by experiments at the condition of 3.0 GPa and 1568˚C, the rock must have been consisted liquidus orthopyroxene and clinopyroxene rather than clinopyroxene exsolved orthopyroxene as subsolidus phase because unreasonable high temperature are needed for reproducing the composition by clinopyroxene solid solution. Because fractional fusion of parent material in Cpx volume must restrict the compositional change of solid residua within same volume, two orthopyroxene-rich GW1 cannot be reproduced by SGC2 melting. Similar arguments were appeared in Beeson and Jackson (1970), which suggested that compositional trend of Hawaiian garnet pyroxenite were controlled by fractional fusion based on comparison between predicted solid trends made by fractional fusion and crystallization on $CaSiO_3$-$MgSiO_3$-Al_2O_3 plane (see Figs. 10 and 11 in Beeson and Jackson, 1970). According to their interpretations, Opx component in solid residua must be highest in liquidus clinopyroxene and Opx rich rock are expected only fractional crystallization process. GW1 with lower Opx component have equivalent composition and texture as liquidus clinopyroxene (e.g. SAE134). These evidences suggest that an origin of observed trend might have been constructed by fractional crystallization as discussed before.

Origin of granoblastic spinel garnet clinopyroxenite (SGC3)

Granoblastic spinel garnet clinopyroxenite (SGC3) in LT-type pyroxenites is characterized by the contradiction between evolved major element compositions and depleted in REE contents. While SGC2 without granoblastic texture show no REE depletions, indicating that the process involving granoblastic texture formation must

have controlled their REE compositions. One of the important textural features of SGC3 is heterogeneous distributions of spinel. Spinels in SAE110 are localized to one side of the nodule and both sides of spinel abundances are distinctly different (0.3% and 2.5%). Heterogeneous nodule (SAE146) belonging to SGC2 has two types of morphology in garnet. Garnets in spinel-rich side have anhedral in morphology, while garnet in spinel–poor side shows typical granoblastic texture with straight grain boundary and triple junctions. Although there are no significant compositional differences between both sides, this textural variation may display that SGC2 change to SGC3. If SGC2 reheated after solidification by another high temperature melt, SGC2 might have fused in lower temperature owing to their evolved compositions. In that case, their granoblastic texture and depleted REE chemistry result from remelting process. Also if reheating occurred on a small scale with a thermal gradient, spinel might have been localized in due to lower modal abundance. This hypothesis is attractive to account for two characters simultaneously, however may require another corroborative evidence.

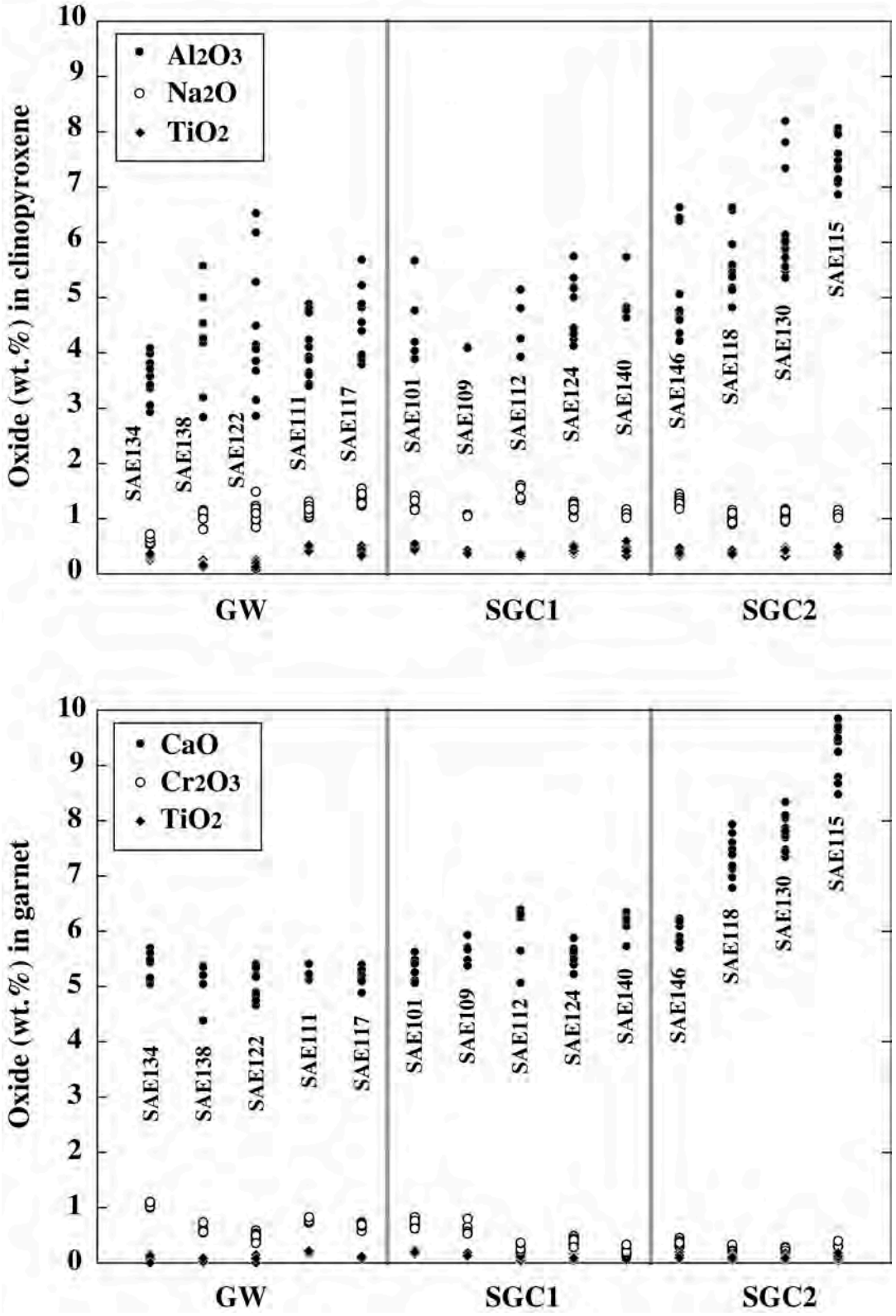

Fig. 5-1 The variations of Al_2O_3, Na_2O and TiO_2 in clinopyroxenes (upper) and CaO, Cr_2O_3 and TiO_2 in garnets from LT-type pyroxenites.

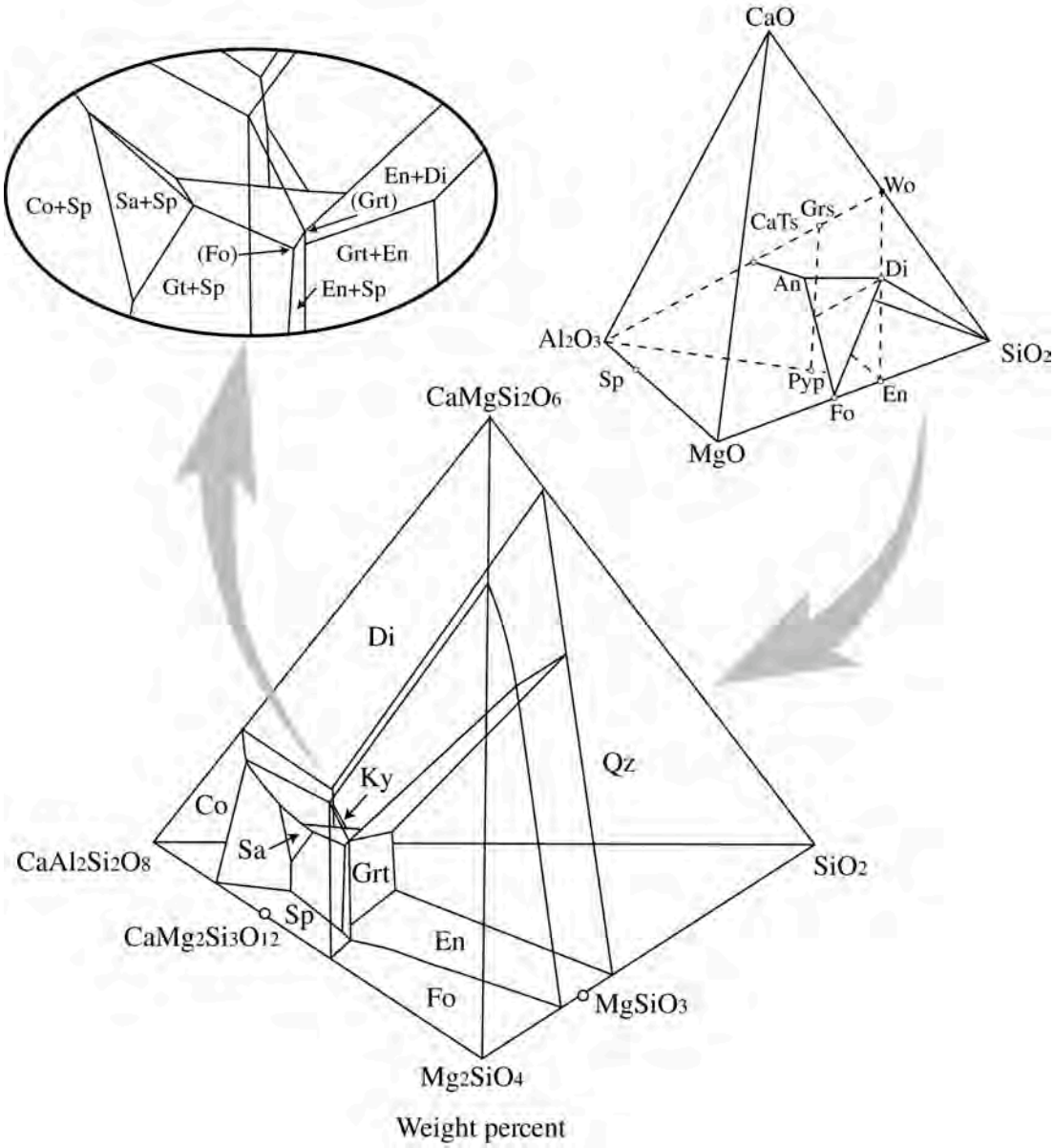

Fig. 5-2. Liquidus phase relations in the system $CaMgSi_2O_6$-$CaAl_2Si_2O_6$-Mg_2SiO_4-SiO_2 at a pressure slightly below 3.0 GPa (Milholland and Presnall, 1998). Phases in parentheses label some invariant points according to the absent phases in the reactions. Abbreviations are: Di=diopside, En=enstatite, Wo=wollastonite, CaTs=Ca Tschermak's molecule Sp=spinel, Fo=forsterite, Pyp=pyrope, Grs=grossular, Grt=garnet, Qz=quartz, Ky=kyanite, Sa=sapphirine, Co=corundum.

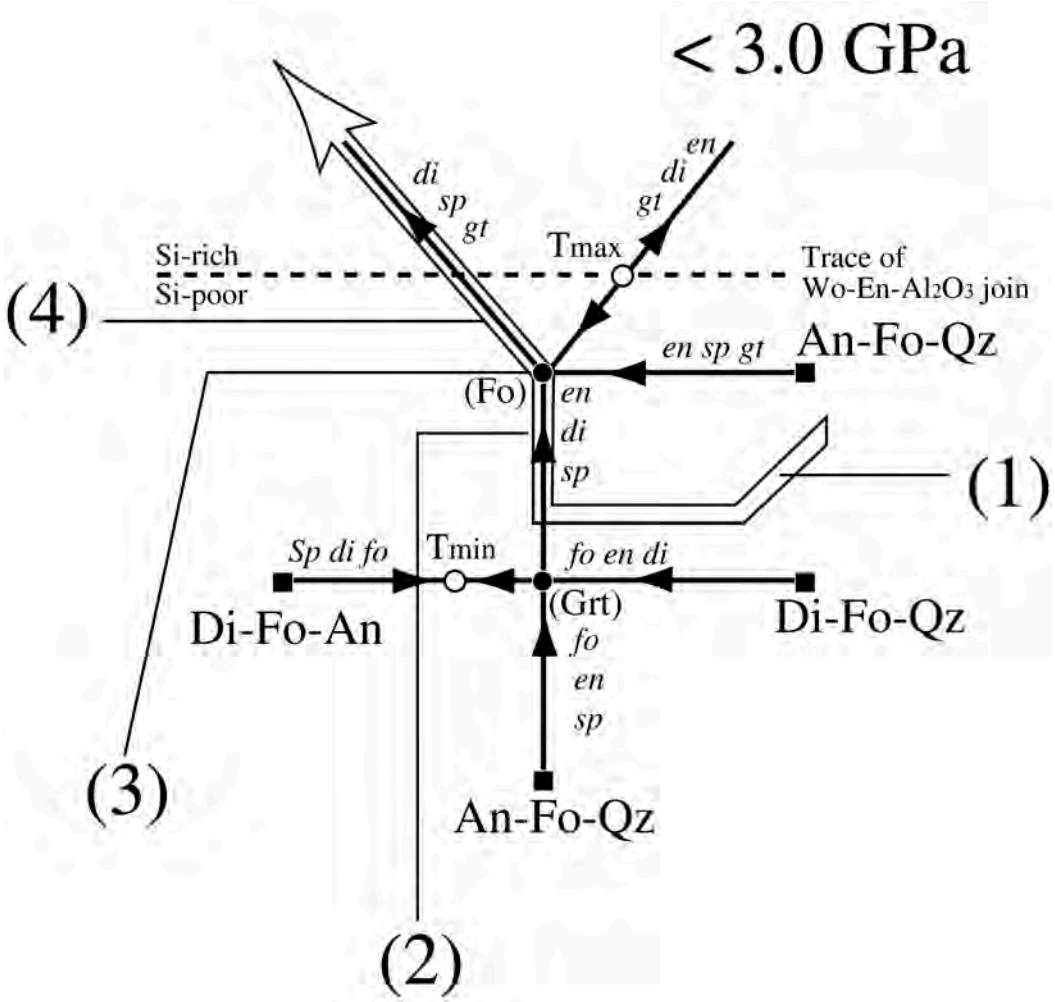

Fig. 5-3. Schairer diagram showing schematic arrangement of liquidus invariant points (filled circles) and univariant lines at a pressure slightly below 3.0 GPa (Milholand and Presnall, 1998). Invariant points labeled according to the absent crystalline phase in parentheses and univariant lines labeled according to the crystalline phase present. Black arrows indicate directions of decreasing temperature. Filled squares label faces of the tetrahedron. White arrow displays inferred crystallization pass which comprised the LT-type pyroxenites.

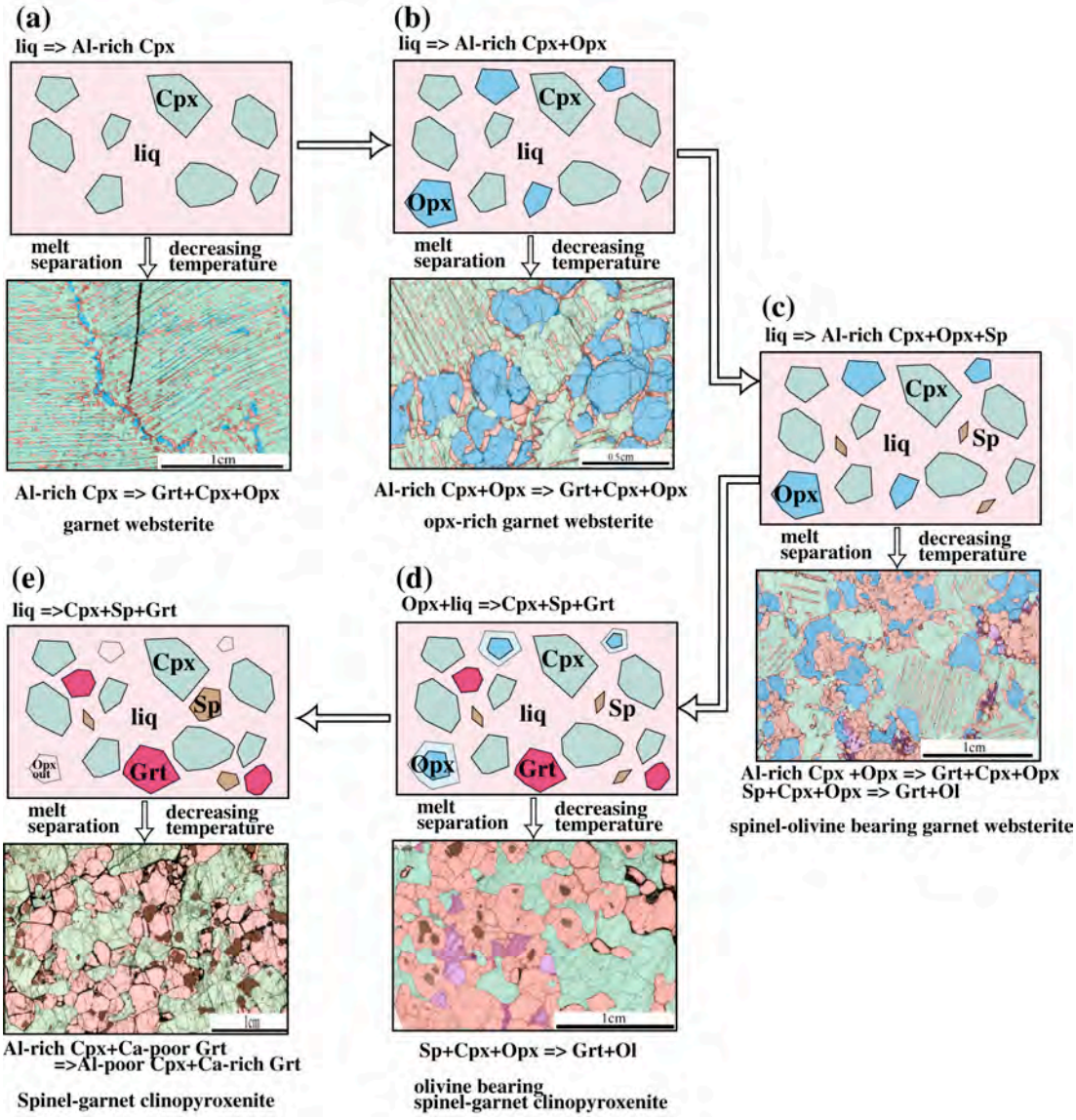

Fig. 5-4. Schematic illustrations of high-pressure cumulate model accounting for the systematic variations of lithology, texture and compositions in LT-type pyroxenite suites. Upper cartoons show the inferred primary assemblage coexisting with liquids. Arrows tied the cartoons indicate the direction of liquid evolution with decreasing temperature. Lower photographs exhibit present mineral assemblages after subsolidus recrystallization. For convenience, constituent minerals were colored as following: garnet, red; clinopyroxene, light green; orthopyroxene, light blue; spinel, brown; olivine, purple. See text for explanation.

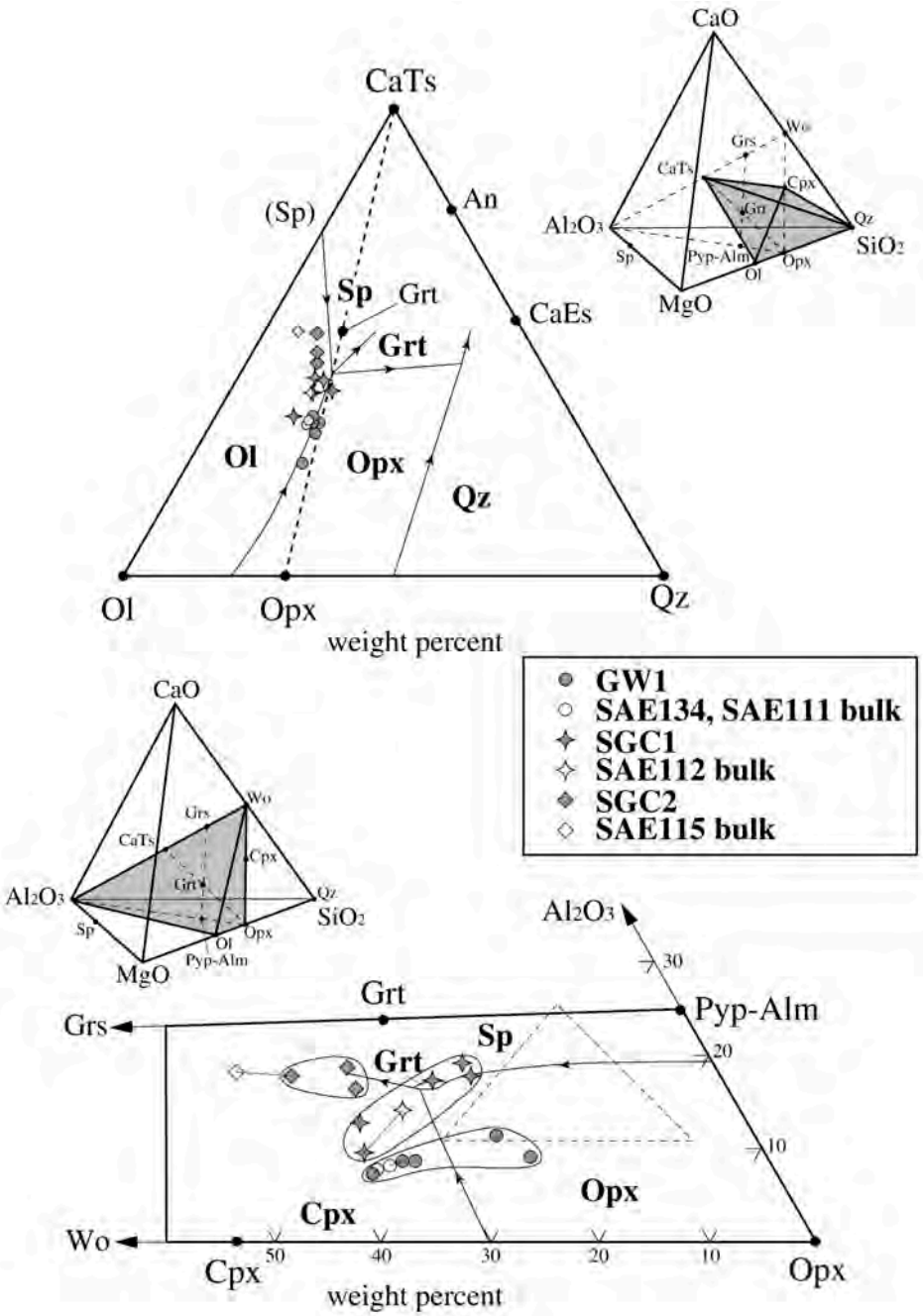

Fig. 5-5. Normative compositions of whole rock xenoliths (reconstructed: filled-gray symbols, XRF analyses: open symbols, same samples are tied by thin lines); Upper figure indicates that projections from clinopyroxene (Cpx: diopside-hedenbergite) onto olivine (Ol: forsterite-fayalite)-Ca Tschermak molecule (CaTs)-quartz (Qz) plane comparing with diopside saturation surface of liquidus phase relations at 3.0 GPa (Milholand and Presnall, 1998), Lower figure shows the projections from Ol onto Al_2O_3-$CaSiO_3$(Wo)-orthopyroxene(Opx: enstatite-ferrosilite) plane (lower). Bold lines are liquidus boundary lines for the join Di-En-Pyp-Grt (Grs : Pyp=1 : 2) at 3.0 GPa (Milholand and Presnall, 1998). Dashed lines connect coexisting diopside, enstatite and garnet compositions in equilibrium with liquid.

5-2 Petrogenesis of LT-type peridotite (SL-GSL)

5-2-1 LT-type spinel peridotite

Two stage evolution model

Mineral compositions and REE contents in clinopyroxene from LT-type spinel peridotites reveal their close similarity with group I peridotite xenoliths from world-wide localities (McDonough and Frey, 1989). Generally, REE patterns of group I peridotite xenoliths display a wide range from relative to LREE-enrichment to LREE-depletion. They can be accounted for a two stage evolution model; (1) partial melting of an initially undepleted peridotite, (2) metasomatic addition or interaction with a mobile melt or fluid and both combinations with degree of (1) and (2) make their diversity (Frey and Prinz, 1978). Variable LREE-enriched patterns with large inflections in clinopyroxene can be attributed by chromatographic metasomatism that trace elements in melt or fluid, which percolated into matrix peridotite fractionate according to their bulk solid/melt partition coefficients (e.g. Navon and Stolper, 1987; Bodinier et al., 1990; Takazawa et al., 1992; Hauri and Hart, 1994; Bedini et al., 1997). On the other hand, inverse correlation between LREE abundances and refractoriness of the peridotite have been usually observed in each localities and pointed out that they could be achieved by single process such as LREE-enriched melt/fluid influx melting (e.g. Ozawa and Shimizu, 1995) or harzburgite formation by ascending melt / wall rock reaction (Kelemen et al., 1992). For studied samples, there is a possibility that REE enrichment coupled on major element depletion process on group3 harzburgite because all samples have clinopyroxene without LREE-depleted patterns. However, it is difficult to presume how process was dominated for group3 harzburgite because: (1) several REE patterns with inflected at Dy or Er indicate that chromatographic fractionation process were worked on these samples. (2) No correlations between observed REE patterns and major element composition were detected among group3 harzburgite. On the other hand, less-depleted group1 and 2 displays significant variable patterns from LREE-depleted to enriched relative to restricted HREE abundances and refractoriness. No correlation between LREE enrichments and HREE depletions in group1 and 2 supports that the depletion process may be decoupled and preceded the enrichment process in most of studied samples.

Fig. 5-6 illustrates the schematic representation of the melt/peridotite reaction model proposed by Bodinier et al (1990) based on detailed study of Lherz orogenic peridotite. When conduits of infiltrated magma develop in host peridotite, various metasomatic modifications are given host peridotites according to their composition and distance from conduits. Diffusion-controlled metasomatism occurs in the wall-rocks, whereas percolation-controlled metasomatism occurs further into the host. In the case harzburgite matrix, metasomatic effects of infiltrated magma reach to further into host than lherzolite matrix. Although this feature has been accounted for higher melt permeability in olivine-rich harzburgite than pyroxene-rich lherzolite (Toramaru and Fujii, 1986), model calculations by Bedini et al. (1997) suggest that for the case that low porosity values are used (0.1 %), only differences of modal composition and initial REE content are needed for enhancing the contrasted evolutions of REE in clinopyroxene from harzburgite and lherzolite.

If two stage evolution model is valid for accounting the observed variation, former partial melting process can be read by using weaker-modified samples and/or indicators such as Cr# in spinel, Fo# in olivine and HREE in clinopyroxene. Their variations of studied samples are equivalent to those of abyssal peridotites and need the near-fractional melting process with < 20% degree based on REE variations in clinopyroxenes. Although abyssal peridotites show significant variations from larger scale, such as Mid-Atlantic, Indian and Pacific Ocean, intermediate scale such as distance from hotspot region, to smaller scale, such as distance from ridge axis along the fracture zones (Johnson et al., 1990; Johnson and Dick, 1992; Dick and Natland, 1996; Ross and Elthon, 1997), all of them originated from the surface of uppermost mantle and can not be directly compared with the variations of xenoliths which originated from various depths. Abyssal peridotites are usually regarded as the most melted peridotites from the top of the mid-ocean ridge melting column. Most depleted harzburgite in LT-type peridotites also support that they represent as fragments of oceanic mantle lithosphere after MORB generation based on equivalent values of Cr# in spinel and HREE in clinopyroxene.

Variations between temperature and depletion

If LT-type of spinel peridotites derived from varied depth in the residual mantle column formed after former partial melting, their depletions should correlate

with derived depths. One of the questions for studied spinel peridotites is whether temperatures estimated by two-pyroxene thermometer represent their derived depths or not. In light of this question, two variations between temperature and Yb_N may give significant constraints. There is correlation between temperatures and Yb_N in weaker-metasomatised samples, temperatures decreases with lowering Yb_N. This correlation is consistent with the hypothesis that these regarded as residues of melting column at spreading ridge, later metamorphosed in lower temperature according to their depth and distance from the active ridge. On the other hand, LREE enriched samples tend to show higher temperature relative to same Yb_N (Fig. 4-13). This evidence implies that migrating magma raised temperature of matrix peridotite. Therefore, pyroxene temperatures in LREE enriched samples recorded the progressive temperature changes by melt/rock interaction or retrograde metamorphism controlled by the geotherm, which was imperfect. If the olivine-spinel temperature of LREE-enriched samples can monitor the thermal history of individual samples, this hypothesis may be verified. In assuming that olivine-spinel Mg-Fe exchange were quenched at the time entrapped by host alnöite, if local heating raised the two-pyroxene temperature in low temperature domain, the magnitude of disparity of calculated temperature values between both methods may change from those in other samples, which constantly cooled according to geothermal gradient change. In the case that pre-heating event was occurred shortly before entrapment, the disparity between both must be smaller than those in others. On the other hand, if pre-heating event preceded the entrapment with significant time interval and two-pyroxene temperature were stayed at higher than actual temperature, the disparity may become larger than others because olivine-spinel temperature is easy to approach of actual temperature. However, observed strong correlation between two-pyroxene and olivine-spinel temperature could not give any constraints for the hypotheses.

Another considerations are derived from P-T variations of GSL, GW and group1 SL. The plots by two-pyroxene temperature and Al in orthopyroxene pressure in GSL display clear line in spite that they display variable degrees of REE enrichment and abundance of amphibole, showing that two-pyroxene temperature about 900-1000˚C recorded by retrogressed temperature (Fig. 3-16). Furthermore, if GW precipitated as cumulate from the melt representing the heat source for host

peridotite, they should hold highest temperature at the time which metasomatism proceeded. Lowest temperature and pressure estimated from SAE122 strongly indicate that two-pyroxene temperatures in the matrix peridotite with the equivalent derived depth (855˚C and 17.2 kb) must be retrogressed. Although group1 SL suffered variable degree of metasomatic process indicated by variable LREE-enrichment in clinopyroxenes, their two-pyroxene temperatures display limited variations (approximately 900-1000˚C) below those of group3 harzburgites. This evidences are also accounted that two-pyroxenes recorded retrograde temperatures after the metasomatic process and they may indicate that their derived depth. One convenient explanation for that REE-enriched group2 and 3 could not take retrogressive temperatures is that their derived depth was too shallow and actual temperature was too cool for reaction proceeding. Then, the critical boundary whether retrogressive reaction achieved or not might have located approximately 850˚C.

As another interpretation for the origin of correlations of REE enrichment and temperature, there is the possibility that two-pyroxene temperature of all samples might have been reflected the derived depth and the correlation was related to the different generation of harzburgite. If harzburgite formed by melt/rock reaction process (Kelemen et al., 1992) or LREE-rich melt infiltrated melting (e.g. Ozawa and Shimizu, 1995), such processes could be dominated at the base of lithosphere, which would receive high rate of melt influx from asthenosphere. Although this hypothesis would explain strong REE enrichment and high-equilibrated temperature in some harzburgite simultaneously.

At present, it is difficult to choose the accounting for the strong correlation REE enrichment and two-pyroxene temperature. Further detail investigations for compositional zoning of constituent minerals are obviously demanded for evaluation. However, it is important to note observed correlation between temperature and refractoriness in weak-modified sample must be produced by former partial melting event similar to mid-oceanic ridge process.

Constraints for former partial melting process

Over the years, in order to constrain dynamics of melt production on ridge and compositional variation of MORB, many studies such as thermodynamic,

experimental and geochemical basis have been conducted (e.g. Klein and Langmuir, 1987; McKenzie and Bickle, 1988; Johnson et al., 1990; Salters and Hart, 1991, Kinzler, 1997). General model of ridge melting is accepted as adiabatic decompression melting of asthenospheric mantle during upwelling by many researchers. One of the important parameter for settling each locality of MORB composition is the melt fraction of each depth which source melting occurs because MORB has been believed as aggregates of segregated melt from variable pressure range. The detail studies of abyssal peridotite have given the information of melt fraction from assumed source, which required near-fractional melting (Johnson et al., 1990). However, abyssal peridotite represents only the uppermost part of residual mantle column. The study of lithospheric xenoliths is the only and direct way for the knowledge of the bottom of residual mantle column and may have a distinctive advantage for these purposes.

REE patterns in clinopyroxene from LREE-depleted group1 and group2 show strong similarity of those in abyssal peridotite, however significant difference is appeared in Fig. 5-7. Actually, large REE variations given on one location is only available from the study of Atlantis II fracture zone, which is located along Southwest Indian Ridge (Johnson and Dick, 1992). The difference is characterized by high Yb abundances given Sm/Yb ratio relative to Atlantis II peridotite field. One interpretation for this discrepancy may result the different degree of low-temperature recrystallization according to age difference. Although actual age of studied xenoliths is unclear, they must be older than most of abyssal peridotite which were recovered near active ridge. Decreasing of modal clinopyroxene during subsequent cooling stage can account for high Yb abundance with nearly constant Sm/Yb in clinopyroxene from group1 and group2 xenoliths. However, relative to depleted Hawaiian xenoliths, whose age estimated about 90 Ma, the difference is still large enough (Yang et al., 1998). This evidence indicates that there is the possibility that high Yb nature attributed to the difference of melting scheme. Fig. 5-7 also demonstrates the result of model calculations of spinel lherzolite melting. First model was calculated by using the similar parameters accounting for the Atlantis II and Hawaii. Calculated REE patterns are plotted in Fig. 4-11. The result clearly shows that source composition or source mode do not fit for high Yb nature of group1 clinopyroxene because bulk solid/melt D_{Yb} is below 1 in spinel lherzolite melting. If

modal clinopyroxene of source peridotite is permitted to change from 18 to 13 % with identical source composition (model 2 in Fig. 5-7; source mode 2 in Table 4-9), group1 and group2 compositions can be reproduced by near-fractional melting within spinel peridotite stability field. However, if considering an alternative model that first melting occurred within garnet peridotite stability field, high Yb_N in group1 lherzolite may be accounted because bulk solid/melt D_{Yb} increase. During garnet peridotite melting, clinopyroxene component significantly eliminates from solid residue with leaving high Yb abundance in due to the presence of garnet. For model calculation of garnet to spinel peridotite melting, multistage model involving decompression reaction of the residual garnet have been used (Johnson et al., 1990; Hauri and Hart, 1994). Then, reaction coefficients not only garnet peridotite melting but also garnet decompression are critical for the results of model calculation because clinopyroxene mode is largely changed between garnet and spinel stability field in due to solid solution effect. Although reasonable coefficient cannot be selected at present state, group1 composition may be attained by relatively low degree of melting in garnet peridotite.

Another REE character is found in the shape of trend in $(Sm/Yb)_N$ and Yb_N field. From group1 to group2, clinopyroxene REE variation exhibits large change of Sm/Yb ratio with relatively small change of Yb abundance, while Sm/Yb ratio remains nearly constant with larger Yb variation between group2. Generally, in the case of spinel peridotite melting, the slope of trend is controlled by clinopyroxene proportion entering in melt. High contribution of clinopyroxene (high *P* Cpx) makes steep trend, while low contribution of clinopyroxene (low *P* Cpx) produces gentle trend. Curve of model 2 is reproduced by multistage model that melting mode of clinopyroxene is changed at 6% of melting from high *P* Cpx (melting mode 2) to low *P* Cpx (melting mode 2), showing the model fits the data better than using single melting mode. Kinzler (1997) experimentally determined the melting stoichiometry of spinel peridotite at pressures from 1.5 to 2.3 GPa. The result demonstrated that coefficient for clinopyroxene appears to increase with increasing P according to compositional change of liquid. In further high pressure, garnet peridotite melting also enhances angle of slope toward standing. Therefore, this evidence indicates that observed slope change from group1 to group2 is attributed to polybaric melting with pressure dependent *P* Cpx and/or garnet involvement. This interpretation is

consistent that they represent as residual mantle column related to MORB generation, which accounted by adiabatic decompression melting.

5-2-2 LT-type garnet bearing peridotite

Garnet-Spinel transition

Petrological observations of LT-type GSL reveal that most of them originated as spinel peridotite and garnet appeared at lower temperatures by metamorphic reaction,

Spinel + Pyroxene = Garnet + Olivine

Experimental investigations have been indicated garnet-spinel transition depends on the composition of peridotite; lower pressure on fertile peridotite and higher pressure on depleted peridotite (e.g. O'Neil, 1981; Robinson and Wood, 1998), showing that the garnet-spinel transition boundary determined by pyrolite III composition give minimum pressures for normal depleted peridotite. Estimated limitations for existence of fertile spinel lherzolite were about 1000˚C by two-pyroxene thermometry, whereas the lowest pressure and temperature for GSL about 900˚C at 2.0 GPa. Judgment from these estimations, garnet-spinel transition for LT-type peridotite intersect with the geotherm about 900-1000˚C at 2.0-2.2 GPa. This estimation is 2-4 kb higher pressure than those of pyrolite, showing consistency with their depleted compositions relative to pyrolite.

Origin of GSL protolith

HREE abundances in clinopyroxenes are very sensitive to garnet appearance and they usually display HREE depletions. Some of the samples with lesser amounts of garnet preserve REE contents in original clinopyroxene, which display close similarity with those of group1 spinel lherzolite. Although it is difficult to estimate REE abundances of bulk and original clinopyroxene, it is clear that their abundances are equivalent to those of spinel lherzolite rather than spinel harzburgite. This evidence shows consistency with common occurrences of spinel and clinopyroxene. This interpretation indicates that limited partial melting occurred in spinel peridotite field and they entered in garnet stability field later according to decreasing temperature. They might have been formed by low degree of partial melting and composed the part of melting column where LT-type spinel peridotite melted.

Furthermore, there is the possibility that some of spinel-free garnet lherzolite preserve primary garnet. In that case, they did not enter in spinel lherzolite field or did not cross the peridotite solidus. However, similar to LT-type spinel peridotite, various degree of LREE enrichment is observable in all clinopyroxenes in GSL. At present state, it cannot be determined whether melting occurred in garnet peridotite field or not from these samples because the signatures of low degree of melting before metasomatism are difficult to detect.

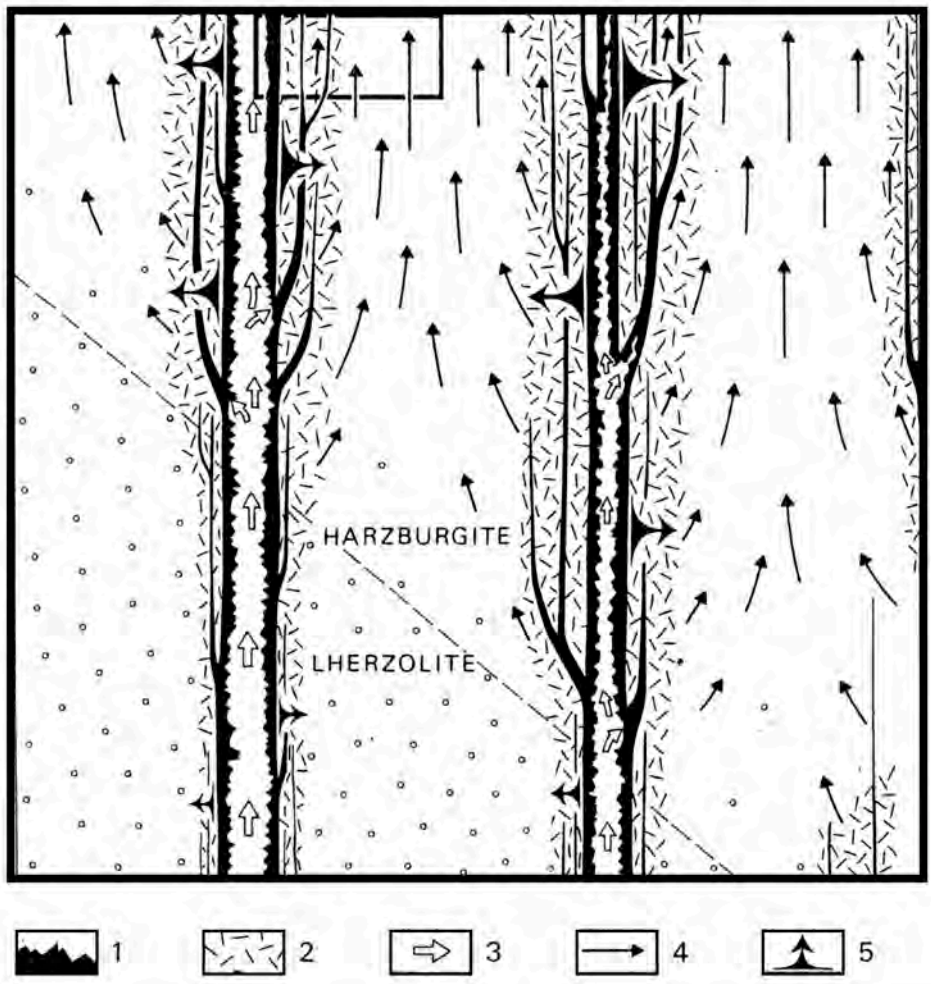

Fig. 5-6. Schematic illustration of the model of silicate-melt metasomatism showing infiltration of basaltic melt into lherzolite and harzburgite hosting vein-conduits (Bodinier et al., 1990). The horizontal scale is about 5-20 m and the vertical scale is 20-200 m. 1: Mineral segregates in vein-conduits; 2: amphibole peridotites; 3: magma flow in vein-conduits; 4: porous-flow percolation in the harzburgite host peridotites; 5: diffusion through the infiltrated melt phase.

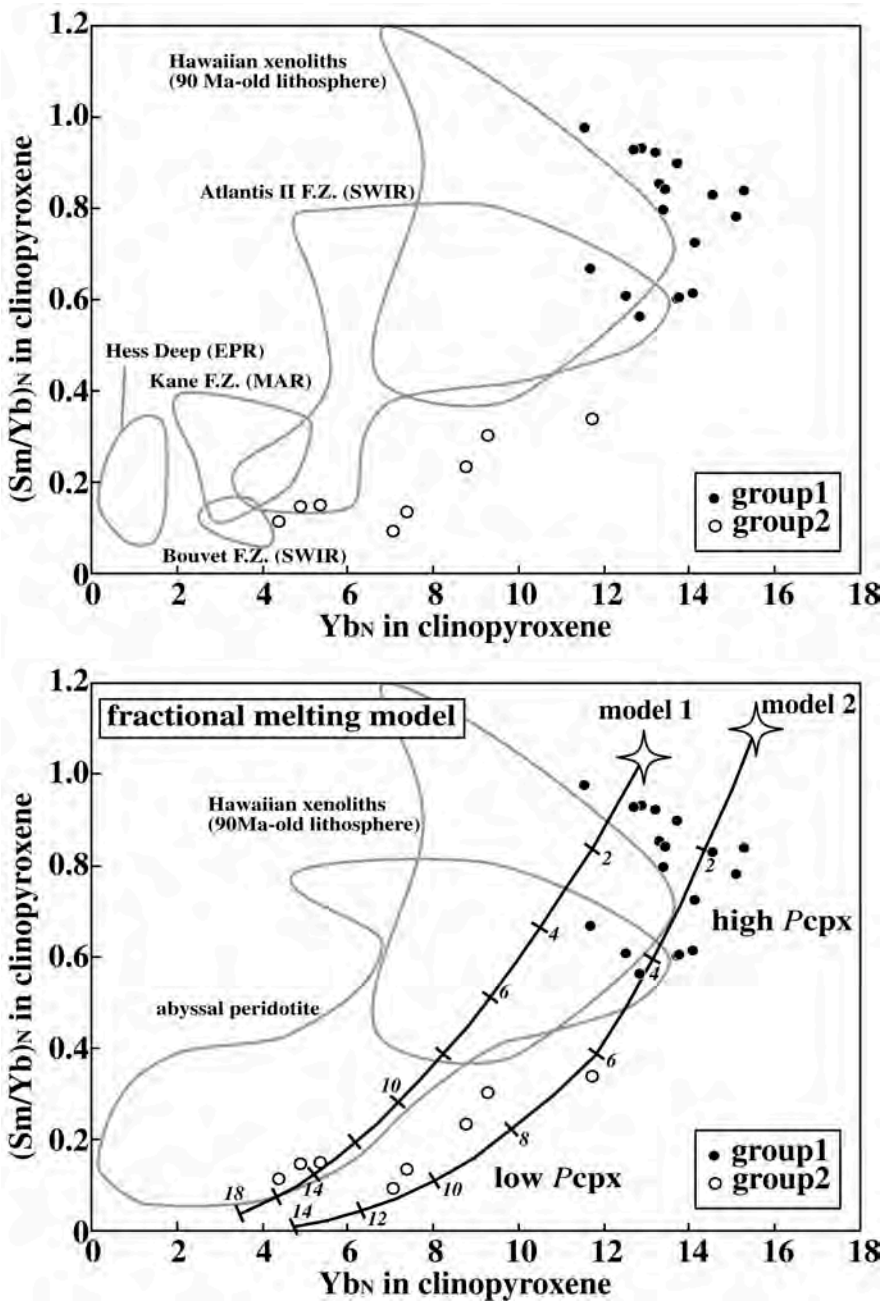

Fig. 5-7. Upper: $(Sm/Yb)_N$ ratio versus Yb_N diagram for comparing between abyssal peridotite (data sources are same in Fig. 4-12), Hawaiian xenoliths (Yang et al., 1998) and LT-type spinel lherzolite from Malaitan xenoliths (upper). Lower: The results of modeling calculations expressed as residual clinopyroxene trends for the fractional melting of spinel peridotite. Two curves (model 1 and model 2) indicate different source and melting mode with identical source composition and partition coefficients, which are listed in table 4-9. Numbers with bar on the curves indicate extent of melting (%). Source mode 1 and melting mode 1 are used for model 1, while source mode 2 and melting mode 2 (0-6%) and 1 (> 6%) are used for model 2.

5-3 Petrogenesis of HT-type pyroxenite

5-3-1 Characteristics of quartz-garnet clinopyroxenite (QGC): Comparison with the products of melting experiments

The unique occurrences of the xenolith with eclogitic assemblage in oceanic regions may give important constraints for the diverse nature of Malaitan xenoliths and must be described in detail. Temperature estimation for SAE116 is available by use of the garnet-clinopyroxene thermometer. This value however must be considered to be on overestimation, as indicated by comparisons with two-pyroxene temperature estimations obtained on GO samples. Assuming that the equilibrated temperature of SAE116 is equivalent to those from GO, the equilibrium condition locates near the quartz-coesite boundary (Fig. 5-13). Although careful investigation for the presence of coesite was conducted by using a laser Raman spectrometer, the apparent lack of coesite itself and also as the psuedomorph suggest that SAE116 equilibrated in quartz stability field. Intersection between several reported quartz-coesite boundary lines (Bohlen and Boettcher, 1982: BB82 represented as lowest P, Boyd, 1964: B64 represented as highest P) and the geotherm consisting HT-type of rocks reveals that the equilibrated conditions of SAE116 is open to argument. Previous studies have been favored the quartz-coesite boundary line of Bohlen and Boettcher (1982), because numerous tight reversals were conducted in contrast to previous experimental determinations. However, quartz stability for SAE116 is mismatched with the line of Bohlen and Boettcher (1982) owing to higher-pressure equilibration for SAE116 inferred by the geotherm and temperature of GO. Although there are many unclear problems, I prefer that equilibrated P-T conditions for SAE116 was equivalent to those of GO giving weight to its resembrance to temperature estimates of other GC and GO.

Mineral chemistries for SAE116 are characterized by depleted compositions dissimilar to those of ‘normal eclogites’ with basalt protolith from metamorphic terrains, for example high Mg# in garnet and low Na contents in clinopyroxene (Table 5-1). These compositions are comparable for those of solid phases from (1) basalt melting, (2) homogeneous mixture of peridotite + basalt melting and (3) layered peridotite + basalt melting experiments at 3.0-3.5 GPa (Tables 5-2 and reference therein). Na and Ti contents in clinopyroxene and garnet in SAE116 are

barely plotted in the field of those from fused basalt or basalt + peridotite materials, showing the depletions are notable (Fig. 5-8). One of the important features of clinopyroxenes in SiO_2 saturated system is that CaEs component with M-site vacancies is stabilized by pressures above 3.0 GPa (Wood and Henderson, 1978; Smyth 1980; Gasparik 1986). The endmember calculations following Smyth (1980) reveal that clinopyroxenes in SAE116 contain detectable CaEs component with average 7 mol%. This evidence supports that SiO_2-rich characteristics was not a low-pressure incident and clinopyroxenes preserved the composition at high-pressure conditions. Furthermore, there is the possibility that significant amounts of quartz and garnet in SAE116 exsolved from clinopyroxene according to pressure and/or temperature change. If bulk composition, which were determined by XRF analysis, is represented as pre-exsolution clinopyroxene composition assuming its higher temperature origin, it contains 10 mol % of CaEs component. Common occurrences of CaEs-rich clinopyroxene have been reported from eclogite-grospydtie xenoliths in kimberlite and eclogite-pelitic gneiss in UHP metamorphic terrains and maximum values reach to 17 mol % (Smyth 1986; Katayama et al. 2000). Significant CaEs in clinopyroxenes are also observable in compilation values from basalt melting experiments. Fig. 5-9 plots the normative compositions of clinopyroxenes and bulk of SAE116 and various experiments projected from Cpx onto CaTs – Ol – Qz plane and from CaTs onto Cpx – Ol – Qz plane. In the case of starting material as basalt composition, all of them are plotted in Qz-rich side of the aluminous pyroxene plane and make further Qz-rich melt relative to starting compositions. Also coexisting clinopyroxenes tend to deviate from aluminous pyroxene plane toward Qz-rich side. On the other hand, starting compositions from homogeneous peridotite + basalt mixtures with their proportions from 2:1 to 1:3 are plotted in Ol-rich side and make Qz-poor relative to their starting compositions. Coexisting clinopyroxenes display limited variations along the aluminous pyroxene plane. Although both bulk and clinopyroxene of SAE116 are enriched in Opx component relative to those of basalt melting, they display close similarity in terms of Qz-rich, indicating that SAE116 coexisted with Qz-rich melt. Most of peridotite melting experiments have resulted that the production of SiO_2-rich tholeiitic magma must be forbidden above 3.0 GPa because the melt generated from garnet lherzolite melting have the composition of SiO_2-poor side of the aluminous pyroxene plane and cannot penetrate into SiO_2-rich

side by fractional crystallization at same pressure owing that the aluminous pyroxene plane effects as thermal divide (O'Hara and Yoder, 1967; Kushiro and Yoder, 1974; Milholland and Presnall, 1998). This evidence strongly supports that SiO_2-rich melt existed in deeper region above 3.0 GPa, if vertical movement of SAE116 was negated after rock formation.

In Ca-Mg-Fe* diagram (Fig. 5-10), Mg# in garnet and clinopyroxene of SAE116 display intermediate characteristics between those of basalt melting and hybrid basalt-peridotite material. Similar to Mg#, intermediate composition of Opx component is clearly appeared in ACF diagram (Fig. 5-10). In the case of basalt starting material, Mg# for both phases and Opx component in clinopyroxenes systematically increase with increasing temperature. This trend may express that compositions of SAE116 cannot reproduce by melting of basalt with similar starting compositions (average MORB composition), because their solidus temperatures at 3.0-3.5 GPa are around 1500˚C and it must be totally melt out (Tsuruta and Takahashi, 1998; Takahashi et al., 1998; Yaxley and Green, 1998). On the other hand, basalt-peridotite layered experiments display that clinopyroxene and garnet in original basalt layer can obtain equivalent Mg# and Opx component with those of SAE116 at lower temperatures (≤ 1400˚C; Yaxley and Green, 1998) because Mg# and other elements approach to equilibrate with surrounding peridotite through melt phase (Takahashi and Nakajima, 2002). In conclusion, SAE116 might have been restite after extraction of "ephemeral" SiO_2-rich melt and the SiO_2-rich composition relived the modification causing by surrounding mantle peridotite excluding its Fe/Mg ratio.

5-3-2 Origin of petrochemical variation

If siliceous melt was present in the mantle depth as indicative that the presence of quartz-garnet clinopyroxenite, they must react with surrounding peridotite and expected to accompany with orthopyroxene crystallization in wallrock peridotite. Such as orthopyroxene enrichment process has been discussed about the explanation for high modal orthopyroxene in mantle peridotite xenoliths from Archean cratons (e.g. Kelemen et al. 1998). Also some experimental results conducted by sandwiching layer of basalt against peridotite displayed extensive crystallization of orthopyroxene in reaction zone (e.g. Takahashi and Kushiro, 1983;

Yaxley and Green, 1998, Takahashi and Nakajima, 2002). Fig. 5-11 shows the backscattered electron images of basalt / peridotite layered run products, which reported by Yaxley and Green (1998). The experiment (run 9117) conducted with approximately half proportions of basalt and peridotite at 1300˚C, 3.5 GPa representing below peridotite solidus and above basalt solidus. Former basalt layer (left hand side) on the further contact consists of partially melted eclogite with dacitic liquid, while near the contact, dacitic liquid are not observed and consisted refractory garnet and clinopyroxene. Contact with the peridotite represent as orthopyroxene-rich zone, which dominated by orthopyroxene, with minor garnet. In subsolidus garnet peridotite layer (right hand side), Fe enrichment was observed near the contact (Mg# in olivine ~ 0.87).

This systematic petrochemical variation may be applicable to HT-type pyroxenite and Fe-enriched garnet lherzolite. Most of GC might have formed by partial melting of basaltic rock and their chemistries were significantly affected by surrounding peridotite. That is, variation of Mg# may reflect the degree of reaction with peridotite much rather than degree of fractionation or melting. It is evident that GC with lowest Mg# have high grossular garnet and lowest total REE contents, indicating that low Mg# and high grossular garnet attained by remaining from affection of surrounding peridotite rather than the results of fractional crystallization effect. Takahashi and Nakajima (2002) also conducted basalt/peridotite sandwich melting experiments and focused on chemical reaction rate between basalt and peridotite. They noted that Mg# and Al_2O_3 of clinopyroxene in former basalt layer effectively change to reach chemical equilibrium with surrounding peridotite at the condition which peridotite melted. Chemistries of GC might be changed by not only solid-state diffusion and must be controlled by interstitial migrating melt. On the other hand, GO may represent as the reacted peridotite whose chemistries were modified by siliceous melt generated by basalt melting. Small inclusions of olivine relieved from the reaction with siliceous melt, however their Fe/Mg ratio was significantly affected. Only in core of some large garnets, high Mg# is leaved equivalent to those of peridotite. These observations strongly support the interpretation.

5-3-3 Relation with megacryst suites

It is apparent that GC-GO is genetically related to the megacryst suites and their relations must be considered. Origin of megacryst suites in silica-undersaturated magma is one of unclear problem for the mantle-derived material. Well-constrained compositional variations have been found in each locality and most researchers favored that they represent a series of crystal fractionation from single magma (e.g. Nixon and Boyd, 1974, Gurney et al., 1979; Schulze, 1987). In the case of Malaita, they also display constrained variations, supporting the crystal fractionation hypothesis. Neal and Davidson (1989) suggested that megacryst suites in Malaita alnöite are products of crystal fractionation from “proto-alnöite” which have alkali basalt in character. Fig. 5-11 shows calculated REE patterns of equilibrium liquids using published crystal/liquid partition coefficients (Hauri et al.,1994; Johnson, 1998) and compared with those of tholeiite, alkali basalt and alnöite in the Ontong Java Plateau (Mahoney and Spencer, 1991; Mahoney et al., 1993; Tejada et al., 1996; Nixon et al., 1980; Neal and Davidson, 1989), showing the similarity with those of alkali basalt rather than alnöite and tholeiite in the point of intermediate LREE/HREE ratios.

Neal and Davidson (1989) further interpreted that augite megacrysts crystallized before subcalcic diopsides from single magma based on isotopic ratios. If so, reversed fractionation (increases in Mg# as crystallization proceeds) were occurred in megacryst suites. Actually, augite megacryst, subcalcic diopside and alnöite have different $^{143}Nd/^{144}Nd$ and $^{87}Sr/^{86}Sr$ ratios and their disparities were accounted by assimilation fractional crystallization (AFC) process. I would reject the reversed fractionation hypothesis based on some evidences, (1) There is well-defined correlation between Mg# and Ti in MG, (2) MG with lowest Mg# has highest total REE content. (3) There is no association between garnet and ilmenite. These characteristics can be accounted by normal fractionation scheme. On the other hand, REE variations in clinopyroxene consisting megacryst suites are complex to understand because MCI with intermediate Mg# have highest REE contents (Fig. 4-15). If they crystallized from single primary melt and either normal or reverse fractionation scheme acted, it is necessary to fractionate the phase with crystal/liquid partition coefficient of 1 > for REE. No megacryst phases with such characteristics present in the Malaita alnöite excluding apatite in mica-amphibole-ilmenite-augite

rock. However, augite coexisting with apatite has distinctly high REE contents, inferring that apatite occurred only highly fractionated rock and there was no contribution of apatite fractionation for REE variations between MSD and MA. This evidence indicates that MSD and MA crystallized from two unrelated magmas, showing as disparity of isotopic ratios obtained by Neal and Davidson (1989). Although melt coexisting with MA are not constrained, MG and MSD might be invoked as the crystallized phases from the melt, which formed by reaction with basalt and peridotite represented by GC-GO. If original magma has siliceous in composition and ascent of this magma is arrested, reaction between peridotite and basalt may be completed and chemically homogenized mixture is attained. The results of the melting experiments on homogeneous mixtures of basalt and peridotite have been revealed that their partial melts become silica-undersaturated alkali basalt and the solidus temperature for the mixture is significantly lower than those of genuine peridotite depending on the proportions between peridotite and basalt (Kogiso et al., 1998; Yaxley, 2000). In the case that temperature of the region is higher than the solidus of the homogeneous mixture, silica-undersaturated basalt may be constructed from originally siliceous melt with peridotite. Actually, characteristics of equilibrated melts with megacryst suites and GC-GO is only inferred by their equivalent REE patterns to those of alkali basalt, however apparent lack of detectable CaEs component in clinopyroxenes strongly supports that last equilibrated melts with GC-GO and megacryst suites are silica-undersaturated in nature.

From these considerations, formation of megacrysts in Malaitan alnöite may be pre-eruption event consistent with their homogeneity of single crystals, which can be up to 30 cm across (Nixon and Boyd, 1979). Furthermore, megacryst crystallization was subsequent to the original differentiation of pyroxenite and coexisting melt. They might have evolved in deep mantle owing to prohibition from erupting. How related the host alnöite and the megacryst magma is still remaining question. Simple model with megacrysts representing cogenetic material with host alnöite may be negated by the REE variations and previous isotopic study similar to the relation between kimberlite and their megacryst suites (e.g. Harte, 1983; Jones, 1987). Recently, detailed Sr-Nd-Pb isotopic investigations for Namibian kimberlites have been reported by Davies et al. (2001). They revealed that apparent Sr-Nd-Pb isotope disequilibrium between megacryst and host kimberlites and interpreted that

megacrysts formed in lithospheric mantle associated with former basaltic volcanism. Although my interpretation for the origin of Malaitan megacryst is closely matched, detailed isotopic work must be needed for understanding the relation between Malaitan alnöite and megacryst suites.

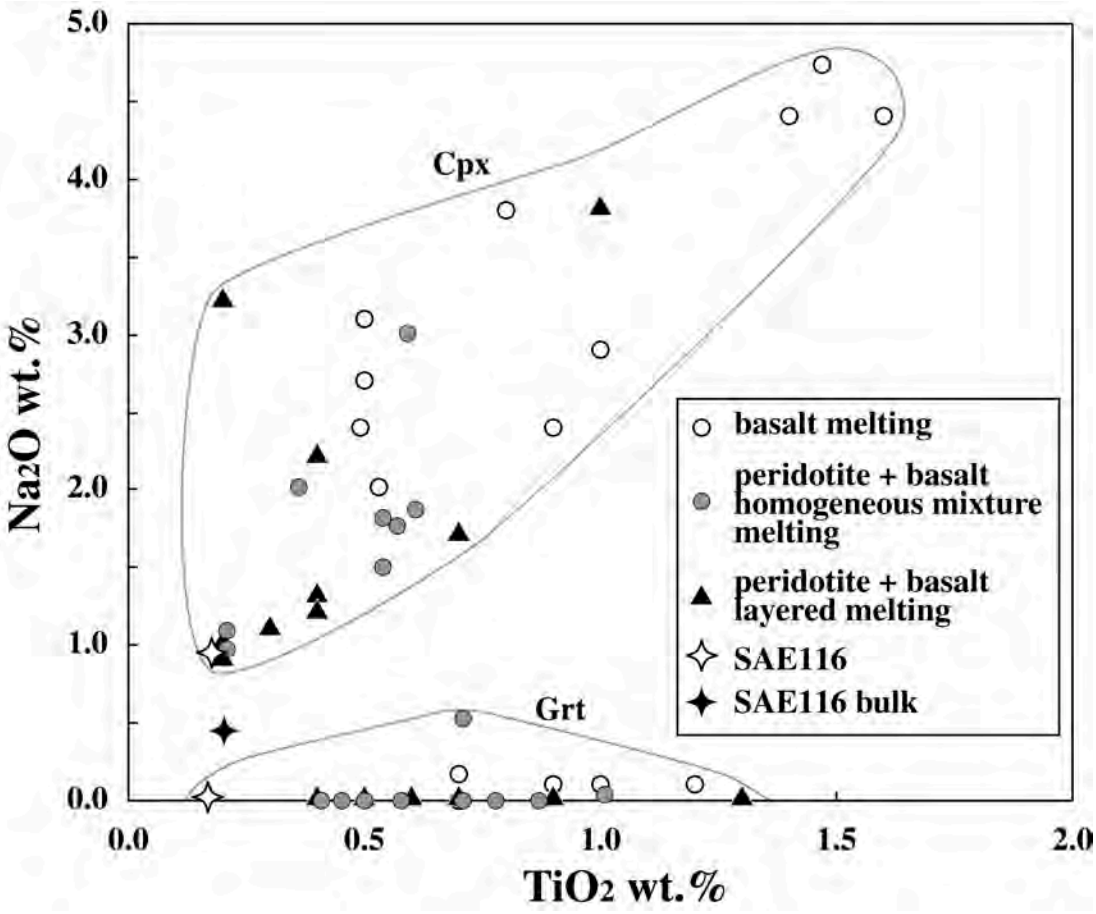

Fig. 5-8. Na_2O versus TiO_2 (wt.%) in clinopyroxenes and garnets from quartz-garnet clinopyroxenite (SAE116, indicated as stars) and several melting experiments at pressures ranging between 3.0 and 3.5 GPa and various temperatures. Circles: basalt melting (Yasuda et al., 1994; Takahashi et al., 1998; Tsuruta and Takahashi, 1998; Yaxley and Green, 1998). Shaded circles; homogeneous basalt and peridotite mixture melting (Kogiso et al., 1998; Yaxley, 2000). Filled triangles: basalt and peridotite layered melting (Yaxley and Green, 1998). Noted that clinopyroxene and garnet in SAE116 are greatly depleted in Na and Ti contents.

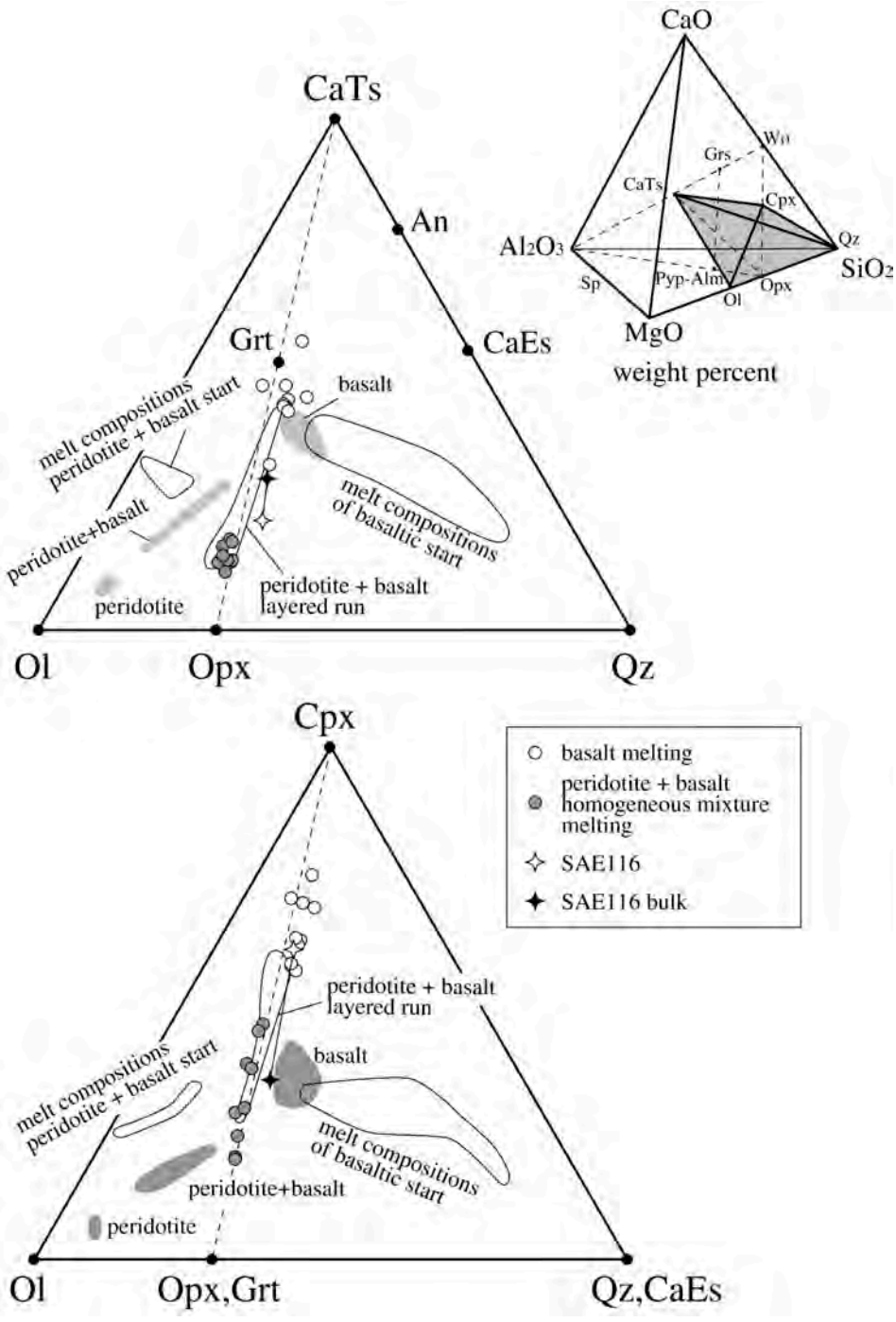

Fig. 5-9. Normative compositions of clinopyroxenes projected from clinopyroxene (Cpx: diopside-hedenbergite) onto olivine (Ol: forsterite-fayalite)-Ca Tschermak molecule (CaTs)-quartz (Qz) plane (upper) and from CaTs to Ol-Cpx-Qz (lower) in weight percent. Dashed lines are the trace of the aluminous pyroxene plane, which is a thermal divide at pressure > 3 GPa (e.g. O'Hara and Yoder, 1967). Shaded fields and blank fields indicate the starting material and melt compositions from several melting experiments, respectively (references are same with Fig. 5-7). Tie lines connect data for clinopyroxene and bulk of SAE116.

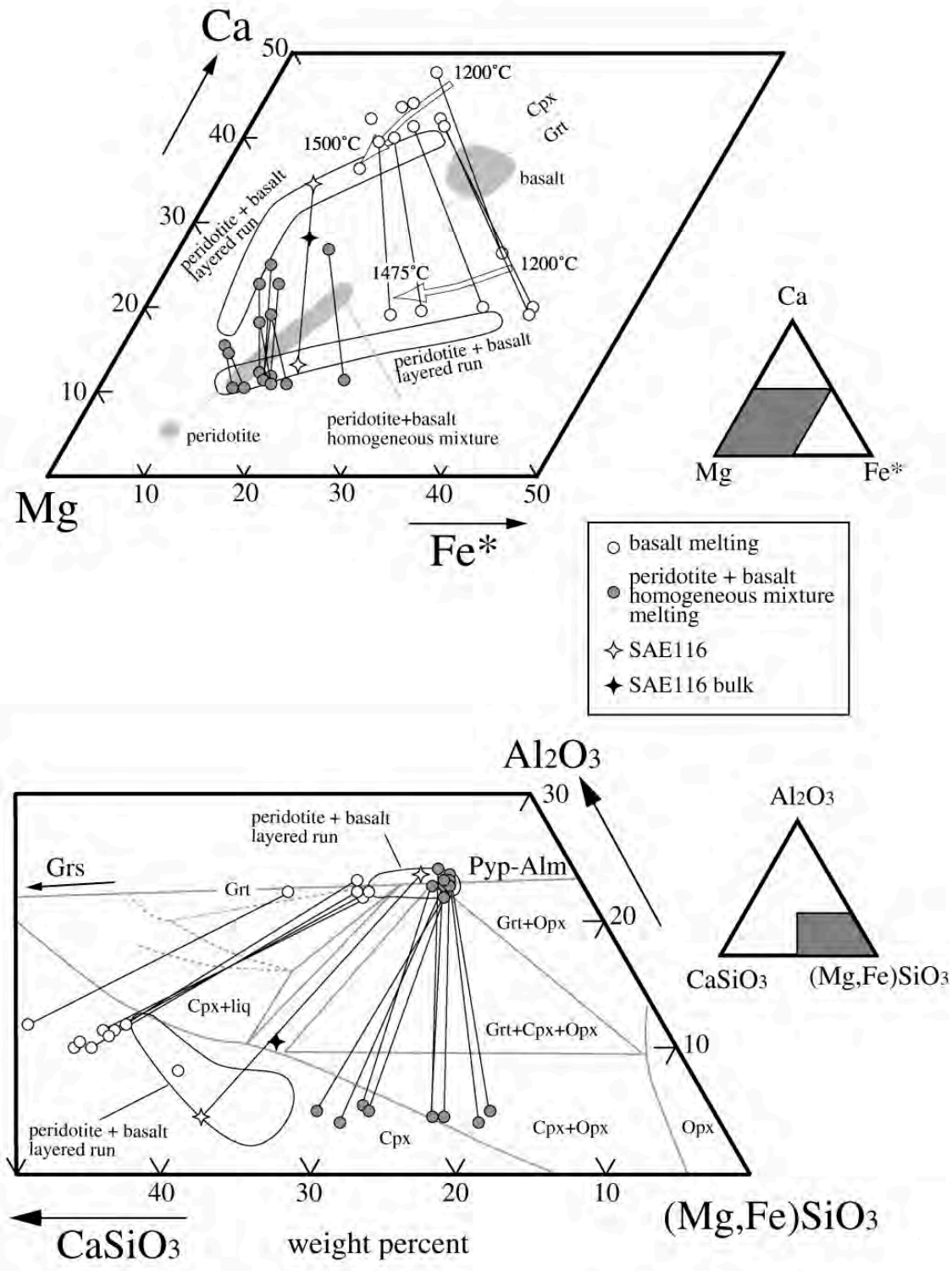

Fig. 5-10. Compositions of clinopyroxenes (Cpx) and garnets (Grt) from SAE116 and several melting experiments represented on Ca-Mg-Fe* diagram in molecular proportion (upper) and ACF diagram in weight percent (lower). Phase relations in a part of $CaSiO_3$-$MgSiO_3$-Al_2O_3 at 3.0 GPa and 1600˚C are indicated in ACF diagram (O'Hara and Yoder, 1967). The data are same with those in Figs. 5-7 and 5-8.

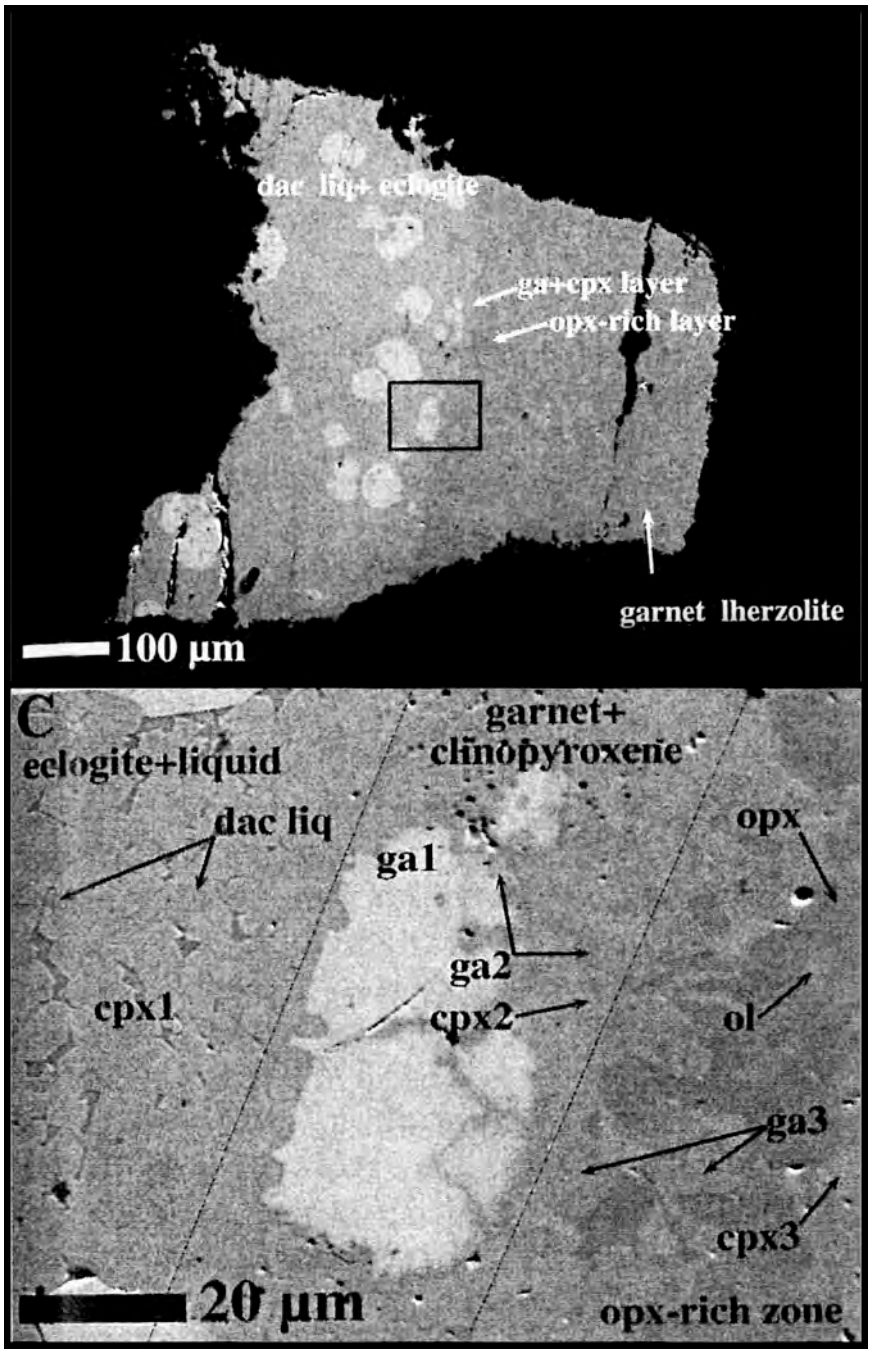

Fig. 5-11. Backscattered electron images of run product (run 9117 at 1300˚C and 3.5 GPa) of basalt and peridotite layered melting experiment conducted by Yaxley and Green (1998). Upper image: former basalt layer in the left hand side and subsolidus lherzolite in the right hand side. Lower image; enlarged photo of the interface region of the layered run 9117. The left of the image consists garnet (ga1), omphasitic clinopyroxene (cpx1) and dacitic glass (dac liq). Center of the image consists refractory garnet (ga2) + clinopyroxene (cpx2) without glass. The right of the image is dominated by orthopyroxene (opx) with minor garnet (ga3), clinopyroxene (cpx3) and Fo_{87} olivine (ol).

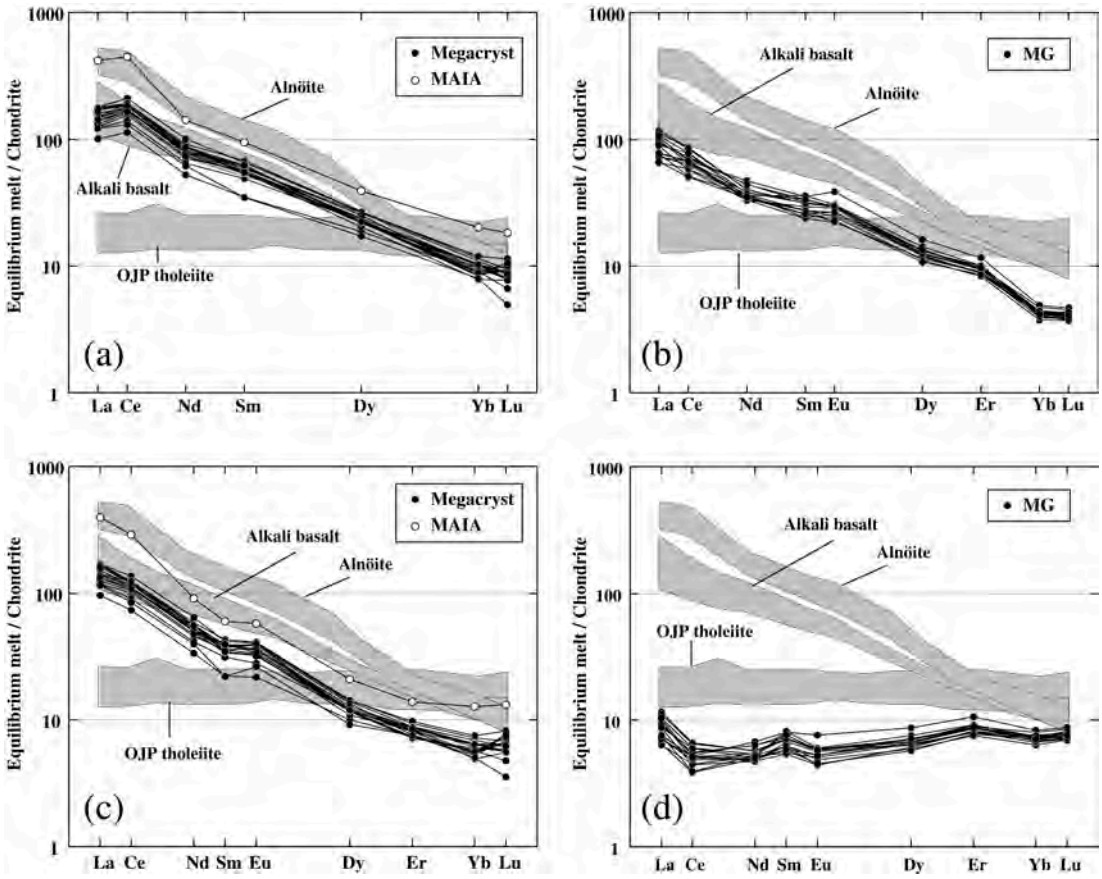

Fig. 5-12. Calculated “equilibrium melt” for (a) and (c) clinopyroxenes in the megacryst suites using the partition coefficient values of Johnson (1998) and Hauri et al. (1994), respectively; (b) and (d) garnet megacrysts using the partition coefficient values of Johnson (1998) and Hauri et al. (1994), respectively. Shaded fields indicate the REE variations of the tholeiite, alkali basalt and alnöite in Ontong Java Plateau for reference (Mahoney and Spencer, 1991; Mahoney et al., 1993; Tejada et al., 1996; Nixon et al., 1980; Neal and Davidson, 1989).

Table 5-1. Major element compositions of clinopyroxene, garnet and whole-rock of quartz-garnet clinopyroxenite (QGC)

	Quartz-garnet clinopyroxenite		
	SAE116		
	Cpx	Grt	Bulk*
SiO_2	54.35	41.22	51.61
TiO_2	0.18	0.17	0.21
Al_2O_3	5.79	23.72	10.45
Cr_2O_3	0.10	0.17	-
FeOt	5.69	9.69	6.89
MnO	0.15	0.30	0.16
MgO	17.82	19.27	18.18
CaO	15.36	5.24	12.03
Na_2O	0.95	0.02	0.47
K_2O	0.01	0.00	0.00
P_2O_5	0.00	0.00	0.05
total	100.38	99.80	100.00
O=12			
Si	3.879	2.952	3.679
Ti	0.010	0.009	0.011
Al(4)	0.121	0.048	0.321
Al(6)	0.366	1.954	0.557
Cr	0.006	0.010	0.000
Fe*	0.339	0.580	0.411
Mn	0.009	0.018	0.010
Mg	1.896	2.057	1.931
Ca	1.174	0.402	0.919
Na	0.131	0.003	0.064
K	0.001	-	0.000
Total	7.931	8.034	7.903
Mg#	0.848	0.780	0.825
$KAlSiO_4$	0.0	-	0.0
$NaCrSi_2O_6$	0.3	-	0.0
Jd	6.3	-	3.2
NaRTiSi	0.0	-	0.0
$CaTiAl_2O_6$	0.5	-	0.6
CaTs	5.1	-	14.9
CaEs	6.9	-	9.7
$CaMnSi_2O_6$	0.4	-	0.5
Wo	24.6	-	12.6
En	47.4	-	48.3
Fs	8.5	-	10.3
total	100.0	-	100.0

Fe* Total Fe as FeO; Mg#=Mg/(Mg+Fe*); End-member calculations are after Smyth (1980); Bulk composition is normalized as 100 wt.%

Table 5-2. Compilation of major element compositions of clinopyroxenes and garnets from several melting experiments of basalt, basalt + peridotite homogeneous mixture and layered basalt/peridotite as starting material.

	Basalt melting									
Reference	Takahashi et al. (1998)		Tsuruta & Takahashi (1998)		Yasuda et al. (1994)	Yaxley & Green (1998)				
Start	CRB72-31		JB-1		NAM-7	GA1				
Run	49	50	P194	P182	MP5	C338	9099	C321	9104	C383
Assemblage	Grt+Cpx +L	Grt+Cpx +L	Grt+Cpx +L	Cpx+L	Cpx+L	Co+Grt+ Cpx+L	Co+Grt+ Cpx+L	Grt+Cpx +L	Grt+Cpx +L	Grt+Cpx +L
T(°C)	1400	1420	1200	1500	1400	1250	1300	1350	1450	1475
P(GPa)	3.0	3.0	3.0	3.0	3.0	3.5	3.5	3.5	3.5	3.5
Clinopyroxenes										
SiO_2	52.00	51.50	50.96	51.17	49.53	51.1	51.3	51.3	51.3	51.1
TiO_2	1.00	0.90	1.47	0.49	0.53	1.6	1.4	0.8	0.5	0.5
Al_2O_3	12.60	12.60	15.58	10.21	11.83	14.9	14.8	14.1	14.4	13.8
Cr_2O_3	-	-	0.04	0.22	-	-	-	-	-	-
FeOt	6.70	6.90	5.91	6.37	6.01	7.1	7.4	6.8	6.7	6.2
MnO	0.10	0.10	0.01	0.17	-	0.2	0.2	0.1	0.2	0.1
NiO	-	-	-	-	-	-	-	-	-	-
MgO	10.00	11.30	7.51	13.21	12.89	8.2	8.2	9.7	11.0	11.6
CaO	15.20	16.40	13.71	13.33	16.67	12.4	12.2	13.3	13.7	13.8
Na_2O	2.90	2.40	4.74	2.40	2.02	4.4	4.4	3.8	3.1	2.7
K_2O	0.00	0.00	0.01	0.04	-	0.0	0.1	0.0	0.0	0.1
P_2O_5	-	-	-	0.04	-	0.2	0.1	0.1	0.1	0.1
total	100.50	102.10	99.93	97.56	99.48	99.90	99.90	99.90	100.90	99.80
O=12										
Si	3.726	3.652	3.658	3.763	3.606	3.676	3.690	3.689	3.650	3.664
Ti	0.054	0.048	0.079	0.027	0.029	0.087	0.076	0.043	0.027	0.027
Al(4)	0.274	0.348	0.342	0.237	0.394	0.324	0.310	0.311	0.350	0.336
Al(6)	0.790	0.705	0.977	0.648	0.621	0.939	0.944	0.883	0.857	0.830
Cr	0.000	0.000	0.002	0.013	0.000	0.000	0.000	0.000	0.000	0.000
Fe*	0.401	0.409	0.355	0.392	0.366	0.427	0.445	0.409	0.399	0.372
Mn	0.006	0.006	0.001	0.010	0.000	0.012	0.012	0.006	0.012	0.006
Mg	1.068	1.194	0.804	1.448	1.399	0.879	0.879	1.040	1.167	1.240
Ca	1.167	1.246	1.055	1.050	1.300	0.956	0.940	1.025	1.044	1.060
Na	0.403	0.330	0.660	0.342	0.285	0.614	0.613	0.530	0.428	0.375
K	0.000	0.000	0.001	0.004	0.000	0.000	0.009	0.000	0.000	0.009
Total	7.889	7.938	7.932	7.934	8.000	7.913	7.919	7.936	7.933	7.919
Mg#	0.727	0.745	0.694	0.787	0.793	0.673	0.664	0.718	0.745	0.769
KAl_2SiO_6	0.0	0.0	0.0	0.2	0.0	0.0	0.5	0.0	0.0	0.5
$NaCrSi_2O_6$	0.0	0.0	0.1	0.6	0.0	0.0	0.0	0.0	0.0	0.0
Jd	20.1	16.5	32.9	16.5	14.3	30.7	30.7	26.5	21.4	18.8
NaRTiSi	0.0	0.0	0.0	0.0	0.0	0.0	0.0	0.0	0.0	0.0
$CaTiAl_2O_6$	2.7	2.4	4.0	1.4	1.5	4.3	3.8	2.2	1.3	1.3
CaTs	8.3	12.6	9.1	9.1	16.8	7.6	8.0	11.2	14.8	14.1
CaEs	11.1	6.2	6.8	6.6	0.0	8.7	8.1	6.4	6.7	8.1
$CaMnSi_2O_6$	0.3	0.3	0.0	0.5	0.0	0.6	0.6	0.3	0.6	0.3
Wo	20.8	22.0	18.1	19.1	23.4	15.5	15.3	17.1	16.1	16.6
En	26.7	29.9	20.1	36.2	35.0	22.0	22.0	26.0	29.2	31.0
Fs	10.0	10.2	8.9	9.8	9.1	10.7	11.1	10.2	10.0	9.3
total	100.0	100.0	100.0	100.0	100.0	100.0	100.0	100.0	100.0	100.0
Garnets										
SiO_2			39.56			39.4	39.6	40.0	40.6	40.9
TiO_2			0.7			1.2	1.0	0.9	1.0	0.7
Al_2O_3			21.84			21.9	22.1	22.3	22.2	23.1
Cr_2O_3			0.04			-	-	-	-	-
FeOt			15.54			18.7	18.5	16.5	13.8	12.5
MnO			0.39			0.4	0.4	0.5	0.4	0.3
NiO			0			-	-	-	-	-
MgO			10.61			10.7	10.9	12.2	14.3	15.1
CaO			9.6			7.3	7.0	7.5	7.5	7.2
Na_2O			0.17			0.1	0.1	0.1	0.1	0.0
K_2O			0.05			0.0	0.0	0.1	0.0	0.0
P_2O_5						0.3	0.3	0.1	0.1	0.2
total			98.5			100.0	99.9	100.2	100.0	100.0
O=12										
Si			2.997			2.970	2.981	2.976	2.984	2.981
Ti			0.040			0.068	0.057	0.050	0.055	0.038
Al			1.950			1.946	1.961	1.955	1.923	1.985
Cr			0.002			0.000	0.000	0.000	0.000	0.000
Fe*			0.984			1.179	1.165	1.026	0.848	0.762
Mn			0.025			0.026	0.026	0.032	0.025	0.019
Mg			1.198			1.202	1.223	1.353	1.567	1.641
Ca			0.779			0.590	0.565	0.598	0.591	0.562
Na			0.025			0.015	0.015	0.014	0.014	0.000
Total			8.000			7.996	7.990	8.004	8.007	7.988
Mg#			0.549			0.505	0.512	0.569	0.649	0.683
XCa			0.261			0.197	0.190	0.199	0.195	0.188

Table 5-2. Continued.

Peridotite + Basalt homogeneous mixture melting									
Reference	Kogiso et al. (1998)				Yaxley (2000)				
Start	KG1		KG2		$GA1_{50}MPY90_{50}$			$GA1_{25}MPY90_{25}$	
Run	KH-22	KH-49	KH-41	KH-26	C546	C736	C520	C739	C564
Assemblage	Grt+Cpx +Ol+L	Grt+Cpx +Ol+L	Grt+Cpx +Ol+L	Grt+Cpx +Ol+L	Grt+Cpx +Ol+L	Grt+Cpx +L	Grt+Cpx +L	Grt+Cpx +L	Cpx+L
T(°C)	1500	1525	1500	1525	1400	1500	1500	1400	1500
P(GPa)	3.0	3.0	3.0	3.0	3.5	3.5	3.5	3.5	3.5
Clinopyroxenes									
SiO_2	52.97	54.58	53.67	53.33	53.70	53.53	54.30	53.38	53.70
TiO_2	0.54	0.21	0.61	0.54	0.57	0.36	0.21	0.59	0.57
Al_2O_3	7.34	5.41	6.46	7.03	6.85	7.12	6.24	8.69	6.85
Cr_2O_3	0.15	0.27	0.25	0.41	0.26	0.12	0.27	0.19	0.26
FeOt	6.84	6.20	5.90	5.80	7.34	7.07	6.60	7.53	7.34
MnO	-	-	-	-	0.14	0.13	0.13	0.17	0.14
NiO	-	-	-	-	-	-	-	-	-
MgO	20.39	24.96	20.30	21.24	21.02	21.56	24.45	16.02	21.02
CaO	9.95	7.28	10.92	10.15	8.16	7.78	6.75	10.35	8.16
Na_2O	1.82	1.09	1.87	1.50	1.77	2.02	0.97	3.01	1.77
K_2O	-	-	-	-	-	-	-	-	-
P_2O_5	-	-	-	-	-	-	-	-	-
total	100.00	100.00	99.98	100.00	99.81	99.69	99.92	99.93	99.81
O=12									
Si	3.774	3.839	3.818	3.782	3.819	3.806	3.821	3.823	3.819
Ti	0.029	0.011	0.033	0.029	0.030	0.019	0.011	0.032	0.030
Al(4)	0.226	0.161	0.182	0.218	0.181	0.194	0.179	0.177	0.181
Al(6)	0.390	0.288	0.360	0.369	0.393	0.402	0.339	0.556	0.393
Cr	0.008	0.015	0.014	0.023	0.015	0.007	0.015	0.011	0.015
Fe*	0.408	0.365	0.351	0.344	0.437	0.420	0.388	0.451	0.437
Mn	0.000	0.000	0.000	0.000	0.008	0.008	0.008	0.010	0.008
Mg	2.165	2.617	2.153	2.245	2.228	2.285	2.565	1.710	2.228
Ca	0.759	0.549	0.832	0.771	0.622	0.593	0.509	0.794	0.622
Na	0.251	0.149	0.258	0.206	0.244	0.278	0.132	0.418	0.244
K	0.000	0.000	0.000	0.000	0.000	0.000	0.000	0.000	0.000
Total	8.011	7.992	8.000	7.987	7.978	8.012	7.967	7.982	7.978
Mg#	0.842	0.878	0.860	0.867	0.836	0.845	0.868	0.791	0.836
KAl_2SiO_6	0.0	0.0	0.0	0.0	0.0	0.0	0.0	0.0	0.0
$NaCrSi_2O_6$	0.4	0.8	0.7	1.1	0.7	0.3	0.8	0.5	0.7
Jd	12.0	6.7	12.2	9.2	11.5	13.5	5.9	20.4	11.5
NaRTiSi	0.0	0.0	0.0	0.0	0.0	0.0	0.0	0.0	0.0
$CaTiAl_2O_6$	1.4	0.6	1.6	1.4	1.5	1.0	0.6	1.6	1.5
CaTs	8.4	6.9	5.8	8.0	6.0	7.7	7.8	5.7	6.0
CaEs	0.0	0.8	0.0	1.3	2.2	0.0	3.3	1.8	2.2
$CaMnSi_2O_6$	0.0	0.0	0.0	0.0	0.4	0.4	0.4	0.5	0.4
Wo	13.9	9.8	17.1	14.2	11.0	10.2	7.5	15.5	11.0
En	53.7	65.4	53.8	56.1	55.7	56.6	64.1	42.8	55.7
Fs	10.1	9.1	8.8	8.6	10.9	10.4	9.7	11.3	10.9
total	100.0	100.0	100.0	100.0	100.0	100.0	100.0	100.0	100.0
Garnets									
SiO_2	42.04	42.88	42.32	42.13	41.44	42.39	42.60	41.70	42.10
TiO_2	0.71	0.41	0.71	1.01	0.87	0.78	0.50	0.58	0.45
Al_2O_3	22.21	22.71	22.46	22.41	23.10	22.23	22.95	22.59	23.51
Cr_2O_3	0.50	0.53	0.36	0.48	0.37	0.42	0.51	0.19	0.39
FeOt	8.78	7.14	8.45	7.96	9.51	8.69	7.66	12.10	8.29
MnO	-	-	-	-	0.23	0.26	0.14	0.33	0.23
NiO	-	-	-	-	-	-	-	-	-
MgO	20.48	22.08	21.08	21.00	19.89	20.33	21.31	17.77	20.49
CaO	4.76	4.26	4.63	4.97	4.37	4.36	4.17	4.41	4.46
Na_2O	0.53	0.00	0.00	0.04	0.00	0.00	0.00	0.00	0.00
K_2O	-	-	-	-	-	-	-	-	-
P_2O_5	-	-	-	-	0.16	0.07	0.10	0.03	0.08
total	100.01	100.01	100.01	100.00	99.94	99.53	99.94	99.70	100.00
Si	2.994	3.016	3.000	2.986	2.961	3.024	3.009	3.014	2.983
Ti	0.038	0.022	0.038	0.054	0.047	0.042	0.027	0.032	0.024
Al*	1.864	1.883	1.876	1.872	1.945	1.869	1.911	1.924	1.963
Cr	0.028	0.029	0.020	0.027	0.021	0.024	0.028	0.011	0.022
Fe*	0.523	0.420	0.501	0.472	0.568	0.518	0.452	0.731	0.491
Mn	0.000	0.000	0.000	0.000	0.014	0.016	0.008	0.020	0.014
Mg	2.174	2.315	2.227	2.219	2.118	2.162	2.244	1.914	2.164
Ca	0.363	0.321	0.352	0.377	0.335	0.333	0.316	0.341	0.339
Na	0.073	0.000	0.000	0.005	0.000	0.000	0.000	0.000	0.000
Total	8.058	8.006	8.014	8.013	8.009	7.988	7.995	7.987	8.000
Mg#	0.806	0.846	0.816	0.825	0.788	0.807	0.832	0.724	0.815
XCa	0.119	0.105	0.114	0.123	0.110	0.110	0.104	0.114	0.113

Table 5-2. Continued.

Peridotite + basalt layered melting										
Reference	Yaxley & Green (1998)									
Start	GA1+MPY90									
Run	C339	C339	C308	C308	9117	9117	9117	C333	C334	C327
Assemblage	GC	GL	GC	GL	Ec	GC	GL	GL	GL	GL
T(°C)	1250	1250	1400	1400	1300	1300	1300	1425	1425	1425
P(GPa)	3.5	3.5	3.5	3.5	3.5	3.5	3.5	3.5	3.5	3.5
Clinopyroxenes										
SiO_2	53.5	53.9	52.2	53.9	49.9	53.4	51.5	53.2	53.5	53.0
TiO_2	0.4	0.4	0.7	0.4	1.0	0.4	0.4	0.2	0.3	0.2
Al_2O_3	5.8	5.7	8.4	5.9	14.6	5.7	5.9	5.4	5.9	5.8
Cr_2O_3	0.3	1.0	0.3	0.6	0.0	0.3	0.7	0.6	0.7	0.7
FeOt	4.5	4.2	4.7	5.5	7.6	5.2	5.0	5.0	5.5	5.0
MnO	0.2	0.2	0.1	0.0	0.2	0.1	0.1	0.2	0.1	0.1
NiO	0.1	0.2	0.0	0.0	0.1	0.0	0.1	0.0	0.1	0.0
MgO	19.1	19.0	19.3	23.1	9.0	19.1	19.2	23.3	23.9	22.9
CaO	13.0	13.4	12.2	9.2	12.0	14.5	13.4	9.3	8.2	9.8
Na_2O	2.2	2.2	1.7	1.2	3.8	1.3	1.2	3.2	1.1	0.9
K_2O	0.0	0.1	0.0	0.0	0.1	0.0	0.0	0.1	0.1	-
P_2O_5	0.0	0.2	0.0	0.1	0.1	0.0	0.0	0.1	0.0	-
total	99.1	100.5	99.6	99.9	98.4	100.0	97.5	100.6	99.4	98.4
O=12										
Si	3.852	3.845	3.725	3.814	3.659	3.825	3.785	3.774	3.800	3.805
Ti	0.022	0.021	0.038	0.021	0.055	0.022	0.022	0.011	0.016	0.011
Al(4)	0.148	0.155	0.275	0.186	0.341	0.175	0.215	0.226	0.200	0.195
Al(6)	0.344	0.324	0.431	0.306	0.921	0.306	0.296	0.225	0.294	0.296
Cr	0.017	0.056	0.017	0.034	0.000	0.017	0.041	0.034	0.039	0.040
Fe*	0.271	0.251	0.280	0.325	0.466	0.311	0.307	0.297	0.327	0.300
Mn	0.012	0.012	0.006	0.000	0.012	0.006	0.006	0.012	0.006	0.006
Mg	2.050	2.020	2.053	2.436	0.984	2.039	2.103	2.464	2.530	2.450
Ca	1.003	1.024	0.933	0.697	0.943	1.113	1.055	0.707	0.624	0.754
Na	0.307	0.304	0.235	0.165	0.540	0.181	0.171	0.440	0.151	0.125
K	0.000	0.009	0.000	0.000	0.009	0.000	0.000	0.009	0.009	0.000
Total	8.025	8.022	7.993	7.984	7.930	7.995	8.002	8.198	7.997	7.982
Mg#	0.883	0.890	0.880	0.882	0.679	0.867	0.873	0.893	0.886	0.891
$KAlSiO_4$	0.0	0.4	0.0	0.0	0.5	0.0	0.0	0.4	0.5	0.0
$NaCrSi_2O_6$	0.8	2.8	0.8	1.7	0.0	0.8	2.0	1.6	2.0	2.0
Jd	14.2	12.2	10.9	6.6	27.0	8.2	6.5	10.2	5.6	4.3
NaRTiSi	0.0	0.0	0.0	0.0	0.0	0.0	0.0	1.0	0.0	0.0
$CaTiAl_2O_6$	1.1	1.1	1.9	1.1	2.8	1.1	1.1	0.0	0.8	0.5
CaTs	5.1	5.5	10.0	7.2	11.5	6.6	8.5	10.6	8.4	8.7
CaEs	0.0	0.0	0.7	1.6	7.0	0.5	0.0	0.0	0.3	1.8
$CaMnSi_2O_6$	0.6	0.6	0.3	0.0	0.6	0.3	0.3	0.6	0.3	0.3
Wo	21.2	21.6	17.1	12.9	14.4	23.7	21.4	11.0	10.8	13.6
En	50.3	49.7	51.3	60.9	24.6	51.0	52.5	57.7	63.3	61.3
Fs	6.6	6.2	7.0	8.1	11.7	7.8	7.7	6.9	8.2	7.5
total	100.0	100.0	100.0	100.0	100.0	100.0	100.0	100.0	100.0	100.0
Garnets										
SiO_2	41.4	42.2	40.2	43.0	39.5	42.3	41.5	42.1	41.7	42.2
TiO_2	0.6	0.6	1.3	0.6	0.9	0.7	0.5	0.5	0.4	0.4
Al_2O_3	23.1	21.9	22.3	23.1	22.1	23.2	22.2	23.0	21.5	22.7
Cr_2O_3	0.1	1.2	0.0	1.6	0.0	0.4	1.3	1.4	1.3	1.5
FeOt	9.7	7.3	13.2	6.9	17.0	8.5	7.2	7.0	6.7	6.4
MnO	0.4	0.3	0.3	0.2	0.5	0.2	0.0	0.3	0.1	0.1
NiO	0.0	0.0	0.0	0.0	0.1	0.0	0.0	0.2	0.1	0.0
MgO	18.5	21.8	15.4	21.8	12.0	19.9	20.0	21.9	22.1	22.3
CaO	5.4	4.6	6.3	4.8	6.6	5.3	5.1	4.8	4.4	4.6
Na_2O	0.0	0.0	0.0	0.0	0.0	0.0	0.0	0.0	0.0	0.0
K_2O	0.0	0.0	0.0	0.0	0.0	0.0	0.1	0.1	0.0	0.1
P_2O_5	0.2	0.1	0.1	0.1	0.2	0.0	0.0	0.0	0.1	0.1
total	99.4	100.0	99.1	102.1	98.9	100.5	97.9	101.3	98.4	100.4
O=12										
Si	2.984	2.992	2.964	2.979	2.981	2.990	3.003	2.951	2.998	2.970
Ti	0.033	0.032	0.072	0.031	0.051	0.037	0.027	0.026	0.022	0.021
Al	1.963	1.830	1.938	1.886	1.966	1.933	1.893	1.900	1.822	1.883
Cr	0.006	0.067	0.000	0.088	0.000	0.022	0.074	0.078	0.074	0.083
Fe*	0.585	0.433	0.814	0.400	1.073	0.502	0.436	0.410	0.403	0.377
Mn	0.024	0.018	0.019	0.012	0.032	0.012	0.000	0.018	0.006	0.006
Mg	1.988	2.304	1.692	2.251	1.350	2.097	2.157	2.288	2.368	2.339
Ca	0.417	0.349	0.498	0.356	0.534	0.401	0.395	0.361	0.339	0.347
Na	0.000	0.000	0.000	0.000	0.000	0.000	0.000	0.000	0.000	0.000
Total	7.999	8.027	7.996	8.003	7.985	7.995	7.986	8.033	8.032	8.026
Mg#	0.773	0.842	0.675	0.849	0.557	0.807	0.832	0.848	0.855	0.861
XCa	0.138	0.113	0.165	0.118	0.179	0.133	0.132	0.117	0.109	0.113

Fe* Total Fe as FeO; Mg#=Mg/(Mg+Fe*); End-member calculations are after Smyth (1980)

5-4 Petrogenesis of HT-type peridotite

5-4-1 Origin of systematic depth-REE variations

REE patterns in garnets and clinopyroxenes are dominated in enrichment characteristics and they can reflect chromatographic enrichment process described above section. Most enriched samples (SAG21 and SAG27) are indistinguishable to the megacryst suites in terms of any major, minor and REE compositions of constituent minerals. Therefore, metasomatic melt infiltrated in peridotite matrix must be megacryst magma. The models considering megacryst magma as metasomatic agents are essentially same with those accounted for the metasomatized nature of deformed xenoliths from sub-cratonic mantle (e.g. Gurney and Harte, 1980; Harte, 1983; Burgess and Harte, 1999). Recently, detailed study of Jagersfontein peridotite xenolith has been conducted by Burgess and Harte (1999). They exhibited the presence of depth-related variations of the metasomatic modification based on chemistry of zoned garnets and P-T determinations, interpreting that melt initially in equilibrium with megacrysts infiltrated upward from 230 km depth (thermal transition zone represented by deformed xenolith which occupy below 130 km depth) to near 120 km depth (in the lithosphere keel). Infiltrating melt were changed own chemistry by percolative fractionation process and different chemical modifications were given to matrix peridotites in individual depth. In the case of HT-type peridotites from Malaita, REE patterns in clinopyroxenes and garnets may allow to be interpreted the presence of depth-related enrichment variation. Fig. 5-12 shows P-T variation determined by two-pyroxene thermometry (TBK90) and Al in orthopyroxene barometry (PBK90), which represented the same way to P-T determinations by Burgess and Harte (1999). Although estimated P-T variation of GL is limited in 1 GPa, deformed, Fe-enriched peridotites (SAG21 and SAG27) consisted the deepest part of the peridotite similar to cratonic peridotite. Other GL may have been derived from two different shallower regions; one group (SAG9, SAG15 and SAG16) displays intermediate depth (3.2 GPa, 1270˚C) and other group (SAG13, SAG1 and SAG7) represent as shallower mantle (3.0 GPa, 1230˚C) among GL. Presumably, SAS21 and SAS46 might located in the “missing region” around 2.7 GPa estimated from intersection between calculated temperature and fitted line consisting the geotherm which host alnöite was erupted. REE patterns in these four

groups of HT-type peridotite systematically change from inflected "chromatographic" patterns in shallower HTSH and GL (SAG1 and SAG7) to "equilibrated" patterns with megacryst melt in deeper deformed peridotites. Distribution of GO spread in deeper part than deformed peridotites to 3.5 GPa and their REE patterns support that close association with the megacryst melt. These REE behaviors are accounted that deeper megacryst magma percolated through upward mantle column. REE evolutions in individual garnets evident that the chromatographic fractionation was a functional to duration time of the process because both core and rim of garnets (SAG1 and SAG7) possess non-equilibrated patterns. Although detailed REE zoning patterns were not realized, variations of core and rim may reflect the various stage of melt/rock reaction in individual depth. If this interpretation is valid, original REE variations before metasomatic enrichment are only recorded in HREE in shallower part of HT-type mantle column.

5-4-2 Presence of depleted zone

There is the sample-missing zone between HT-type and LT-type based on geothermobarometry (Fig. 3-16). Although the origin of "missing zone" may reflect our sampling effects, I would interpret as the garnet-rare "depleted" zone based on the equate temperature of SAS21 and SAS46, which represent as most depleted harzburgite among the studied samples. LREE in clinopyroxene of SAS21 and SAS46 were modified by metasomatic enrichment, however depletion of HREE is notable (Fig. 4-18). Nixon and Boyd (1979) also suggested that the presence of "depleted zone" as lower part of lithospheric mantle based on mineral chemistry. PHN3538, PHN3539 and PHN3549B as "deep-seated nodule" reported by Nixon and Boyd (1979) are garnet lherzolite, garnet-spinel lherzolite and spinel lherzolite, respectively. Their ranges of two-pyroxene temperatures are equivalent to those of SAS21 (PHN3538; 1172˚C, PHN3539; 1178˚C, and PHN3549B; 1147˚C), indicative of derivation from equivalent depth. Although mineral assemblages are variable, constituent minerals regularly illustrate greater depletion, for example, distinctly Cr-rich garnets (Cr_2O_3 ~ 5 wt.%), TiO_2 and Na_2O in clinopyroxenes below 0.03 and 0.8 wt%, respectively. These values are unusual in contrast to those of LT-type peridotites and other HT-type garnet peridotites. If the region between LT-type and HT-type of garnet-bearing peridotite is permitted interpreting as depleted zone, the

region must originate from other upwelling mantle which constructed the LT-type peridotite. Furthermore, potential temperature of the rising mantle which generated depleted zone must be higher than that of LT-type because same temperature cannot produce highly depleted harzburgite in higher pressure. For example, the uppermost mantle (meaning highest degree of melting) of LT-type may be represented by spinel harzburgite of SAS22 and originate from near Moho (~1.5 GPa). Clinopyroxene in SAS22 have still higher HREE abundance than those in SAS21 and SAS46, which derived over 1 GPa deeper than SAS22. Even if melting in garnet stability field is reminded for SAS21, the effect for HREE works in opposite direction because garnet would preserve HREE in residual solid. Higher degree of melting for SAS21 and SAS46 is also represented by Cr# in spinel, which remarks highest value among studied samples (Cr# ~ 0.6). As a result, the presence of depleted zone in high-pressure interval (2.7~3.0 GPa) might have originated from mantle plume with high potential temperature impinged pre-existing lithospheric mantle which represented by LT-type peridotite.

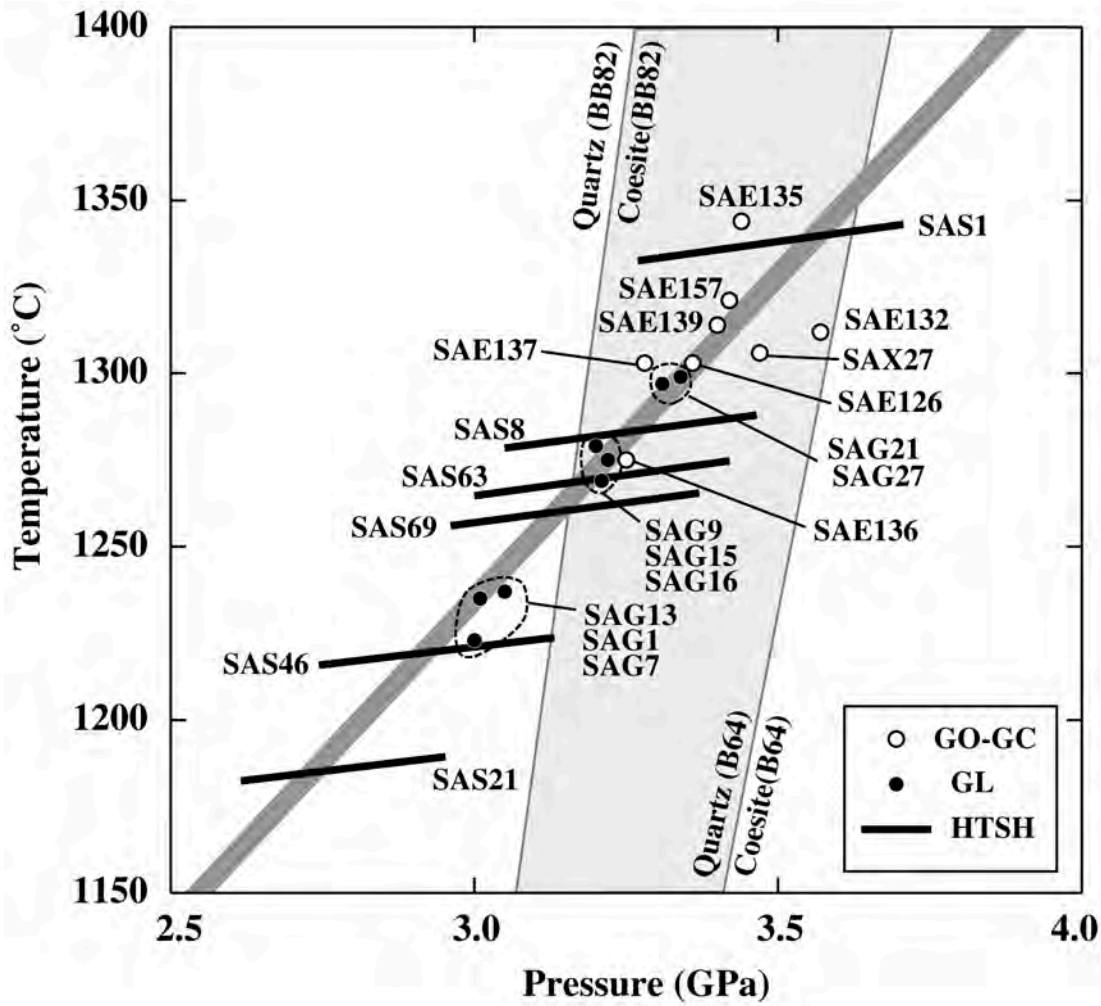

Fig. 5-13. P-T estimates for HT-type GL, GO and GC (SAE132) using two-pyroxene thermometer and Al in orthopyroxene barometer by Brey and Köhler (1990). For HTSH, T lines with dependent P are placed. Heavy-gray thick line indicates fitted line by all of P-T plots. Lowest P(Bohlen and Boettcher, 1982; BB82) and highest P (Boyd, 1964; B64) for reported quartz-coesite reaction boundaries is expressed as light-gray field.

5-5 Heterogeneous mantle plume model

The result of P-T estimation manifests uneven depth distribution for HT-type rocks. GC-GO occupies the deepest region of whole mantle column of studied xenoliths (> 100 km), whereas GL distributes between the pyroxenite-rich (GC-GO) zone and the depleted zone. This depth-lithological variation may be explained by heterogeneous plume melting model proposed by several studies for continental flood basalt and ocean island basalt (e.g. Hofman, 1982; Hauri, 1996; Yasuda et al., 1998; Takahashi et al., 1998; Kogiso et al., 1998; Yaxley, 2000; Takahashi and Nakajima, 2002). If subducted oceanic crust with basaltic composition is embedded in adiabatically upwelling mantle plume, they begin to melt in higher pressure than peridotitic mantle because solidus temperature of basalt is significantly lower than those of the peridotite (Fig. 5-14, Takahashi et al., 1993; Yasuda et al., 1994). Even P-T region of adiabatic pass is below peridotite solidus, basaltic material melts nearly total amount. However, pure basalt melt may prohibit from erupting by low-degree melting of matrix peridotite and react with subsolidus wall of peridotite effectively. In P-T region above solidus of peridotite, the basaltic melt may become to diffuse in matrix peridotite easily. If upwelling and eruption of the melt is relatively slow, the composition of melt converge to that of pure-peridotite melting. On the other hand, if melt separation is proceeded effectively, composition of upwelling melt tends to have simple mixture originated from basalt and peridotite. Therefore, imprint of entrained basalt may not remain in chemistry of residual solid phases or even as modal heterogeneity. From these considerations, three regions of HT-type (pyroxenite-rich deeper zone, garnet lherzolite dominant zone and garnet-poor deplete zone) might have occupied each different depths of one upwelling mantle and the height of column has been preserved after impinging relatively (Fig. 5-13). GC-GO represents lowest part of upwelling mantle plume and imprint of entrained basalt is directly observable as refractory garnet clinopyroxenite and reaction origin of garnet orthopyroxenite. Also some megacryst might have crystallized from evolved magma, which was produced by basalt melting in this region. GL occupied the intermediate part of mantle plume, representing as low-degree melting products of host peridotite. Although mineral chemistry and even modal composition were modified by subsequent metasomatic enrichment, some REE patterns in garnet core supports that they suffered melting event. Depleted zone is represented by spinel harzburgite

consisted top of the mantle plume and garnet were totally consumed by high-degree of melting. If this interpretation is valid, the melting temperature of the rising mantle might be estimated around 1500˚C and the potential temperature needs more than 1500˚C considering the latent heat of melting (Fig. 5-14) in disregard of the presence of hydrous components, vertical movement of the mantle after impinging and garnet appearance accompanying subsequent metamorphic cooling reaction. In other words, if HT-type rocks have been cooled at individual depth range from melting temperature to the geotherm until host alnöite eruption, 1500˚C as the melting temperature is suitable for (1) the depth of depleted zone (about 2.6~3.0 GPa) is represented as final depth of adiabatic mantle plume, then garnet totally consumed and disappeared from residual solid. (2) the depth of GL (about 3.0~3.4 GPa) is needed for remaining of garnet after melting. (3) the depth of GC-GO (approximately > 3.4 GPa) as lower part of impinged mantle situated near peridotite solidus and basalt liquidus.

For the genesis of the OJP, there are numerous merits of heterogeneous mantle plume model as pointed out by several recent studies (e.g. Takahashi, 1998; Petterson et al. 1999; Tejada et al. 2000). Firstly, voluminous eruption of the chemically coherent OJP is required unrealistic volume of homogeneous source peridotite. Even if highest degree of melting is assumed (about 30 %), a diameter of plume head reaches equivalent to whole depth (~ 660 km) of upper mantle (Coffin and Eldholm, 1994). Secondly, almost studied OJP basalt consists Low-K tholeiite with dominant phenocryst phase as clinopyroxene (Mahoney et al. 1993; Tejada et al. 1996; Neal et al. 1997). As noted by high-pressure experimental results (Takahashi, 1983; Hirose 1993), primary melt of peridotite needs to fractionate high proportions of olivine in order to make OJP lava compositions. According to the modeling result of Neal et al. (1997), most of OJP lavas represent after 30-45 % crystal fractionation with 30.1 wt.% MgO as bulk cumulate value. This estimation requires that the cumulate occupies 7-11.3 km thickness of whole crustal section. Such as large amount of fractionation cannot accord with restricted variations of OJP lavas confirmed in several localities. Finally, based on trace element and isotopic studies of 122 Ma OJP tholeiite from central Malaita, Tejada et al. (2000) predicted a hybrid melt containing completely melted recycled oceanic crust and significant proportions (0.5~20 %) of partial melts from plume peridotite. Although estimated values cannot

be justified by my data, the model is clearly consistent with my interpretation in the point that there was the significant contributions of partially melted peridotite and totally melted basaltic component representing recycled oceanic crust.

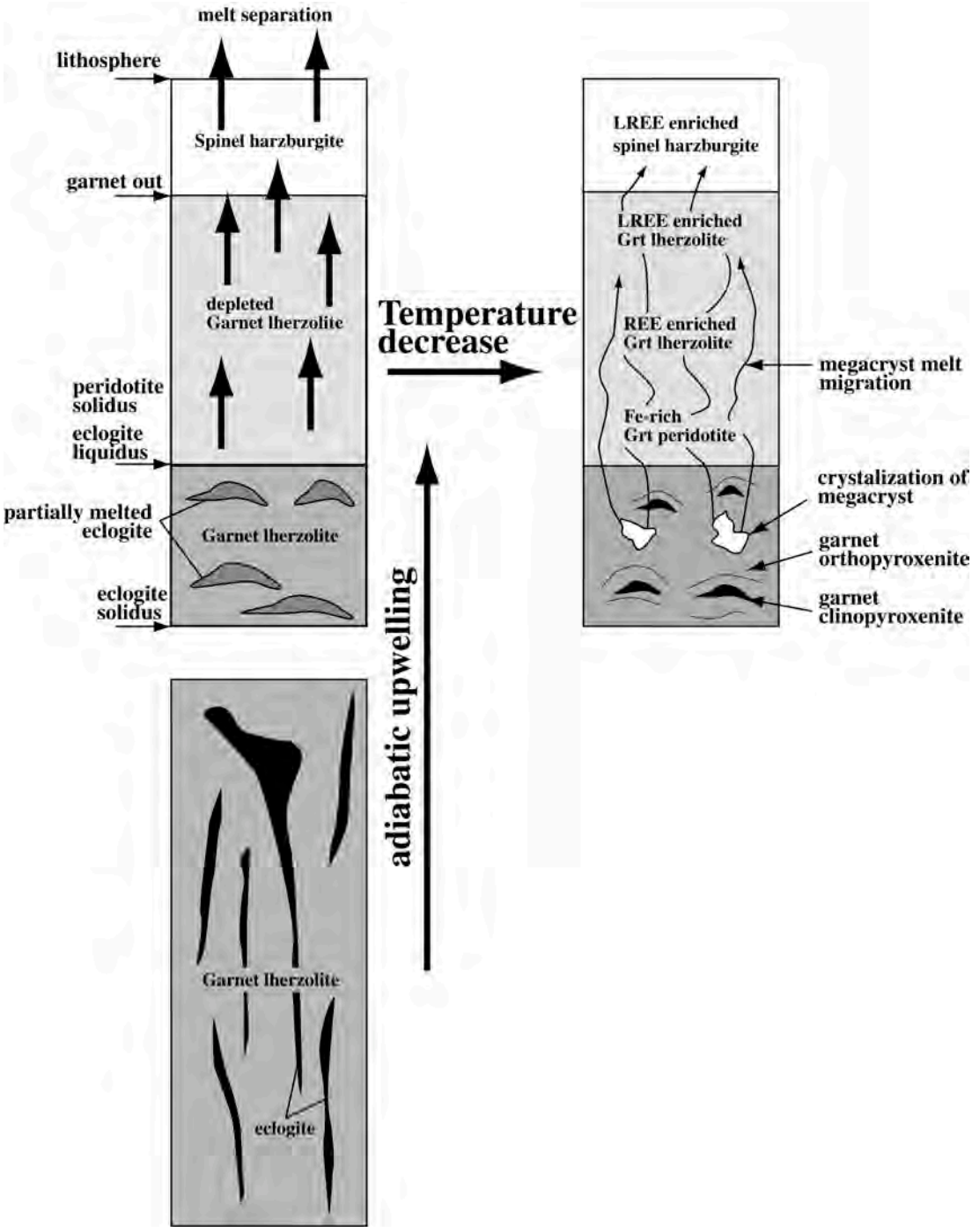

Fig. 5-14. Schematic illustration of the heterogeneous mantle plume model accounting for depth-lithological variation (left) and subsequent metasomatism caused by infiltration of megacryst melt (right) observed in HT-type.

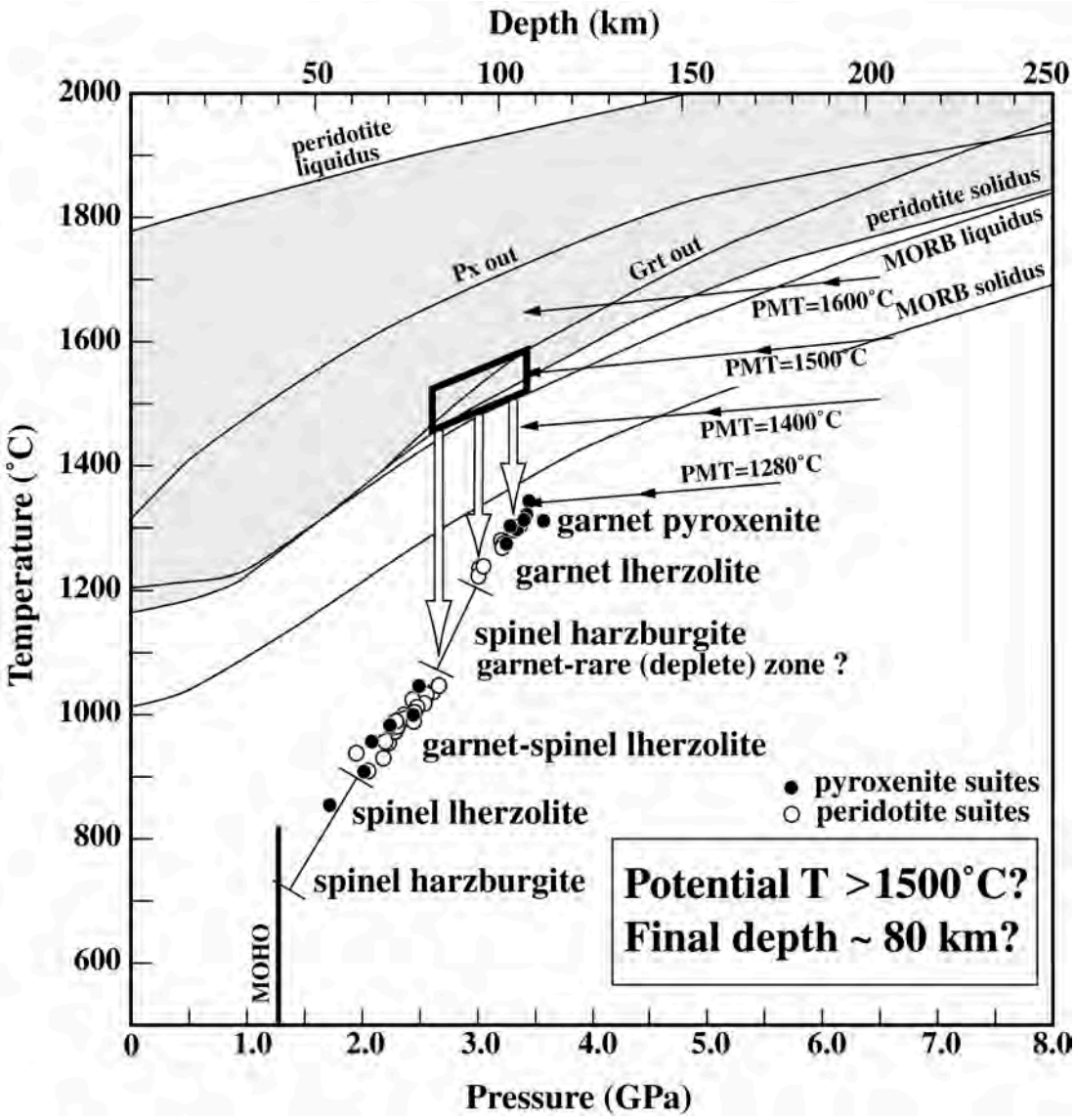

Fig. 5-15. Liquidus and solidus for primitive MORB (Yasuda et al., 1994) and fertile peridotite KLB-1 (Takahashi et al., 1993). Estimated melting site of OJP plume (approximately 1500˚C and 80 km in depth) is suitable for (1) the depth of deplete zone (about 2.6~3.0 GPa) is represented as final depth of adiabatic mantle plume, then garnet totally consumed and disappeared from residual solid. (2) the depth of GL (about 3.0~3.4 GPa) is needed for remaining of garnet after melting. (3) the depth of GC-GO (approximately > 3.4 GPa) as lower part of impinged mantle situated near peridotite solidus and basalt liquidus.

5-6 Evolution of sub-OJP mantle

Fig. 5-15 illustrates the preferred stratigraphy of sub-OJP mantle using the P-T estimates. One of the important findings of the present study is the confirmation of genetically unrelated two-layered structure. The upperpart of the mantle column (Moho ~ 80 km) dominated by LT-type peridotite may have originated from oceanic lithosphere generated by passive upwelling of asthenospheric mantle at a mid-oceanic ridge. Lower part near the boundary may have accreted to the bottom of lithosphere by subsequent conductive cooling of lithospheric mantle. Formation of the upperpart of mantle must precede the OJP volcanism which originated from upwelling of the lower part of mantle column represented by HT-type peridotites and pyroxenites (80 ~ 110 km). Accompanying with the OJP volcanism, lots of magma-conduits formations are expected to develop in the pre-existing lithospheric mantle. LT-type pyroxenites may have originated from cumulate precipitating along the conduits. They brought metasomatic enrichment to spatially-associated peridotites with residual nature. From climax stage of OJP volcanism to entrainment stage by alnöite eruptions, as the general situation, conductive cooling process thought to be effective for the upperpart of lithospheric mantle. After OJP volcanism, metamorphic reaction and possible metasomatic modification continuously caused without ceasing and changed of their chemical characteristics until eruption of host alnöite. On the other hand, chemical nature of lower part of mantle column is characterized by abundant evidence of metasomatic modification rather than cooling. It can be accounted that cooling evidence could not leave as chemical heterogeneity owing to higher temperature. However, in spite of higher temperature, metasomatic heterogeneity was significantly relieved in these samples. In particular, Fe/Mg heterogeneity in single garnet must originate from an event immediately before alnöite eruption considering the diffusional homogenization at mantle temperatures. This situation is essentially same with high temperature xenoliths from cratonic mantle and it must be related to the origin of kimberlite and megacryst representing as one of the general problem.

Fig. 5-16 demonstrates the evolution model of sub-OJP mantle based on a conjunction of several evidences obtained from previous studies. Most of previous studies have been agreed that the OJP volcanism was episodic and caused by rising plume head (e.g. Larson, 1997; Neal, 1997). Well-constrained bimodal ages with

122±3 and 90±4 Ma were obtained by using ^{40}Ar-^{39}Ar methods for basement lavas and brought about the concept of two pulses from same source (Mahoney, et al., 1993; Tejada et al., 1996). Comparing to the 90 Ma event, the122 Ma eruption has been generally considered to be voluminous and construct most part of the OJP area (Kroenke and Mahoney, 1996). The accurate location and setting of the primary OJP emplacement at 122 Ma is one of the subjects for debate. Mahoney (1991) and subsequent studies proposed that the OJP was formed by a near ridge-axis plume originated as the early Louisville hotspot (Fig. 5-17). Ridge-axis model has been widely accepted in due to greater merit accounting for the chemical nature of OJP lavas demanding high-degree of melting (Tarduno et al., 1991; Mahoney and Spencer, 1991; Mahoney et al. 1993). However, evidences provided by the studies of magnetic anomaly lineations favor OJP emplacement at the off-ridge location (Nakanishi et al., 1992; Winterer and Nakanishi, 1995; Nakanishi and Winterer, 1996). The evidences were summarized as (1) apparent lack of well-defined magnetic anomaly lineations on the OJP, (2) ENE-WSW trending M-series lineation sets on the east side of the OJP (Nauru Basin), yielding slight older age than OJP emplacement (M29-M1; ca. 155-124 Ma), (3) confirmation of similar ENE-WSW-oriented anomaly on Lyra Basin situated on the west side of OJP (Taylor, 1978). Actually, an extension of the spreading-ridge formed Nauru Basin and Lyra Basin present as " abandoned ridge", namely Nova-Canton Trough on the SE side of OJP (Fig. 5-18). OJP emplacement, abandonment of the ridge and changes in Pacific Plate motion occurred broadly at the same time between M1 and M0 (ca. 125~120 Ma) and a tripartite relation of cause and effect has been considered by several studies (Larson 1991; Coffin and Eldholm, 1994; Anderson, 1994; Larson, 1997; Neal, 1997). According to the detailed considerations by Larson (1997), abandonment of the Pacific-Phoenix ridge significantly postdated the ceasing of first OJP eruptions based on the discovery of M0 lineation. However, Neal (1997) claimed that existing data do not allow that interpretation and further resolution of age-dating is needed.

Off-ridge location of OJP emplacement can be supported by the present study, at least restricted domain among very large area. The approximate age of upwelling of LT-type peridotite can be equated to those of neighboring magnetic reversal patterns and it might be younger than ~155 Ma as oldest age from M29 (Fig. 5-18). At the 122 Ma, OJP emplacement caused by the upwelling of mantle plume might

have located in slightly north from the active ridge. The rough estimation of the distance using average half-spreading rates (~ 7.7 cm/yr, Gradstein et al., 1994) indicate that northern edge of OJP erupted on the pre-existing oceanic crust constructed at ~ 2500 km away from an active ridge.

If the thickness of pre-OJP lithospheric mantle is allowed to be estimated by using the reconstructed mantle column, the obtained value (~ 50 km) is equivalent to the thickness of 45 Ma-old lithospheric mantle and significantly thicker than the estimated thickness using maximum age gap (~ 33 Ma old lithospheric mantle = 43 km using the equation: $l=7.5\div t$). However, if the cooling time of pre-OJP lithospheric mantle is extended to 90 Ma, pre-OJP lithospheric mantle can grow up to 60 km thickness in the case that lithosphere erosion process are ignored, because the spreading ceased at ~ 120 Ma and movement of Pacific Plate was limited until 90 Ma (Tarduno and Sager, 1992). Actually, there are lots of unclear problems for such as estimation. For example, where located at the center of mantle plume and how large and rate the plume head spread along the bottom of the lithospheric mantle. The detailed data of relative crustal distribution of 122 Ma and 90 Ma lava can be needed for hypothesizing.

After the 90 Ma period, several volcanic events have been recognized in Malaita Islands, namely North Malaita Alkalic suites and Malaita Younger series. Both are composed of alkali basaltic lava with ~ 44 Ma in age (Hughes and Turner, 1977; Tejada et al., 1996). Alnöite eruption with an age of 34 Ma significantly postdated both alkali basalt formations. Based on isotopic study, Malaita Younger series has been believed to consist the part of the tracks when OJP passed over the Samoan hotspot. On the other hand, the North Malaita Alkalic suite has similar isotopic ratios with those of OJP basement. Tejada et al. (1996) interpreted this volcanism resulted from remelting of OJP source caused by hotspot heating. Also epsilon Nd(T) of alnöites show significantly higher values than those of the Samoan hotspot and Malaita Younger series. They display close similarity with those of North Malaita Alkalic suites indicative of similar origin. If source of these lavas was storaged in sub-OJP lithospheric mantle, OJP source mantle representing as “fossil plume” could be dragged by overlaid oceanic lithosphere and they were deliverable to surface by significant later magmatism such as alnöite.

Recently, Richardson et al. (2000) reported the results of detailed

tomographic investigation over the OJP. Fig. 5-19 illustrates the present cross-sections of the seismic structure of the OJP and displays that strong development of low-velocity zone extend to as deep as 300 km below the OJP. According to their estimation, the observed 5 % deficiency of shear velocity is required a temperature anomaly of 350-700 K and it must be attribution of chemical heterogeneity rather than temperature. They also interpreted that the low-velocity root was traveled with Pacific Plate since the OJP was formed and expressed in the term of “blatant violation of the Wilson paradigm”. If this interpretation is valid, their results strongly support that some of studied samples represent the fragments of OJP plume, which was chemically heterogeneous.

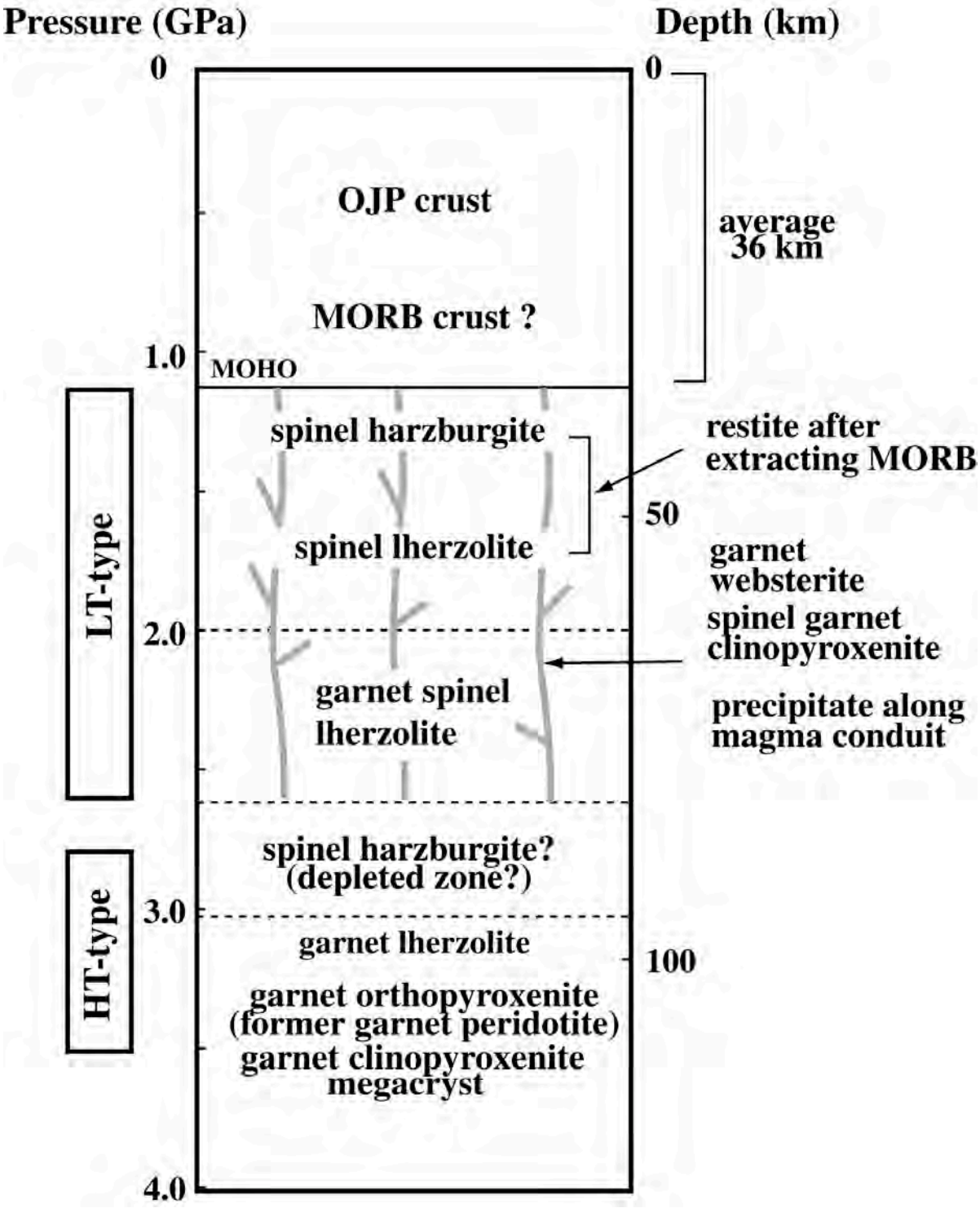

Fig. 5-16. The column of stratigraphic succession beneath the Ontong Java Plateau based on the study of Malaitan xenoliths. Average crustal thickness is obtained from Richardson et al. (2000).

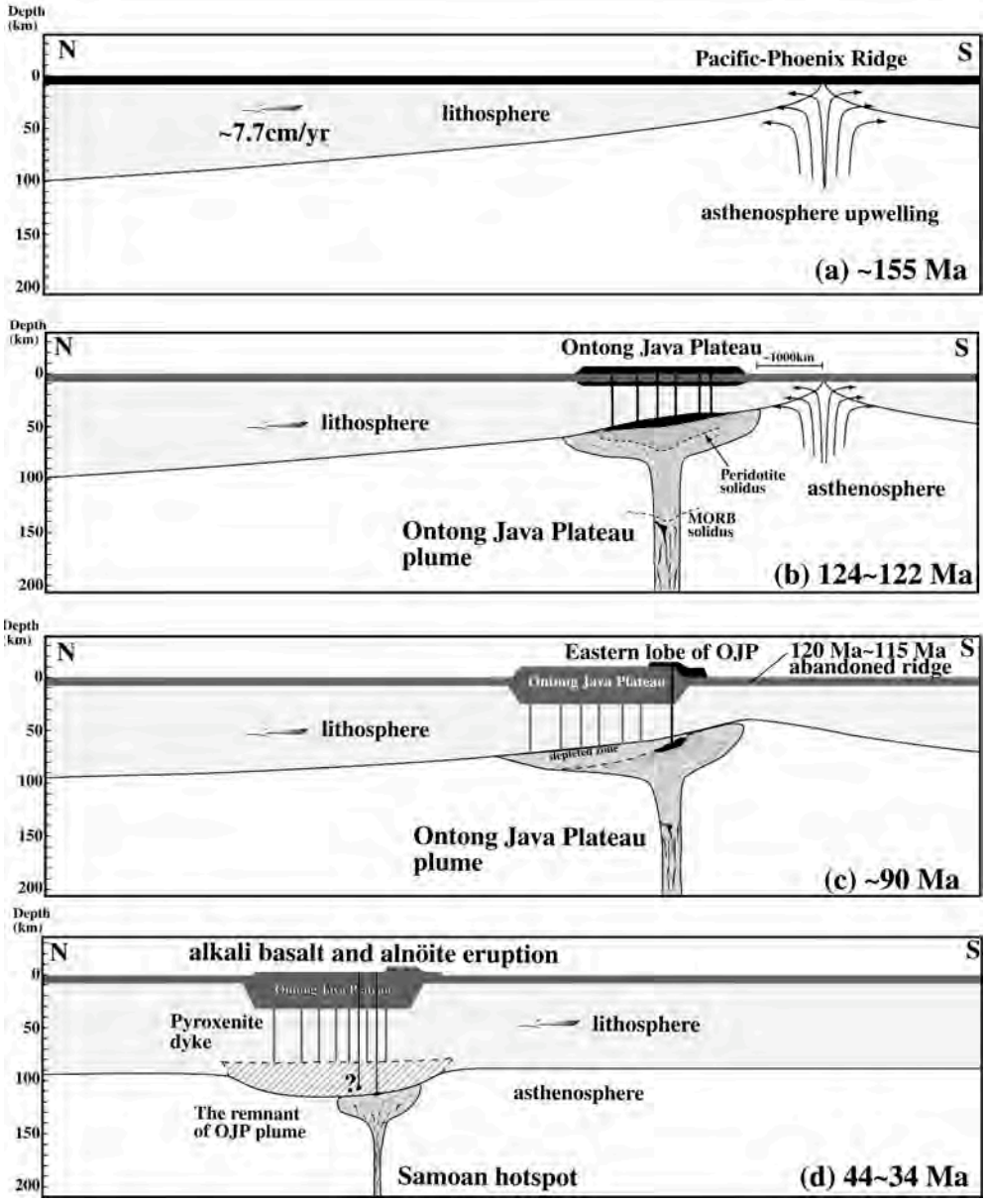

Fig. 5-17. Cartoon illustrated the evolution of Ontong Java Plateau and underlying mantle, showing the possible cross-sections which highlight the following points: (a) Pre-OJP eruption must be represented that normal oceanic lithosphere constructed by Pacific-Phoenix spreading ridge. Paleomagnetic evidences show that oldest age is about 155 Ma and the average spreading rate is about 7.7 cm/yr. (b) OJP basement development at 124~122 Ma as a result of plume-head impinged under the lithospheric mantle. Pacific-Phoenix spreading ridge was activated near ceasing period of the 122 Ma eruption. (c) Second eruption of OJP at 90 Ma consisting the eastern lobe of OJP in due to limited movement of Pacific Plate. Noted that spreading of Pacific-Phoenix ridge abandoned on the suspension of OJP plume. (d) OJP and remnant of the plume traveled toward further north with movement of Pacific Plate and passed on the Samoan hotspot at 44 Ma. Alkali basalt with isotopically equivalent to Samoan lavas might originated from the Samoan plume source. Subsequent alnöite eruptions (34 Ma) occurred near the Samoan hotspot, however isotopic data disagreed about their Samoan hotspot origin.

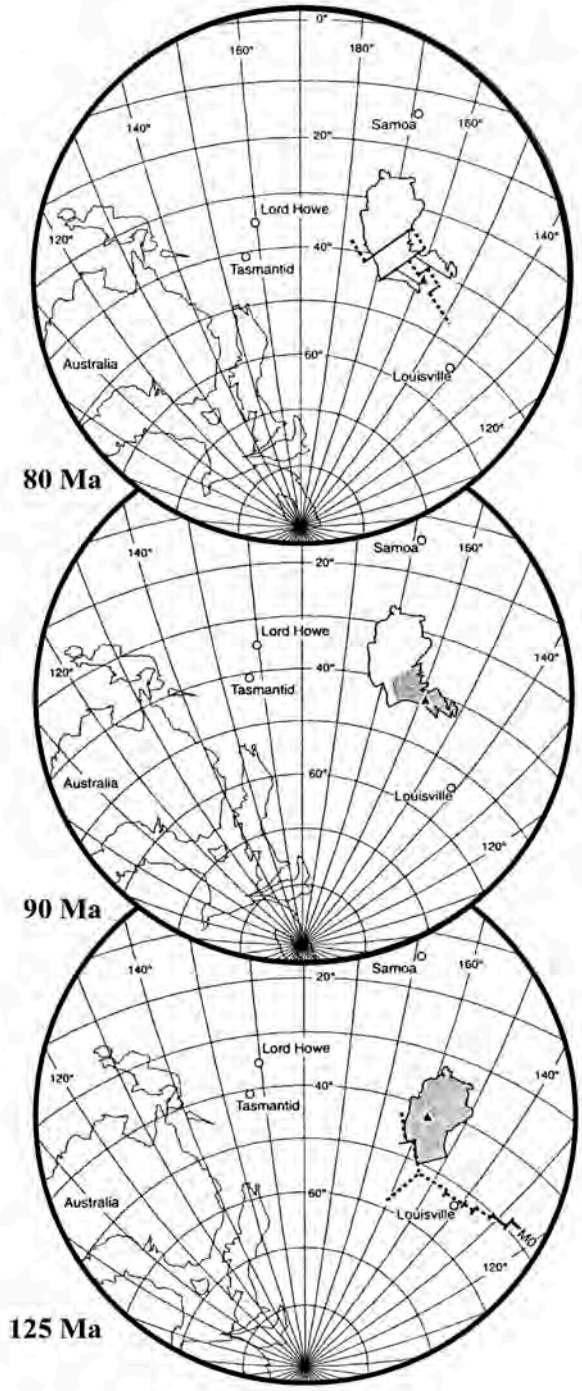

Fig. 5-18. Pacific Plate reconstructions for bottom: 125 Ma; middle: 90 Ma and top: 80 Ma (Neal et al., 1997). The triangle represents the infered location of the OJP plume center beneath the crest of the high plateau. Circles show the locations of several present-day hot spots. Dashed lines indicate the locations of spreading ridge favored by Neal et al. (1997).

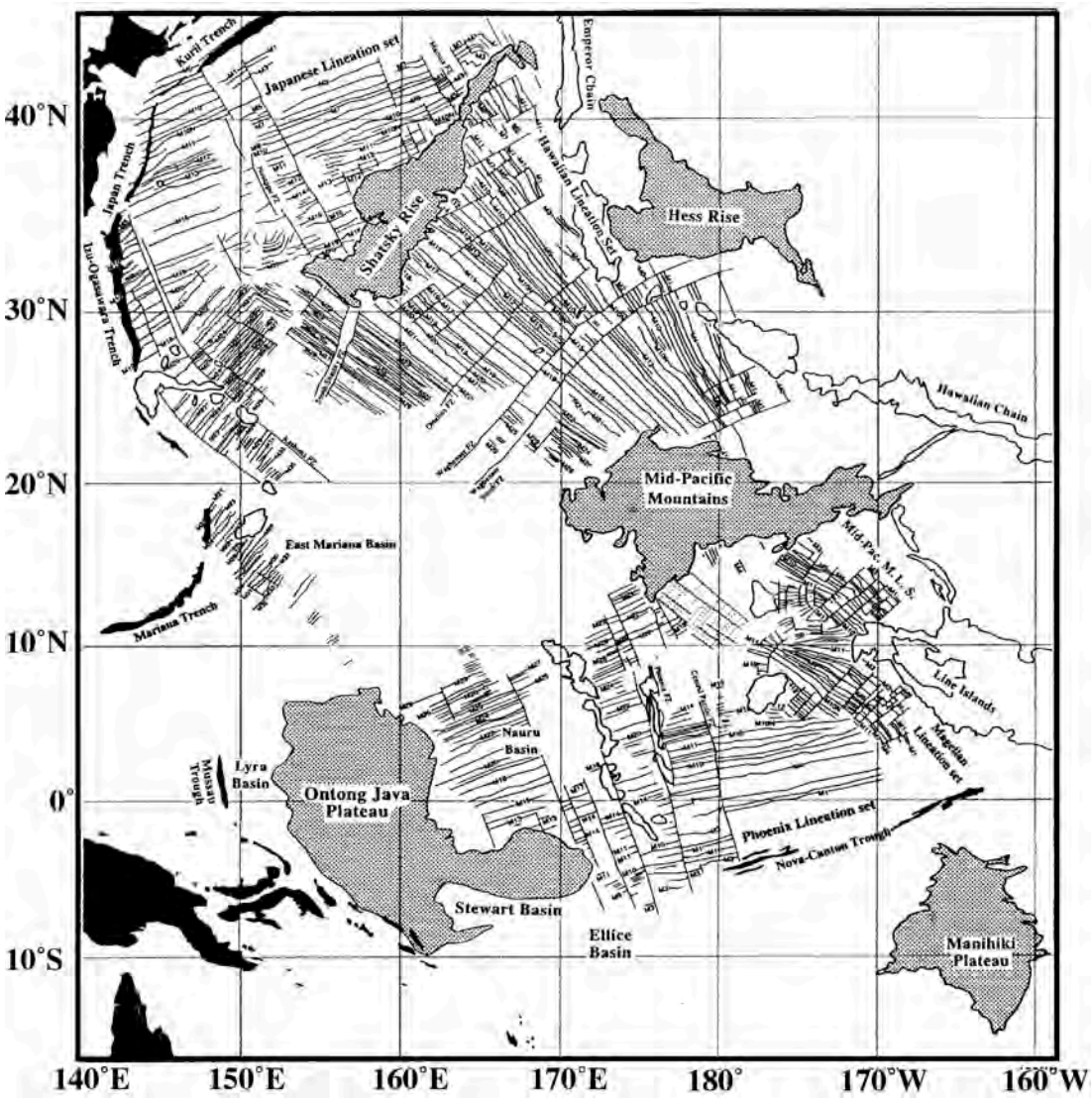

Fig. 5-19. Map of Mesozoic magnetic anormaly lineations and fracture zones in the west-central Pacific (Nakanishi et al., 1992). Shaded areas show the locations of principal oceanic plateaus.

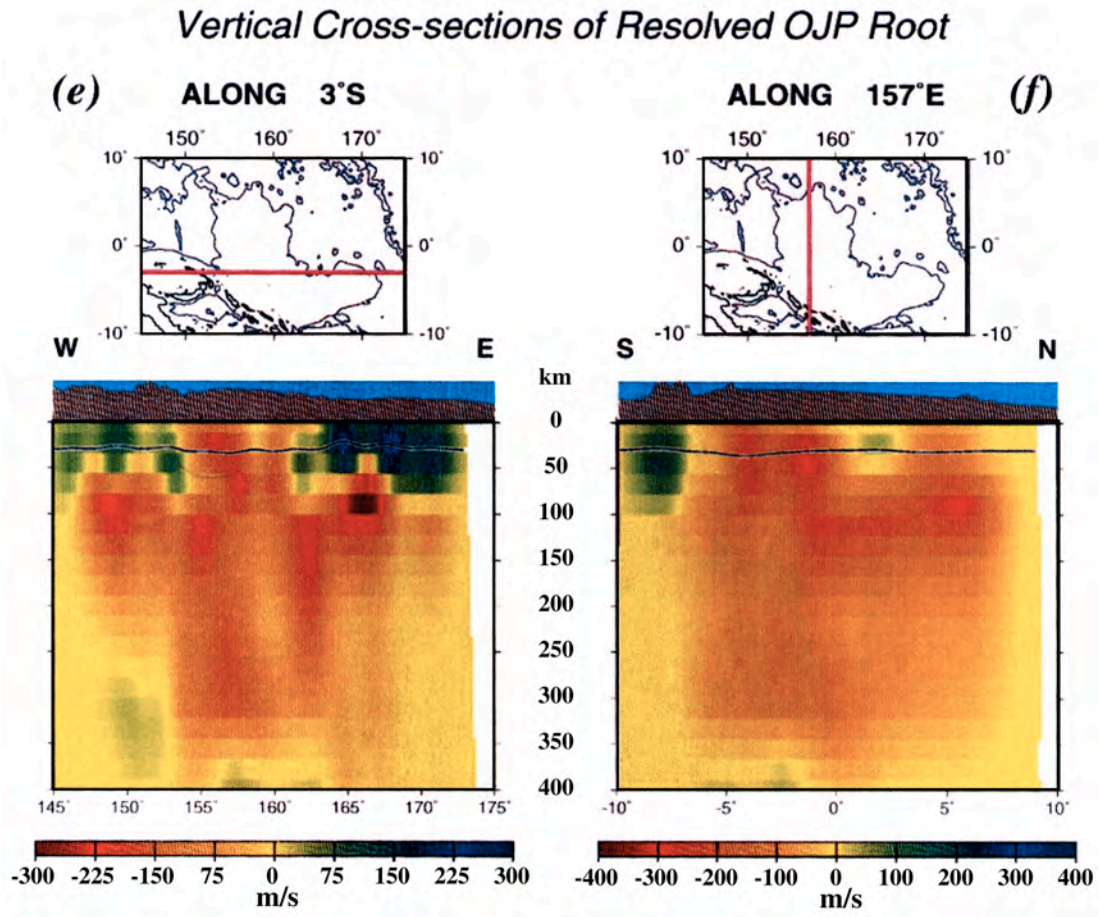

Fig. 5-20. Present (e) west-east and (f) south-north cross-sections of the seismic structure of the OJP from the results of three-dimensional tomographic inversions calculated by Richardson et al. (2000). It is noted that they interpreted that the low-velocity zone extending as deep as 300 km, represent as a keel, dragged along the OJP.

Acknowledgements

I gratefully acknowledge to my supervisor, Professor Shigenori Maruyama of Tokyo Institute of Technology (T.I.T.) for giving the opportunity and encouragement to carry out this study. I greatly appreciate Associate Professor Kei Hirose of T.I.T for his valuable suggestions and discussions. For analytical work on SIMS, I received helpful instruction from Associate Professor Hisayoshi Yurimoto of T.I.T. It is entirely thanks to him that the critical data was obtained in this study. I am grateful to Associate Professor Teruaki Ishi of Ocean Research Institute, University of Tokyo for his permission and instruction of bulk trace element analyses by XRF. Thanks also must go to Drs. Hirokazu Tabata, Natsue Abe and Akiko Miyazaki for helpful guidance and assistance with EPMA analysis and Drs. Tetsu Kogiso, Hironao Shinjoe and Tsuyoshi Komiya for helpful guidance and assistance with XRF analysis.

During fieldwork, I received the kind support from the Ministry of Energy and Mines in Solomon Islands. I would like to thank the Director of Geology, Mr. Don Tolia, and Deputy Director, Mr. Nicholas Biliki for their support and encouragement. Messrs Stanley Basi, Cromwell Qopoto, Peter Auga and other staff of the Ministry of Energy and Mines in Solomon Islands are highly acknowledged for kind assistance in order to success our research trip. Special thanks go to Mr. Fred Fakarii, the Permanent Secretary of Malaita Province and Mr. Hon Benjamin Harottele, the Deputy Premier for permission to work on geology and collect samples in the Malaita province. Also thanks must go to the people of North Malaita for understanding our objective and kind donating the samples.

I wish to thank Dr. Deon de Bruin of Council for Geoscience Pretoria, Republic of South Africa for his helpful guidance of general situations of kimberlitic xenoliths and assistance for studying the Malaitan megacryst suites. I am indebted to Dr. Eiiichi Takazawa of Niigata University for his kind suggestions and useful advices for interpretations of REE variations.

Sincere thanks also due to Drs. Shignori Maruyama, Eiichi Takahshi, Katsuyuki Kawamura, Hisayoshi Yurimoto, Kei Hirose and Kazuhito Ozawa who constructively reviewed the manuscript.

I also sincere thank to the other members of Prof. Maruyama laboratory: Drs.

Kazuaki Okamoto, Yoshiyuki Kaneko, Soichi Omori, Tsutomu Ota, Yuji Orihashi, Ade Kadarusman, Mr. Yuichiro Ueno, Kenji Shimizu, Kouki Kitajima, Hideki Masago, Ikuo Katayama, Atsushi Utsunomiya, Yuko Uchio, Hiroyuki Usui, Junnpei Yamamoto, Noriyuki Takahashi, Motohiko Murakami, Testuya Komabayashi, Nobuhiro Kawano, Norihito Suzuki, Shuji Rino, Tsuyoshi Iizuka, Ryusuke Sakurai for discussions and continuous encouragement. I gratefully thank Mses. Yoshiko Kogiso, Miwako Kato, Shio Watanabe, and Miki Akimoto for their kindness.

References

Anderson, D. L. (1994). Superplumes or supercontinents? Geology 22, 39-42.

Arai, S. (1994). Characterization of spinel peridotites by olivine-spinel compositional relationships: Review and interpretation. Chemical Geology 113, 191-204.

Arai, S. and Fujii, T. (1979). Petrology of ultramafic rocks from Site 395. In: Melson, W. G. and Rabinowitz, P. D. (eds) Init. Repts. DSDP 45, pp. 587-594.

Arai, S. and Matsukage, K. (1996). Petrology of the gabbro-troctolite-peridotite complex from Hess Deep, equatorial Pacific: implications for mantle-melt interaction within the oceanic lithosphere. Proceedings of the Ocean Drilling Program, Scientific Result 147, 135-155.

Bedini, R. M., Bodinier, J.-L., Dautria, J.-M. and Morten, L. (1997). Evolution of LILE-enriched small melt fractions in the lithospheric mantle: a case study from the East Africa Rift. Earth and Planetary Science Letters 153, 67-83.

Beeson, M. H. and Jackson, E. D. (1970). Origin of the garnet pyroxenite xenolites at Salt Lake Crater, Oahu. Mineral Soc. Amer. Spec. Pap 3, 95-112.

Bertland, P. and Mercier, J.-C. C. (1985). The mutual solubility of coexisting ortho- and clinopyroxene: toward an absolute geothermometer for the natural system? Earth and Planetary Science Letters 76, 109-122.

Bielski-Zyskind, M., Wasserburg, G. J. and Nixon, P. H. (1984). Sm-Nd and Rb-Sr systematics in volcanics and ultramafic xenoliths from Malaita, Solomon Islands and the nature of the Ontong Java Plateau. Journal of Geophysical Research 89, 2415-2424.

Bodinier, J. L., Vasseur, J., Vernieres, C., Dupuy, C. and Fabries, J. (1990). Mechanism of mantle metasomatism: geochemical evidence from the Lherz orogenic peridotite. Journal of Petrology 31, 597-628.

Bonnatti, E., Peyve, A., Kepezhinskas, P., Kurentsova, N., Seyler, M., Skolotnev, S. and Udintsev, G. (1992). Upper mantle heterogeneity below the Mid-Atlantic Ridge, 0˚-15˚. Journal of Geophysical Research 97, 4461-4476.

Boyd, F. R. (1973). A pyroxene geotherm. Geochimica et Cosmochimica Acta 37, 2533-2546.

Brey, G. P. and Köhler, T. (1990). Geothermobarometry in four-phase lherzolites II. New thermobarometers, and practical assesment of existing

thermobarometers. Journal of Petrology 31, 1352-1378.

Burgess, S. R. and Harte, B. (1999). Tracing lithosphere evolution through the analysis of heterogeneous G9/G10 garnets in peridotite xenoliths, I: Major element chmistry. In: Gurney, J. J., Gurney, J. L., Pascoe, M. D. and Richardson, S. H. (eds) Proceedings of the VIIth international kimberlite conference. Cape Town: Red Roof Desing cc, pp. 66-80.

Clark, J., S. P. and Ringwood, A. E. (1964). Density distribution and constitution of the mantle. Review of Geophys. 2, 35-88.

Coffin, M. F. and Eldholm, O. (1994). Large Igneous Provinces: crustal structure, dimensions, and external consequences. Review of Geophys. 21, 1-36.

Coleman, P. J. and Kroenke, L. W. (1981). Subduction without volcanism in the Solomon Islands Arc. Geomarine Lett. 1, 129-134.

Collerson, K. D., Hapugoda, S., Kamber, B. S. and Williams, Q. (2000). Rocks from the mantle transition zone: majorite-bearing xenoliths from Malaita, Southwest Pacific. Science 288, 1215-1223.

Davis, G. L. (1977). The ages and uranium contents of zircons from kimberlites and associated rocks. 2nd Int. Kimberlite Conf.: extended abstracts unpaged.

Davies, G. R., Spriggs, A. J. S. and Nixon, P. H. (2001). Journal of Petrology 42, 159-172.

Dawson, J. B. (1980). Kimberlites and their xenoliths, Berlin: Springer-Verlag, 252 pp.

Dick, H. J. B. and Fisher, R. L. (1984). Mineralogical studies of the residues of mantle melting: abyssal and alpine-type peridotites. In: Kornprobst, J. (ed.) Kimberlites II: The mantle and crust-mantle relationships. Amsterdam: Elsevier, pp 295-308.

Dick, H. J. B. and Bullen, T. (1984). Chromian spinel as a petrogenetic indicator in abyssal and alpine-type peridotites and spatially associated lavas. Contributions to Mineralogy and Petrology 86, 54-76.

Dick, H. J. B. and Natland, J. H. (1996). Late-stage melt evolution and transport in the shallow mantle beneath the East Pacific Rise. Proceedings of the Ocean Drilling Program, Scientific Result 147, 103-134.

Ellis, D. J. and Green, D. H. (1979). An experimental study of the effect of Ca upon garnet-clinopyroxene Fe-Mg exchange equilibria. Contributions to

Mineralogy and Petrology 71, 13-22.

Fabries, J. (1979). Spinel-olivine geothermometory in peridoties from ultramafic complexs. Contributions to Mineralogy and Petrology 69, 329-336.

Finnerty, A. A. and Boyd, F. R. (1987). Thermobarometry for garnet peridotites: basis for the determination of thermal and compostional structure of the upper mantle. In: Nixon, P. H. (ed) Mantle Xenoliths. Chichester: John Wiley & Sons, pp.381-402.

Frey, F. A. and Prinz, M. (1978). Ultramafic inclusions from San Carlos, Arizona: petrologic and geochemical data bearing on their petrogenesis. Earth and Planetary Science Letters 38, 129-176.

Furumoto, A. S., Hussong, D. M., Cambell, J. F., Sutton, G. H., Rose, J. C. and Woollard, G. P. (1970). Crustal and upper mantle structure of the Solomon Islands as revealed by seismic refraction survey of November-December 1966. Pac. Sci. 24, 315-332.

Furumoto, A. S., Webb, J. P., E.Odegard, M. and Hussong, D. M. (1976). Seismic studies on the Ontong Java Plateau, 1970. Tectonophysics 34, 71-90.

Garrido, C. J. and Bodinier, J. L. (1999). Diversity of mafic rocks in the Ronda peridotite: evindence for pervasive melt-rock reaction during heating of subcontinental lihtosphere by upwelling asthnosphere. Journal of Petrology 40, 729-754.

Gasparik, T. (1986). Experimental study of subsolidus phase relations and mixing properies of clinopyroxene in the silica-saturated system CaO-MgO-Al_2O_3-SiO_2. American Mineralogist 71, 686-693.

Goto, A. and Tatsumi, Y. (1994). Quantative analysis of rock samples by an X-ray fluorescence spectrometer (I). The Rigaku Journal 11, 40-59.

Goto, A. and Yokoyama, K. (1988). Lherzolite inclusions in olivine nephelinite tuff from Salt Lake Crater, Hawaii. Lithos 21, 67-80.

Gradstein, F. M., Agterberg, F. P., Ogg, J. G., Jardenbol, J., van Veen, P., Thierry, J. and Juang, Z. (1994). A Mesozoic time scale. Journal of Geophysical Research 99, 24051-24074.

Green, D. H. and Ringwood, A. E. (1970). Mineralogy of peridotitic compositions under upper mantle compositions. Physics of the Earth and Planetary Interiors 3, 359-371.

Green, T. H., Blundy, J. D., Adam, J. and Yaxley, G. M. (2000). SIMS determination of trace element partition coefficients between garnet, clinopyroxene and hydrous basaltic liquids at 2-7.5 GPa and 1080-1200˚C. Lithos 53, 165-187.

Griffin, W. L., Smith, D., Boyd, F. R., Cousens, D. R., Ryan, C. G., Sie, S. H. and Suter, G. F. (1989). Trace-element zoning in garnets from sheared mantle xenoliths. Geochimica et Cosmochimica Acta 53, 561-567.

Gudfinnsson, G. and Presnall, D. C. (1996). Melting relations of model lherzolite in the system CaO-MgO-Al_2O_3-SiO_2 at 2.4 to 3.4 GPa and the generation of komatiites. Journal of Geophysical Research 101, 27701-27709.

Gurney, J. J. and Harte, B. (1980). Chemical variations in upper mantle nodules from southern African kimberlites. Philosophical Transactions of the Royal Society of London A297, 273-293.

Gurney, J. J., Jakob, W. R. O. and Dawson, J. B. (1979). Megacrysts from the Monastery kimberlite pipe, South Africa. In: Boyd, F. R. and Meyer, H. O. A. (eds) The Mantle Sample: Inclusions in Kimberlites and Other Volcanics; Washington, DC: American Geophysical Union, pp. 227-243,

Hamlyn, P. R. and Bonnatti, E. (1980). Petrology of mantle-derived ultramafics from the Owen fracture zone, northwest Indian Ocean: implications for the nature of the oceanic upper mantle. Earth and Planetary Science Letters 48, 965-979.

Harte, B. (1983). Mantle peridotites and processes: the kimberlite sample. In: Hawkesworth, C. J. and Norry, M. J. (eds) Contintal Basalts and Mantle Xenoliths. Shiva Geology Series, pp. 46-92.

Harte, B. and Kirkley, M. B. (1999). Partitioning of trace elements between clinopyroxene and garnet: data from mantle eclogites. Chemical Geology 136, 1-24.

Hauri, E. H. (1996). Major-element variability in the Hawaiian mantle plume. Nature 382, 415-419.

Hauri, E. H. and Hart, S. R. (1994). Constraints on melt migration from mantle plumes: A trace element study of peridotite xenoliths from Savai'i, Western Samoa. Journal of Geophysical Research 99, 24301-24321.

Hauri, E. H., Wagner, T. P. and Grove, T. L. (1994). Experimental and natural partitioning of Th, U, Pb and other trace elements between garnet, clinopyroxene and basaltic melt. Chemical Geology 117, 149-166.

Herzberg, C. T. (1978). The bearing of phase equilibria in simple and complex systems on the origin and evolution of some well-documented garnet-websterites. Contributions to Mineralogy and Petrology 66, 375-382.

Hirose, K. and Kushiro, I. (1993). Partial melting of dry peridotites at high pressures: determination of compositions of melts segregated from peridotite using aggregates of diamond. Earth and Planetary Science Letters 114, 477-489.

Hirschmann, M. M. and Stolper, E. M. (1996). A possible role for garnet pyroxenite in the origin of thegarnet signature in MORB. Contributions to Mineralogy and Petrology 124, 185-208.

Hofmann, A. W. and White, W. M. (1981). Mantle plumes from ancient oceanic crust. Earth and Planetary Science Letters 57, 421-436.

Hughes, G. W. and Turner, C. C. (1977). Upraised Pacific ocean floor, South Malaita, Solomon Islands. Geol. Soc. Amer. Bull 88, 412-424.

Hussong, D. M., Wipperman, L. K. and Kroenke, L. W. (1979). The crustal structure of the Ontong Java and Manihiki oceanic plateaus. Journal of Geophysical Research 84, 6003-6010.

Iwamori, H., Mckenzie, D. and Takahashi, E. (1995). Melt generation by isentropic mantle upwelling. Earth and Planetary Science 134.

Jaques, A. L. and Green, D. H. (1980). Anhydrous melting of peridotite at 0-15 kb pressure and the genesis of tholeiitic basaltic magma. Contributions to Mineralogy and Petrology 73, 287-310.

Johnson, K. T. M. (1998). Experimental determination of partition coefficients for rare earth and high-field-strength elements between clinopyroxene, garnet and basaltic melt at high pressure. Contributions to Mineralogy and Petrology 133, 60-68.

Johnson, K. T. M. and Dick, H. J. B. (1992). Open system melting and temporal and spatial variation of peridotite and basalt at the Atlantis II fracture zone. Journal of Geophysical Research 97, 9219-9241.

Johnson, K. T. M., Dick, H. J. B. and Shimizu, N. (1990). Melting in the oceanic upper mantle: An ion microprobe study of diopsides in abyssal peridotites. Journal of Geophysical Research 95, 2661-2678.

Jones, R. A. (1987). Sr and Nd isotopes and REE evidence for the genesis of megacryst in kimberlites of southern Africa. In: Nixon, P. H. (ed) Mantle

Xenoliths. Chichester: John Wiley and Sons, pp. 711-724.

Katayama, I., Parkinson, C. D., Okamoto, K., Nakajima, Y. and Maruyama, S. (2000). Supersilicic clinopyroxene and silica exsolution in UHPM eclogite and pelitic gneiss from the Kokchetav massif, Kazakhstan. American Mineralogist 85, 1368-1374.

Kawasaki, T. (1987). Paleogeotherms: olivine-orthopyroxene-garnet geothermometry and geobarometry. Lithos 20, 263-278.

Kelemen, P. B., Dick, H. J. B. and Quick, J. E. (1992). Formation of harzburgite by pervasive melt/rock interaction in the upper mantle. Nature 358, 635-641.

Kelemen, P. B., Hart, S. R. and Bernstein, S. (1998). Silica enrichment in the continental upper mantle via melt/rock reaction. Earth and Planetary Science Letters 164, 387-406.

Kinzler, R. J. (1997). Melting of mantle peridotite at pressures approaching the spinel to garnet transition: application to mid-ocean ridge basalt petrogenesis. Journal of Geophysical Research 102, 853-874.

Klein, E. M. and Langmuir, C. H. (1987). Global correlations of ocean ridge basalt chemistry with axial depth and crustal thickness. Journal of Geophysical Research 92, 8089-8115.

Kogiso, T., Hirose, K. and Takahashi, E. (1998). Melting experiments on homogeneous mixtures of peridotite and basalt: application to the genesis of oceanic island basalts. Earth and Planetary Science Letters 162, 45-61.

Kroenke, L. W., Resig, J. M. and Leckie, R. M. (1993). Hiatus and tephrochronology of the Ontong Java Plateau: correlation with regional tectono-volcanic events. Proceedings of the Ocean Drilling Program, Scientific Result 130, 423-444.

Kroenke, L. W. and Mahoney, J. J. (1996). Rifting of the Ontong Java Plateau's eastern salient and seafloor spreading in the Ellice Basin: Relation to the 90 Myr eruptive episode on the plateau (abstract). EOS Trans. AGU Fall Meeting 77, 713.

Krogh, E. J. (1988). The garnet-clinopyroxene Fe-Mg geothermometer a reinterpretation of existing experimental data. Contributions to Mineralogy and Petrology 75, 387-393.

Kushiro, I. (1968). Compositions of magmas formed by partial zone melting in the earth's upper mantle. Journal of Petrology 7, 337-362.

Kushiro, I. and H.S. Yoder, J. (1974). Formation of eclogite from garnet lherzolite: liquidus relations in a portion of the system MgSiO3-CaSiO3-Al2O3 at high pressures. Carnegie Instituition of Washington, Yearbook 73, 266-269.

Köhler, T. and Brey, G. P. (1990). Calcium exchange between olivine and clinopyroxene calibrated as a geothermobarometer for natural peridotites from 2 to 60 kb with applications. Geochimica et Cosmochimica Acta 54, 2375-2388.

Larson, R. L. (1991). Latest pulse of Earth: Evidence for a mid-Cretaceous super-plume. Geology 19, 547-550.

Larson, R. L. (1997). Superplumes and ridge interactions between Ontong Java and Manihiki Plateaus and the Nova-Canton Torough. Geology 25, 769-864.

MacGregor, I. D. (1974). The system MgO-Al_2O_3-SiO_2: solubility of Al_2O_3 in enstatite for spinel and garnet peridotite compositions. American Mineralogist 59, 110-119.

Mahoney, J. J. and Spencer, K. J. (1991). Isotopic evidence for the origin of the Manihiki and Ontong Java oceanic plateaus. Earth and Planetary Science Letters 104, 196-210.

Mahoney, J. J., Storey, M., Duncan, R. A., Spencer, K. J. and Pringle, M. (1993). Geochemistry and geochronology of Leg 130 basement lavas: nature and origin of the Ontong Java Plateau. Proceedings of the Ocean Drilling Program, Scientific Result 130, 3-22.

McDonough, W. F. and Frey, F. A. (1989). Rare earth elements in upper mantle rocks. In: Lipin, B. R. and McKay, G. A. (eds) Geochemistry and Mineralogy of Rare Earth Elements, Reviews in Mineralogy. Washington DC: Mineral Soc. Am., 21, pp. 99-139.

McGuire, A. V. (1987). Petrology of mantle xenoliths from Harrat al Kishab: the mantle beneath western Saudi Arabia. Journal of Petrology 29, 73-92.

McKenzie, D. and Bickle, B. J. (1988). The volume and composition of melt generated by extension of the lithosphere. Journal of Petrology 29, 625-679.

Michael, P. J. and Bonnatti, E. (1985). Peridotite composition from the North Atlantic: regional and tectonic variatins and implications for partial melting. Earth and Planetary Science Letters 73, 91-104.

Milholland, C. S. and Presnall, D. C. (1998). Liquidus phase relations in the CaO-

MgO-Al_2O_3-SiO_2 system at 3.0 GPa: the aluminous pyroxene thermal divide and high-pressure fractionation of picritic and komatiitic magmas. Journal of Petrology 39, 3-27.

Mukhopadhyay, B. (1991). Garnet-clinopyroxene geobarometry: the problems, a prospect, and approximate solution with some applications. American Mineralogist 76, 512-529.

Nakanishi, M., Tamaki, K. and Kobayashi, K. (1992). Magnetic anomaly lineation from Late Jurassic to Early Cretaceous in the west-central Pacific Ocean. Geophys. J. Int. 109, 701-719.

Nakanishi, M. and Winterer, E. L. (1996). Tectonic events of the Pacific Plate related to the formation of the Ontong Java Plateau (abstract). EOS Trans. AGU Fall Meeting 77, 713.

Navon, O. and Stolper, E. (1987). Geochemical consequences of melt percolation: the upper mantle as a chromatographic column. Journal of Geology 95, 285-307.

Neal, C. R. (1985). Mantle studies in the western pacific and kimberlite-type intrusives. Ph. D. thesis, University of Leeds. 360 pp.

Neal, C. R. (1988). The origin and composition of metasomatic fluids and amphiboles beneath Malaita, Solomon Islands. Journal of Petrology 29, 149-179.

Neal, C. R. and Davidson, J. P. (1989). An metasomatized source for the Malaitan alnöite (Solomon Islands): petrogenesis involving zone refining, megacryst fractionation, and assimilation of oceanic lithosphere. Geochimica et Cosmochimica Acta 53, 1975-1990.

Neal, C. R., Mahoney, J. J., Kroenke, L. W., Duncan, R. A. and Petterson, M. G. (1997). The Ontong Java Plateau. In: Mahoney, J. J. and Coffin, M. F. (eds) Large Igneous Provinces. Washington DC: American Geophysical Union, 100, pp.183-216.

Neal, C. R. and Nixon, P. H. (1985). Spinel-garnet relationships in mantle xenoliths from the Malaita alnoites, Solomon Islands, southwestern Pacific. Trans. Geol. Soc. S. Africa 88, 347-354.

Neal, C. R. and Taylor, L. A. (1989). A negative Ce anomaly in a peridotite xenolith: Evidence for crustal recycling into the mantle or mantle metasomatism.

Geochimica et Cosmochimica Acta 53, 1035-1040.

Nickel, K. G. and Green, D. H. (1985). Empirical geothermobarometry for garnet peridotites and implications for the nature of the lithosphere, kimberlites and diamonds. Earth and Planetary Science Letters 73, 158-170.

Nixon, P. H. (1987). Mantle Xenoliths. New York: John Wiley & Suns, 844 pp.

Nixon, P. H. and Boyd, F. R. (1973). The discrete nodule association in kimberlites in northern Lesotho. In: Nixon, P. H. (ed) Lesotho Kimberlites. Cape Town: Cape and Transvaal Printers pp. 67-75

Nixon, P. H. and Boyd, F. R. (1979). Garnet bearing lherzolites and discrete nodule suites from the Malaita alnöite, Solomon Islands, S.W. Pacific, and their bearing on oceanic mantle composition and geotherm. In: Boyd, F. R. and Meyer, H. O. A. (eds) The mantle sample: Inclusions in kimberlite and other volcanics. Washington DC: American Geophysical Union, pp. 400-423.

Nixon, P. H., Mitchell, R. H. and Rogers, N. W. (1980). Petrogenesis of alnöitic rocks from Malaita, Solomon Islands, Melanesia. Mineralogical Magazine 43, 587-596.

Nixon, P. H. and Neal, C. R. (1987). Ontong Java Plateau: deep-seated xenoliths from thick oceanic lithosphere. In: Nixon, P. H. (ed) Mantle Xenoliths. Chichester: John Wiley & Suns, pp. 335-345.

O'hara, M. J. and H.S. Yoder, J. (1967). Formation and fractionation of basic magmas at high pressures. Scotttish Journal of Geology 3, 67-117.

O'Neil, H. S. C. (1981). The transition between spinel and garnet lherzolite and its use as a geobarometer. Contributions to Mineralogy and Petrology 77, 185-194.

Ozawa, K. (1983). Evaluation of olivine-spinel geothermometry as an indicator of thermal history for peridotites. Contributions to Mineralogy and Petrology 82, 52-65.

Ozawa, K. and Shimizu, N. (1995). Open-system melting in the upper mantle: constraints from the Hayachine-Miyamori ophiolite, northeastern Japan. Journal of Geophysical Research 100, 22315-22335.

Pearson, D. G., Shirey, S. B., Carlson, R. W., Boyd, F. R. and Nixon, P. H. (1995). Stabilisation of Archean lithospheric mantle: A Re-Os isotope study of peridotite xenoliths from the Kaapvaal craton. Earth and Planetary Science

Letters 134, 341-357.

Petterson, M. G. (1995). The geology of north and central Malaita, Solomon Islands (including implications of geological reseach on Makira, Savo Island, Guadalcanal, and Choiseul between 1992 & 1995) Geolocical Memoir. 1/95. Water and Mineral Resources Division, Ministry of Energy, Water and Mineral Resources, Honiara, Solomon Islands.

Petterson, M. G., Babbs, T. L., Mahoney, J. J., Saunders, A. D., Duncan, R. A., Tolia, D., Magu, R., Qopoto, C., Mahoa, H. and Natogga, D. (1999). Geological-tectonic framework of Solomon islands, SW Pacific: crustal accretion and growth within an intra-oceanic setting. Tectonopysics 301, 35-60.

Powell, R. (1985). Regression diagnosis and robust regression in geothermometry/geobarometry calibration: the garnet-clinopyroxene geothermometer revisited. Journal of Metamorphic Geology 3, 231-243.

Presnall, D. C., Dixon, J. R., O'Donnell, T. H. and Dixon, S. A. (1979). Generation of mid-ocean ridge tholeiites. Journal of Petrology 20, 3-35.

Raheim, A. and Green, D. H. (1975). Experimental determination of the temperature an pressure dependence of the Fe-Mg partition coefficient for coexisting garnet and clinopyroxene. Contributions to Mineralogy and Petrology 48, 179-203.

Ravna, E. J. K. (2000). The garnet-clinopyroxene Fe^{2+}-Mg geothermometer: an updated calibration. Journal of Metamorphic Geology 18, 211-219.

Reid, J. B. and Frey, F. A. (1971). Rare Earth distributions in lherzolite and garnet pyroxenite xenoliths and the constitution of the upper mantle. Journal of Geophysical Research 76, 1184-1196.

Richardson, S. H., Erlank, A. J. and Hart, S. R. (1985). Kimberlite-borne garnet peridotite xenoliths from old enriched subcontinental lithosphere. Earth and Planetary Science Letters 75, 116-128.

Richardson, W. P., Okal, E. A. and Van del Lee, S. (2000). Rayleigh-wave tomography of the Ontong Java Plateau. Physics of the Earth and Planetary Interiors 118, 29-51.

Robinson, J. A. C. and Wood, B. J. (1998). The depth of the spinel to garnet transition at the peridotite solidus. Earth and Planetary Science Letters 164, 277-284.

Rock, N. M. S. (1986). The nature and origin of ultramafic lamprophyres: alnöite and allied rocks. Journal of Petrology 27, 155-196.

Ross, K. and Elthon, D. (1997). Extreme incompatible trace-element depletion of diopside in residual mantle from south of the Kane Fracture Zone. In: Karson, J. A., Cannat, M., Miller, D. J. and Elthon, D. (eds) Proceedings of the Ocean Drilling Program, Scientific Result 153, 277-284.

Sack, R. O. and Ghiorso, M. S. (1991). Chromian spinels as petrogenetic indicators: thermodynamics and petrological application. American Mineralogist 76, 827-847.

Schubert, G. and Sandwell, D. (1989). Crustal volumes of the continents and of oceanic and continental submarine plateaus. Earth and Planetary Science Letters 92, 234-246.

Schulze, D. J. (1987). Megacrysts from alkaline volcanic rocks. In: Nixon, P. H. (ed) Mantle Xenoliths. Chichester: John Wiley & Suns pp. 433-452.

Sen, G. and Presnall, D. C. (1984). Liquidus phase relationships on the join anorthite-forsterite-quartz at 10 kbar with applications to basalt petrogenesis. Contributions to Mineralogy and Petrology 85, 404-408.

Shibata, T. and Thompson, G. (1986). Peridotites from the Mid-Atlantic Ridge at 43˚N and their petrogenetic relation to abyssal tholeiites. Contributions to Mineralogy and Petrology 93, 144-159.

Shimizu, N. (1999). Young geochemical features in cratonic peridotites from Southern Africa and Siberia. In: Fei, Y., Bertka, C. M. and Mysen, B. O. (eds) Mantle Petrology: Field observation and high pressure experimentation: A tribute to Francis R. (Joe) Boyd, 47-55.

Shimizu, N., Pokhilenko, N. P., Boyd, F. R. and Pearson, D. G. (1997). Geochemical characteristics of mantle xenoliths from the Udachnaya kimberlite pipe. Russian Geology and Geophysics 38, 205-217.

Simakov, S. K. (1999). Garnet-clinopyroxene geobarometry of deep mantle eclogites and eclogite paleogeotherms. In: Gurney, J. J., Gurney, J. L., Pascoe, M. D. and Richardson, S. H. (eds) Proceedings of the VIIth international kimberlite conference. Cape Town: Red Roof Desing cc, pp. 783-787.

Sinton, J. M. (1979). Petrology of (Alpine-type) peridotites from Site 395, DSDP Leg 45. In: Melson, W. G. and Rabinowitz, P. D. (eds) Init. Repts. DSDP, 45.

Smith, D. and Boyd, F. R. (1987). Compositonal heterogeneities in a high temperature lherzolite nodule and implications for mantle processes. In: Nixon, P. H. (ed) Mantle Xenoliths. Chichester: John Wiley & Suns, pp. 551-562.

Smyth, J. R. (1980). Cation vacancies and the crystal chemistry of breakdown reactions in kimberlitic omphasites. American Mineralogist 65, 1185-1191.

Suen, C. J. and Frey, F. A. (1987). Origins of the mafic and ultramafic rocks in the Ronda peridotite. Earth and Planetary Science Letters 85, 183-202.

Sun, S.-s. and McDonough, W. F. (1989). Chemical and isotoic systematics of oceanic basalts: implications for mantle composition and processes. In: Saunders, A. D. and Norry, M. J. (eds) Magmatism in the Ocean Basins. Geological Society Special Publication, pp. 313-345.

Takahashi, E. and Kushiro, I. (1983). Melting of a dry peridotite at high pressures and basalt magma genesis. American Mineralogist 68, 859-879.

Takahashi, E., Nakajima, K. and Wright, T. L. (1998). Origin of the Columbia River basalts: melting model of a heterogeneous plume head. Earth and Planetary Science Letters 162, 63-80.

Takahashi, E., Shimazaki, T., Tsuzaki, Y. and Yoshida, H. (1993). Melting study of a peridotite KLB-1 to 6.5 GPa and the origin of basaltic magmas. Philosophical Transactions of the Royal Society of London 342, 105-120.

Takahashi, E. and Nakajima, K. (2002). Melting process in the Hawaiian plume: an experimental study. In: (eds.) Hawaiian volcanoes: deep underwater perspectives. Washington: American Geophysical Union, pp.

Takazawa, E., Frey, F. A., Shimizu, N., Obata, M. and Bodinier, J.-L. (1992). Geochemical evidence for melt migration and reaction in the upper mantle. Nature 359, 55-58.

Takazawa, E., Frey, F. A., Shimizu, N., Saal, A. and Obata, M. (1999). Polybaric petrogenesis of mafic layers in the Horoman peridotite complex, Japan. Journal of Petrology 40, 1827-1851.

Tarduno, J. A. and Sager, W. W. (1995). Polar standstill of the mid-Cretaceous Pacific plate and its geodynamic implications. Science 269, 5226-5228.

Tarduno, J. A., Sliter, W. V., Kroenke, L. W., Leckie, M., Mahoney, J. J., Musgrave, R. J., Storey, M. and Winterer, E. L. (1991). Rapid formation of the Ontong

Java Plateau by Aptian mantle plume volcanism. Science 254, 399-403.

Taylor, B. (1978). Mesozoic magnetic anormalies in the Lyla Basin (abstract). EOS Trans. AGU Fall Meeting 59, 320.

Tejada, M. L. G., Mahoney, J. J., Duncan, R. A. and Hawkins, M. P. (1996). Age and geochemistry of basement and alkalic rocks of Malaita and Santa Isabel, Solomon Islands, Southern margin of Ontong Java Plateau. Journal of Petrology 37, 361-394.

Tejada, M. L. G., Mahoney, J. J., Neal, C. R., Duncan, R. A. and Petterson, M. G. (2000). Modeling the mantle source of the Ontong Java Plateau (OJP): peridotitic plume vs. composite diapir model (abstract). EOS Trans. AGU Fall Meeting 81, 921-922.

Toramaru, A. and Fujii, N. (1986). Connectivity of melt phase in a partially molten peridotite. Journal of Geophysical Research 91, 9239-9252.

Tsuruta, K. and Takahashi, E. (1998). Melting study of an alkali basalt JB-1 up to 12.5 GPa: behavior of potassium in the deep mantle. Physics of the Earth and Planetary Interiors 107, 119-130.

Vernieres, J., Godard, M. and Bodinier, J.-L. (1997). A plate model for the simulation of trace element fractionation during partial melting and magmas transport in the Earth's upper mantle. Journal of Geophysical Research 102, 24771-24784.

Walker, R. J., Carlson, R. W., Shirey, S. B. and Boyd, F. R. (1989). O, Sr, Nd and Pb isotope systematics of southern African peridotite xenoliths: Implications for the chemical evolution of subcontinetal mantle. Geochimica et Cosmochimica Acta 563, 1583-1595.

Walter, M. J. (1998). Melting of garnet peridotite and the origin of komatiite and depleted lithosphere. Journal of Petrology 39, 29-60.

Wang, W. and Yurimoto, H. (1994). Analysis of rare earth elements in garnet by SIMS. Ann. Rep. Inst. Geosci., Univ. Tsukuba 19, 87-91.

Wells, P. R. A. (1977). Pyroxene Thermometry in Simple and Complex Systems. Contributions to Mineralogy and Petrology 62, 129-139.

Winterer, E. L. and Nakanishi, M. (1996). Evidence for a plume-augmented, abandoned spreading center on Ontong Java Plateau (abstract). EOS Trans. AGU Fall Meeting 76, 617.

Wood, B. J. and Banno, S. (1973). Garnet-orthopyroxene and clinopyroxene-

orthopyroxene relationships in simple and complex systems. Contributions to Mineralogy and Petrology 42, 109-124.

Wood, B. J. and Henderson, M. B. (1978). Composition and unit cell parameters of synthetic non-stoichiometric tchermakitic clinopyroxenes. American Mineralogist 63, 66-72.

Xu, Y. G., Menzies, M. A., Bodinier, J. L., Bedini, R. M., Vroon, P. and Mercier, J. C. C. (1998). Melt percolationand reaction atop a plume: evidence from the poikiloblastic peridotite xenoliths from Boree (Massif Central, France). Contributions to Mineralogy and Petrology 132, 65-84.

Yang, H. J., Sen, G. and Shimizu, N. (1998). Mid-oceanic ridge melting: constraints from lithospheric xenoliths at Oahu, Hawaii. Journal of Petrology 39, 277-295.

Yasuda, A., Fujii, T. and Kurita, K. (1998). Ascending subducted oceanic crust entrained within mantle plumes. Geophysical Research Letters 25, 1561-1564.

Yasuda, A., Fujii, T. and Kurita, L. (1994). Melting phase relations of an anhydrous mid-ocean ridge basalt from 3 to 20 GPa: implications for the behavior of subducted oceanic crust in the mantle. Journal of Geophysical Research 99, 9401-9414.

Yaxley, G. M. (2000). Experimental study of the phase and melting relations of homogeneous basalt + peridotite mixtures and implications for the petrogenesis of flood basalt. Contributions to Mineralogy and Petrology 139, 326-338.

Yaxley, G. M. and Green, D. H. (1998). Reactions between eclogite and peridotite: mantle refertilisation by subduction of oceanic crust. Schwiz. Mineral. Petrogr. Mitt. 78, 243-255.